ABSTRACT

YOUM, HYESEON. Discrete Element Modeling of Geosynthetic Reinforcement in Pavement Overlays. (Under the direction of Dr. Mohammed A. Gabr and Dr. Y. Richard Kim).

Reflective cracking is one of the most serious problems in AC overlays. The application of geosynthetics in pavement rehabilitation has been considered to strengthen pavement and extend its service life, with one of the effects being the mitigation of reflective cracking. There is a major gap in the understanding of the contributing mechanisms of geosynthetics in overlays under applied loading conditions. To quantify the benefits of geosynthetics in pavement overlay for reducing or retarding reflective cracking, a better understanding of the contributing mechanisms is needed. The discrete element method (DEM) is the most suitable for capturing the particle-level behavior of complex systems such as reinforced overlays with geosynthetics.

A DEM fracture model based on field scale is used for model calibration, and reflective cracking is analyzed and compared with field data with respect to both overlay thickness and geosynthetic properties, with and without reinforcement. Based on model calibration, the current research uses the discrete element method to quantify the mechanisms that govern the response of reinforced overlays with geosynthetics under different loading conditions (e.g., constant loading, constant loading rate, and dynamic wheel loading). The DEM pavement model is developed and analysis is conducted under constant loading. Analyses of displacement of overlay on top of asphalt concrete, as well as strain and stress distributions, are performed both with and without reinforcement. In addition, the stress and porosity contours of the overlay are displayed in order to enable visual evaluation. To evaluate the effects of geosynthetics, the following factors are investigated without and with

reinforcement: i) effect of an initial crack on overlay (including geosynthetic properties, geosynthetic locations and aggregate distribution), ii) effect of existing pavement conditions (PCC properties, PCC crack widths), and iii) effect of overlay thickness. In addition, DEM pavement modeling is conducted under a constant loading rate of y-velocity equals 0.7 mm/s. This study includes the comparisons of maximum stress and maximum strain observed from 5 different measurement circles at a local level, and macro and micro cracks are displayed in order to enable visual comparison of reflective cracking. Finally, moving wheel load tests, as one of the different loading conditions for unreinforced and reinforced overlays, are conducted by using a DEM model. The effect of wheel movement from the left to the right side of the overlay is examined only once because of the issue of computational time. Stress and strain are monitored from measurement circles at 5 different positions along the moving wheel.

The results obtained under different loading conditions clearly indicate that geosynthetic reinforcement provides significant benefit in reducing/retarding reflective cracking by reducing stress and strain. Reinforcement at one-third of depth is most effective, and increasing overlay thickness also has a strong effect on decreasing stress and strain.

Discrete Element Modeling of Geosynthetic Reinforcement in Pavement Overlays

by
Hyeseon Youm

A dissertation submitted to the Graduate Faculty of
North Carolina State University
in partial fulfillment of the
requirements for the degree of
Doctor of Philosophy

Civil Engineering

Raleigh, North Carolina

2012

APPROVED BY:

_____	_____
Dr. M. Shamim Rahman	Dr. T. Matthew Evans
_____	_____
Dr. Mohammed A. Gabr Co-Chair of Advisory Committee	Dr. Y. Richard Kim Co-Chair of Advisory Committee

DEDICATION

To my parents

Dong-mahn Youm

Jung-ae Jung

To my parents-in-law

Jung-Oh Lee

Ok-Hee Kim

and my husband

Bongmook Lee

BIOGRAPHY

Hyeseon Youm received Bachelor of Science in Civil from Chungang University in 1999 and obtained Master of Science degree in Civil Engineering from Chungang University (Seoul, South Korea) in 2001. She worked in Univec Engineering & Construction Co., Seoul, Korea as an entry-level engineer from April in 2001 to December in 2001. In August 2004, she began her Ph.D study in the Department of Civil, Construction and Environmental Engineering at North Carolina State University, Raleigh.

ACKNOWLEDGMENTS

First of all, I would like to express my deepest appreciation to my advisor, Dr. Mohammed A. Gabr for his invaluable guidance, encouragement and constant support during my graduate career. Without his supervising and inspiring this could not be happen. I would also like to thank Dr. Y. Richard Kim, Dr. M. Shamim Rahman, and Dr. T. Matthew Evans for their sincere advice on my research work and for being on my dissertation committee.

One reason that I consider myself fortunate is to have a chance to meet the geotechnical group members of NCSU: Dr. Wansoo Kim, Dr. Jongkoo Jeon, Dr. Youngjin Park, Dr. Nadia Sharmin, Dr. Xueling Zhao, Sangchul Pyo, and Jungmok Lee for their help, friendship, and great times. I am thankful to my friends Dr. Kosok Chae, Minkyung Kim, and Dr. Sol-A Park for their encouragement and friendship. I specially thank to Diana Genest for editing this dissertation nice and smooth.

I am very grateful to my parents, parents-in-law, and my sister, Hyejung for believing in me and showing their endless support and love at every step. Last but not the least I wish to thank my husband, Bongmook and my boys, Hyoseon and Woojin. Any word in the world cannot express my gratitude to them.

TABLE OF CONTENTS

LIST OF TABLES

LIST OF FIGURES

Chapter 1 Introduction

Pavement rehabilitation is one of the most important issues contributing to creating robust highway infrastructure. Asphalt concrete overlay is a common method for rehabilitating deteriorated pavements. When an overlay is placed above existing pavement, cracks may propagate through the overlay due to movement of the joints or due to the upward extension of cracks in the existing pavement layer. This phenomenon is known as reflective cracking. Reflective cracking in asphalt concrete overlay leads to structural deficiencies and poor performance. In general, reflective cracking in pavement overlay is mainly caused by driving forces generated by load and temperature (Cleveland et al., 2002).

Applied wheel load induces shear stresses and leads to reflective cracking in the overlay above an existing crack as shown in Figure 1.1 (Buttlar, 2002). Additionally, reflective cracking expands due to the horizontal movement of the slab with temperature changes and thermal expansion/contraction. During cold weather, stresses induced by both wheel loading and thermal changes can increase significantly because the asphalt concrete becomes stiffer and brittle at low temperatures (Buttlar, 2002).

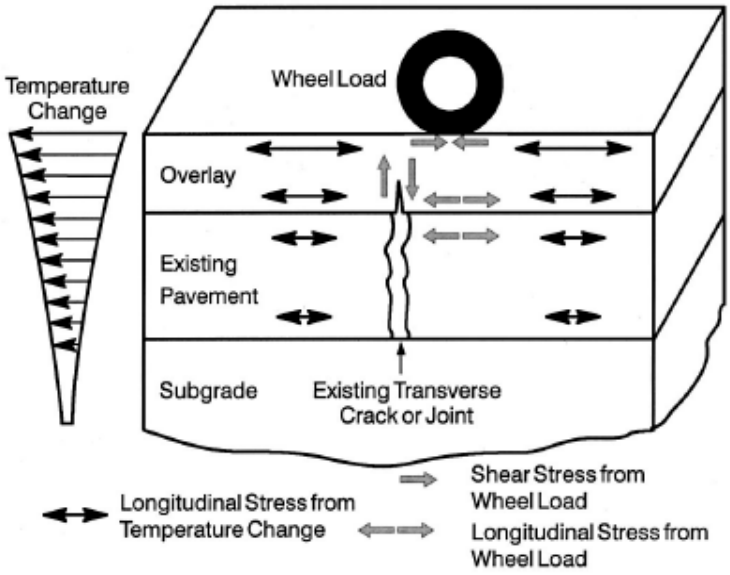

Figure 1.1 Reflective cracking and principal crack driving forces (Buttlar, 2002)

Since the early 1930s, considerable effort has been expended to find economical techniques to minimize reflective cracking (Barksdale et al. 1989). Some of these efforts included increased overlay thickness, the use of asphalt mix additives such as polymer, sulfur, or dry lime, the use of bond breakers at pavement joints, and the use of stress-absorbing interlayers such as paving fabrics (Barksdale, 1991). In recent years, geosynthetic grids have been used in pavement rehabilitation as well, to strengthen pavement and extend its service life, with one of their attributes being the mitigation of reflection cracking.

The Guide for Mechanistic-Empirical Design of New and Rehabilitated Pavement Structures (M-E PDG) (AASHTO, 1993, 2002) includes design procedures to be used by Departments of Transportation in pavement technology; however, no explicit guidelines are provided for tensile reinforcement in the rehabilitation of asphalt overlays. As experimental

evidence points to the beneficial contribution of geosynthetics to the performance of pavement overlays (Sposito et al. 1999, Barnhart 1989, Button and Lytton 1987, Amini 2005), there is a need to study the mechanistic aspects forming the basis of that contribution, and to systematically evaluate the factors that control the overlay response when geosynthetics reinforcement is used.

According to field and laboratory testing data (Sherman, 1982; Finn and Monismith, 1984; Holtz et al., 1998; Barksdale, 1991; Lytton et al., 1989; Cleveland et al., 2002; Amini, 2005), geosynthetics can reduce and retard reflective cracking, as well as function as a moisture barrier, stress relief layer, and reinforcement (Figure 1.2 from Marienfeld et al., 1999). Several studies on the use of geosynthetics to reduce the reflective cracking have been focused, however, on empirical assessments and therefore results interpretation and extension to other situations are limited (Lytton et al., 1989; Cleveland et al., 2002; Amini, 2005). One major gap is the limited understanding of the contributing mechanisms of geosynthetics to overlay layers under applied loading conditions. To quantify the benefits of geosynthetics in pavement overlay for reducing reflective cracking, a better understanding of the contributing mechanisms is needed.

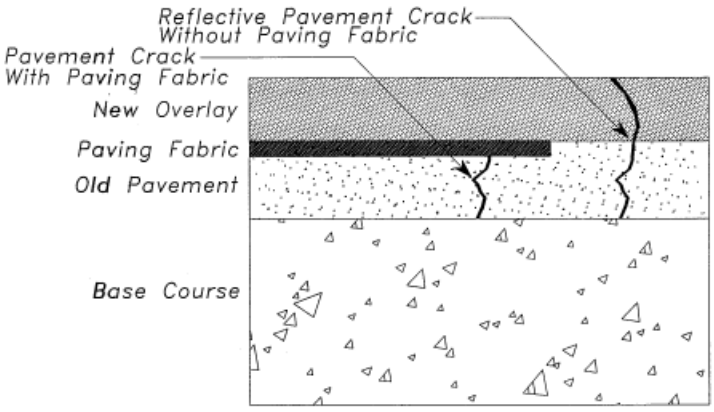

Figure 1.2 Cross section with and without paving fabric in a rehabilitated pavement section (Marienfeld, et al., 1999)

While the finite element method (FEM) is commonly used in pavement applications for computing mechanics problems, the discrete element method (DEM) has some advantages in this case. Cundall and Stack (1979) mentioned that DEM is a powerful tool for simulating the response of granular and bonded materials because macro-scale constitutive equations are not needed. According to previous research (Sadd et al. 2004, Chang et al. 1997, Kose et al, 2000), DEM can properly model fractures in heterogeneous materials, since the materials can be represented by discontinuous particles at certain levels, on the micro- and the meso-scale (Kim, 2005). Due to its intrinsic flexibility, DEM modeling is the most suitable for capturing the particle-level behavior of complex systems, such as overlays reinforced with geosynthetics. The main benefits of DEM studies (Konietzky et al., 2000, 2004; McDowell et al., 2006), in comparison with the continuum approach, can be summarized as follows (Kwon, et al., 2008):

- Direct and exact reproduction of the structure and properties of the geosynthetic;

- Fully accounting for the kinematics of the aggregate particles such as rotation and translation;
- Directly and fully accounting for the aggregate particle size distribution and shape;
- Simulating the most realistic interaction of the aggregate with the geogrid.

1.1 Study Objectives

The general objective of this research is to develop a DEM model and implement it for the assessment of the effects of geosynthetic reinforcement in stabilizing pavement overlays. The scope of the proposed research is focused on using the discrete element method to quantify the mechanisms that govern the response of overlays reinforced with geosynthetics under different loading conditions. Several factors will be investigated including the optimum placement of the geosynthetic layer, the impact of the properties and types of geosynthetic interfaces, and the effect of the total thickness of the overlay on reflective cracking characteristics. Performance parameters including deformation of overlay on top of asphalt concrete, as well as strain and stress distributions will be addressed. In addition, the stress and porosity contours of the overlay are displayed in order to enable visual evaluation. Specifically the following objectives will be pursued:

1) Develop a DEM model of AC overlays on PCC pavement with and without geosynthetic reinforcement;
2) Calibrate the developed DEM model with field data as found from literature;
3) Perform sensitivity analysis and parametric analysis of the DEM model for overlay incorporating a geosynthetic interlayer under loading conditions to study;

i) Effect of initial crack in AC overlays including different geosynthetic properties, locations, and aggregate distributions

ii) Effect of old pavement conditions including properties of the PCC and crack width,

iii) Effect of the overlay thickness;

4) Investigate displacement of the overlay, stress and strain around initial crack tip and;

5) Display stress and porosity contours for AC layer;

6) Recommend usage of geosynthetics based on the sensitivity and parametric analysis of a DEM model.

1.2 Scope of thesis

In this study, some simplified models are developed and implemented. The layout of this study is presented in Figure 1.3. The scope of this study is as follows:

Chapter 2 reviews the past work to identify the successful studies of reducing/retarding reflective cracking of overlay pavements with geosynthetic reinforcement, including both laboratory and field data.

Chapter 3 provides the fundamental model descriptions of the DEM and presents the model properties for this study including pavement section modeling, and model parameters determination. Parametric analyses are conducted for the time step safety factor, friction coefficient and particle stiffness.

Chapter 4 develops and calibrates the DEM fracture model based on field dimensions, and studies the effects of geosynthetic reinforcement, overlay thickness, the

properties of the geosynthetic material, and its placement in relation to the overlay, and then compares these with field case studies.

Chapter 5 develops the DEM model under constant loading conditions (80 psi), conducts the parametric studies, and describes not only the effects of initial crack including geosynthetic locations, geosynthetic properties, and asphalt aggregate distribution, but also the effects of old pavement conditions including properties of the PCC and crack width. In addition, the effects of overlay thickness are studied, especially, as an aspect of displacement, stress and strain distributions around initial crack tip, and stress and porosity contours for AC layer are displayed as well.

Chapter 6 develops the DEM fracture model under y-velocity controlled monotonic loading to investigate the effects of the geosynthetics on stress, strain in a local level, and macro- and micro-crack patterns.

Chapter 7 develops DEM model under moving wheel loading to investigate stress and strain distributions in a local level according to moving wheel load.

Chapter 8 summarizes the main conclusions of the current work and makes recommendations for future study.

References will be provided at the end of this thesis.

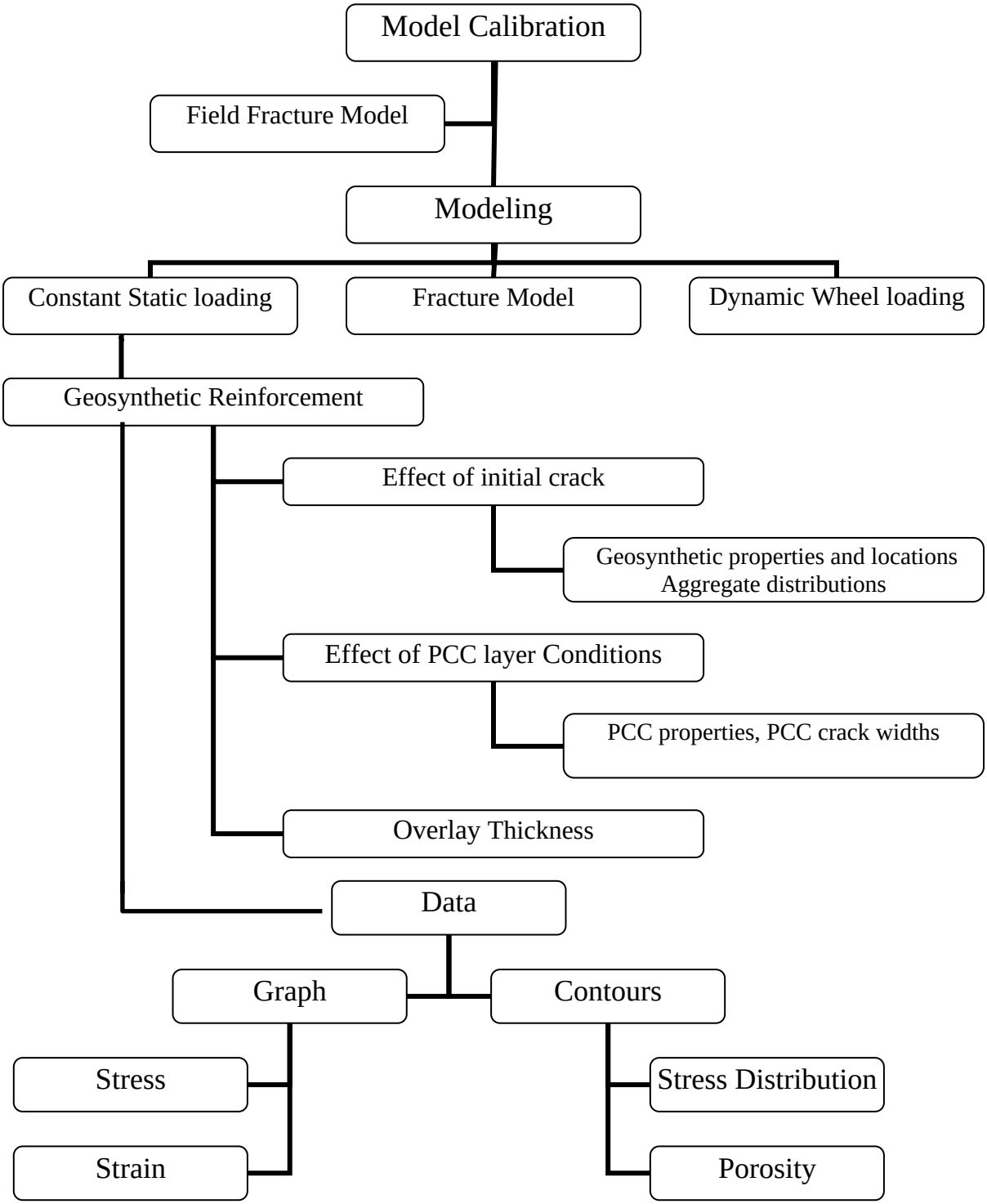

Figure 1.3 Layout of data analyses

Chapter 2 Literature Review

2.1 Introduction

Many pavements that are considered structurally sound after overlay, untimely exhibit a similar cracking pattern to that of the old pavement layer. In analyzing issues of reflective cracking, it is necessary to understand the mechanisms associated with fracture behavior. Techniques aimed to reduce, or even prevent, reflective cracking include reinforcement of the overlay layer. This chapter focuses on the use of geosynthetic reinforcement to reduce reflective cracking. A brief overview of fracture modeling of asphalt concrete is also presented in view of linear elastic and non linear fracture mechanics. Various numerical methods such as the finite element method (FEM), the discrete element method (DEM) and others are briefly reviewed with a focus on their applications in the area of asphalt materials.

2.2 Mechanisms of Reflective Cracking

Cracking in new overlay surfaces maybe induced by shear and tensile stresses created by traffic loading (tire pressure) and/or by thermal loading (expansion and contraction). Lytton (1989) pointed out that whenever a load passes over a crack in the old pavement, three types of pulses of high stress concentrations are induced at the tip of the crack as it propagates upward through the overlay (see Figure 2.1). The first stress pulse is a maximum shear stress pulse at point A. The second stress pulse is a maximum bending stress pulse at point B. The third stress pulse is another maximum shear stress pulse; however, it has the opposite direction of the first shear pulse. In some instances where there is a void beneath the

old surface, the maximum shearing stress (load at point C) is usually larger than shear stresses at point A. These stress pulses occur within a very short time. The stiffness of the asphalt concrete overlay and existing pavement is very high at high loading rates (Cleveland et al., 2002). A small increase in crack length in the overlay is caused with each increase in the number of load repetitions. As the number of loadings increases, the crack growth rate increases. As a result, reflective cracking in the overlay progresses rapidly from the existing pavement surface.

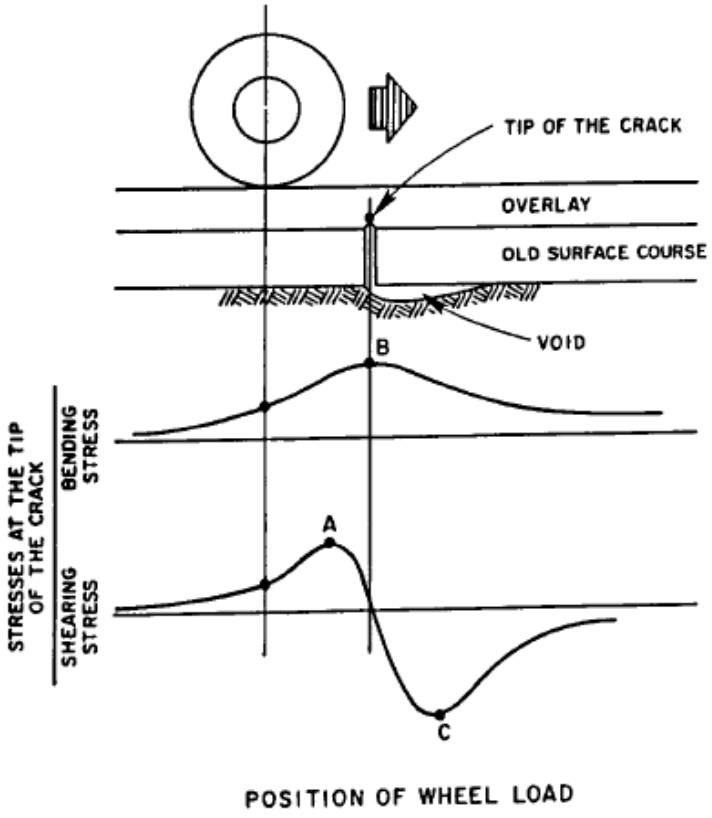

Figure 2.1 Shear and bending stress induced at a crack caused by a moving wheel load (Lytton, 1989)

Another factor contributing to the occurrence of reflective cracking is the change of temperature in an overlaid pavement as shown in Figure 2.2. Temperature changes cause the contraction and curling of the underlying old pavement (at Point B). It has been observed that cracks that propagate both from the top and the bottom of the overlay can be induced by thermal stresses. The contraction and curling behaviors of the old pavement cause a shear stress along the bottom of the overlay, hence, developing a concentration of tensile stress at Point B. Temperatures in pavement change very slowly over the course of several hours in a day. Whenever loading or temperature changes, reflective cracks in an old pavement grow. Lytton (1989) suggested that the best way to retard growth of these cracks in an overlaid pavement was to embed a geotextile layer in it.

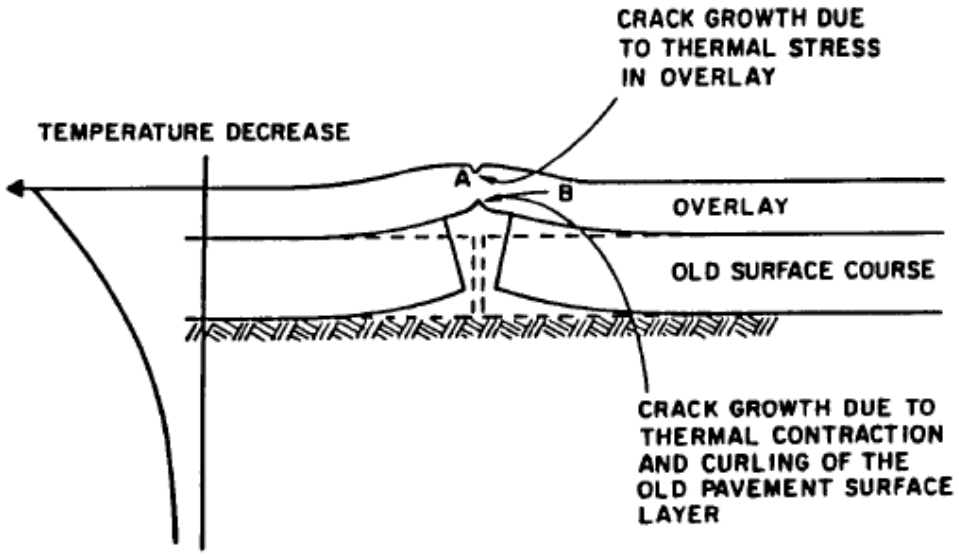

Figure 2.2 Temperature changes and consequent crack growth in overlays (Lytton, 1989)

2.3 Methods of Reducing Reflective Cracking

In general, the methods described in the literature attempt either to decrease or to redistribute the stresses at the bottom of the overlay or to increase the tensile strength of the AC (Alden and Darling, 2004). Depending on the types of overlay and existing pavement, four possible measures have been categorized in literature (Huang, 1993): i) hot mix asphalt (HMA) overlays on asphalt pavements, ii) HMA overlays on Portland cement concrete (PCC) pavements, iii) PCC overlays on asphalt pavement, and iv) PCC overlays on PCC pavements. A major challenge, however, in the design of hot mix asphalt overlays on Portland cement concrete pavements is reflective cracking (Huang, 1993). Huang (1993) and Roberts et al. (1996) categorized several methods to address the issue of reflective cracking. Cleveland et al. (2002) conducted a literature review of approaches for minimizing reflective cracking. Methods reported in literature to minimize the reflective cracking include the following (Barksdale 1991, Huang 1993, Roberts et al 1996, Cleveland et al. 2002).

(1) Design a thicker HMA overlay.

(2) Crack and seat the existing PCC slab into smaller sections.

(3) Use a crack relief layer with drainage system.

(4) Saw and seal joints in an HMA overlay.

(5) Use a stress-absorbing membrane interlayer with an overlay.

(6) Incorporate a fabric membrane interlayer with an overlay.

Method (1) may be used if the thickness of the overlay does not exceed 9 inches (229 mm) (Huang, 1993). Barksdale (1991) provided a minimum overlay thickness. He

recommended a minimum of 2 inches of overlay when alligator cracking exists, over 2 inches for base failures, and a minimum of 3 inches (3.5 desirable) when block cracking is present. Methods (2) and (3) are special treatments on the existing surface investigated by McLaughlin (1979), Lyon (1970), Sherman (1982) and Button et al. (1994) as alternate techniques for reducing reflective cracking. Method (4) is used as a method of minimizing reflective cracking in HMA overlays. Gurjar et al. (1997) provided guidelines for the selection, testing, and performance of joint sealants used in PCC pavements. Jackson (1980) reported performance results of bond breakers on PCC pavement ranging from ineffective to excellent on overlay thicknesses of 1.5 to 4.75 inches. Methods (5) and (6) are being used in some areas and appear to be effective in reducing reflective cracking. However, the available documentation on the performance of these interlayers is not sufficient to indicate the optimal thickness of overlay. Therefore, if the interlayer method is considered, the overlay thickness should be addressed as well (Huang, 1993). The literature reviewed herein is focused on the use of geosynthetic-interlayers for reinforcing HMA overlays to reduce reflective cracking.

2.4 Geosynthetics in Asphalt Pavements

North America is the second largest consumer of geotextiles in asphalt overlays of pavement. According to Holtz et al. (1998), an estimated 100 million square yards (26% of all geotextiles) was consumed for overlays in 1993 (Holtz et al., 1998). There are three types of geosynthetics currently available; geotextiles, geogrids and composites.

Geotextiles

Geotextiles used to improve pavement performance are made from polypropylene or polyester. There are two types of geotextiles categorized according to manufacturing process: woven and nonwoven. In general, nonwoven paving fabrics typically show relatively low moduli and thus can mobilize only limited strength at low strain levels in comparison to woven geotextiles (Cleveland et al., 2002). Carmichael and Marienfeld (1999) mentioned three benefits of these fabric interlayers: waterproofing of the lower layers, retarding of reflective cracking in the overlay, and providing for more stable subgrade moisture contents.

Geogrids

Geogrids are typically made from high-modulus filaments of glass fibers or drawn polymers. Geogrids have a higher modulus than that of asphalt overlay, which reduces reflective cracking as a function of decreasing stresses in the new overlay. The main function of the geogrid is as a reinforcing interlayer with high stiffness. To have sufficient stiffness, a geogrid must be tightly stretched, or slightly pretensioned (Cleveland et al., 2002). In general, geogrids for overlay reinforcement exhibit stiffnesses varying from 80 to over 1000 lb/inch. However, only the stiffest grids can act as overlay reinforcement (Barksdale, 1991).

Composites

Composites were introduced in 1990 (Carver and Sprague, 2000). Composites generally consist of a combination of geotextile and geogrid materials. Within the composite, the geotextile is serves primarily to hold asphalt and to give adequate adhesion of the composite onto a pavement surface. The geogrid contributes high tensile strength and stiffness (Cleveland et al., 2002). According to Carver and Sprague (2000), laboratory

research on composites showed them to be highly beneficial; on the other hand, field research on composites in pavement applications has produced varying results. Hermann et al. (1997) reported that because of the combined benefits of fabrics and grids, composites have shown effectiveness in minimizing reflective cracking in HMA overlays. Also, Saraf et al. (1996) found that asphalt concrete beams reinforced with composite showed significantly better performance than beams reinforced with fabric alone, though beams reinforced with fabric performed better than unreinforced beams.

2.4.1 Laboratory Tests of Geosynthetics in Overlays

Laboratory tests are useful to show and prove the effectiveness of overlay systems under controlled loading and environmental conditions. However, Cleveland (2002) indicated that laboratory tests should be used only as an initial screening technique and not as a replacement for field test sections. The behavior in the laboratory of paving fabric, grids, asphalt rubber, fiber-reinforced HMA, and other materials has been studied by Button and Lytton (1987), Smith (1984, 1983), Jayawicrama and Lytton (1987), Germann and Lytton (1979) and others. Tests were typically conducted to determine the number of load cycles required to produce a certain measured crack length. In order to accurately simulate field behavior of pavements, most researchers prepare and test asphalt concrete beams either in the tensile or bending mode. In general these studies showed that geotextiles provide a level of improvement when compared to beams with no geotextile reinforcement.

2.4.2 Field Performance of Geosynthetics in Overlay

The propagation of cracks from the existing pavement into the new overlay is known as reflective cracking (Jayawicrama and Lytton 1987, Lytton 1989). Reflective cracking problems in asphalt concrete (AC) overlays, especially Portland cement concrete (PCC) pavements, have been observed for many years. These cracks can cause severe degradation and consequently reduce the service life of asphalt pavements. As mentioned earlier, methods have been used to redistribute tensile stresses with varying degrees of success (Aldea and Darling, 2004; Elseifi et al., 2003; Shuler and Harmelink, 2004). Reducing the stress can be accomplished by installing a soft stress absorbing layer or by using material with high tensile strength such as geosynthetics or steel reinforcement. In general, geosynthetic interlayers have major three functions as i) a moisture barrier, ii) stress relief layer and iii) reinforcement through tension membrane contribution or providing confinement through interface friction.

Many studies have concluded that asphalt concrete pavement overlays benefit from the inclusion of paving fabric interlayers (Barnhart 1989, Yamaoka et al. 1990, Heins 1989, Allison 1989). Holtz et al. (1988) provided information about geosynthetic reinforcement in asphalt or concrete overlays to prevent infiltration of water into the subbase, or to relieve stresses transferred into the overlay by underlying reflective cracking. They recommended following the AASHTO (1993) guidelines, designing the thickness of the overlay as if the geotextile was not present. They proposed changing the drainage coefficients in the "structural thickness equation" to allow for an overall reduction in the thickness of the overlay with the inclusion of geosynthetics. No specific recommendation was presented regarding use of geosynthetics as a stress relief layer. Lytton (1989) developed an equation to

determine the thickness of the asphalt overlay for a given geosynthetic interlayer, according to material types. For the fabrics, the optimum overly thickness is estimated using the following equation (Lytton, 1989).

$$d_0 = \frac{k_0 \Delta}{(f_{t0})\beta \sinh\left(\frac{\beta w}{2}\right)}\left[\cosh\frac{\beta w}{2} - 1\right] - nt_f \tag{2.1}$$

For the grid, the optimum overlay thickness can be calculated by following equation.

$$d_0 = \frac{k_0 \Delta}{(f_{t0})(1+np)\beta \sinh\left(\frac{\beta w}{2}\right)}\left[\cosh\frac{\beta w}{2} - 1\right] \tag{2.2}$$

where k_0 = the initial slope of shear stress versus shear displacement relation of overlay, and

Δ = the cracking opening

$$\beta = \sqrt{\frac{k_0}{E_u d_u}} \tag{2.3}$$

where, E_u is the elastic stiffness of the underlayer

d_u is the thickness of the underlayers

nt_f = the stiffness of the fabric

f_{to}= the design tensile strength of the overlay

w = the minimum width of fabric or grids placed above the old pavement surface crack

n = the elastic stiffness ratio of the overlay

p = the ratio of the cross-sectional area of the grid or fabric divided by the cross-sectional area of the overlay

Maxim technology Inc. (1997) looked at more than 200 reports that used geosynthetics in asphalt overlays and suggested a model for design. Maxim suggested that the inclusion of a geosynthetic layer allowed a corresponding reduction in asphalt thickness that ranged from 25 to 45 mm (1 to 1-3/4 in). This equivalence has also been reported by Carmichael and Marienfeld (1999), and 15 mm (0.6 in) equivalence by cost was reported by Marienfeld and Smiley (1994). The biggest challenge with citing equivalent thicknesses is that the design properties of the geosynthetics, asphalt concrete, the base course, and the subgrade are often not reported alongside the resulting equivalent thickness. Carver and Sprague (2002) concluded that asphalt reinforcement technology is still relatively new, and its use in pavement is complex. They mentioned that more experience and data are needed for acceptable determinations of performance and economic benefits in practice. The authors compared actual and expected performance using available design and analysis techniques. Similarly, Cleveland et al. (2002) evaluated the placement of geotextiles under, or within, a hot mix asphalt overlay to reduce the severity or delay the appearance of reflective cracks. They summarized several decades of overlay research, frequently citing Barksdale (1991). They reported the results of laboratory testing on six geosynthetics used in overlays. They proposed a “reinforcing factor” based on fracture mechanics. Based on data from lab testing,

the authors observed that the geosynthetics consistently increased the number of cycles to failure in the overlay tester. Elseifi and Al-Qadi (2003) presented the development of an overlay design procedure to predict the service life of rehabilitated flexible pavement structures against reflective cracking. They proposed a model that can be used to predict the number of cycles to failure. However, they recommended validation and long-term field evaluation of their proposed model. Perkins et al. (2005) focused on two main benefits of geosynthetics in a bound layer: i) to allow reduction of the thickness of the asphalt layer or ii) to provide a longer life compared to unreinforced asphalt overlays of the same thickness. Perkins et al. (2005) noted that selection of pavement overlays is largely based on local experience.

From a design point of view, Perkins et al. (2005) noted that no model currently used for design considers the wide range of factors that affect the field performance of asphalt pavement. Perkins et al. (2005) also mentioned that the causes of success and failure in projects with and without geosynthetics are still largely unknown. Amini (2005) surveyed a number of field reports that described the performance of geosynthetic overlays meant to reduce reflective cracking. He concluded that, unless the asphalt overlay was very thin (on the order of 25 to 37 mm or 1 to 1.5 in. thick), geosynthetics are very effective in reducing reflective cracking based on the results of long-term monitoring. Amini (2005) also looked at cost effectiveness and life cycle costs surveys in literature, noting the difficulty in identifying and assigning costs to the benefits that may be realized from the use of geosynthetic reinforcement. He further noted that overlays tended to be more effective in warmer climates, due to freeze-thaw cyclic stresses occurring in colder climates between the overlay fabric and

the new pavement (instead of cracks developing from the base and reflecting into the new asphalt).

In summary, although there are somewhat different recommendations regarding the overlay thickness, geosynthetics may not reduce cracking significantly with thin overlays. Factors such as the local climate and the traffic volume should also be considered prior to design.

2.4.3 Cost effectiveness of Geosynthetics

In examining the life cycle costs of paving fabrics, Sprague (2005) developed a technique to compare the relative costs of fabrics with overlays, overlays only, and full recycling. By comparing South Carolina road records, Sprague (2005) concluded the cost-effectiveness of a particular application depended largely on the initial condition of the roadway prior to application of the overlay. The roadway condition was defined by a "Pavement Condition Index", a scale that is likely not measured in the same way from state to state. Yang and Al-Qadi (2006) conducted life cycle cost analysis for an optimum secondary road flexible pavement design with geotextile incorporated. They presented a cost-analysis process that includes costs for the initial construction, each rehabilitation, work-zone queue delays, moving delays, accidents, and fuel consumption. Both methods by Al-Qadi and Perkins showed a positive traffic benefit ratio (TBR) or increase in number of cycles to failure at a low cost benefit ratio (CBR).

2.5 Overview of Fracture Mechanics

Stresses around cracks are of great interest in design. The evaluation of the stresses around cracks is very important in predicting the failure mode and the resistance of the material to loading conditions.

There are two main approaches for predicting the failure of laminated composites where used to rehabilitate cracked pavement (Seif et al. 2001). The first approach is linear elastic fracture mechanics (LEFM) for isotropic materials, which has been used and modified by, among others, Waddoups et al. (1971), Poe (1983), Anderson (1995) and Daniel (1993). The second approach is based on the analysis of stress fields near cracks. Wells (1963) promoted a concept that employs the crack opening displacement (COD) as the parameter governing crack extent. Dugdale (1960) developed a closed-form solution for plane stress conditions to advance the COD concept. Whitney and Nuismer (1974) proposed a simplified stress fracture criterion based on the actual stress distribution near the notch. Based on the average stress criterion proposed, failure occurs when the average stress over an assumed characteristic dimension from the boundary of the notch equals the tensile strength of the unnotched material (Seif et al. 2001).

2.5.1 Linear Elastic Fracture Mechanics

The stress intensity factor is one of the important properties in fracture criteria. It is determined by the state of the applied load and by material configurations (Seif et al. 2001). In general, a cracked pavement system can be loaded in one of three fracture modes or a combination of them as seen in Figure 2.3 (Anderson, 1995). When thermal and traffic

loading are applied to the crack plane, Mode I (i.e., opening mode K_I) occurs. Mode II (i.e., sliding mode K_{II}) occurs when in-plane shear loading is applied, which leads to crack faces sliding against each other normal to the leading edge of the crack, and Mode III (i.e., tearing mode K_{III}) occurs when out-plane shear loading is applied, which causes sliding of the crack faces parallel to the crack leading edge. Mode III deformation does not occur in the plane problem of elasticity and is negligible for pavements. Extending Anderson's (1995) work, Ruiz et al. (2001) reported that the critical stress required to fail Portland cement concrete in Mode II is greater than that required in Mode I because of interlocking aggregates along the crack plane. That is, Mode I parameters can be the critical criteria to enable crack propagation through the material ligament (Kim, 2007).

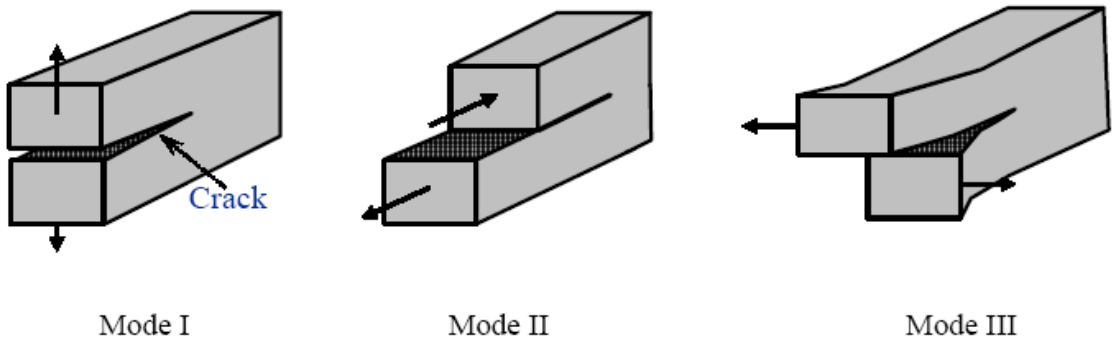

Figure 2.3 Three types of fracture modes (Anderson, 1995)

2.5.2 Nonlinear Fracture Mechanics

The linear models do not apply when the combination of geometry and loading is such that a plastic zone is developed and propagated through the media (Shet et al., 2002).

Linear elastic fracture mechanics is valid only if nonlinear material deformation is limited to a small region surrounding the crack tip (Kim, 2007). It is not practically possible to characterize the fracture behavior for many materials with linear elastic fracture mechanics; therefore, alternative fracture mechanics models are needed. Broek (1984) mentioned that a considerable plasticity occurs at the crack tip; the elastic energy release rate, G, "cannot be determined from the elastic stress field, since G may be affected considerably by the crack tip plastic zone". Dugdale (1960) and Barenblatt (1962) proposed the cohesive zone concept to simulate the fracture process for materials both ductile and brittle. The cohesive zone model (CZM) for simulating the fracture process has been extended to many materials including polymers, metallic materials, ceramic materials, metal matrix composites, and fiber reinforced plastic composites under static, dynamic, and cyclic loading conditions (Shet et al., 2002). This method is preferred not only because it removes the stress singularity but also because it can be easily implemented in a numerical method such as the finite element, boundary element, or discrete element methods (Shet et al., 2002). Kim (2007) summarized historical cohesive zone model approaches in the literature focused on the shape and the model parameter values in Table 2.1.

Table 2.1 Summary of Various Cohesive Zone Models (Kim, 2007)

Year and author	Proposed Model	Problem solved	Comments
Barenblatt (1959, 1962)	Brittle Model	Perfectly brittle materials	The first to propose the cohesive zone concept.
Dugdale (1960)	Ductile (Plastic) Model	Yielding of thin ideal elastic-plastic steel sheets containing silts	Cohesive stress equated to yield stress of material.
Hillerborg (1976)	Fictitious Crack Model	Portland cement concrete	The first to consider cementitious materials
Needleman (1987)	Polynomial Normal and Linear Shear Model	Particle-matrix decohesion	Phenomenological model predicts normal separation.
Rice and Wang (1989)	Model based on Atomic Fit	Solute segregation	Ascending part is equated to E0; considers normal separation and ignores shear separation.
Needleman (1990)	Polynomial and Exponential Model	Particle-matrix decohesion	Predicts normal separation
Needleman (1990)	Exponential Normal and Trigonometric Shear Model	Decohesion of interface under hydrostatic tension	Periodic shear traction to model
Tvergaard (1990)	Quadratic model	Interfaces of whisker reinforced metal matrix composites	
Tvergaard & Hutchinson (1992)	Trapezoidal Model	Crack growth in elasto-plastic material, peeling of adhesive joints	Claims shape of separation law is relatively unimportant
Xu & Needleman (1993)	Exponential Normal and Shear Model	Particle-matrix decohesion	Predicts shear and normal separation
Camacho and Oritiz (1996)	Linear Separation Model without any Ascending Curve	Impact Loading	Uses additional fracture criterion. Predicts failure by both shear and normal separation in tension, and by shear separation in compression.
Geubelle & Bayler (1997)	Bilinear Model	Delamination by low-velocity impact	Ascending curve can be matched to initial stiffness of the material.

2.6 Micromechanics in Asphalt Concrete

Micromechanical models were started by Voigt (1889), Einstein (1911), and Reuss (1929) to predict effective stiffness or compliance terms based upon the material properties of the individual constituents. Micromechanical models can be classified into two categories; i) non-interacting particles and ii) interacting particles (Buttlar and You, 2001). The former category is defined by specified geometries and not-specified geometries. The non-interacting particle models are represented by the lower bound model by Reuss (1929), the upper bound model by Voigt (1889), and Hirsh's (1992) and Counto's (1964) models (see Figure 2.4).

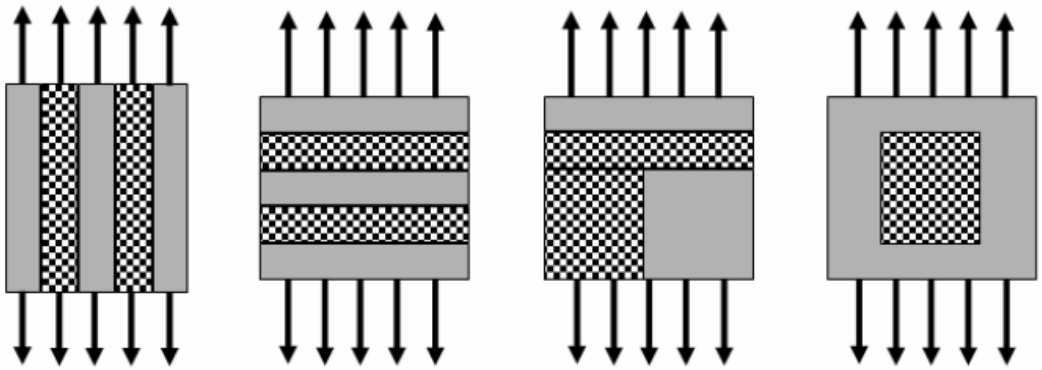

(a) Lower Bound Model (b) Upper Bound Model (c) Hirsh's Model (d) Counto's Model

Figure 2.4 Simplified non-interacting particle models

For the geometry specified models, Hashin (1965) introduced a model taking into account a gradation of spherical particles but not including aggregate-to-aggregate contacts.

Non-interacting particle models, however, result in poor predictions of asphalt concrete behavior due to the over-simplification of AC microstructure (Buttlar and You, 2001).

Asphalt mixtures are a combined material with graded aggregates bound by a mastic mortar. The physical properties and performance of asphalt are determined by the properties of the aggregate and of the asphalt binder, and by asphalt-aggregate interactions (You and Buttlar, 2004). Micromechanical models can describe the fundamental material properties of an HMA based on its individual constituents (Kim, 2007). The advantage of this approach is that it is possible to account for the material anisotropy and heterogeneity resulting from the aggregate shape and size distribution within the HMA. Models allowing for particle interaction can be divided into two categories according to whether they call for a simplified geometry specification or a complex geometry specification. Two numerical approaches have been generally used to simulate the micromechanical behavior of HMA. These are the finite element method (FEM), and the discrete element method (DEM).

For FEM modeling, Kose et al. (2000) used photographic and x-ray computed tomography images to explain the internal structure of asphalt mixtures. Finite element modeling was then used to study asphalt mastic strains at the microstructural level. The binder and aggregate were included as elastic materials. Masad et al. (2002) used image analysis techniques and FEM simulations of the microstructure to investigate the stiffness anisotropy of asphalt mixtures. Papagiannakis et al. (2002) presented a procedure to process an asphalt mix image for modeling purposes. According to Papagiannakis et al. (2002), due to resolution limitations in capturing and processing HMA images, the binder thickness as represented in the image was larger than the actual film thickness. Further, the smallest

microstructure element (image pixel) did not represent the binder as well as the fine particles embedded in the binder. To account for these two factors, they noted that it was necessary to multiply the measured binder stiffness by a factor to obtain the stiffness of the mastic. In 2004, Abbas et al. used FEM with a nonlinear viscoelastic material model to analyze the asphalt mixture microstructure. The model geometry was described using the same procedure presented by Papagiannakis et al. (2002).

In DEM modeling, Rothenburg et al. (1992) presented a micromechanical model which considered simple, polygonal aggregate particle shapes with contact behavior for asphalt concrete to investigate pavement rutting. Chang and Meegoda (1997) proposed a micromechanical model called ASBAL, which was a modified version of an early discrete element model by Cundall, to simulate the asphalt mixture response with provisions for aggregate-to-aggregate and asphalt-to-aggregate interaction. Ullidtz (2001) utilized the discrete element method to study the effect of repeated loading on permanent deformation and fatigue failure of HMA. Buttlar and Roque (1996) and You and Buttlar (2005) considered the interaction of particles with DEM to predict asphalt concrete stiffness properties. A summary of micromechanics models by Kim (2007) is presented in Table 2.2.

Table 2.2 Evolution of Micromechanical Models for Asphaltic Materials (Kim, 2007)

<table>
<tr><th></th><th colspan="2">Non-Fracture</th><th>Fracture</th></tr>
<tr><td>Non-Interacting Particles (Closed-Form Solution)</td><td>Feature</td><td>Development or Application</td><td>Application</td></tr>
<tr><td>Non-Interacting Particles, Geometry NOT Specified</td><td> 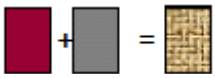 </td><td>1880's - 1930's</td><td rowspan="3">Homogeneous Models (FEM, DEM, BEM)</td></tr>
<tr><td>Non-Interacting Particles, Geometry Specified</td><td> 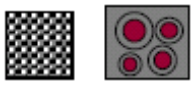 </td><td>1960's - 1970's</td></tr>
<tr><td>Particle Interacting Allowed (Numerical Method)</td><td></td><td></td></tr>
<tr><td>Simplified Geometry Specification (FEM, Lattice Model)</td><td> 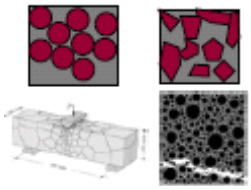 </td><td>1990's -</td><td>1990's -</td></tr>
<tr><td>Complex Geometry Specification (FEM, DEM)</td><td> 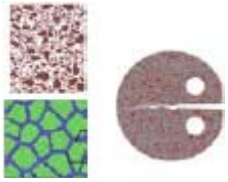 </td><td>2000's</td><td>2000's</td></tr>
</table>

2.7 Discrete Element Method

2.7.1 Principles of the Discrete Element Method

DEM is a discontinuous numerical method developed by Cundall (1979), who applied it in analyzing rock mechanics and studying the micromechanics of materials such as soil at the particle level. Cundall (1979) presented a computer model, named BALL, to simulate the two-dimensional movement of assemblies of granular particles. In the discrete element method, the interaction of the particles is treated as a dynamic process. The states of

equilibrium of contact forces and continuity of displacements of a stressed assembly of discs are achieved through the application of Newton's second law as well as a force-displacement law at the contacts (Cundall and Strack, 1979). Newton's second law is used to determine the motion of each particle arising from the contact and body forces acting upon it including gravitational forces, external forces expressed by boundary conditions, and internal forces developed at element contact. The force-displacement law is used to find the contact forces as a function of the relative motion at each contact.

One popular computer program for using discrete element modeling is PFC2D by Itasca. PFC2D provides a simplified approach to estimate translational and rotational motions through the use of governing differential equations to estimate critical time step. As presented in Itaca (2004), critical time step t_{crit} can be expressed by $\sqrt{m/k^{\text{tran}}}$ (translational motion) as follows:

$$t_{crit} = \begin{cases} \sqrt{m/k^{tran}}, & (\text{translational motion}) \\ \sqrt{I/k^{rot}}, & (\text{rotational motion}) \end{cases} \tag{2.4}$$

where m is the mass, k^{tran} is the translation stiffness, I is the moment of inertia, and k^{rot} is the rotational stiffness. The analysis time step is given as a fraction (with a default of 0.8) of the minimum time step of both motions in all particles.

The calculation cycles in the DEM consist of two main parts, based on the law of motion and the force-displacement law as seen in Figure 2.5. At the start of each time step, the set of contacts is updated from the known particle and wall positions. The force-

displacement law is then applied to update the contact forces based on the relative motion between the two entities. Next, the law of motion is applied to update velocity and position based on the resultant force and movement arising from the contact forces and from any body forces acting on the particle. The constitutive models used in PFC2D consist of three parts: i) a contact stiffness model, ii) a slip model, and iii) a bonding model. First, the linear contact model is described by the normal and shear stiffnesses, k_n and k_s [force/displacement]. The contact force vector, F_i, can be determined with normal and shear components with regards to the contact plane with details presented in Itasca, 2004.

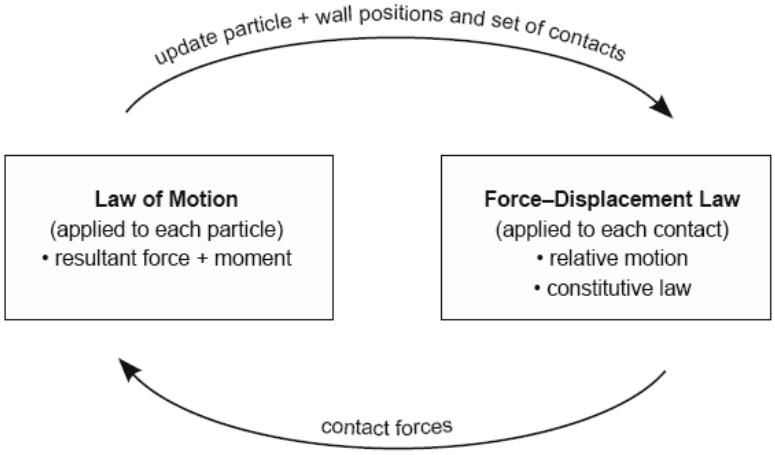

Figure 2.5 Calculation cycle in Discrete Element Method (Itasca, 2004)

The slip model is defined by the relationship between shear and normal contact forces and allows slip to occur by limiting the shear force. If the allowable shear contact force exceeds the maximum allowable shear contact force, which is the product of the friction coefficient and the normal contact force at the contact, then slip occurs during the next calculation cycle. Bonding particles, which can be joined together at contact, can be

represented by two models: the contact-bond model which can only transfer a force, and a parallel-bond model which can transfer both a force and a movement. The following section of this chapter discusses the displacement-softening model implemented by PFC2D.

2.7.2 Microparameters and macroproperties of PFC2D specimens

In a DEM modeling, the mechanical properties of a specimen depend on the microparameters defined at the particle level as investigating Young's modulus and Poisson's ratio for some special contact models (Yang et al., 2006). Duffy and Mindlin (1957), Deresiewicz (1958) and Walton (1987) studied the effective moduli with regular packing of spheres by using the Hertz-Mindlin contact model. They indicated that effective elastic moduli are a function of confining pressure. Some researchers showed that the stress-strain relationship and the effective modulus could be derived from a microstructural continuum approach (Walton 1987, Bathurst and Rothenburg 1988, Chang and Misra 1989, 1990). Chang and Misra (1990) investigated the relationship between the symmetry of mechanical properties and the packing structure using random granular packing. According to Yang et al., (2006), theoretical analyses found in the literature lead to the conclusion that the parameters related to the effective modulus and Poisson's ratio depend on interparticle contact stiffness, the ratio of normal contact stiffness to tangential stiffness, particle size, porosity, coordination number (the number of contacts per particle), particle size distribution, and contact radius. Huang (1999) studied the relationship between microparameters and macroproperties with PFC2D using a contact-bonded model. Also, Yang et al. (2006) investigated the relationships between microparameters and macroproperties of the

specimens using a PFC2D model of bonded particles and determined quantitatively the relationships between particle level parameters and the mechanical properties of the specimens.

There are two groups of microparameters. One consists of geometric and physical parameters, including the dimension of the specimen, particle size and quantity. The other group is the constitutive parameters which determine the contacts and bonds. Parameters for specimen generation in PFC2D are presented in Table 2.3. In this study, these parameters were used for generating particles.

Table 2.3 Parameters for specimen generation in PFC2D

Group	Parameters
Geometric and physical parameters	Specimen height
	Specimen width
	Particle size
	Particle density
Constitutive parameters	Particle contact modulus
	Particle stiffness ratio
	Particle friction coefficient

2.7.3 Bilinear Cohesive Zone Model in PFC2D

Dugdale (1959) and Barenblatt (1962) developed cohesive zone models (CZM) to simulate the fracture of both homogeneous and non-homogeneous materials under a variety of loading conditions. The two most commonly used cohesive failure models are the intrinsic

potential-based model and extrinsic linear law model (Song et al., 2006). The intrinsic model used by Xu and Needleman (1994) is a potential-based cohesive model, using the finite element method. An alternative is the extrinsic model which is a stress-based cohesive law model as used by Camocho and Ortiz (1996). Further investigations were carried out to apply the cohesive fracture modeling (Mosalam and Paulino 1997, Siegmund and Needleman 1997, Jin et al. 2003).

For pavements, Soares et al. (2003) applied this approach to heterogeneous HMA materials to investigate mode I crack propagation of the Superpave Indirect Tension Test (IDT) using the cohesive laws proposed by Tvergaard (1990). Buttlar (2001), Wagoner (2005), Song (2006), and Kim (2005a, 2005b, 2007) applied this approach to heterogeneous HMA materials to investigate mode I crack propagation of the double cantilever beam test, single-edge notched beam test, and disk-shaped compact tension test. They also applied this approach for time-dependent fracture modeling using bulk elastic and viscoelastic properties. An intrinsic general cohesive softening model is the form of bilinear cohesive zone model which is available in PFC2D. The main parameters of bilinear CZMs are cohesive energy G, cohesive strength σ_{max}, and separation/critical length δ_{sep}. Ortiz and Pandolfi (1999) defined the cohesive fracture energy by the following equation:

$$G = \int_0^{\infty} td\delta = e\sigma_{\max}\delta_{sep} \tag{2.5}$$

Figure 2.6(a) illustrates the cohesive zone concept in the opening mode and, Figures 2.6(b) and (c) illustrate the same concept, simplified. “Crack tip” indicates a point where traction is zero, and the cohesive zone tip is a point where the traction reaches a maximum. δ_{max}, δ_{sep} $(=\delta_{cr}=U_{p\max})$, and $\sigma_{\max}$ represent cohesive crack tip location, complete material separation of the material crack tip, and the normal cohesive strength, respectively. Point B indicates the starting point of unrecoverable material degradation, plasticity, or micro-crack initiation, and point C indicates the condition of a fully separated crack face which has released the energy potential associated with decohesion.

As presented in Itasca 2004, under the consistency condition (i.e., $F - F_{\max} = 0$), the elastic (or plastic) displacement increment can be determined. Based on the assumption that contact strength is a function of plastic displacement, the contact force is calculated. Details of the cohesive softening model are presented in Itasca, 2004.

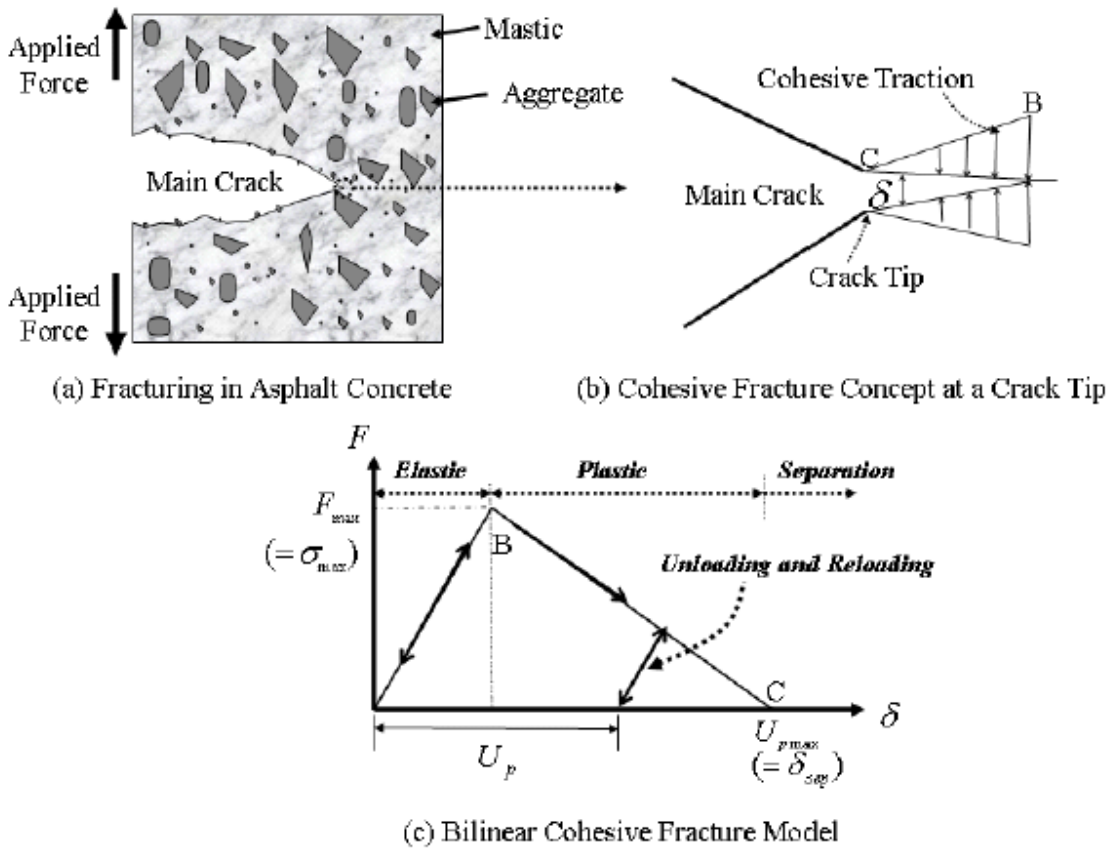

Figure 2.6 Schematic of the Bilinear Cohesive Softening Model (Kim, 2006)

2.7.4 DEM for geosynthetic-soil interaction

Up to this time, discrete element models have been focused on the geogrid-soil interaction through large triaxial tests, pullout tests, and plate load tests (Han et al., 2010). Representative research for geosynthetic-soil interaction with DEM modeling was summarized in Table 2.4, above.

According to Konietzky et al. (2004), DEM is an ideal tool for studying the interaction between geogrid and aggregate. They conducted the back-analysis of triaxial tests

using DEM for geogrid-reinforced aggregates and determined that increased strength resulted from not only the tensile strength of the geogrid but also the confinement effect of the geogrid. They concluded that geogrid reinforcement increased the shear strength of aggregates. Also, they noted that the contact forces in aggregates with particle sizes between 0.6 mm and 20 mm do not change significantly beyond a confinement influence zone of 100 mm on either side of a punched-drawn biaxial geogrid. Subsequently, McDowell et al. (2006) studied that simulating aggregate shapes had an important effect in the modeling of the peak strength and dilation behavior of railway ballasts by triaxial sample with 300 mm (diameter) by 600 mm (height), using the clumps of overlapping spheres to represent the actual shape of aggregates. They also determined numerically that there was a 50% reduction in displacements with the use of multiple geogrid layers (i.e., three layers) compared with a single geogrid layer.

The pullout test developed by Chareyre and Villard (2002) is a commonly used experimental method for evaluating the geosynthetic-soil interaction. Using the calibrated parameters based on the simulation of two dimensional biaxial compression tests of soil and a geogrid pullout test in a horizontal plane for interface characterization, they simulated the force-displacement curves for the geogrid anchored in sand and silt. Furthermore, Villard and Chareyre (2004) conducted similar pullout tests using different anchorage shapes for geosynthetics, such as L- and V-shaped anchorages, in the laboratory. Comparisons between the experimental and numerical results enabled practical conclusions regarding anchorage failure mechanisms of geosynthetic reinforced slopes. McDowell et al. (2006) demonstrated that the ratio of aperture size to aggregate diameter played an essential part in the peak

strength, and the minimum displacement required to mobilize this peak strength, using a three dimensional DEM model in laboratory pullout tests.

In addition to these, a plate load test is commonly used to evaluate bearing capacity and stiffness of foundations, and can be used to evaluate the benefits of geosynthetic reinforcement in the foundations as well (Han et al., 2008). DEM modeling was used to investigate particle movement and contact forces between particles interacting under plate loading by Lim and McDowell (2005) and Lu and McDowell (2007). Lim and McDowell (2005) conducted single particle crushing tests on a range of ballasts and found that the size effect on average strength was inconsistent with that predicted by Weibull statistics in spite of a Weibull distribution of strengths. This is in opposition to the results by McDowell and Amon (2000) and McDowell (2002) for sand particles, which follow the Weibullian size effect. In addition, Lu and McDowell (2007) used angular clumps and they found that angular clumps increased contact force between particles and improved rolling resistance which provided more particle interlocking.

.

Table 2.4 Researchers for geosynthetic-soil interaction

Tests	Researchers
Large triaxial test	Konietzky et al. (2004)
	McDowell et al. (2006)
Pull out test	Chareyre and Villard (2002, 2004)
	McDowell et al. (2006)
Plate load test	Lim and McDowell (2005)
	Lu and McDowell (2007)

2.8 Summary

Based on the results of previous research, some evidence exists to support the notion that geosynthetic reinforcement can be used to minimize reflective cracking. The contribution of geosynthetics can be either to allow reduction of the thickness of the resurfacing bituminous layer, or to extend the performance life of the overlay if the same thickness is maintained. Reported design methods in the literature are generally empirical. Few studies were presented in literature to explain the mechanics of tensile reinforcement, how it will work, and to predict improvement in performance when it is included.

Chapter 3 DEM Modeling Approach

3.1 Introduction

Continuum methods such as the finite element, finite difference, and boundary element methods have been generally used in the past to study the mechanical behavior of particulate systems (Kose et al., 2000; Masad et al., 2002; Papagiannakis et al., 2002). The major advantages of continuum methods are well-established constitutive models, well-understood continuum parameters such as stress and strain, and the readily quantifiable parameters that are used in the modeling. Based on these advantages, the finite element method (FEM) is the most commonly used numerical method in pavement analysis. Many studies have used FEM models to determine the crack propagation properties of pavement layers. However, FEM simulations tended to significantly under-predict HMA stiffness, due to the lack of proper representation of the interlock between aggregates (Abbas et al., 2004). One of the emerging methods that has the potential of providing additional insight is the discrete element method (DEM), which represents the material as a structure of discontinuous particles. The material mesh of a continuum can be represented as a finite number of particles, with interactions between each particle defined. DEM has advantages in describing the effect of the aggregate shape and distribution on the susceptibility of asphalt mixtures to permanent deformation (or rutting) especially at high strain levels. This deformation can be predicted through the ability of DEM to account for aggregate sliding, which is known to be the dominant mechanism contributing to permanent deformation or rutting (Sousa et al. 1993, Abbas et al. 2007). In addition, the inclusion of geosynthetics can be analyzed with the potential of having interface properties better represented.

3.2 Model Properties

3.2.1 Modeling of the Pavement Section

PFC2D provides FISH programming language to define user-specific parameters and functions to develop more complicated models. To achieve the research objectives, a pavement model is developed to simulate a multi layer pavement section including overlay, geosynthetics, PCC, base course and subgrade layers.

To generate base and subgrade layers, random packing is specified. PFC2D provides two primary ways to generate particles. One is generation by expansion, which produces a specified number of small-radius particles at random coordinates within a given space (to avoid particle overlapping). The particles are then expanded until the desired porosity is obtained. The particle numbers are specified, while their radii are changed during the expansion. The second method is generation by explosive repulsion, which is used to generate the particles with their final radii in sufficient numbers at random in the given space to obtain desired porosity. The radii of the particles are not changed after generation, but particle numbers are not pre-specified.

In order to control the particle size, the explosive repulsion method is used herein. The explosive repulsion method leads to large forces due to large overlaps, which in turn, leads to particles escaping through the boundary walls. To prevent this, the kinetic energy is dissipated by setting the velocity of the particles to zero several times during several thousand steps, and setting layer converges to equilibrium. After generation, the particles are subjected to isotropic compression, using a servo-control, to reach a desired stress level. For the appropriate representation of grain size this model relies on Evans et al. (2009), who

studied grain size distribution (GSD) effects using two-dimensional discrete numerical experiments. Four GSD cases -- fine, baseline, coarse, and linear -- were simulated in terms of stress-strain-strength behavior at the macro scale. As seen in Figure 3.1, there are few differences in the four stress-strain curves in spite of large differences in particle numbers. Thus, Evans et al. suggested using linear GSD, namely specifying the size of particles within narrow limits, so as to reduce computation time.

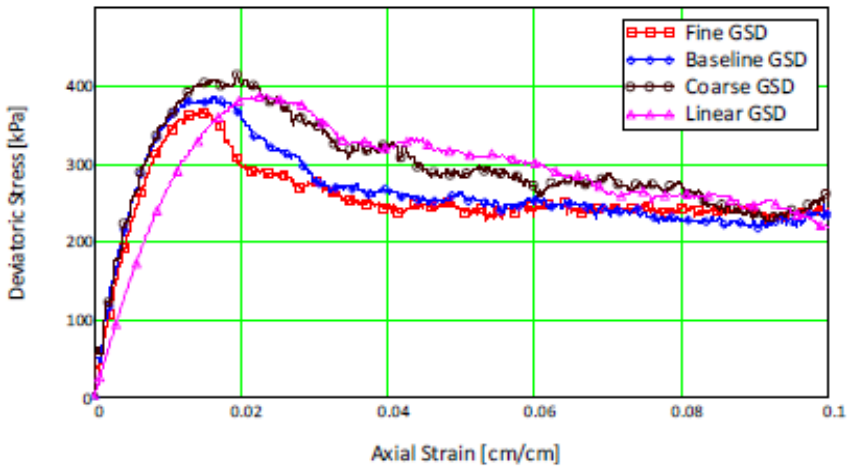

Figure 3.1 Stress-strain response of DEM simulations (Evans et al., 2009)

After generating the base and subgrade layers, the PCC and AC layers are generated on top of the granular base with regular packing. For a realistic representation, a picture showing the microstructure of the asphalt mixture, including fine aggregate matrix (FAM) and aggregate can be projected onto the discrete element particles using the MATLAB program (Figure 3.2 (a)). Original picture and projected DEM meshes can be seen in Figure 3.2 (b).

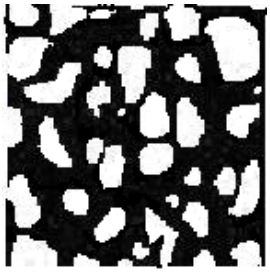

(a) Original AC mixture

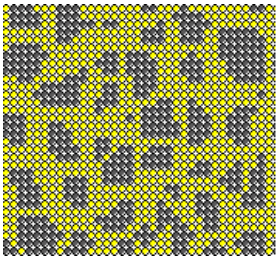

(b) Discrete element particles

Figure 3.2 Projected onto the discrete element particles

After the pavement section is generated, the particles are subjected to gravity loading and cycled to an initial at-rest state. Before applying external load, the displacement is set to zero. The stress and porosity ratio is checked with “measurement circles” indicating regions of interest at several locations. The displacement is estimated at the top of the modeled section at key locations to monitor for indications of rutting and strain, is monitored as well.

3.2.2 Particle size determination

A parametric study is conducted to determine the particle size for the four layers including AC overlay, PCC layer, and base/subgrade layer. If particle size in one layer is selected to be variable, in the other layers it is kept constant. Results for the particle size effects are presented in Figure 3.3. In the base/subgrade layer, particle sizes of 5 mm and 6 mm radius show a slight difference in displacement; in comparison, however, the displacement around 7 mm radius particles increases considerably(see Figure. 3.3(a)). In the PCC layer, particle sizes of 2.25 mm, 3 mm, and 4.5 mm radii were used. As the results show in Figure 3.3(b), displacements are not too much different for these three sizes. For the

asphalt concrete layer, radii of 1 mm, 1.5 mm, and 2 mm are used. The analyses indicate that displacements on top are 10 mm, 10.1 mm and 10.8 mm, respectively. Displacement at the tops with 1 mm and 1.5 mm particle radii are almost the same, but it somewhat increases when the radius is 2 mm. The dotted red circles indicates the values used in this study.

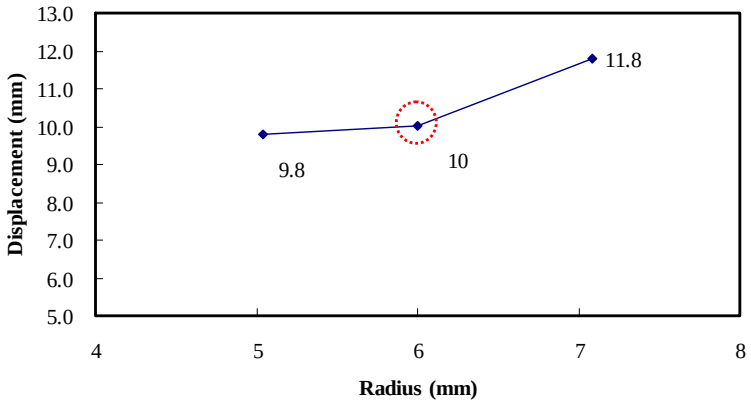

(a) Base/Subgrade

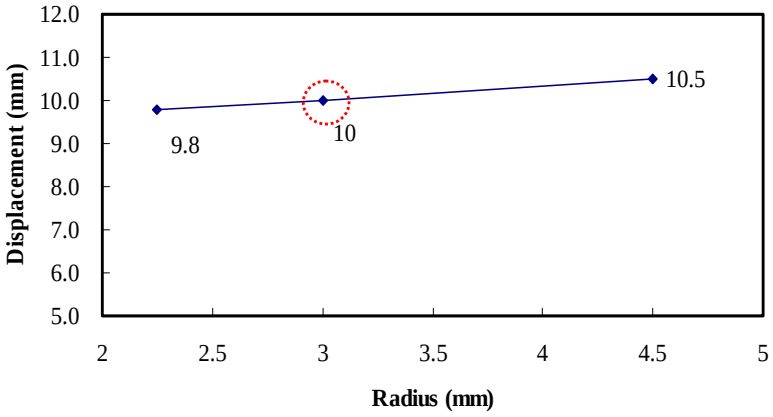

(b) PCC

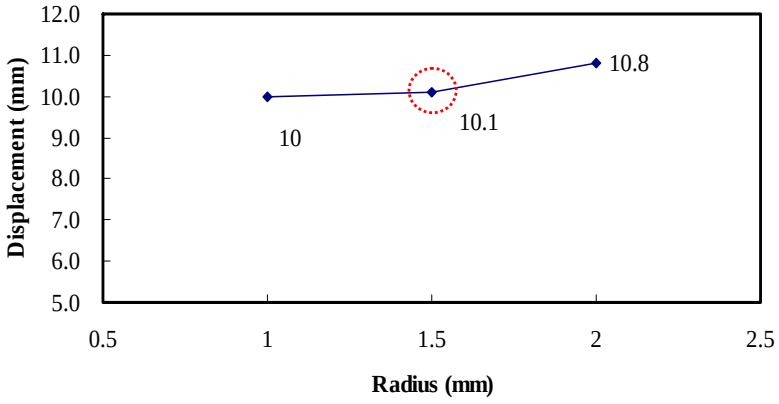

(c) Asphalt Concrete

Figure 3.3 Particle size effects on Pavement Section

3.2.3 Model Parameters determination

This section summaries the selection of model parameters for the study. Model parameters such as model size and number of particle should be determined first and then particle properties determined. Micro-properties such as friction coefficient can be derived directly from measurement on laboratory specimens. Other properties such as the interaction of micro-scale components are reported in literature (Potyondy and Cundall, 2004; Yang et al., 2006). Important parameters that govern behavior include particle stiffness and particle friction coefficient. Mass scaling or density scaling is commonly used in a quasi-static simulation to increase the time step (see Thornton, 2000; Evans, 2005; Zhao, 2009). Significant research exists on mass scaling or density scaling for both the finite element method (Alves and Oshiro, 2006; Olovsson et al., 2004; Olovsson et al., 2005) and the discrete element method (Thornton, 2000; O'Sullivan et al., 2003; O'Sullivan and Bray, 2004; Cui and O'Sullivan, 2006). In the DEM, the scaling method relates to the maximum stable time of solution of the system, overall numerical stability of the solution, and computational cost of the simulation (Zhao, 2009).

In order to perform the simulation with a reasonable computational time, Thornton (2000) scaled up the particle density by a factor of 10^{12} to get a ~1s time step. He found that the velocity and acceleration were reduced by one order of magnitude due to density scaling, but there were no significant effects on the forces or displacements, and hence the stresses and strains. Thornton concluded that velocity and acceleration were not of concern in the quasi-static behavior. O'Sullivan et al. (2003) scaled up particle density to 2×10^{8} kg/m^{3}. The next year, O'Sullivan and Bray (2004) proposed that density or mass scaling could be used to

relax time step for the quasi-static condition assuming that the response was not sensitive to inertia effects. It was noted that mass scaling was not recommended if high frequency response was important. Cui and O'Sullivan (2006) also used density scaling to reduce the computation time for analyzing the macro- and micro-scale response results from the direct shear testing.

In summary, it seems that the important factor is that the forces and displacements, and hence the stresses and strains, will not be affected if the mass or density scaling is used. The reduction of the velocities and accelerations are not of concern under quasi-static conditions, as mentioned by Thornton (2000).

3.2.3.1 Base/Subgrade Parameters

Input parameters of a model such as finite element or finite difference can be derived directly from measurements on laboratory samples (Potyondy and Cundall, 2004). However, it is rather challenging to choose such properties on a discrete level so that real material response is simulated in PFC2D models. To estimate the properties of the microscopic constituents, a number of assumed properties are used in DEM and the results are compared with the desired macro response of the material. In order to match given laboratory results of a given property, numerical analyses which simulate the laboratory tests are needed.

The elastic properties of a sample can be determined by performing a loading/unloading biaxial test under elastic conditions. Initial Young's modulus (E) and Poisson's ratio (ν) can be measured through this test. From the plots of axial deviatoric stress

($\Delta\sigma_d$) and volumetric strain ($\Delta\varepsilon_a$) versus axial strain ($\Delta\varepsilon_x$), the Young's modulus can be determined (Thornton, 1979; Itasca, 2004)

$$\frac{\Delta\sigma_a}{\Delta\varepsilon_a} = \bar{E} = \frac{k_n}{2t} \tag{3.1}$$

and the Poisson's ratio is

$$\nu = -\frac{\Delta\varepsilon_x}{\Delta\varepsilon_a} = 1 - \frac{\Delta\varepsilon_v}{\Delta\varepsilon_a} \tag{3.2}$$

It should be noted that the value of Poisson's ratio is not strictly comparable to the Poisson's ratio as obtained from a triaxial test, because the biaxial test conditions in PFC2D include neither plane strain nor plane stress.

Simulation of biaxial test results by Chandra et al. (2008), who investigated the benefits of reinforcing the subgrade soils in flexible pavements, is conducted using PFC2D and the results are summarized in Figure 3.4. To match the elastic properties including Young's modulus and Poisson's ratio, PFC2D's input parameters are varied. As seen in Figure 3.4, good matches have been found between two results. Input parameters used to obtain the match are also shown in Figure 3.4 and input parameters of DEM simulations of biaxial tests are presented in Table 3.1 as well.

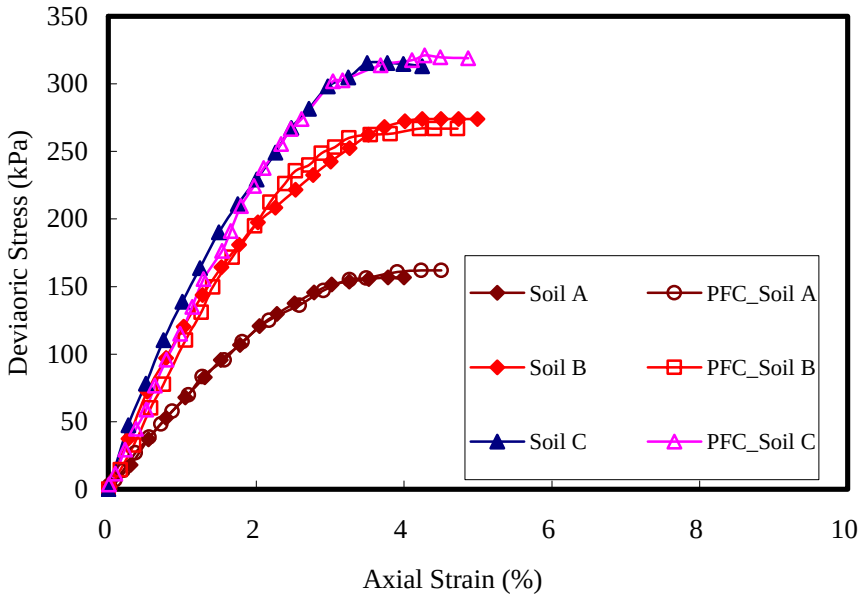

(a) Stress vs. Strain curve

Soil	***E* (MPa)**		***ν***	
	Ref.	PFC	Ref.	PFC
A	7.56	7.51	0.35	0.4
B	11.18	11.13	0.35	0.32
C	16.21	12.4	0.35	0.3

(b) Results of E and ν

Figure 3.4 Comparison with Lab tests and biaxial test with PFC2D

Table 3.1 Parameters for biaxial test for DEM simulations

Soil	PFC2D Parameters		
	Stiffness (Pa)	Particle friction	Time step safety factor
A	2.0×10^7	0.31	0.8
B	2.8×10^7	0.31	0.8
C	4.0×10^7	0.31	0.8

3.2.3.2 Determination of Parameters for Asphalt Concrete

Cohesive parameters

The cohesive zone model input parameters include two experimental fracture properties: tensile strength, and fracture energy of the asphalt concrete. The first material property, tensile strength, is determined from the Indirect Tension (IDT) test at -10ºC and 1HZ. For the calibration of the cohesive zone model of the first-failure strength, results from the IDT test are used. The material strength obtained from the IDT test is 3.56 MPa. The second parameter of the cohesive zone model is the fracture energy of asphalt concrete and can be determined from the single-edge notched beam (SE(B)) test. The fracture energy of 344 J/m^2 is obtained from the SE(B) test. Test controls and a detailed procedure for specimen preparation are described in Wagoner et al. (2004a). The crack-mouth opening displacement (CMOD) is increased at a linear rate to produce a stable post-peak fracture. The fracture energy is determined by calculating the area under the load-CMOD curve and normalizing by the cross-sectional area of the beam (Song et al. 2005, Kim and Buttlar 2005).

Stiffness of FAM and Fine Aggregate

Buttlar and You (2001) presented a method for estimating the stiffness of the asphalt FAM (Fine Aggregate Matrix) and fine aggregate portion of a mixture. They noted that it is necessary to model aggregate particles smaller than the sand range (0.6 to 2.36 mm), and it is desirable to determine the stiffness of the binder plus all aggregate finer than the sand range. They used the Bending Beam Rheometer (BBR) device as the first step in preparing and testing asphalt FAM specimens (smaller than 0.075 mm sieve), and then used a simple micromechanics approach to estimate the stiffness of asphalt FAM plus fine aggregate between 0.075 mm and the cut-off diameters used in the micro-fabric discrete element method (MDEM) or FEM model of the coarser aggregate structure. The FAM plus fines stiffness can be predicted using the approach developed by Buttlar et al. (1999) as follows:

$$\frac{S_{FAM}}{S_b} = Ae^{B(0.357 S_b)} \tag{3.3}$$

Where, $A = 25.083c^3 - 10.154c^2 + 4.8767c + 0.831$ (3.4)

$$B = (-1.28\times10^{-3})c^3 + (3.37\times10^{-4})c^2 - (3.08\times10^{-4})c + 6.53\times10^{-6} \tag{3.5}$$

S_b = Binder Stiffness Modulus (MPa) = (Inverse of Creep Compliance)

S_{FAM} = FAM Stiffness Modulus (MPa) at similar temperature and loading time as a binder

c = Volume concentration, by total volume of FAM-fines mixture

They specified that equations were valid for 0.1 < c < 0.6 and this technique could also be applied for other modeling approaches, including FEM. Buttlar and You (2000)

obtained a stiffening ratio of 2.19, and an estimated stiffness modulus of the FAM and fines fraction of 3.444 GPa using equations (3.3) to (3.5).

3.2.3.3 Determination Relationship of Particle Stiffness and Elastic Moduli

There are four typical particle packing arrangements in DEM including square, horizontal hexagonal, vertical hexagonal and random packing are shown in Figure 3.5 (Chang et al, 2002; Chen et al., 2001).

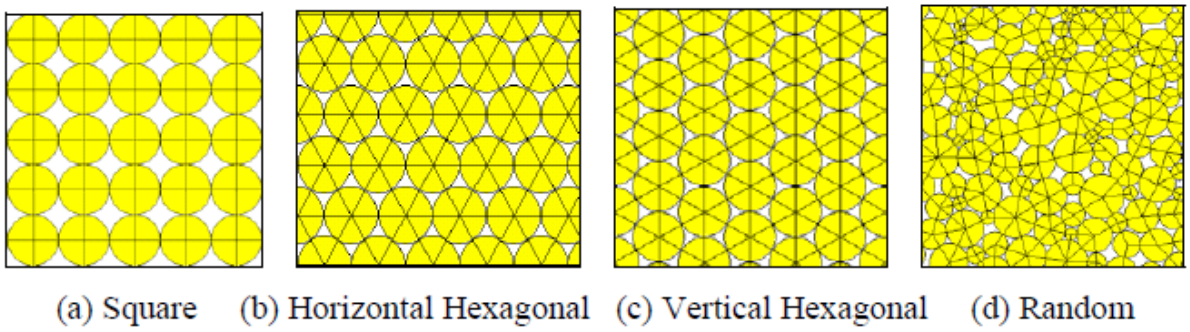

Figure 3.5 Particle arrangements of DEM (Kim, 2007)

Young's modulus E and Poisson's ratio ν are important elastic constants for characterizing the macroscopic linear elastic behavior of isotropic materials. The model parameters of DEM modeling (K_n and K_s) usually are determined by validating a numerical simulation of laboratory testing with actual experimental results (Potyondy et al., 1996; Magnier et al., 1998). However, those results are dependent on DEM element size. Therefore, if a new particular problem is produced, repeating the calibration process is necessary to obtain the new DEM parameters. Mustoe and Griffiths (1998) developed a relationship between solid

elasticity and spring stiffness of discrete particles using a small region of material. They used the strain energy density of three DEM elements in a close-packed hexagonal arrangement, computed as a function of the normal and tangential stiffnesses and the in-plane strains of the contact elements as shown in Figure 3.6.

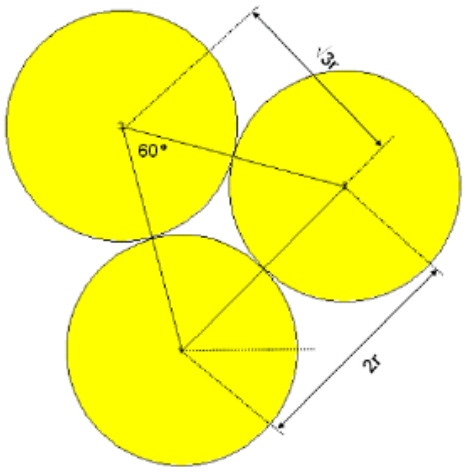

Figure 3.6 Three DEM elements in a closed-packed hexagonal arrangement

Similarly, Tavarez and Plesha (2007) attempted to theoretically establish the inter-element normal and tangential (shear) stiffnesses as function of element size and material parameters including Young's modulus and Poisson's ratio, which is done by developing a DEM model of a unit cell of material as shown in Figure 3.7. The material element will show rigid body motion and uniform straining if loading is applied as shown in Figure 3.7(a). Thus, they imposed displacement constraints on the unit cell of material shown in Figure 3.7(b)

which described a uniform straining deformation including the Poisson effect. To investigate possible anisotropy in the unit cell, the loading shown in Figure 3.7(c) was considered.

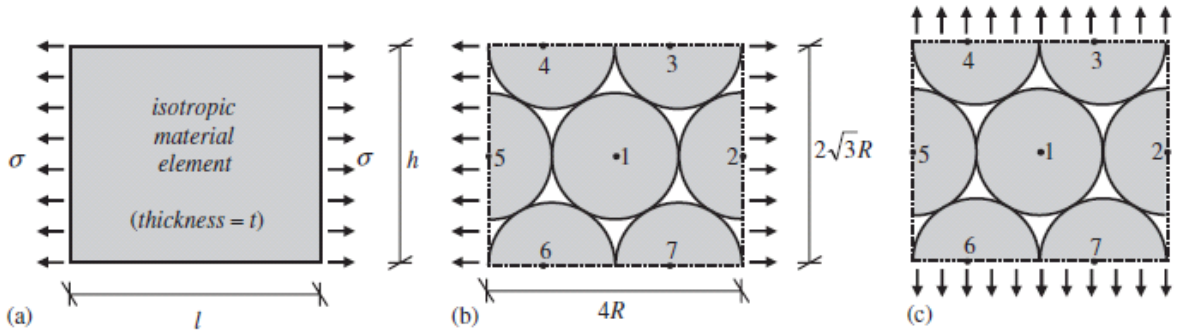

Figure 3.7 Close-packed DEM unit cell of inter-element spring constants
(Tavarez et al., 2007)

Mustoe et al., (1998) and Tavarez et al. (2007) developed the same equations of relationship between the discrete element springs and the elastic properties under plane stress and plane strain conditions even though they used different approaches. The equations under plane stress and plane strain conditions are as follows:

For plane strain conditions:

$$K^n = \frac{E}{\sqrt{3}(1+\upsilon)(1-2\upsilon)}t \tag{3.6}$$

$$K^s = \frac{E(1-4\upsilon)}{\sqrt{3}(1+\upsilon)(1-2\upsilon)}t \tag{3.7}$$

For plane stress conditions:

$$K^n = \frac{E}{\sqrt{3}(1+\upsilon)}t \tag{3.8}$$

$$K^s = \frac{E(1-3\upsilon)}{\sqrt{3}(1-\upsilon^2)}t \tag{3.9}$$

They noted that these equations have limitations in that the maximum value of Poisson's ratio was 0.33 for plane stress and 0.25 for plane strain from the equations corresponding to a shear stiffness of zero. The normal and shear stiffnesses produced by this exercise agree exactly with Equations (3.6) to (3.9). Also these equations were validated by Kim (2007) using cantilever beam in plane stress condition and uniform axial compression in plane strain condition by DEM simulations.

Potyondy et al. (2004) and Masuya et al, (1994) have derived a different expression for the normal stiffness, as given by:

$$K^n = \frac{k_n^{(A)} k_n^{(B)}}{k_n^{(A)} + k_n^{(B)}} = Et \tag{3.10}$$

where, $k_n^{(A)}$ and $k_n^{(B)}$ are the particle normal stiffnesses of particle A and B.

$$k_n = k_n^{(A)},\ k_n^{(B)} = \begin{cases} 2tE, t = 1, & PFC2D \\ 4RE, & PFC3D \end{cases} \tag{3.11}$$

It is important to note that this equation can only be theoretically obtained by assuming a simple cubic arrangement of DEM elements.

The shear stiffness usually can be chosen arbitrarily as a fraction of K^n because there is no basis for determination of the shear stiffness. This is given by:

$$k^s = \frac{k_s^{(A)} k_s^{(B)}}{k_s^{(A)} + k_s^{(B)}} \tag{3.12}$$

where, $k_s^{(A)}$ and $k_s^{(B)}$ are the particle shear stiffnesses of particle A and B.

$$k_s = k_s^{(A)}, k_s^{(B)} = \frac{k_n}{(k_n / k_s)} \tag{3.13}$$

Also, they note that this analysis does not yield a relationship between Poisson's ratio and particle stiffness at the micro level; however, at a macroscopic level, Poisson's ratio will be affected by particle shape, packing, and the ratio (k_n/k_s). When particle shape and packing are determined, the Poisson's ratio increases if the (k_n/k_s) ratio increases.

3.3 Parametric Analyses

3.3.1 Time step safety factor

Selecting appropriate parameters is important for numerical simulations to reproduce the macro-scale response and to understand micro-scale behavior. Several parametric studies

are performed on the base/subgrade layer with the whole pavement section, including AC overlay and PCC layer. The parametric analyses are used quantitatively to evaluate the effects of changing one of the key parameters on the macro-scale response of the specimen, and to evaluate whether the chosen parameters are suitable in terms of their impact on the response. Material and model properties used in the simulations are presented in Table 3.2.

Table 3.2 Properties for numerical simulations

Parameter	Granular Base	Subgrade	Reference
Particle Stiffness (N/m)	10^8	$4\times10^{7*}$	Santamarina et al.(2001)
Particle friction coefficient	0.31	0.31	Proctor and Barton (1974)
Particle specific gravity	2.65	2.65	Yang (2002)
Time step safety factor	0.8	0.8	Default

* Calculated from biaxial test using PFC2D

The model parameters considered herein include friction, stiffness of the base/subgrade layer, and time step safety factor. While one parameter is being studied, the other parameters are kept constant. Porosity of the specimen is also important in discrete element modeling. Two-dimensional porosity is different from three-dimensional porosity. The porosity of the sample is often set to be around 0.15 in two-dimensional simulation (Masson and Martinez, 2001; Bagi, 2003) but around 0.35 in three-dimensional simulation (Thornton, 2000; O'Sullivan et al., 2003). According to Hainbuchner et al. (2002), the equation for relative density in three-dimensional simulation is expressed by:

$$D = \frac{n_{\max} - n}{n_{\max} - n_{\min}} \tag{3.10}$$

Where, $n_{\max}$ and $n_{\min}$ are the maximum and the minimum porosity, respectively and n is the porosity at a specific density, which is related to relative density (D). And, this equation can be converted into the two dimensional porosity as a linear interpolation as following.

$$n_{2D} = n_{2D,\max} - D(n_{2D,\max} - n_{2D,\min}) \tag{3.11}$$

In this study, a void ratio of 0.1595 for medium density (e.g. Bhandari et al., 2008) is used for the parametric studies, and stress of under 560 kPa (around 80 psi), which simulates single wheel load pressure, is applied.

Time step safety factor is a model parameter that affects the time step which is a critical parameter for DEM simulation. O'Sullivan and Bray (2004) stated that time step is related to "particle motion condition (translation, rotation, or both), packing configuration, simulation dimension (2D or 3D), particle size distribution, and particle shape". In this study, simulations are conducted using four different time step safety factors: 0.15, 0.2, 0.5, and 0.8 (default) to investigate the impact of the specified value on the results. Results of the four cases are shown in Figure 3.8, and indicate no significant differences in the computed displacement of pavement section given the assumptions used in the analysis. To reduce the computation time, a time step safety factor of 0.8 is used in this study.

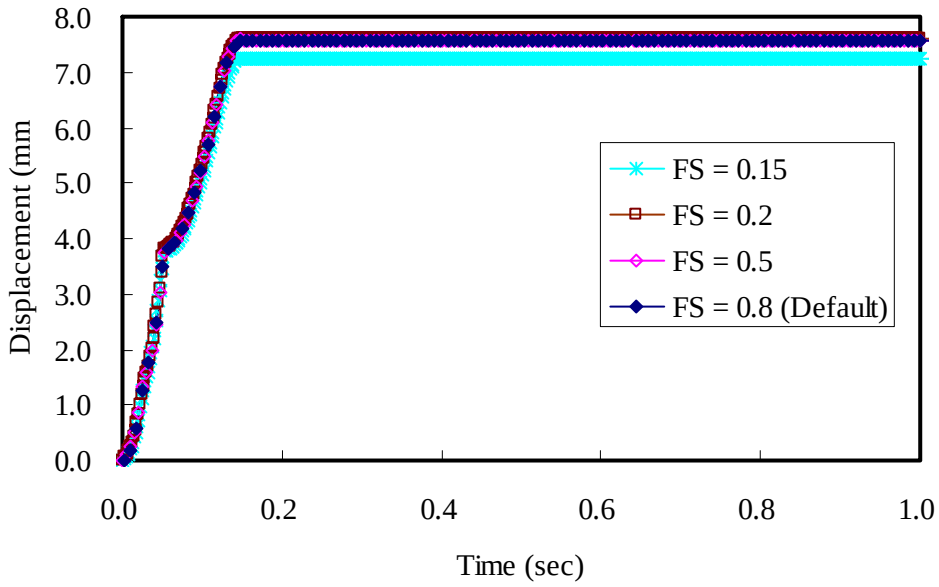

Figure 3.8 Time step safety factor effects on displacement for parametric analyses

3.3.2 Base/Subgrade Layers

In addition, the effects of particle friction coefficients and particle stiffness are investigated. Three cases of particle friction coefficients are used. The reference value of 0.31 used in the current study is based on results from experiments (Proctor and Barton, 1974). The other two values of 0.15 and 0.5 are selected. One is higher and the other is lower than that of reference point. Results of the three particle friction coefficients are shown in Figure 3.9. There are no significant differences in displacement response, with the higher friction coefficient yielding a lower displacement due to the restraint of the slide and rotation of particles, which results in lower displacement. A particle friction coefficient of 0.31 will be used in this study.

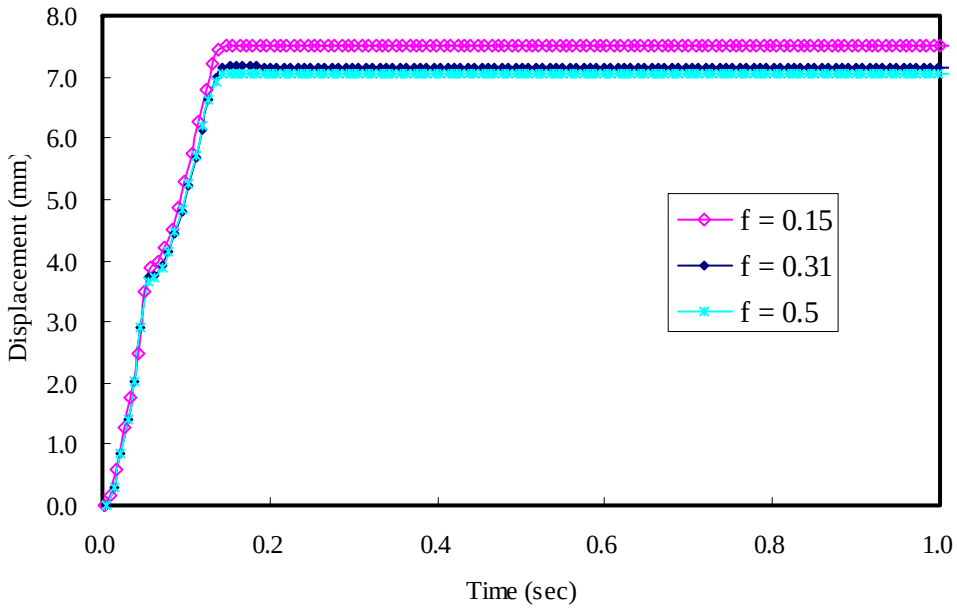

Figure 3.9 Particle friction coefficient effects on parametric analyses

The next set of parametric studies is to investigate the effects of particle stiffness. As in the case of particle friction coefficients, a reference value (1.0K), higher value (10K), and lower value (0.1K) are used for the base and subgrade layer, respectively. For the granular base, the reference value is based on the work of Santamarina et al. (2001), and the reference value (1.0K) for the subgrade layer comes from the biaxial test simulation using PFC2D. The results are shown in Figure 3.10, and indicate that less total displacement develops on the pavement section if particles have a higher stiffness.

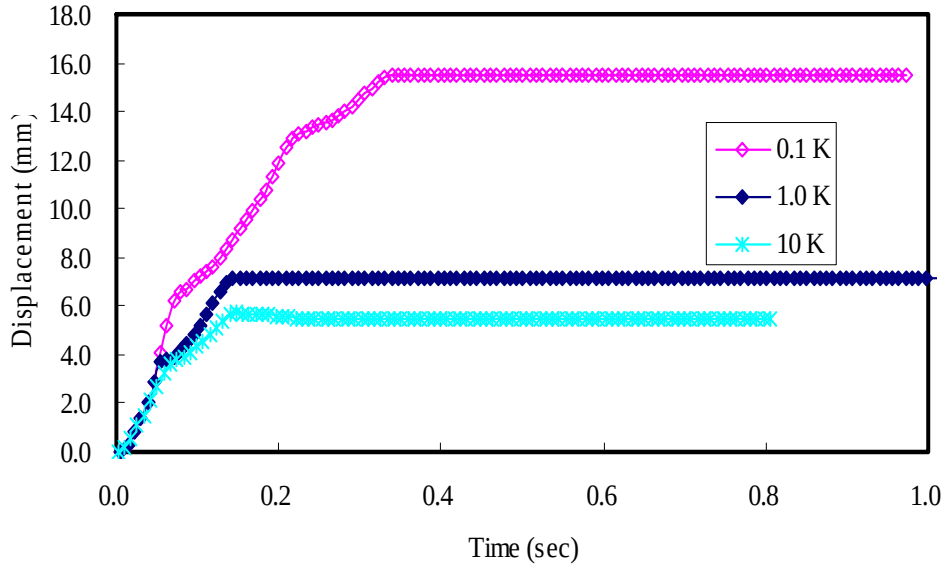

(a) Base layer

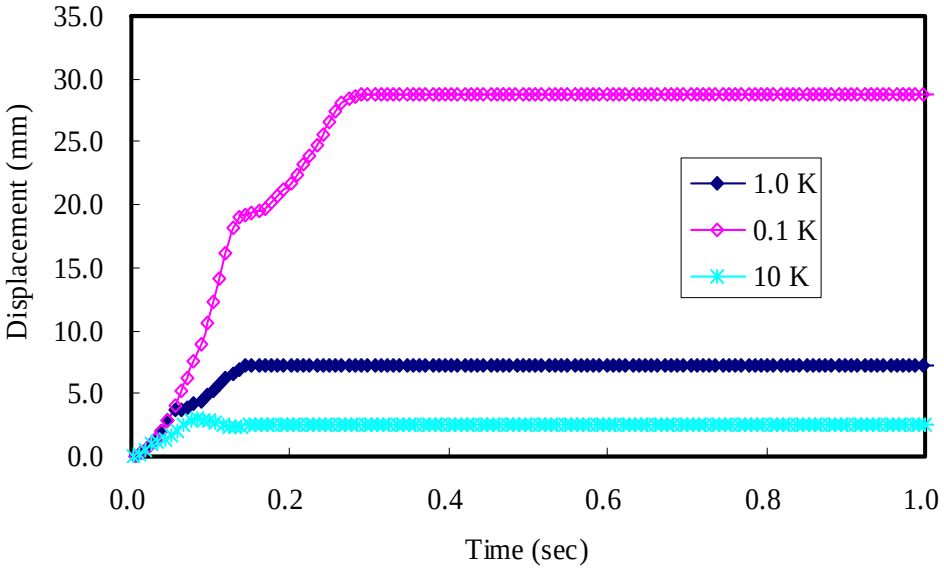

(b) Subgrade layer

Figure 3.10 Particle stiffness effects on parametric analyses

3.3.3 Effect of particle friction of Asphalt Concrete Overlay

As in the base/subgrade friction coefficient studies in the previous section, three particle friction coefficients are used. The reference value of 0.5 used in the current study is based on reference (Kim, 2007). The other two values of 0.31 and 0.7 are selected. One is higher and the other is lower than that of reference value. Results of these three particle friction coefficients are shown in Figure 3.11. The analyses indicate that displacements are 10.3, 9.4, and 8.3 mm for 0.31, 0.5, and 0.7 of friction coefficient respectively. Based on the reference value of 0.5, total displacement is increased by 9.57% for friction coefficient 0.31 and decreased by 11.7% for friction coefficient 0.7. There are similar differences in displacement corresponding to particle friction changes. A higher friction coefficient yields a lower displacement due to the restraint of the slide and rotation of particles, which results in lower displacement.

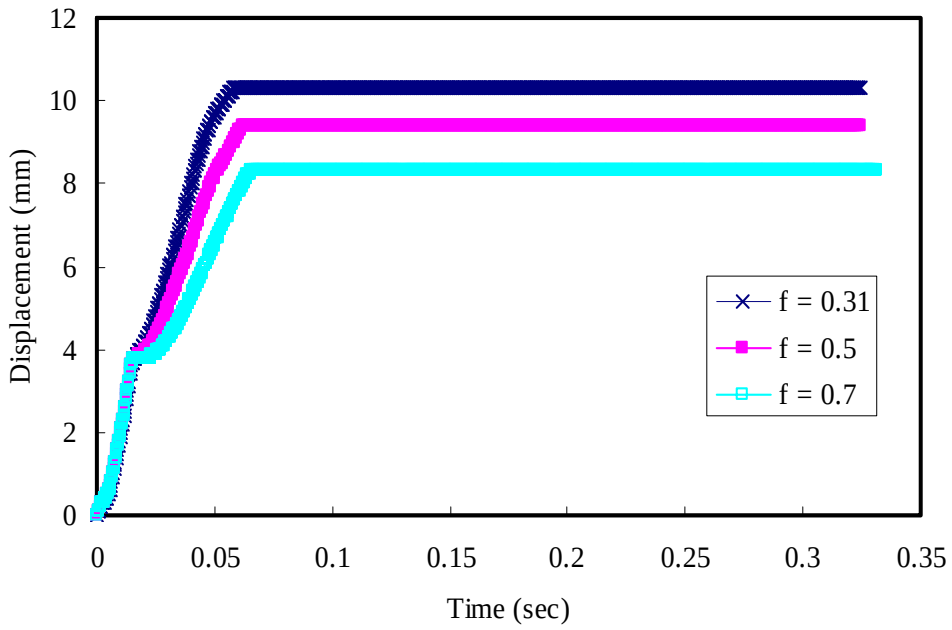

Figure 3.11 Particle friction coefficient effects on pavement section

3.4 Summary

In this chapter, the bilinear cohesive zone model was introduced for fracture modeling based on the overview of discrete elements. Mass or density scaling was mentioned briefly. Model properties of simulation were determined by biaxial test in PFC2D, and parametric studies on factor of safety, particle friction coefficient, and particle stiffness were conducted to check the feasibility of the selected parameters and to assess the effects of the specific parameters on macro-scale response.

CHAPTER 4 Model Calibrations

4.1 Introduction

Several field applications of paving fabric in the rehabilitation of existing PCC pavements were evaluated by Maxim Technology Inc. (1997) including fourteen sites in eight states within the United States and locations in Belgium and Austria, over the course of three to ten years. Maxim reported that the use of a paving fabric in the rehabilitation of PCC pavements does retard reflective cracking. This chapter will examine such fracturing using DEM pavement modeling. Reflective cracking due to the contraction of joints and major transverse cracks in Portland cement concrete (PCC) pavements usually begin to spread through asphalt concrete overlays in a relatively short time, sometimes within less than a year for overlays up to three inches thick (Mascunana, 1981).

The main object of this study is to calibrate the DEM pavement fracture model for evaluating the effectiveness of geosynthetics in controlling reflective cracking of asphalt concrete overlays. This study includes the comparison of field performance with DEM pavement fracture modeling, and investigates the effects of overlay thickness, geosynthetic locations, and geosynthetic properties. Finally, calibration factors based on different locations (specifically Atlanta and Florida) will be calculated and compared.

4.2 Model Description of AC overlay on Existing PCC pavement

The DEM pavement model is developed based on test pavements by Ballinger Construction Company constructed on April 9, 2001, as part of Texas DOT construction contract CPM 1804-2-19 (Button et al., 2005). The existing roadway consisted of 12 inches

of lime-stabilized subgrade, 14 inches of lime-stabilized flexible base, and 8 inches of PCC pavement in this study instead of 2.5 inches of HMA pavement with a length of 1,002 mm. For the asphalt concrete overlay thickness, the range of 2 inches (50.8 mm) to 6 inches (152.4 mm) is used to investigate the effects of overlay thickness. Single large sized particles are used in order to reduce computational time, though particles are not a real size. Uniform particles with 8 - 12 mm diameters, 5,848 in quantity, are used for base and subgrade materials; 11,356 particles with 3 mm diameters, and 5,379 particles with 6 mm diameters are used for representing the AC layer and PCC layer, respectively. The dimension and geometry of the DEM pavement model can be seen in Figure 4.1. All particle generation procedures are addressed in the previous chapter. A constant loading rate controlled by y-velocity is used in this model in order to see the fracture behaviors of pavement.

The right and the left side edge are set to free displacement boundaries because it is assumed that 10 times of loading diameters is possible to ignore the boundary conditions by applied loading. Also, wall is used to the boundary conditions of Base/Subgrade layers not to allow x,y displacements.

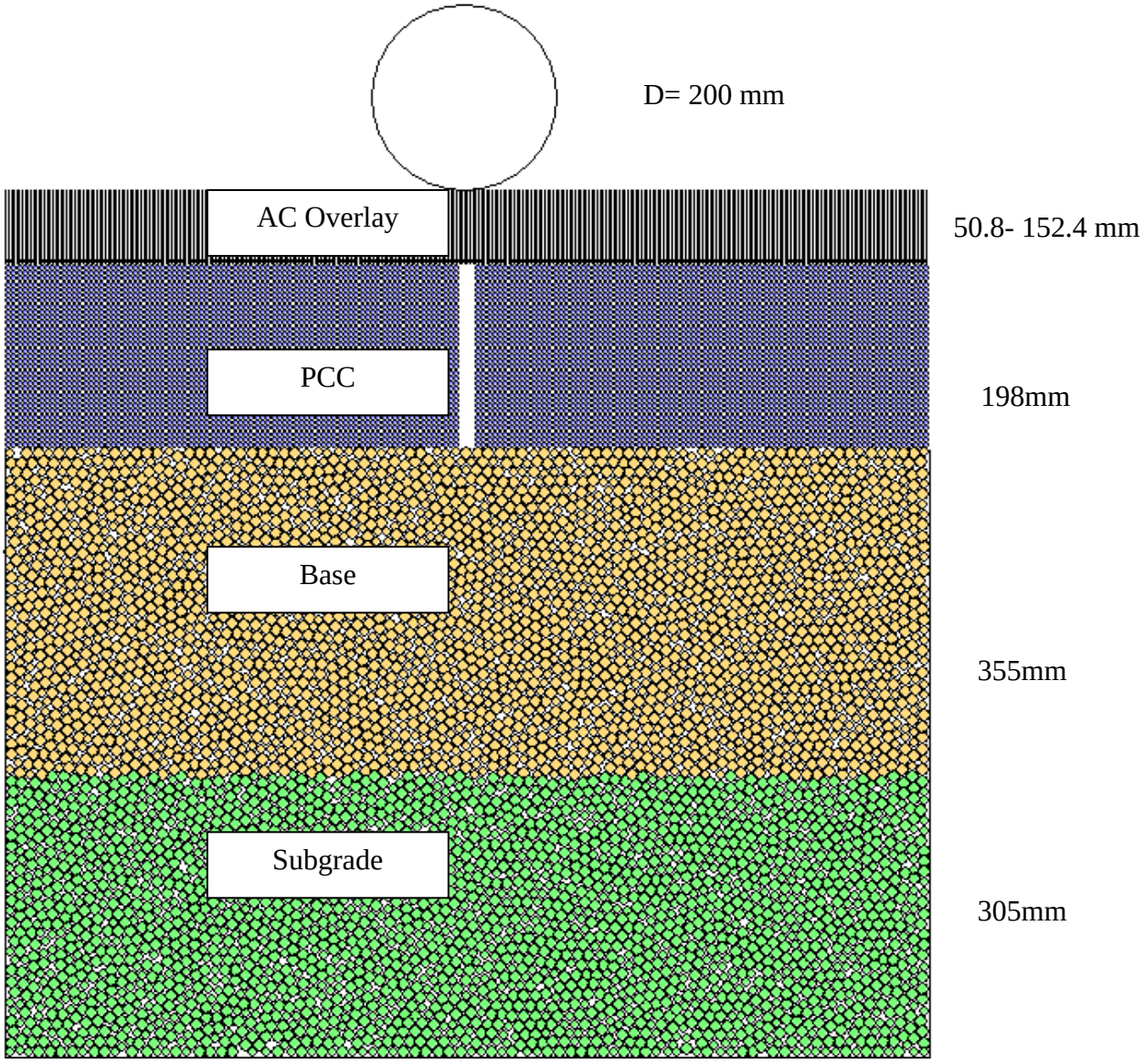

Figure 4.1 Dimension of DEM pavement model-Reinforced case

As shown in Figure 4.2, to represent the fracture simulation, the potential crack area of 378 mm length and various AC thicknesses are assigned using the cohesive softening model. The rest of the AC overlay uses Burger's model representing viscoelastic material

properties for the creep and relaxation behaviors of bulk asphalt concrete. To reduce the computational time to simulate reflective cracking, the PCC joint/crack with 24 mm gap conditions are assumed to represent poor condition. A tack coat layer, which is modeled with bonded particles of 1.5 mm radius, is used to adhere the geosynthetic and PCC together easily before embedding the geosynthetic, which is composed of 501 particles and modeled using bonded particles of 1 mm radius.

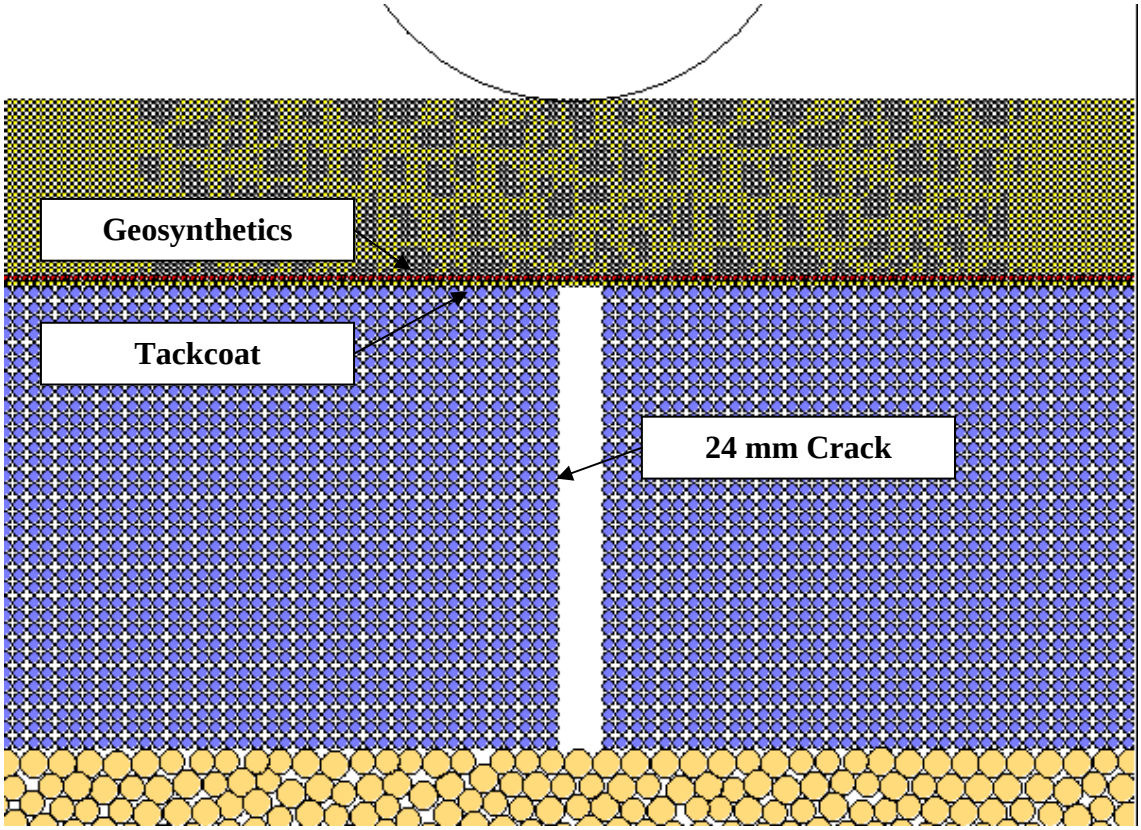

Figure 4.2 Dimensions of DEM pavement model-Reinforced case

Model properties for the pavement section are presented in Table 4.1. All properties used for the asphalt concrete are from the works of Wagoner (2006) and Kim (2007). The fracture parameters are assumed from experimental test data by Wagoner (2006). Like Kim (2007), material properties are converted to DEM contact properties by using Eq. (3.10)

Table 4.1 Material Properties of DEM pavement model

Layer	Phase	Young's Modulus (GPa)	Strength (MPa)	Stiffness (GN/m)	Bond Strength (kN)
AC	Mixture	23.7	3.56	23.7	10.68
	Aggregate	56.8	6.59	56.8	19.77
	Mastic	13.8	2.87	13.8	8.61
	Interface	13.8	2.61	13.8	7.83
PCC		27.6	2.61	27.6	15.66

Base/Subgrade

Parameter	Granular Base	Subgrade	Reference
Particle Stiffness (N/m)	10^8	$4\times10^{7*}$	Santamarina et al.(2001)
Particle friction coefficient	0.31	0.31	Proctor and Barton (1974)

* Calculated from biaxial test using PFC2D

For the tire loading, a single wheel load is applied above the PCC crack. The effect of loading rate in the DEM pavement model is investigated in order to observe fracture behaviors under different loading conditions: 0.7 mm/sec, 3.5 mm/sec, and 7 mm/sec. As shown in Figure 4.3, loading rate can affect reflective cracking behavior, where reflective

cracking is defined by current crack length against total overlay length. The results show that, compared to the time it takes to reach 100% reflective cracking with a loading velocity of 7 mm/sec, it takes 1.92 times as long, and 8.4 times as long to reach the same level of reflective cracking at 3.5 mm/sec and 0.7 mm/sec, respectively. The comparison of these three cases indicates that the behavior of reflective cracking is non-linear under increasing loading time. As loading rate increases, applied force behaviors like linear are affected as well, as shown in a force versus time curve (see Figure 4.4).

Wagoner et al. (2005b) experimentally investigated the effect of loading rate at the crack mouth opening on fracture energy using the Disk-Shaped Compact Tension (DC(T)) test. They found that loading rate can significantly influence on fracture energy. Fracture energy decreases if the loading rate increases, accompanied by increased brittleness. For a realistic simulation of the material behavior of asphalt concrete, a lower loading rate is necessary; however, the increased computational time must also be considered.

In this study, a loading rate of 7 mm/sec is used not only to minimize the computational time but also to represent cracking trends regardless of inelastic behavior of the asphalt concrete.

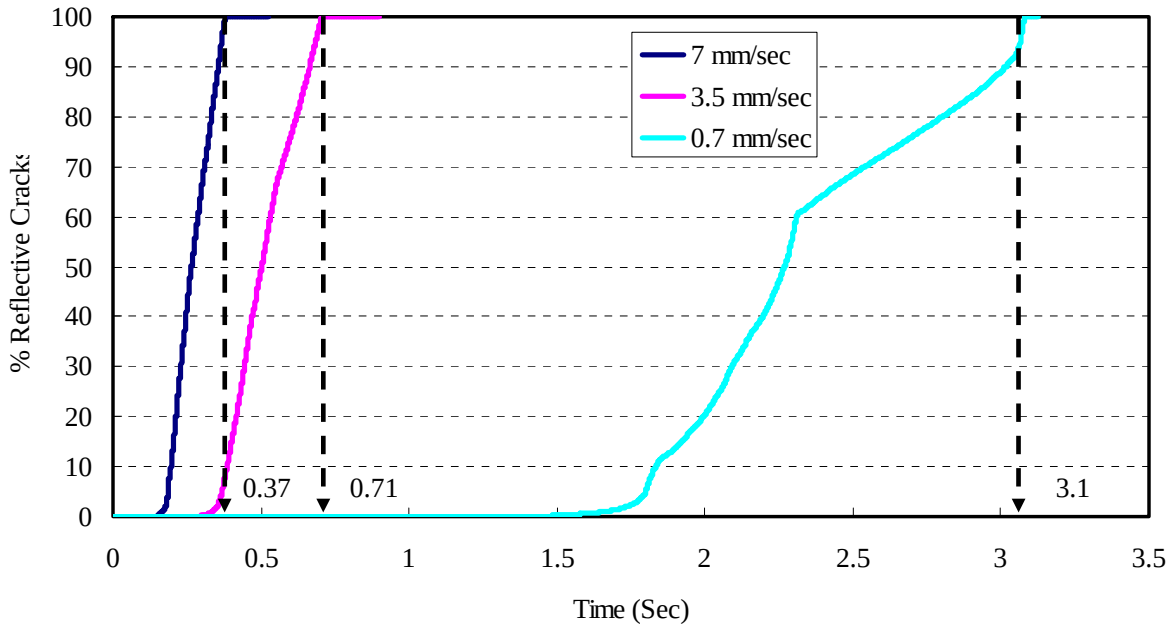

Figure 4.3 Numerical Force versus Reflective Cracks with different loading rates

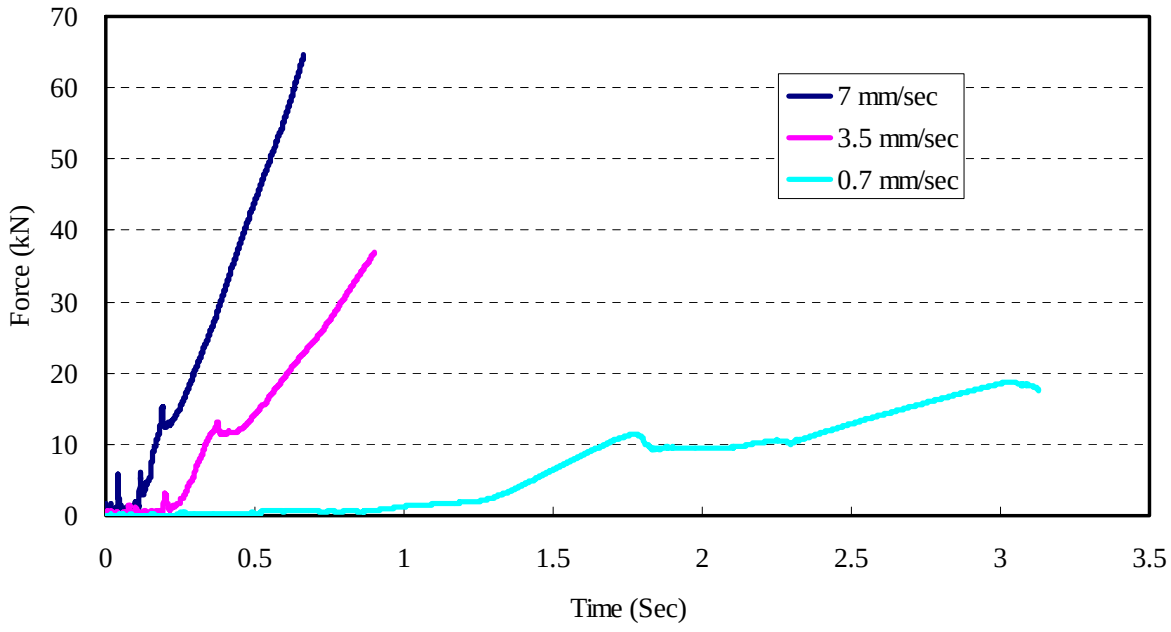

Figure 4.4 Numerical Force versus Time with different loading rates

4.3 Results of DEM pavement Model

4.3.1 Effect of Overlay Thickness without Fabric

The effect of overlay thickness has been studied by several researchers (Ahlrich, 1986; Button, 1989; Predoehl, 1990). As an example, the Georgia Department of Transportation (DOT) has performed an extensive amount of work to rehabilitate PCC pavements in its interstate system (Ahlrich, 1986). This case study in Georgia provides important information on reflective cracking retardation by means of the AC thickness alone, and informs our study of the relationship between geosynthetic reinforced AC thickness to original conditions of PCC pavements. The performance of pavements without paving fabrics in Atlanta, Georgia is summarized in Figure 4.5. The Georgia DOT used these projects to compare overlay thicknesses of 2, 4, and 6 inches (50.8, 101.6, and 152.4 mm). The results show that reflective cracking at a 60% level may be predicted at one year for a 2-inch AC overlay, three years for a 4-inch AC overlay, and nine years for a 6-inch AC overlay. The thicker overlays showed longer service life than the thinner overlays. The 2-inch overlay displayed almost immediate reflective cracking, while two thicker overlays showed a delay in the initiation of reflective cracking.

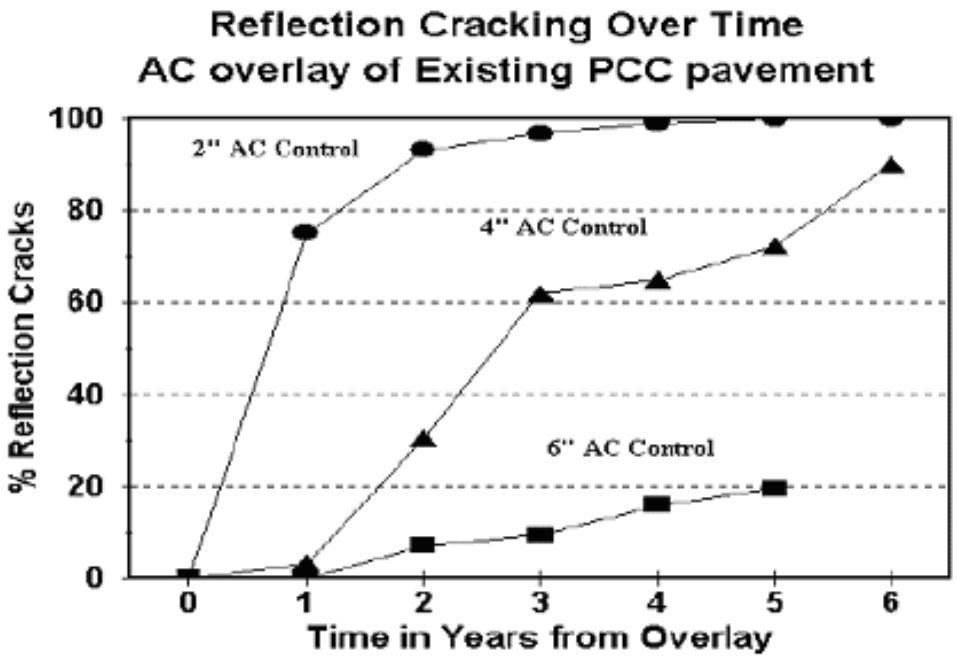

Figure 4.5 AC Overlay of Existing PCC pavements – Atlanta, Georgia Case Study (Maxim, 1997)

Numerical simulations using PFC2D are performed for overlay thickness of 2", 4", and 6" as in the Georgia case study and the results are presented in Figure 4.6. There are limitations in comparing field data and simulation data because of the difficulty in considering all of the loading conditions, such as wheel loading type, climate, temperature, asphalt concrete type, etc. Therefore, it is not possible to draw exact comparisons between field and simulation data. Thus, in this study, the focus is on the trends, whether illustrated by simulation or by field data, and regardless of the huge difference in observation time. Simulation results show that the times required to reach the 60% level of reflective cracking were 0.28 sec, 0.4 sec, and 0.5 sec for 2" overlay, 4" overlay, and 6" overlay, respectively, as

shown in Figure 4.6. These results indicate that thicker overlays offer benefit in retarding reflective cracking, confirming the previous results of the Georgia field case study.

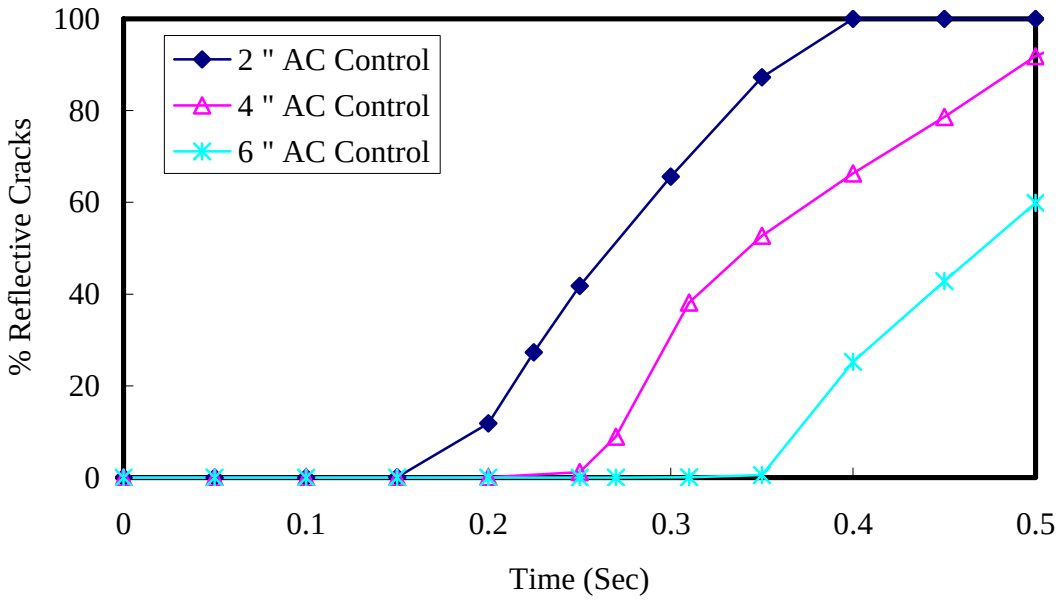

Figure 4.6 Reflective cracking over time using DEM pavement modeling without Geosynthetic Reinforcement - Atlanta, Georgia Case Study

Figure 4.7 presents the results from the DEM pavement model and shows the crack pattern in the fracture process zone in the asphalt concrete layer according to different overlay thickness. Cracks occur just over the joint/crack of PCC layer. Then cracks developed by loading continue to penetrate the entire overlay and reach the top of the overlay. As shown in Figure 4.7, the different cracking patterns are produced according to different overlay thickness. In the 2", relatively thinner overlay, the cracking follows a straight line pattern (Figure 4.7(a)). Meanwhile, the cracking patterns of relatively thicker overlays of 4" and 6" seem to be somewhat complicated instead of straight lines (Figure 4.7 (b) and (c)).

The crack initiation location with a 6” overlay thickness is also different from the other two cases under the same loading condition.

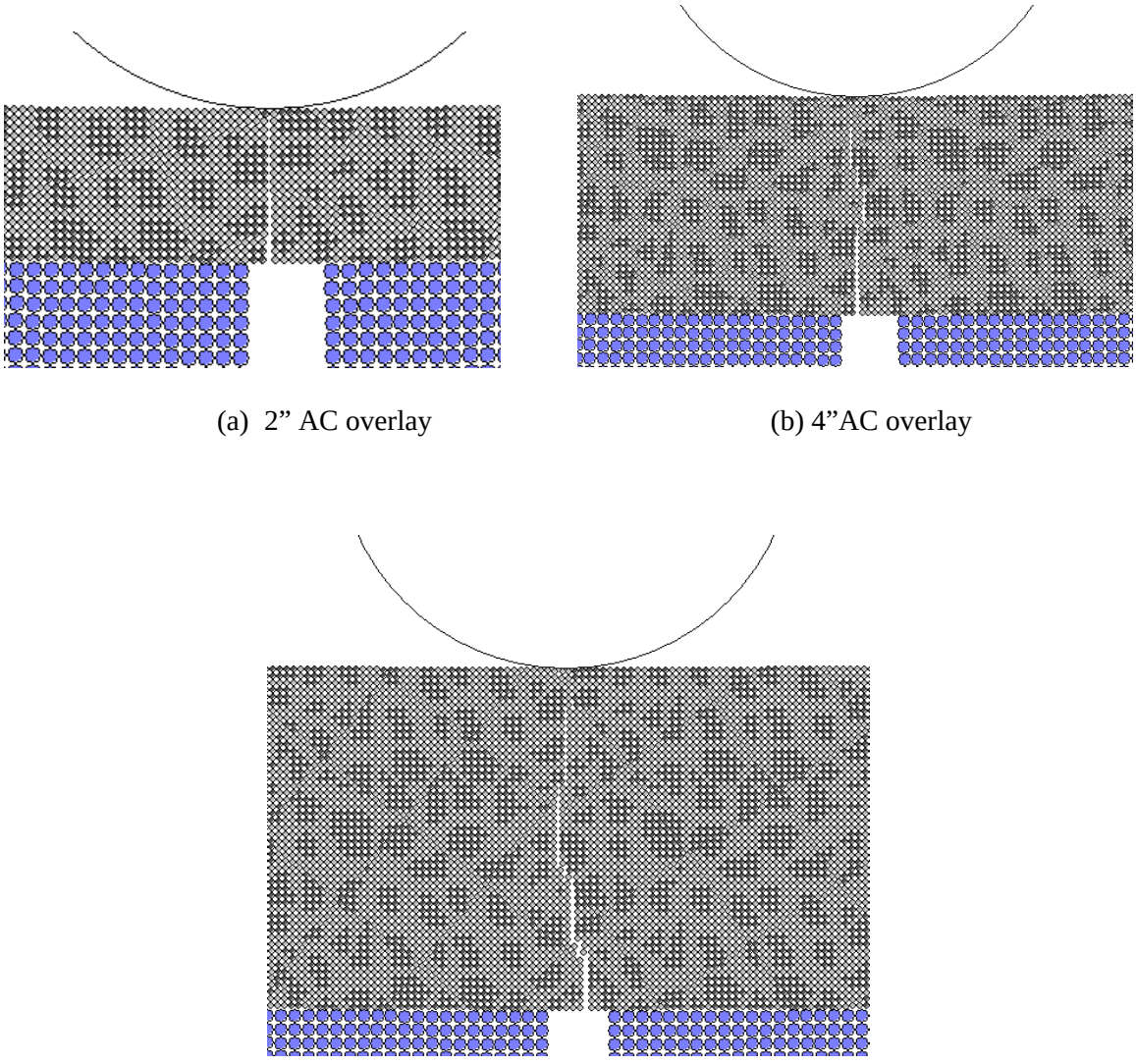

(a) 2” AC overlay

(b) 4”AC overlay

(c) 6”AC overlay

Figure 4.7 Macro-Cracks in DEM Pavement Model

4.3.2 Effect of Overlay Thickness with Fabric

In the same study by Georgia DOT, the effect of reinforcement of the AC overlay with paving fabric was also investigated, and similar relationships were observed for sections with paving fabric, as shown in Figure 4.8. The results show that reflective cracking at the 60% level may be predicted at three years for a 2" AC overlay and six years for a 4"AC overlay with fabric. Reflective cracking at the 60% level could not be predicted for the 6" overlay with fabric because this combination of reinforcement and thickness was so effective that only a very low percentage level of reflective cracking was achieved during the monitoring period. Although the performance trends for overlays with and without fabric are basically the same, it is clear that the reinforcement of the AC overlay can significantly improve service life.

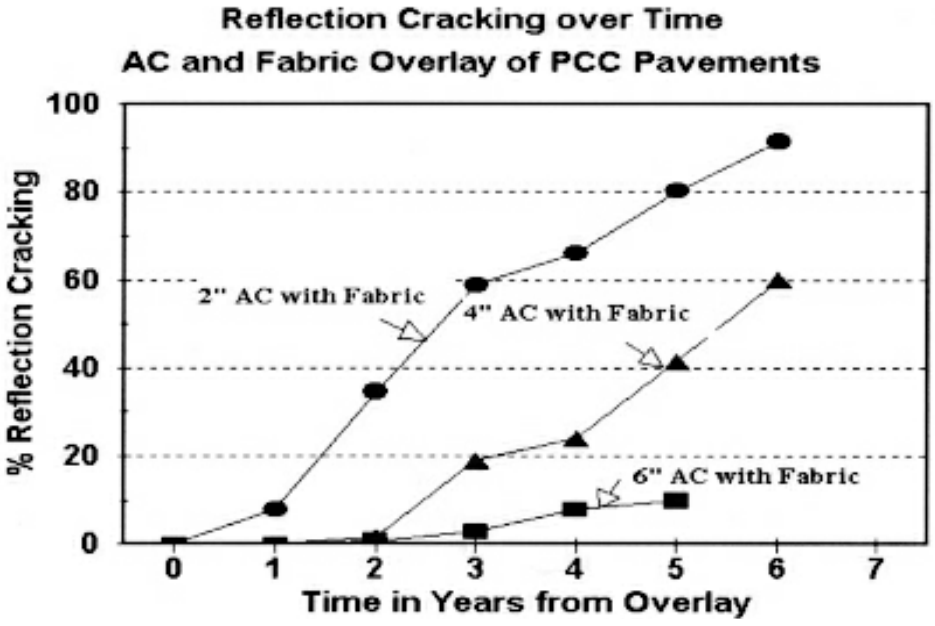

Figure 4.8 AC/Fabric Overlays of Existing PCC Pavements – Atlanta, Georgia Case Study (Maxim, 1997)

Numerical simulations using PFC2D are performed for the overlay thickness of 2", 3", 4", and 6" as in the Georgia case study and the results are presented in Figure 4.9. The result shows the time to reach 60% level of reflective cracking is 0.32 sec, 0.43 sec, and 0.52 sec for 2" overlay, 4" overlay, and 6" overlay, respectively. This result indicates that the inclusion of geosynthetics increases service life as in the Georgia case study. And improvement by geosynthetic is also shown with DEM modeling but marginal. Like the field data from the Georgia case, the performance trends for both studies with and without reinforcement are basically the same.

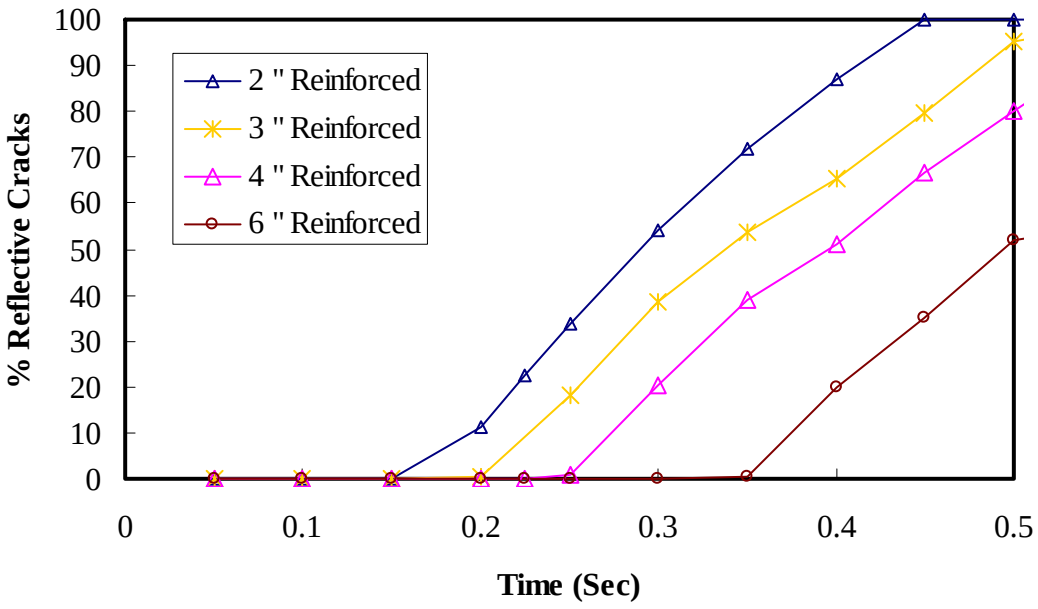

Figure 4.9 Reflective cracking over time using DEM pavement modeling with Geosynthetic Reinforcement - Atlanta, Georgia Case Study

The results from Figure 4.5 and 4.8 are combined in Figure 4.10 in order to illustrate the benefit of geosynthetic reinforcement in the rehabilitation overlay of existing PCC pavements. As shown in Figure 4.10, the 2" reinforced overlay appears to be equivalent to the 4" AC control overlay. The DEM simulation results from Figures 4.6 and 4.9 are combined in Figure 4.11. In DEM simulations, it seems that the 3" reinforced overlay is very similar to the 4" AC control overlay. The difference between the two results can be explained by the fact that the Georgia environment is not considered in the DEM simulations. However, the basic finding that geosynthetics can retard or reduce reflective cracking is the same. In the thicker overlays (especially the 6" overlay), the benefits attributable to the geosynthetic are relatively low because less deflection occurs (Maxim Technologies, 1997).

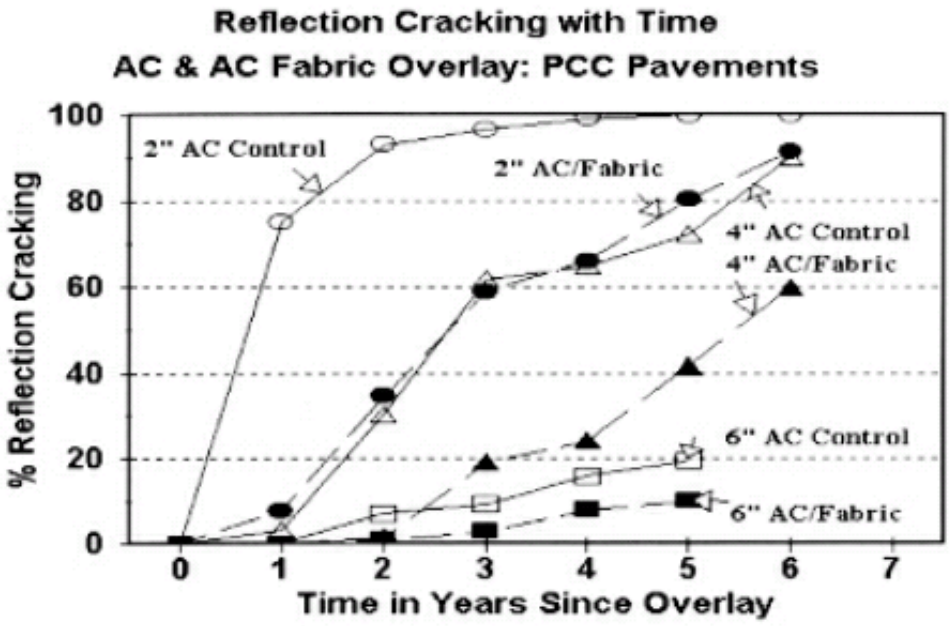

Figure 4.10 Combined reflective cracking with time on AC / AC Fabric overlay -Georgia Case study

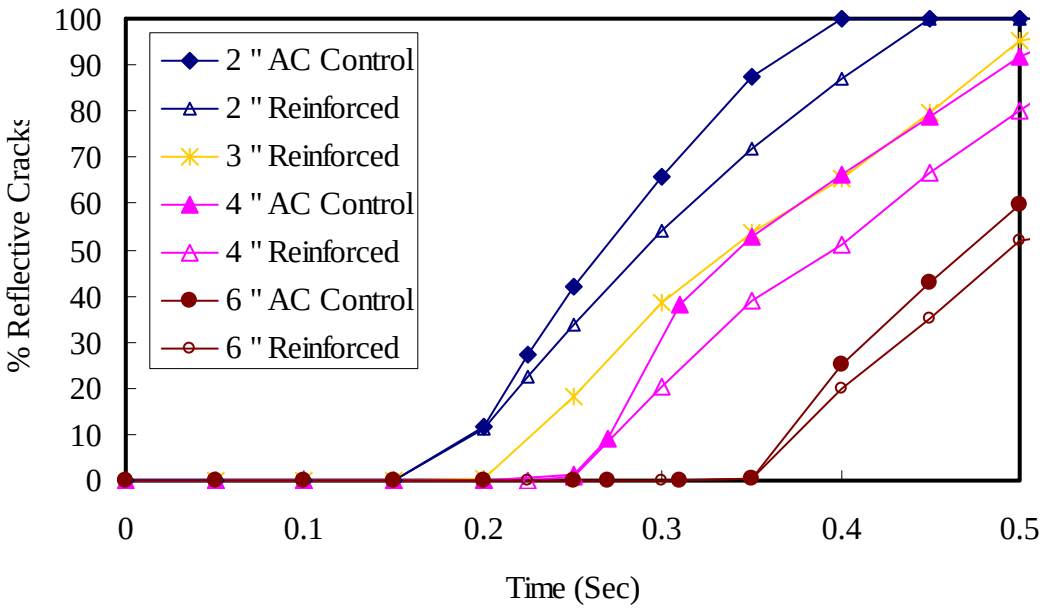

Figure 4.11 Combined DEM results of Reflective cracking versus time-Georgia Case study

4.3.3 Contact forces for AC layer

Figures 4.12 to 4.14 illustrate the contact forces developed between ball contacts, and plotted as lines with thickness proportional to force magnitude, after reflective cracking on AC overlays, both unreinforced and reinforced sections with varying overlay thicknesses of 2", 4", and 6". According to figures, compression and tension seem not to be affecting the boundary condition as assumed previously. The contact forces are distributed along the cracking as shown in Figures. As overlay thickness increases, the PCC layer is less affected by compression because of that overlay thickness.

The distribution of contact forces given a 2" overlay thickness are compared in reinforced and unreinforced overlays as shown in Figure 4.12. The contact forces under the

overlay are less condensed when the geosynthetic is used with the AC overlay as shown within the dotted red circle. This illustrates that the geosynthetic reinforcement helps distribute the contact forces, encouraging them to spread out beneath the reinforced layer. And as a benefit of reinforcement, tension converts to compression at the interface between overlay and PCC layer. In 4” overlays, the compression forces are relatively less converged at the bottom of the overlay compared to 2” overlays; the contact force distributions do not show much difference these two cases. Compression, in the overlay with reinforcement, is indicated along the geosynthetic at the bottom of the overlay as shown in Figure 4.13. As overlay thickness increases from 2” to 6”, compression at the interface also increases both with and without reinforcement.

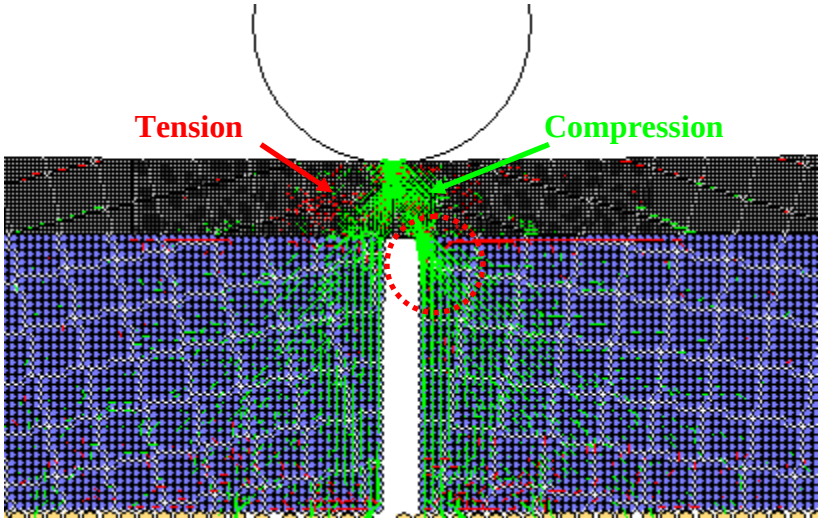

(a) Unreinforced AC overly

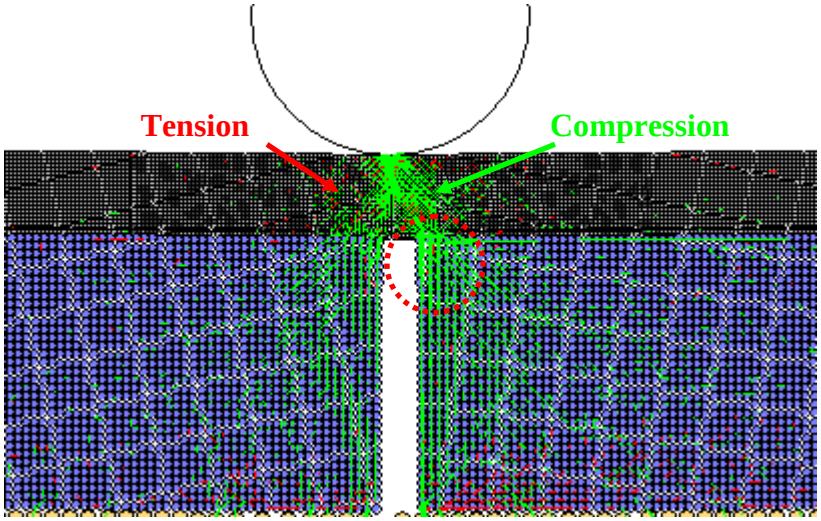

(b) Reinforced AC overly

Figure 4.12 Contact force distribution of Reinforced 2” overlay thickness

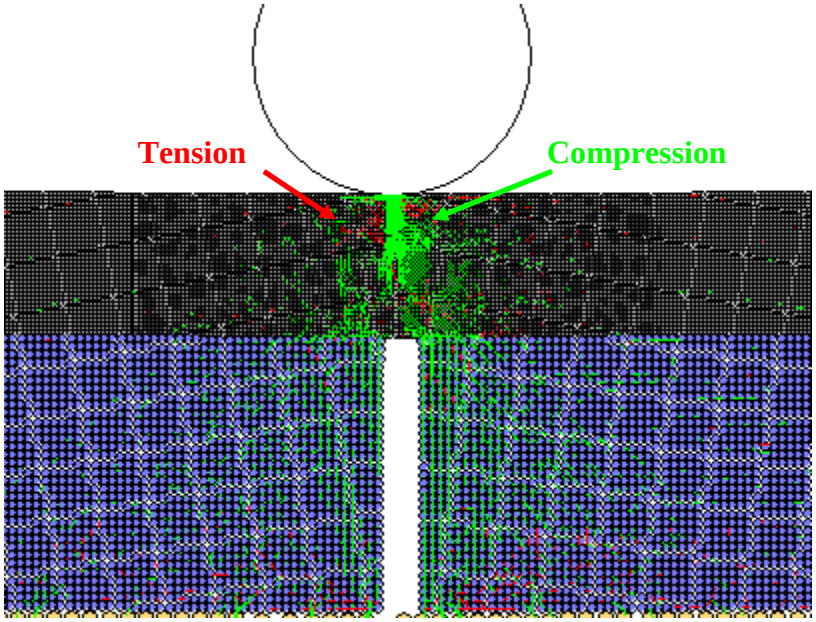

(a) Unreinforced AC overly

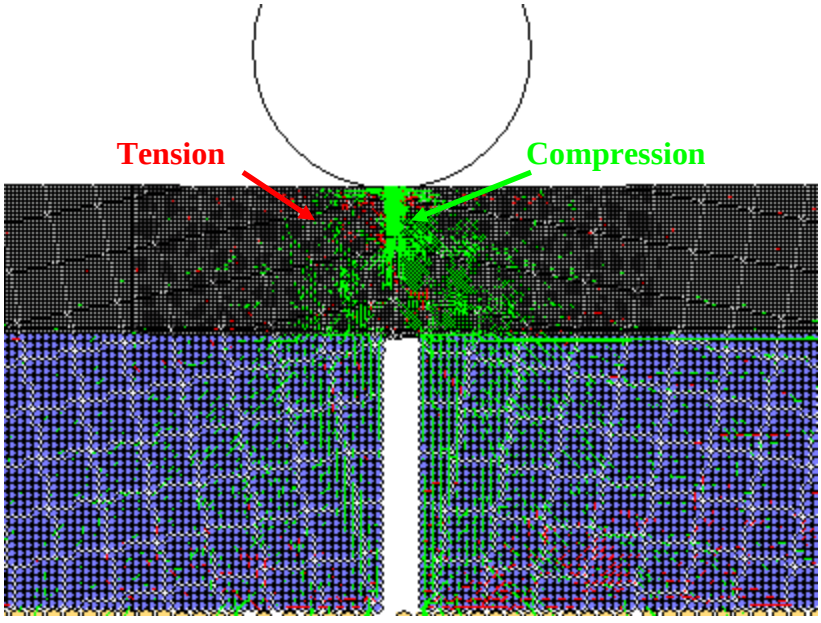

(b) Reinforced AC overly

Figure 4.13 Contact force distribution of Reinforced 4” overlay thickness

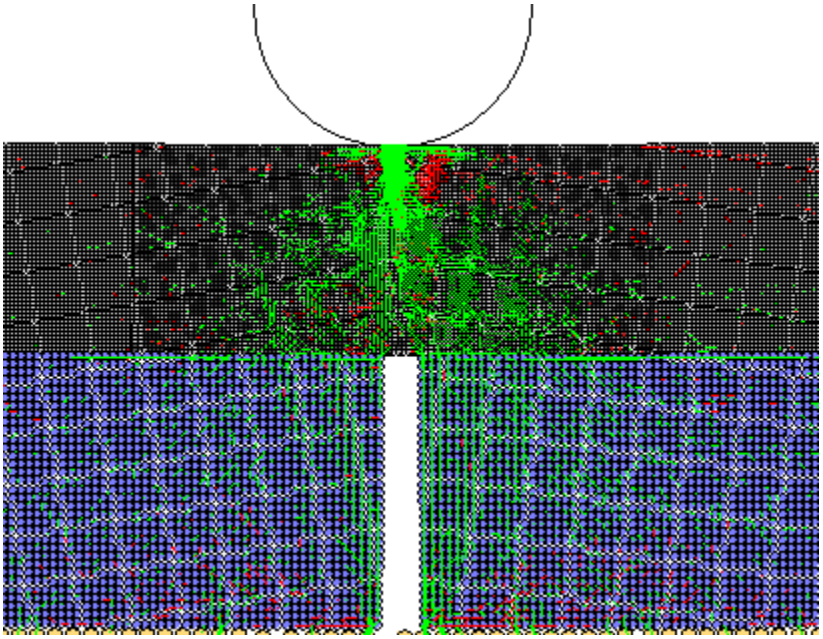

(a) Unreinforced AC overly

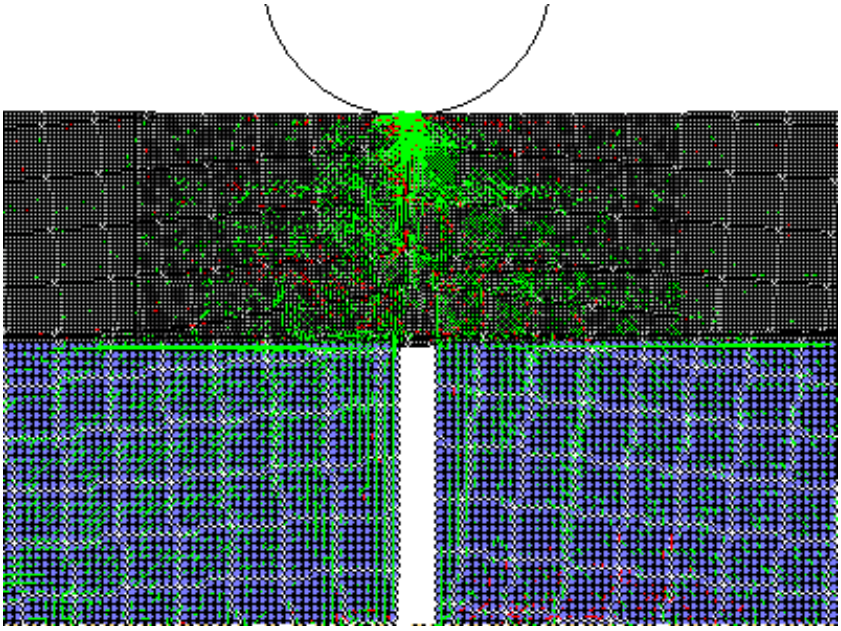

(b) Reinforced AC overly

Figure 4.14 Contact force distribution of Reinforced 6” overlay thickness

4.3.4 Effect of Geosynthetic Location

The crack propagations over existing concrete pavements are different according to the location of the geosynthetic in the overlay. In this chapter, the results of only two locations are investigated, specifically at the bottom and at 1/3 thickness from the bottom of the overlay. The affects of these different geosynthetic placements can be seen in Figure 4.15. The result shows that the time to reach a 60% level of reflective cracking is 0.28 sec, 0.32 sec, and 0.33 sec for only overlay, overlay reinforced at the bottom, and overlay reinforced at 1/3 overlay thickness from the bottom, respectively. Analysis shows that geosynthetic reinforcement at a one-third depth from the bottom is more effective than geosynthetic embedded at the bottom of the overlay. This result is in agreement with a previous chapter and with the works of Kuo and Hsu (2003) and Khodaii et al. (2009), as well.

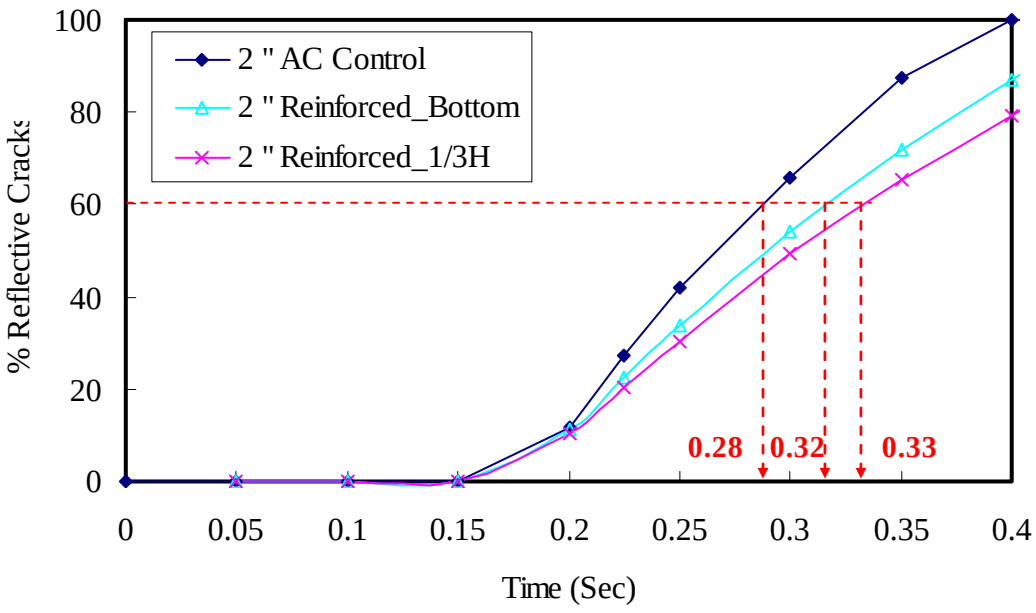

Figure 4.15 Effect of Geosynthetic location using DEM pavement model

The reflective cracking of AC overlays which are reinforced at the bottom and at one-third depth from the bottom is presented in Figures 4.16 and 4.17. Reflective cracking starts to develop just over the joint/crack of PCC layer, as in an unreinforced overlay. The locations of crack initiation are the same even though reinforcement locations are different as seen in figures.

Contact force distributions within overlay reinforced at one-third depth and reinforced at the bottom are presented in Figure 4.17. Green and red colors represented compression and tension, respectively. Both reinforced at one-third depth and at the bottom, the contact force distribution seems to be similar. Moreover, tension is observed at the interface of between overlay and PCC layer. But maximum tension is 37.3 kN at bottom reinforcement and 35.2 kN at one-third reinforcement, respectively. This means that one-third reinforcement is more effective than bottom reinforcement case because less tension is generated as an effect of reinforcement location.

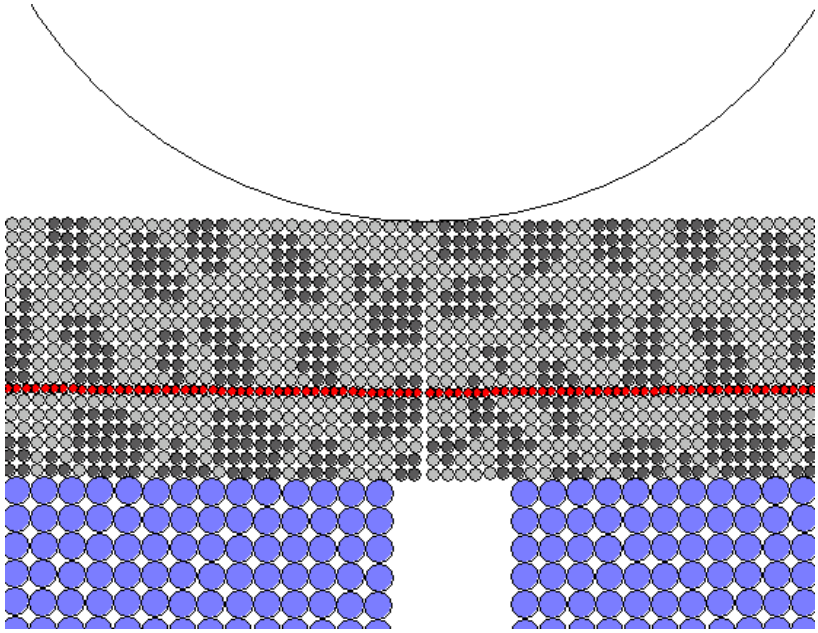

(a) Reinforced at 1/3 overlay thickness from the bottom

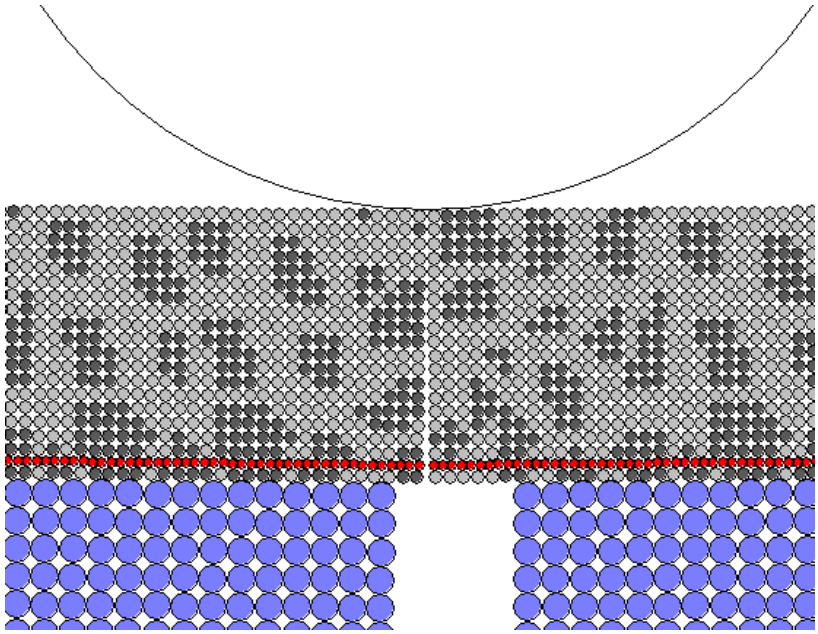

(b) Reinforced at the bottom of overlay

Figure 4.16 Reflective cracking in the reinforced AC overlay

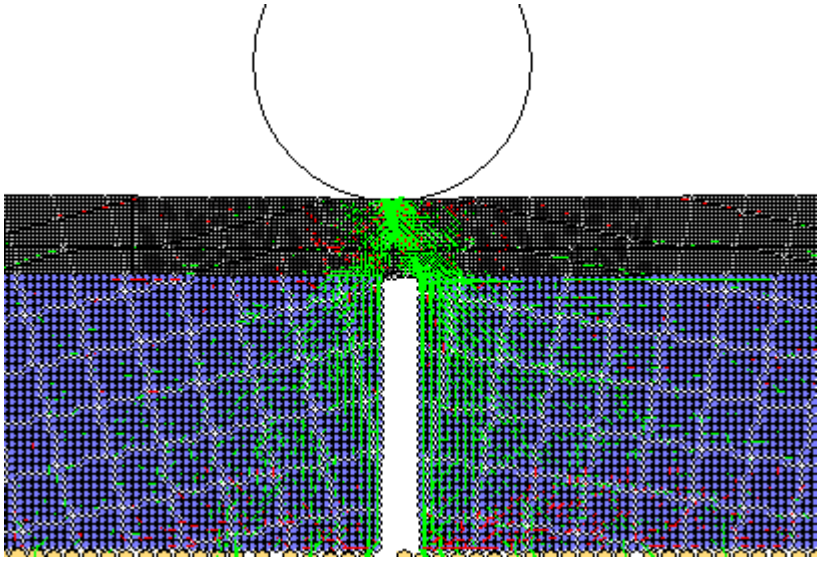

(a) Reinforcement at 1/3 overlay thickness from the bottom

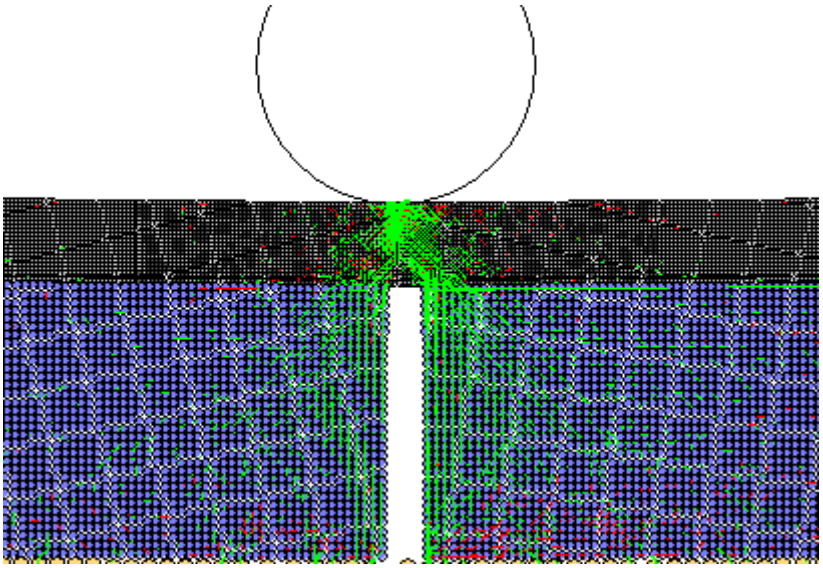

(b) Reinforcement at the bottom of overlay

Figure 4.17 Contact force distributions by DEM pavement model

4.3.5 Effect of Geosynthetic Properties

The properties of geosynthetics considered in this study are presented in Table 4.2. Details of the properties of geosynthetic materials are addressed in the work of Chareyre et al. (2002).

Table 4.2 Parameters selected for modeling the geosynthetic

Parameters selected for the geosynthetic	GTX01	GTX02
Tensile strength, a_n^{gg} (kN/m)	30	95
Shear strength, a_s^{gg} (kN/m)	30	95
Normal stiffness, k_n^{gg} (kN/m^2)	80/d^{g*}	624/d^{g}
Shear stiffness, k_{gg} (kN/m^2)	0.5×10^5	0.5×10^5
Friction angle, μ_{gg}	0	0

*d^g is the diameter of geosynthetics.

Results according to these properties are presented in Figure 4.18. The result shows that the time to reach 60% level of reflective cracking is 0.38 sec for no reinforcement, and 0.43 sec and 0.45 sec for reinforcements with two different properties, respectively. A geosynthetic with higher strength and stiffness is better able to reduce/retard reflective cracking, as shown in Figure 4.18. Figure 4.19 shows reflective cracking versus time in a Florida case study. Data from 0 to 4 years appear somewhat variable, so a trend line is added in order to predict a time of 3.6 years to reach a 60% level of reflective cracking without reinforcement. As in the DEM simulations, geosynthetics are shown to have benefit in reducing reflective cracking although the results differ according to the type of geosynthetic. It can be presumed that the differences in crack initiation between modeling and case study

are due to environmental variables such as geosynthetic properties, loading conditions, and regional conditions.

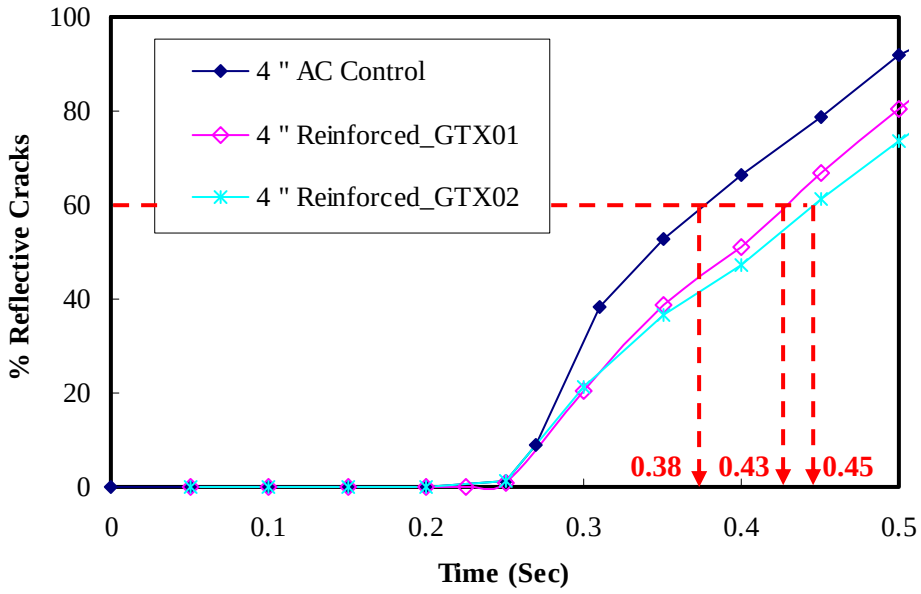

Figure 4.18 DEM results with different Geosynthetic properties – 4" AC overlay

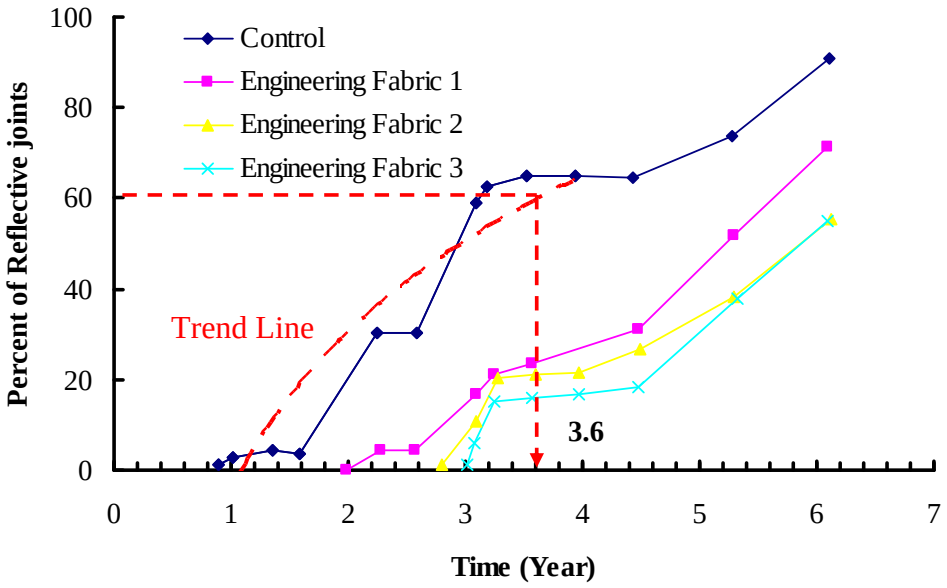

Figure 4.19 Percent Reflected joints versus Time – 4" AC overlay PCC Pavement (Florida)

Times to reach 60% reflective cracking of 4” AC control sections in the Georgia and Florida studies are summarized in Table 4.3. From these results, calibration factors for fitting field data to the DEM model are determined to be 7.9 and 9.5 (8.2), respectively. Where (8.2) is calculated value from original curve. Even though the studies are conducted at two different sites, calibration factors are estimated to be close to each other. Thus, it seems that the DEM model can perform successful evaluation of the pavement section.

Table 4.3 Time to reach 60% reflective cracking according to different field cases

Location	Time		Calibration Factor
	Field (years)	DEM (sec)	
Atlanta	3	0.38	7.9
Florida	3.6 (3.1)	0.38	9.5 (8.2)

4.3.6 Effect of Porosity

According to the PFC2D manual, the default initial air void ratio (porosity, *n*) of a cubic packing arrangement in which each ball is in contact with four neighbors as seen in equation (4.1) is 0.2146, even though air void ratio of asphalt ranges between 4 and 8 %.

$$n = 1 - \frac{\pi R^2}{(2R)(2R)} = 1 - \frac{\pi}{4} \approx 0.2146 \quad \text{(simple cubic packing)} \tag{4.1}$$

To represent realistic asphalt mixture conditions, preloading is applied on the pavement section. Figure 4.20 shows the change of air void ratio after preloading. Rearrangement of particles has occurred and, consequently, the scattered cracks can be monitored.

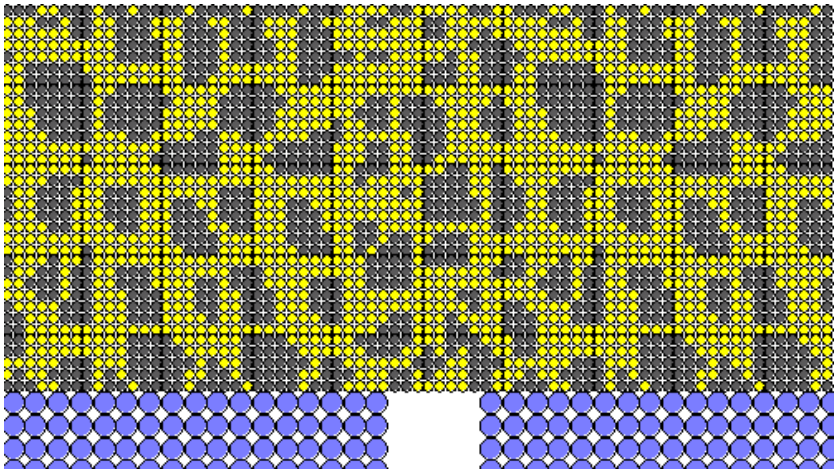

(a) Initial air void ratio, n = 0.2146

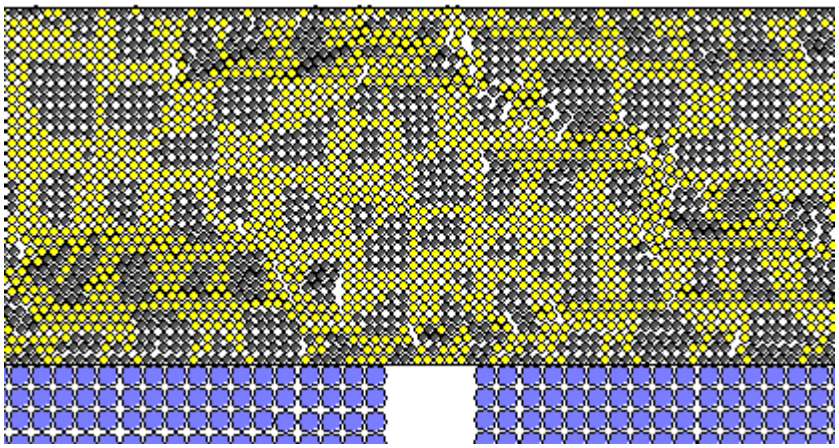

(b) After preloading air void ratio, n = 0.1952

Figure 4.20 Change of air void ratio after preloading

Figure 4.21 shows the crack pattern after applying external loading. Because of the rearrangement of particles due to the preloading, macro-crack paths are similar but not the same.

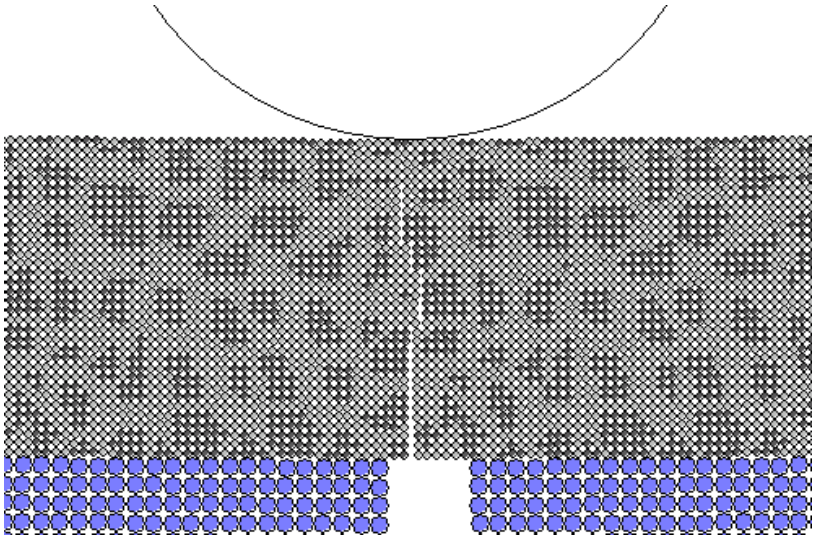

(a) Cracking without preloading

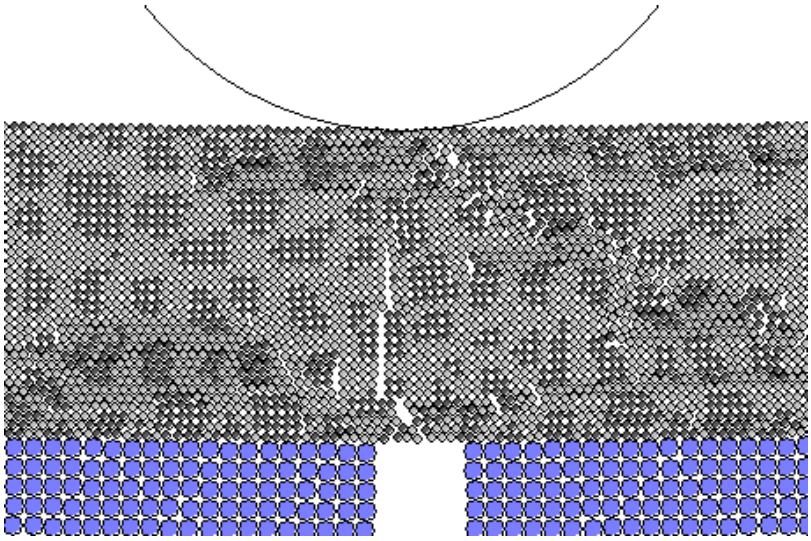

(b) Cracking after preloading

Figure 4.21 Crack pattern with DEM model

4.4 Summary

In this chapter, the DEM pavement model was developed and calibrated with field scale but not with real particle sizes. Results were presented for evaluation of the effects of overlay thickness (specifically, 2”, 4”, and 6”), of geosynthetic location (at the bottom, or at one-third of the overlay thickness from the bottom), and of specific geosynthetic properties, and these results were compared with field data, especially Georgia DOT data. In addition, cracking patterns and contact forces according to overlay thickness, and geosynthetic reinforcement were investigated. Through the use of calibration factors derived from studies at two different sites in Georgia and Florida, it can be seen that the DEM model is an appropriate method for representing the pavement section for purposes of this study.

CHAPTER 5 DEM Model under Constant Loading

5.1 Introduction

The repair and rehabilitation of existing pavement is one of the most important issues nowadays. Asphalt concrete overlay on the existing pavement is commonly used as a cost-saving surface treatment for deteriorating pavements. However, a major problem in the asphalt overlay is reflective cracking which leads to roughness, spalling, and moisture infiltration due to stress concentration in the vicinity of joints and cracks in the underlying pavement layer. Finally, reflective cracking can greatly reduce the service life of the overlay. Huang (2004) describes that reflective cracking is a major problem in the design of HMA overlays on PCC pavement. According to Buttlar and Bozkurt (2000), transversely-aligned reflective cracks tend to be the most severe in highways because of the combined effects of weak underlying PCC transverse joint and the directionality of thermal stresses in the asphalt overlay.

Several methods are used to minimize or prevent reflective cracking. Studies have indicated that the cost of reflective crack treatment is usually very high (Buttlar et al., 2000). However, some literature suggests that a fabric interlayer with an overlay is being used in some areas and appears to be effective in reducing reflective cracking (Huang 2004), as well as being relatively economical (Buttlar et al., 2000; Synthetics Industries, 2003).

With the introduction of geosynthetic materials in pavement applications, various analysis methods have been explored to identify the causes of reflective cracking with the objective of improving future overlay designs. Early research at the Texas Transportation Institute (Button et al., 1983; Lytton, 1989; Pickett and Lytton, 1983; Germann and Lytton,

1979; Chang et al., 1976; and Kohutek, 1983) was based on identifying fracture properties of the geosynthetics-mixture system using a fracture mechanics based approach. Bhandari et al. (2008) measured the rut depth of geotextile-reinforced pavement to evaluate geosynthetic-soil interaction. In their research, it was observed that the geotextile helped distribute contact forces to a wider area and reduced the rut depths slightly in a medium dense state.

Although DEM has been extensively used to simulate the behavior of granular materials, only a few studies attempted to simulate the behavior of an asphalt material. Previous studies conducted by Chang and Meegoda (1997), Buttlar and You (2001), Collop et al. (2004), Wagoner et al. (2004), Kim (2006) have only focused on simulating small specimens for laboratory experiments, not whole pavement sections. Vallejo et al. (2006) simulated the combined behavior of the complete pavement structure using DEM to study particle crushing. Kim (2007) simulated a PCC pavement section to examine reflective cracking of the asphalt concrete overlay without reinforcement. Tutumluer et al. (2009) explained the behavior of geogrid-reinforced pavement, implementing PFC3D for numerical modeling, and field studies of geogrid-base-reinforced pavement systems have shown that such reinforcement improves pavement performance.

In this chapter, a DEM pavement model of a whole pavement section is developed based on previous research and adding missing parts such as more pavement layers and geosynthetic reinforcement. In addition, the displacement on the top of the pavement section, stress, and strain of overlay are observed, mainly under constant single wheel load pressure condition (80 psi).

5.2 Pavement Model Description

5.2.1 Dimension of Model and Boundary condition

A DEM pavement model is generated to simulate a rigid pavement section 378 mm in length with an asphalt surface thickness of 99 mm, a Portland cement concrete (PCC) thickness of 198 mm, a granular base thickness of 100 mm, and a subgrade thickness of 1,300 mm. This dimension is extended to four layers from Single-Edge Notched Beam test. The dimensions and geometry of the pavement DEM model can be found in Figure 5.1 and Figure 5.2. As shown in Figure 5.2, single large sized particles are used, rather than attempting exact reproduction of real particles, in order to reduce computational time. The base and subgrade materials are represented with a uniform size of 3,054 particles of 12 mm diameter, and 4,449 particles with 3 mm diameters and 2,043 particles with 6 mm diameters are used for representing the AC layer and the PCC layer, respectively. A notch is then inserted with a length of 18 mm, having a notch to depth (a/H) ratio of 0.18 (a similar ratio of 0.19 was used in the past by Wagoner et al. (2005) and Kim (2007)). In order to reduce computation time, the PCC conditions are assumed to be poor with no aggregate interlocking. The heterogeneity of asphalt concrete is considered for the AC overlay as presented by several researchers (Buttlar et al., 2000; Wagoner et al., 2004; Kim, 2007). The asphalt concrete is composed of three phases: aggregate, FAM, and interface between aggregate and FAM. Only a monotonic tire loading is applied herein over the DEM pavement model using the cohesive softening model around the potential crack area. For the tire loading, a constant tire loading stress of 540 kPa (80 psi) is applied directly above the crack tip location on the pavement surface, which simulates single wheel tire pressure. It is assumed that the radius

wheel is 3 cm, its density is 2,650 kg/m^3, its normal and shear stiffness is 1×10^9 N/m, and its friction coefficient is 0.7, respectively as used similarly in the past by Vallejo et al. (2006) and Han et al. (2008). Their density and coefficient of normal and shear stiffness are similar to those of AC layer.

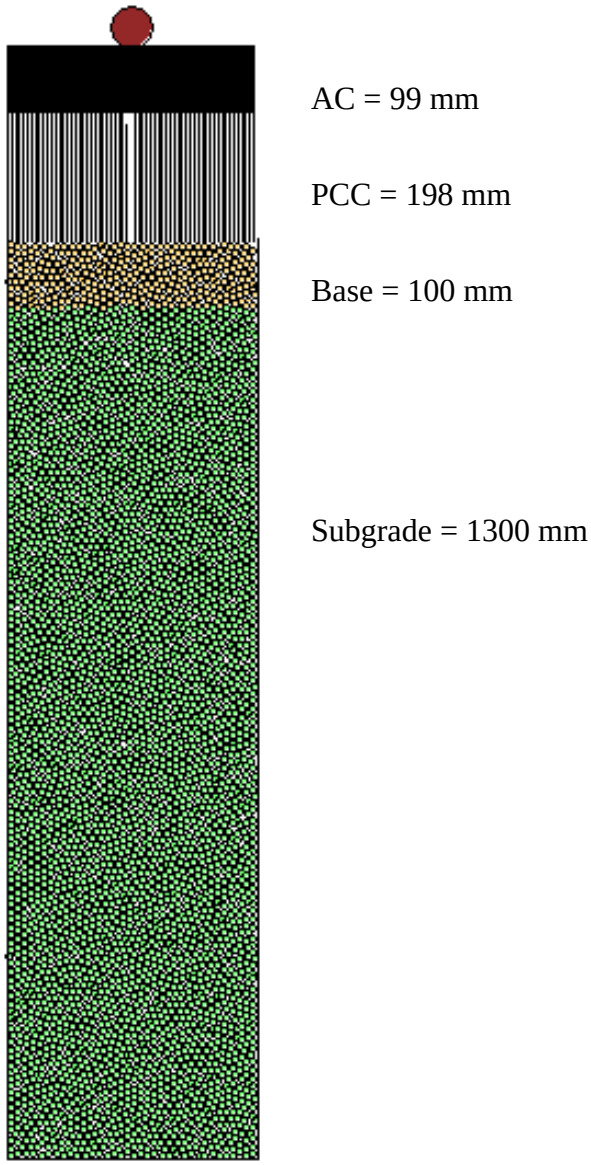

Figure 5.1 Dimension of Pavement DEM model

For the base/subgrade boundary, walls are used and set to $\delta y = 0$ to simulate fixed boundary. The right and left side edges above the base layer are assigned a free boundary condition because it is assumed that the size of the pavement model is large enough to ignore boundary effect. The stress magnitude, which is shown later, is negligible at the boundary.

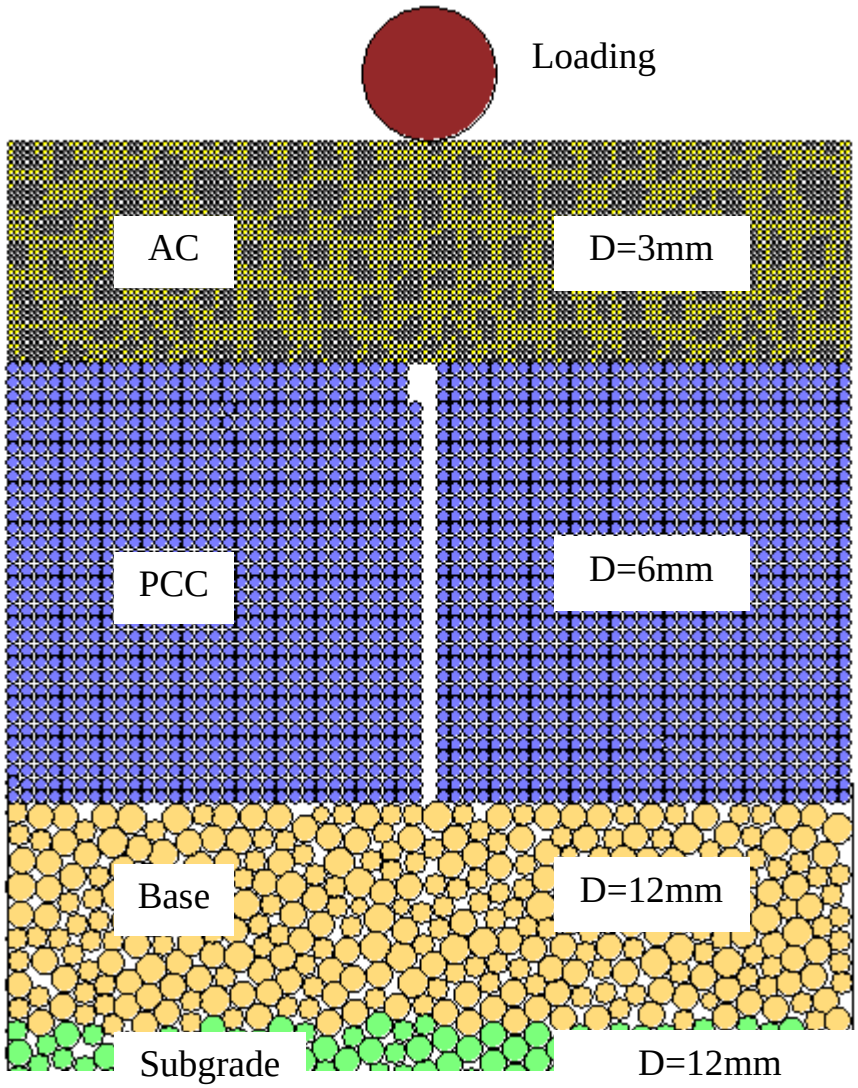

Figure 5.2 Geometry of Pavement DEM model for Unreinforced section

DEM modeling for a reinforced section is presented in Figure 5.3. The geosynthetic is placed at one-third depth of overlay thickness. According to previous studies (Brown et al., 2001; Kuo and Hsu, 2003; Sobhan et al., 2005; Khodaii et al., 2009), this location is recommended. The geosynthetic is represented by 191 particles with a 2 mm diameter. In Figure 5.3(b), “gg-type contact” means geosynthetic-to-geosynthetic contact. The geosynthetic is modeled by successively assembling particles with the same diameter, bonded to each other by contact conditions; contacts have no bending strength because geosynthetics, especially geotextiles, deform like a membrane when a force is applied perpendicularly (Chareyre et al., 2002). Other conditions are the same as in the unreinforced section.

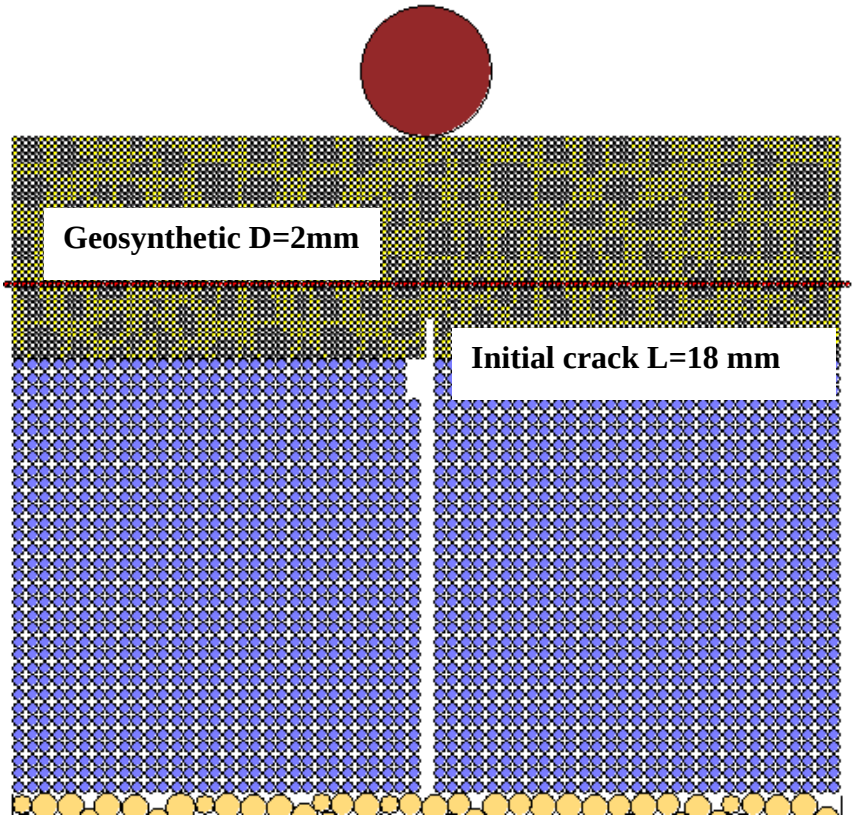

(a) Pavement section with geosynthetic reinforcement

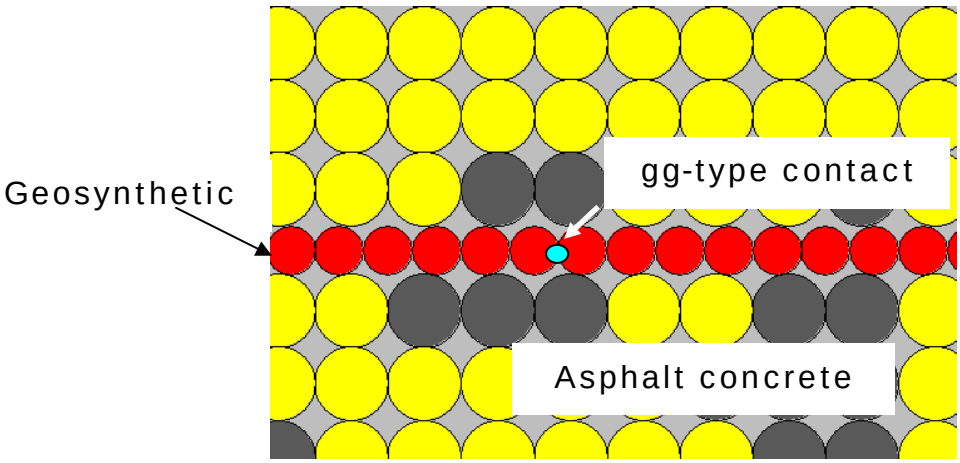

(b) Modeling of Geosynthetic

Figure 5.3 Geometry of Pavement DEM model for Reinforced section

5.2.2 Model Parameters

Material parameters used for the DEM pavement model are presented in Table 5.1. The parameters are from Kim's work (2007). The material parameters of aggregate and FAM were obtained through the indirect tension (IDT) and dynamic modulus tests by You (2003). They assumed that the material parameters of the interface were similar to the FAM. The fracture energies of FAM and interface were estimated and calibrated based on the experimental fracture test data of the mixture. The details of these parameters were presented in the Ph.D dissertations of Wagoner (2006) and Kim (2007). They developed DEM model and the DEM results were compared to the experimental results of the disk-shaped compact tension (DC(T)) fracture test and single-edge notched beam (SE(B)) test. For the asphalt concrete material properties, three phases were assigned: linear elastic for aggregate, bilinear elasto-plastic for FAM, and bilinear elasto-plastic for interface because of the softening of one side FAM as shown in Figure 5.4 (Kim, 2007). According to Ince et al. (2003), the softening displacement of interface is much smaller than that of FAM. Their friction coefficient of 0.5 was used.

In design, concrete is often assumed to fail when it reaches a compressive strain of 0.003 (Carino and Clifton, 1995). When there was no initial crack, the compressive strain was 4.45×10^{-5}. To represent a deteriorated concrete condition, the particle stiffness of the concrete was changed to a lower value having compressive strain of 0.00345. Details on the base/subgrade layer properties and generations were presented in Chapter 3. It is assumed that the interface between the AC and PCC layers were fully bonded with the binder strength

and had a friction coefficient of 0.5. An unbonded condition for the interface between the PCC and base/subgrade is assumed, thus, frictional sliding between these layers is possible.

Table 5.1 Parameters of DEM pavement model

Pavement Section		Material Properties		DEM Properties	
Layer	Phase	Young's Modulus (GPa)	Strength (MPa)	Stiffness (GN/m)	Bond Strength (KN)
AC	Aggregate	56.8	6.59	56.8	19.77
	FAM	13.8	3.78	18.2	8.61
	Interface	13.8	3.44	18.2	7.83
PCC	No Crack	27.6	2.61	27.6	15.66
	Crack	1.0	2.61	1.0	15.66
Granular Base*		-	-	0.1	-
Subgrade**		0.16	-	0.04	-

* Referred to Santamarina et al.(2001)

** Calculated from biaxial test using PFC2D

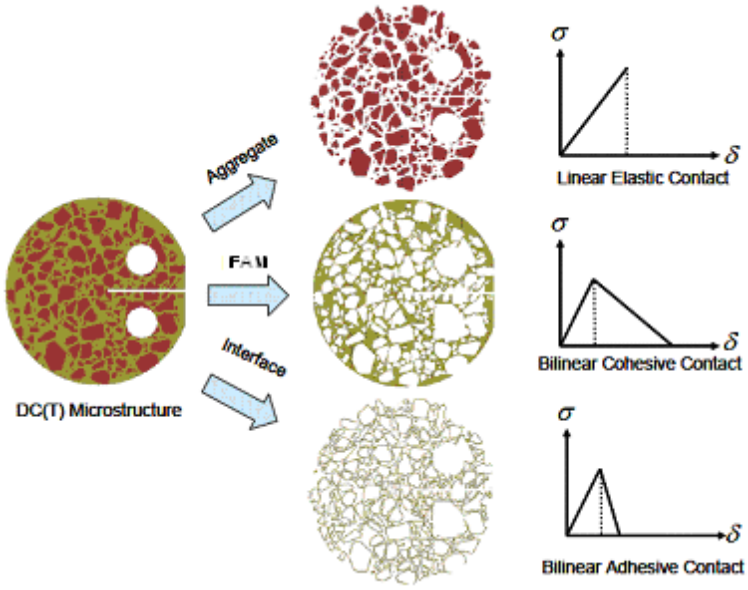

(a) Multi-Phase Geometry (b) Assumed Material Fracture Properties

Figure 5.4 Multi-Phase Geometries and Assumed Material Fracture Properties (Kim, 2007)

For the properties of geo-materials, numerical biaxial tests and shear tests are commonly used. Geosynthetics are thin materials characterized by a tensile stiffness J and a tension at failure, T_r. In this study, the properties derived from numerical biaxial tests and shear tests by Chareyre et al. (2002) are used. The tension at failure, T_r, of the geotextile corresponds to the tensile strength, a_n^{gg}, of the bonds between the particles ($T_r = a_n^{gg}$), and the tensile stiffness, J, of the geotextile is dependent on the normal stiffness of the contacts k_n^{gg} and the diameter of the particles d^g ($J = k_n^{gg} d^g$) (Chareyre et al., 2002). They compared with analytical solutions (Delmas, 1979) and numerical solutions (Villard and Giraud, 1998), and their results were approximately identical.

For the geosynthetics in this study, a nonwoven, needle-punched geotextile (Bidim P50) with tensile stiffness J = 80 kN/m (at 5% strain) and tension failure T_r = 30 kN/m (at 85% strain) is used. The geosynthetics' properties by Chareyre et al. (2002) are presented in Table 5.2.

Table 5.2 Geosynthetics Parameters of DEM pavement model (Chareyre et al., 2002)

Parameters selected for the geosynthetics	Value
Tensile strength, a_n^{gg} (kN/m)	30
Shear strength, a_s^{gg} (kN/m)	30
Normal stiffness, k_n^{gg} (kN/m^2)	80/d^{g*}
Shear stiffness, k_{gg} (kN/m^2)	0.5×10^5
Friction angle, μ_{gg}	0

* d^g is the diameter of geosynthetics

5.3 Effect of Geosynthetics

5.3.1 Effect of initial crack in AC overlay

5.3.1.1 Displacement and Strain

To evaluate the benefits of geosynthetic reinforcement, displacement is calculated on top of the pavement section for four cases: no initial crack without reinforcement, no initial crack with reinforcement, initial crack without reinforcement, and initial crack with reinforcement. The results are presented in Figure 5.5, which shows that displacements of geosynthetic-reinforced pavement sections are smaller that those where there is no reinforcement. Analyses indicate that the difference in displacement at the top due to the

geosynthetic reinforcement is 2.4 mm. It can be explained that geosynthetics prevent the particles from moving vertically, thus, can reduce the vertical deformation (Bhandari et al., 2008). However, differences of only 0.1 mm are assessed as due to initial crack on AC overlay. This indicates that initial crack on AC overlay may not significantly affect displacement.

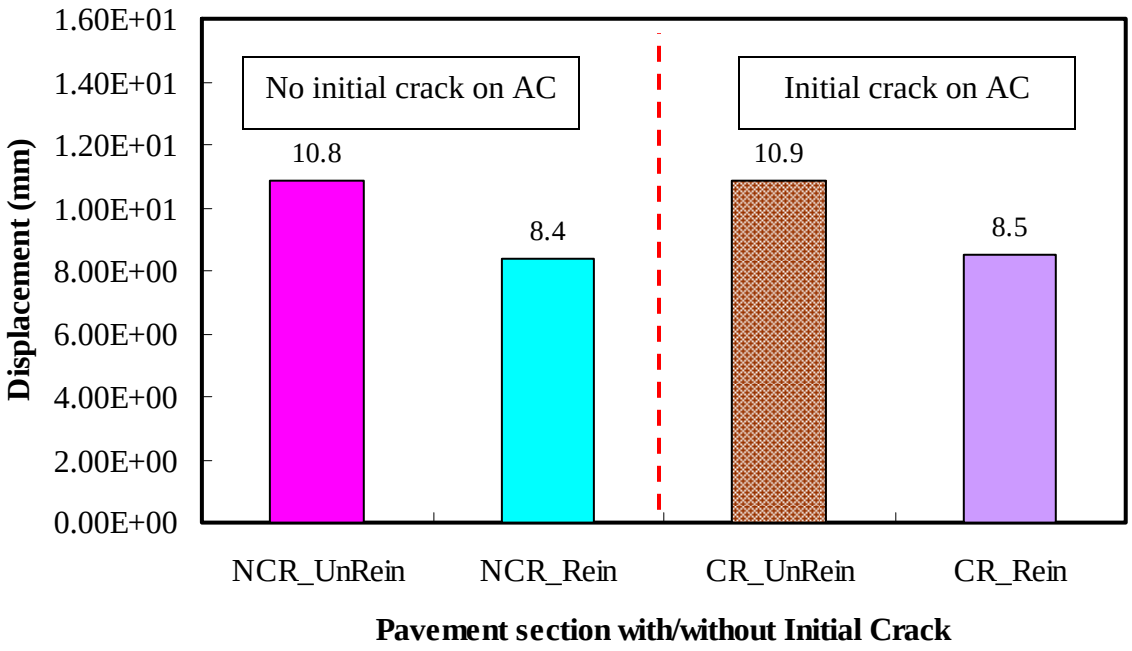

Figure 5.5 Displacement on top according to initial crack on AC overlays

Also, tensile strain is obtained from measurement circles to evaluate the effect of geosynthetic reinforcement for four cases. Measurement circles were assigned in 5 locations below the reinforcement as seen in Figure 5.6. The results are presented for without and with initial crack on AC overlay in Figures 5.7 and 5.8, respectively.

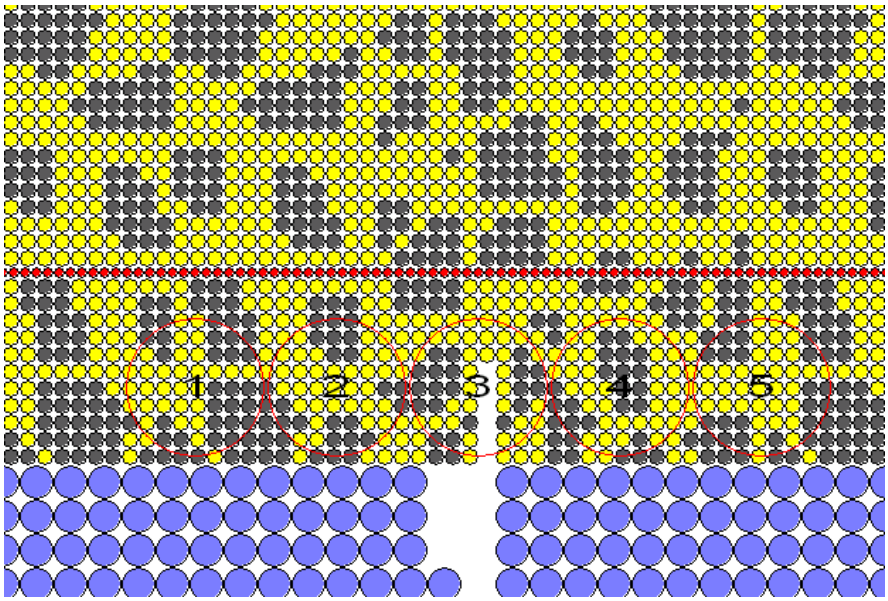

Figure 5.6 Measurement circles for strain

With reference to Figure 5.7, tensile strains below reinforcement are distributed in the shape of an arch for both with and without reinforcement. Results show that geosynthetic reinforcement has the benefit of decreasing lateral strain by around 2% under the reinforcement layer and by around 8% above reinforcement; thus, the geosynthetic works more effectively above reinforcement. It can be explained that geosynthetics perform as tensile reinforcement by preventing lateral spreading of AC overlay when placed within the AC layer (Kwon et al., 2008). The geosynthetic reinforcement naturally develops a stiffer layer associated with the interlocking action which generates around geosynthetic reinforcement (Konietzky et al., 2000, 2004; Budkowska and Yu, 2003; Perkin and Svano, 2004).

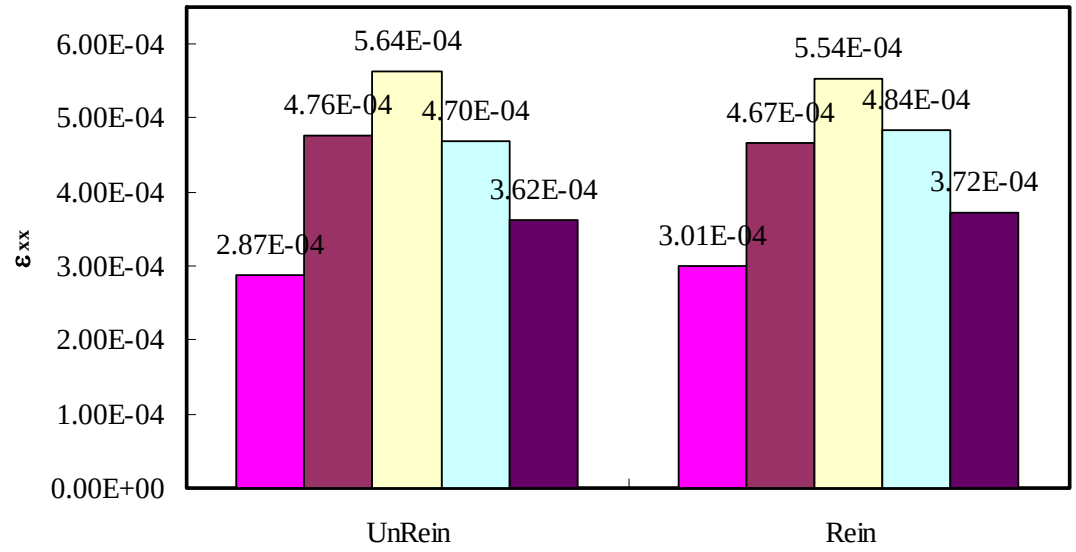

(a) Without initial crack (Under Geosynthetic)

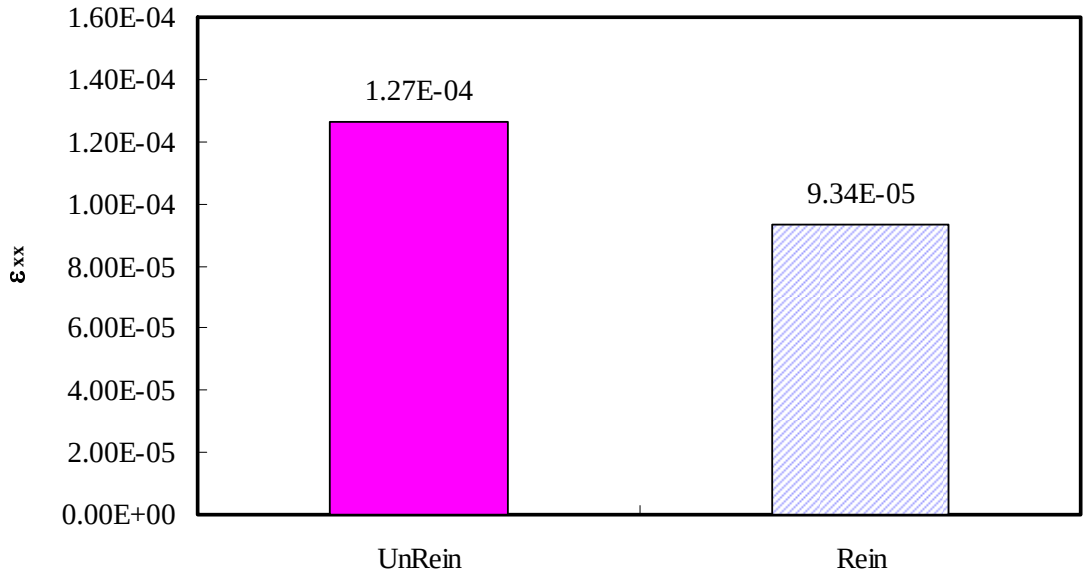

(b) Without Initial Crack (Above Geosynthetic)

Figure 5.7 Strain distributions without initial crack in overlay

To see the initial crack effect on AC overlay, results for horizontal strains are also presented in Figure 5.8. As is the case without an initial crack, strain distributions are shown as arching below the reinforcement. However, significantly greater tensile strain occurs compared with that in overlay without an initial crack because the presence of a crack promotes horizontal movement. Moreover, analyses indicate that when reinforcement is placed in initial-cracked AC overlay, tensile strain increases by 18.5% over that without reinforcement as seen in Figure 5.8(a). This result is consistent with that obtained by Elseifi and Al-Qadi (2005). It can be explained that the use of a soft interlayer causes an increase in pavement deformations, which leads to larger tensile strain at the bottom of the overlay based on the crack state of stresses (Elseifi and Al-Qadi, 2005). However, it is noted that tensile strain decreases by around 8% above the reinforcement compared to without reinforcement as seen in Figure 5.8(b).

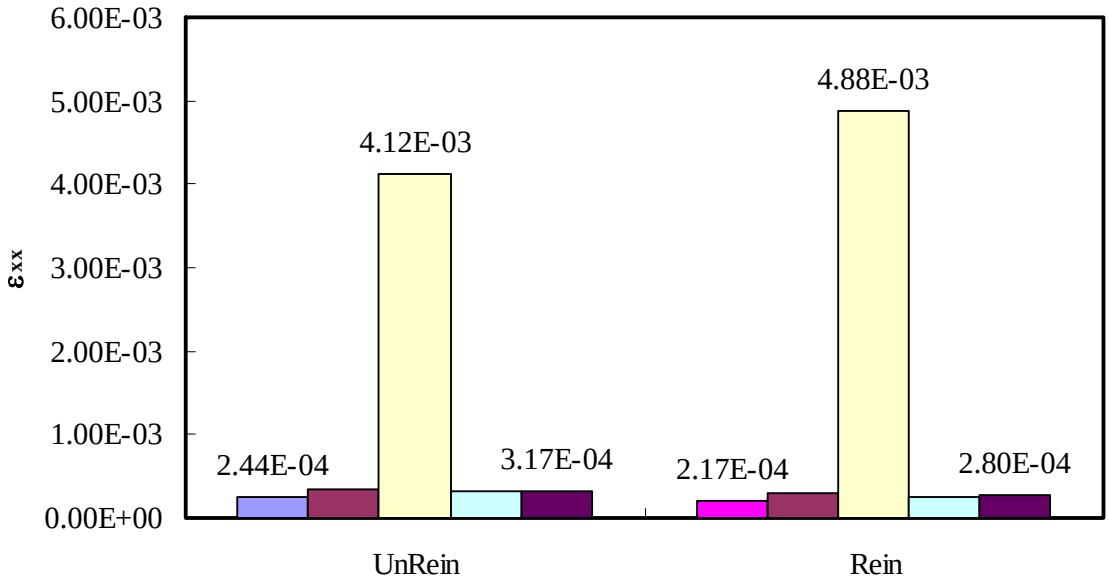

(a) With initial crack (Under Geosynthetic)

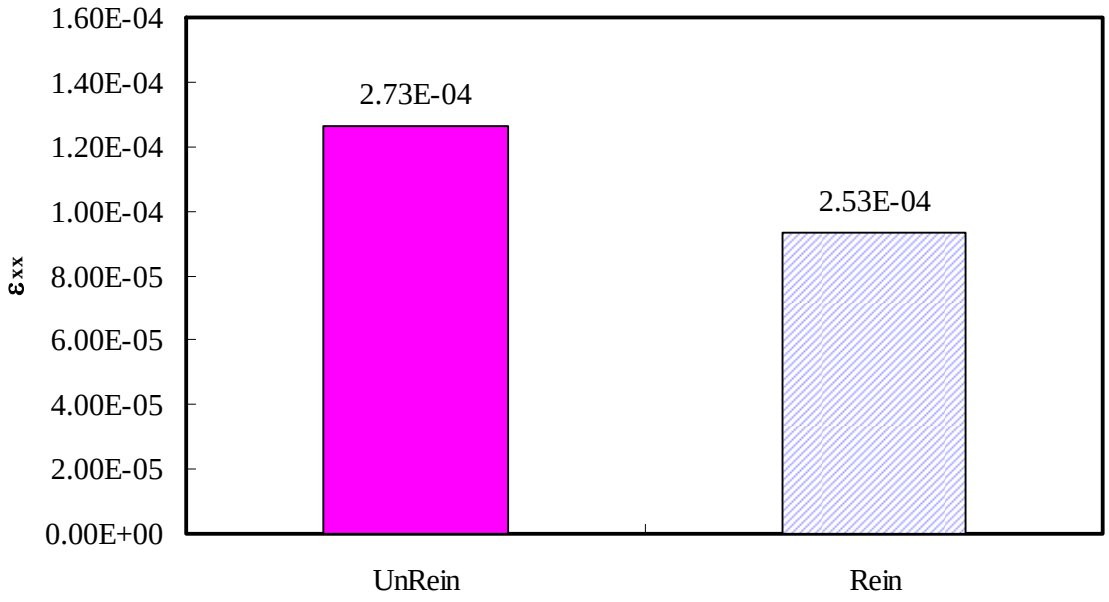

(b) With initial Crack (Above Geosynthetic)

Figure 5.8 Strain distributions at the bottom of overlay

5.3.1.2 Stresses and Porosity

In the DEM model, because particles are not continuous, stress does not exist at each point of a particle. Contact forces and particle displacements which are useful to study the material behavior on a micro-scale are computed. But they cannot be transferred directly to a continuum model. To make the step from the micro-scale to a continuum model, averaging procedures are necessary. According to Itasca (2004), the average stress tensor used in PFC2D within a measurement circle can be expressed by the following.

$$\bar{\sigma}_{ij} = -\left(\frac{1-n}{\sum_{N_p} V(p)} \right) \sum_{N_p} \sum_{N_c} \left| x_i^{(c)} - x_i^{(p)} \right| n_i^{(c,p)} F_j^{(c)} \tag{5.1}$$

Where, N_p is balls with centroids within measurement circle

N_c is contacts of these balls

n is the porosity within the measurement circle

$V^{(p)}$ is the volume of particle (p), taken equal to the area of particle (p) times a unit-thickness

$x_i^{(p)}$ and $x_i^{(c)}$ are the locations of a particle centroid and its contact, respectively;

$n_i^{(c,p)}$ is the unit normal vector directed from a particle centroid to its contact location, and

$F_j^{(c)}$is the force acting at contact *(c)* arising from both particle contact and parallel bonds.

The stresses are measured from measurement circles in PFC2D. Measurement circles of 1,008 with 6 mm diameter are assigned to the whole overlay as shown in Figure 5.9.

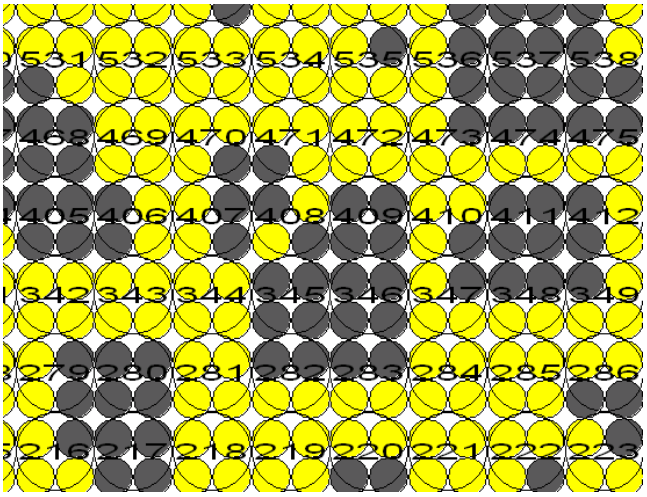

Figure 5.9 Measurement circles for stress

To investigate the effect of the geosynthetic, stress distributions are explored both with and without reinforcement in AC overlays. The investigated location is above the initial crack of the overlay. Figure 5.10 shows the horizontal stress in the vicinity of the crack tip. Strain curves for both unreinforced and reinforced overlays have a maximum value around 0.2 mm at the middle of the AC overlay where loading is applied, then the stresses dissipate toward both sides. That means that stresses are not affected at the boundaries as assumed previously. Moreover, reinforcement significantly affects the stress field in the vicinity of the crack tip; thus, maximum horizontal stress is significantly reduced by around 800 kPa (i.e., 44%) when geosynthetic is used. It can be explained that geosynthetics have a function as a stress absorbing layer around the crack tip. Also, the geosynthetic creates a protective shield

around the crack tip, which separates the critical condition of the stress field in the cracked area from the bottom of the overlay; thus, the resultant stress field helps close the crack rather than open it (Elseifi and Al-Qadi, 2005). Besides, high tensile stress developed around the crack tip can initiate and accelerate the propagation of the crack into the overlay.

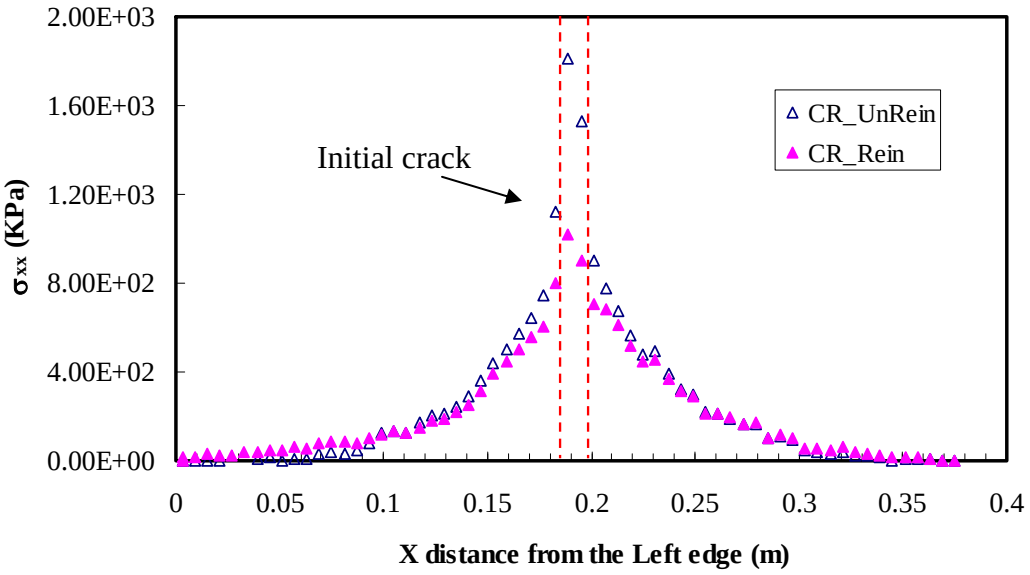

Figure 5.10 Horizontal stress distributions with initial crack

Distribution of the change in vertical stress above the crack tip is shown in Figure 5.11, which shows that vertical stress is governed by compression except stress in the vicinity of crack tip where subjected to tension due to external loading. This result (i.e., arching effect) is consistent with that explained by Finn (1963) shown in Figure 5.12. The estimated stresses match the stress configuration for the trap door analogy perhaps due to the assumption of cubic packing as apposed to random packing. In this case the particles are aligned over the crack width which leads to transfer of the stress to the edges of the crack.

Analysis indicates that the geosynthetic seems to play a role as a stress absorber though the difference of 135 kPa (i.e., 27%) around the crack is smaller than that of horizontal stress.

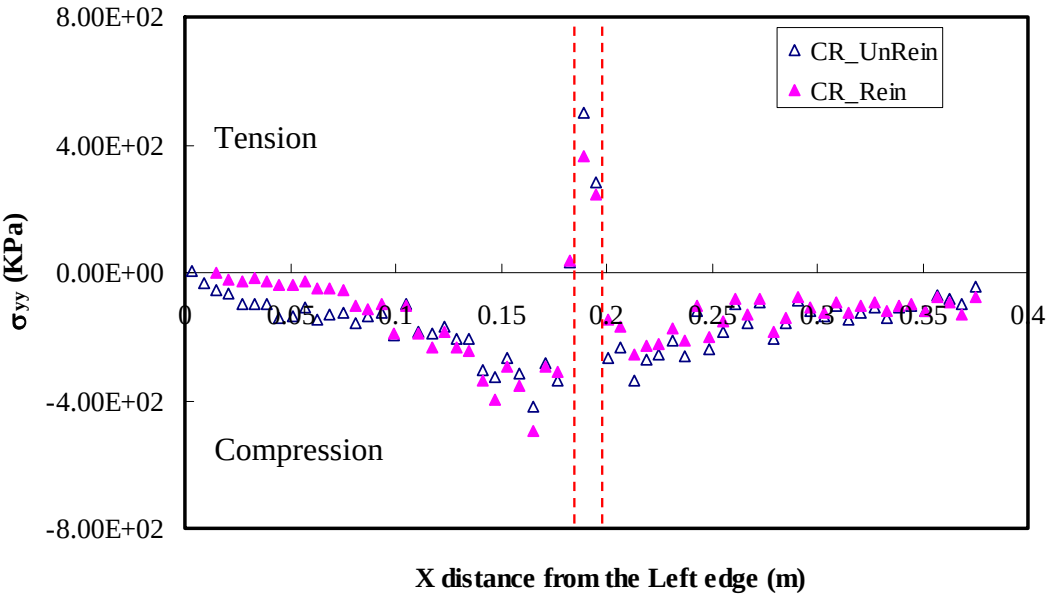

Figure 5.11 Vertical stress distributions with initial crack

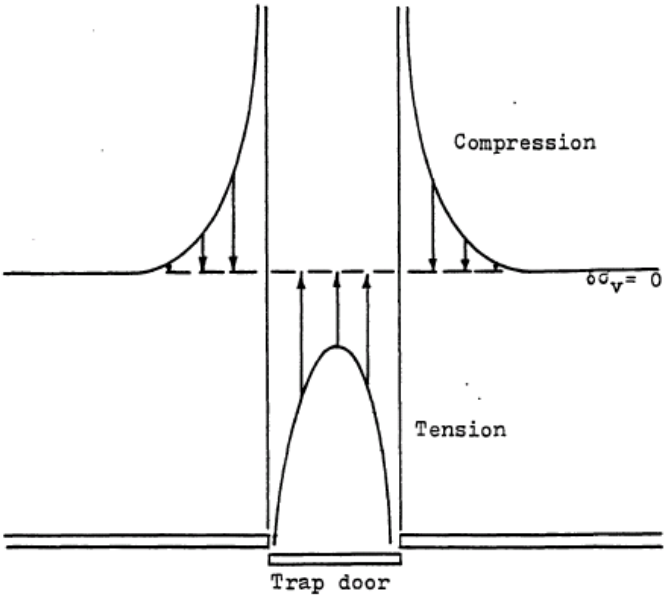

Figure 5.12 Typical Distribution of Change in Vertical stress for Downward Translating Trap Door (After Finn, 1963)

Figure 5.13 shows the shear stress distribution monitored in the vicinity of crack tip. It appears from the figure, that the section of the AC overlay from the left to the middle is governed by negative, whereas the right-hand section is the reverse. Maximum shear stress reduction of 110 kPa at around crack also can be seen through the figure because the geosynthetic functions as a stress absorber.

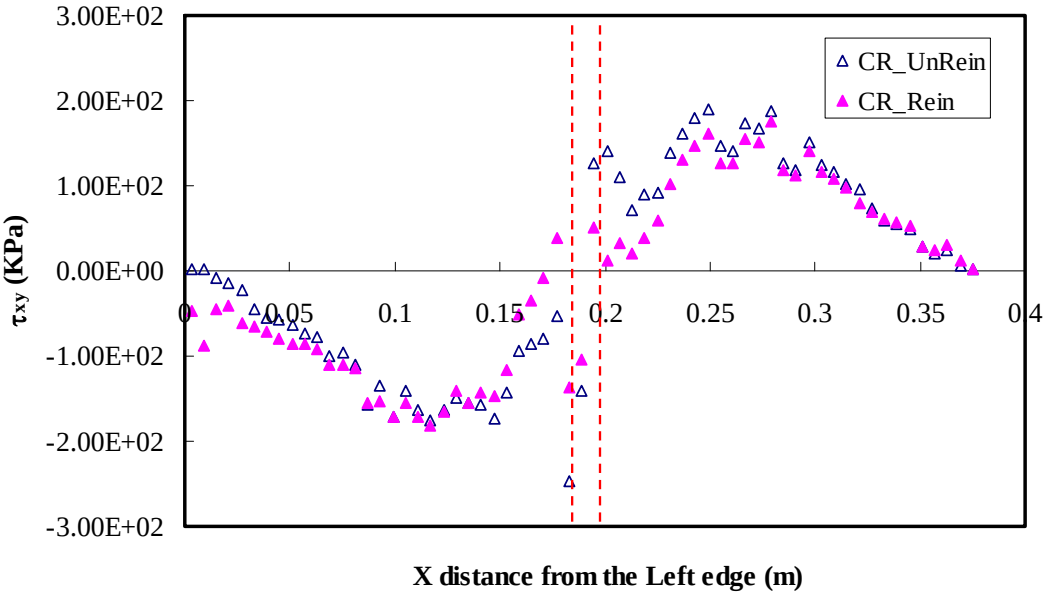

Figure 5.13 Shear stress distributions with initial crack

To see the effect of an initial crack in the overlay, combined stress distributions for unreinforced overlays are presented in Figures 5.14 to 5.16. Results of horizontal stress distributions are presented in Figure 5.14. These analyses show that the presence of a crack in the pavement substantially affects the stress distribution in the vicinity of the crack tip and consequently leads to significant increase of the horizontal stress, from 439 kPa to 1,810 kPa.

Figure 5.15 shows the combined results of vertical stress distribution. Analyses show that, in general, vertical stresses without initial crack are relatively lower than those with initial crack, and that maximum vertical stress of 499 kPa and (-)277 kPa are obtained in the middle. Also, it is noted that no tension in the middle of overlay appears if no crack exists, unlike the other cases. Figure 5.16 show the combined results of shear stress distribution. Analyses show that stress values without a crack are relatively higher than those with a crack, but reverse around the crack. Moreover, the effect of the initial crack can be seen clearly in the middle. Shear stress in the middle is significantly increased by 247 kPa due to the crack.

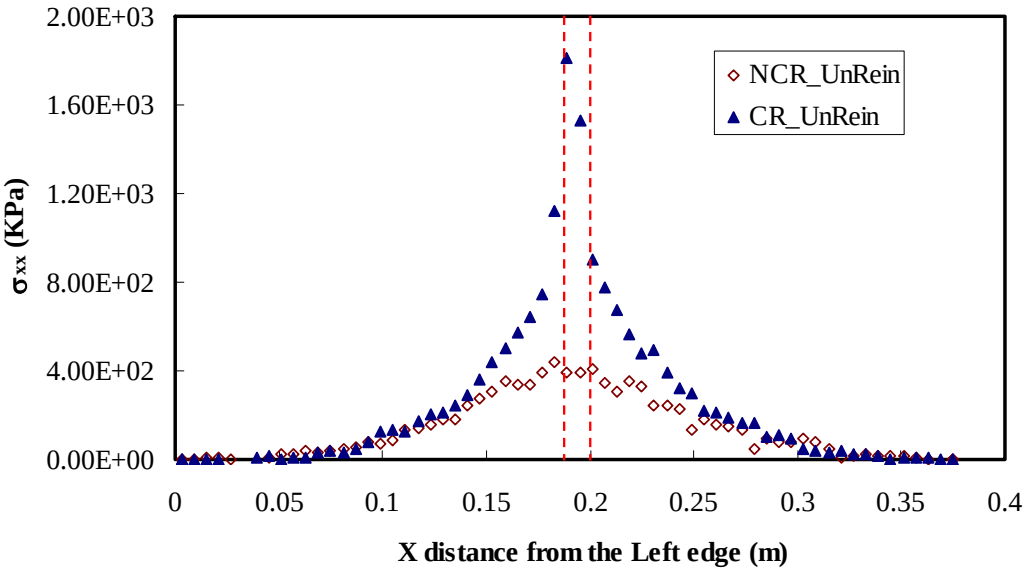

Figure 5.14 Horizontal stress distributions with/without initial crack for unreinforced overlays

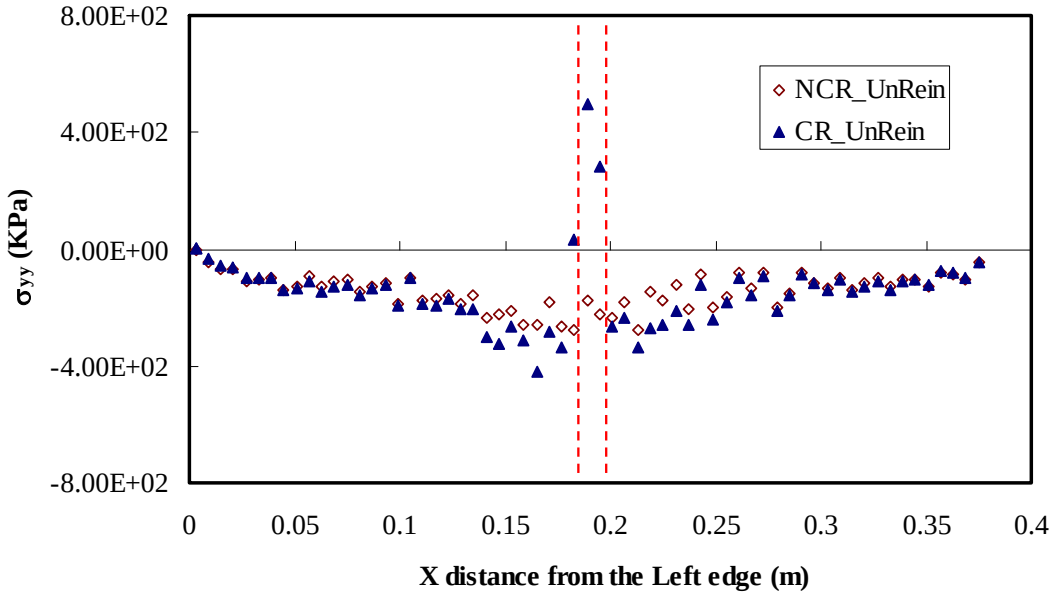

Figure 5.15 Vertical stress distributions with/without initial crack for unreinforced overlays

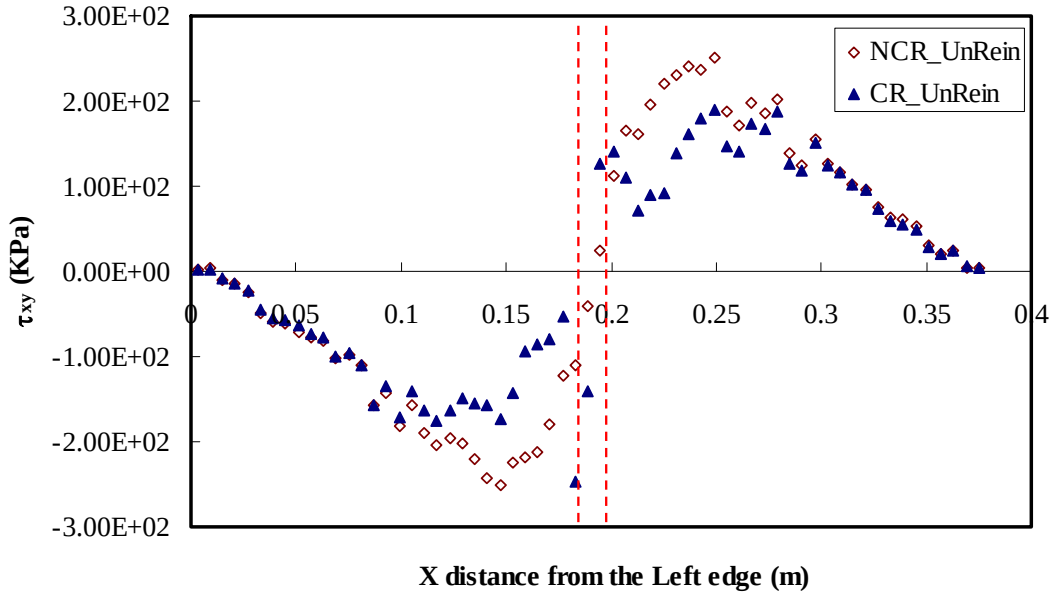

Figure 5.16 Shear stress distributions with/without initial crack for unreinforced overlays

The stress contours of vertical, horizontal, and shear stress for the whole overlay are presented in Figure 5.17. Left and right columns represent unreinforced and reinforced pavement with initial crack, respectively. The horizontal stress contours are largely divided into two sections which are concentrated on stresses due to the initial crack tip and applied loading. The image shows that the upper part of the overlay is subjected to tension, while the lower part is not. The lower concentration of stresses in the reinforced pavement, especially under the geosynthetic reinforcement in the vicinity of the crack, is due to the benefits of reinforcement as already explained above. The vertical stress contour is mostly governed by compression except around the crack, which is indicated in the figure. The shear stress contour image shows that left section of overlay is governed by negative value while is applied in both cases positive value exists mostly in the right part, but this pattern is reversed at the bottom due to the crack. Both contours look generally similar, differences exist under applied loading in the middle where there is a crack.

In addition, stress contours without initial crack are shown in Figure 5.18. Comparing this with Figure 5.17, it can be clearly seen that an initial crack affects the stress field in the vicinity of the crack comparing. As shown in the horizontal stress contours, maximum stress appears at the bottom of the overlay, a location which differs from the case of overlay with initial crack. Also, tensions at the bottom due to an initial crack cannot be seen in vertical stress contour. Additionally, the shear stress contours show that both sides are perfectly governed by positive and negative respectively, even at the bottom, unlike the case of overlay with initial crack.

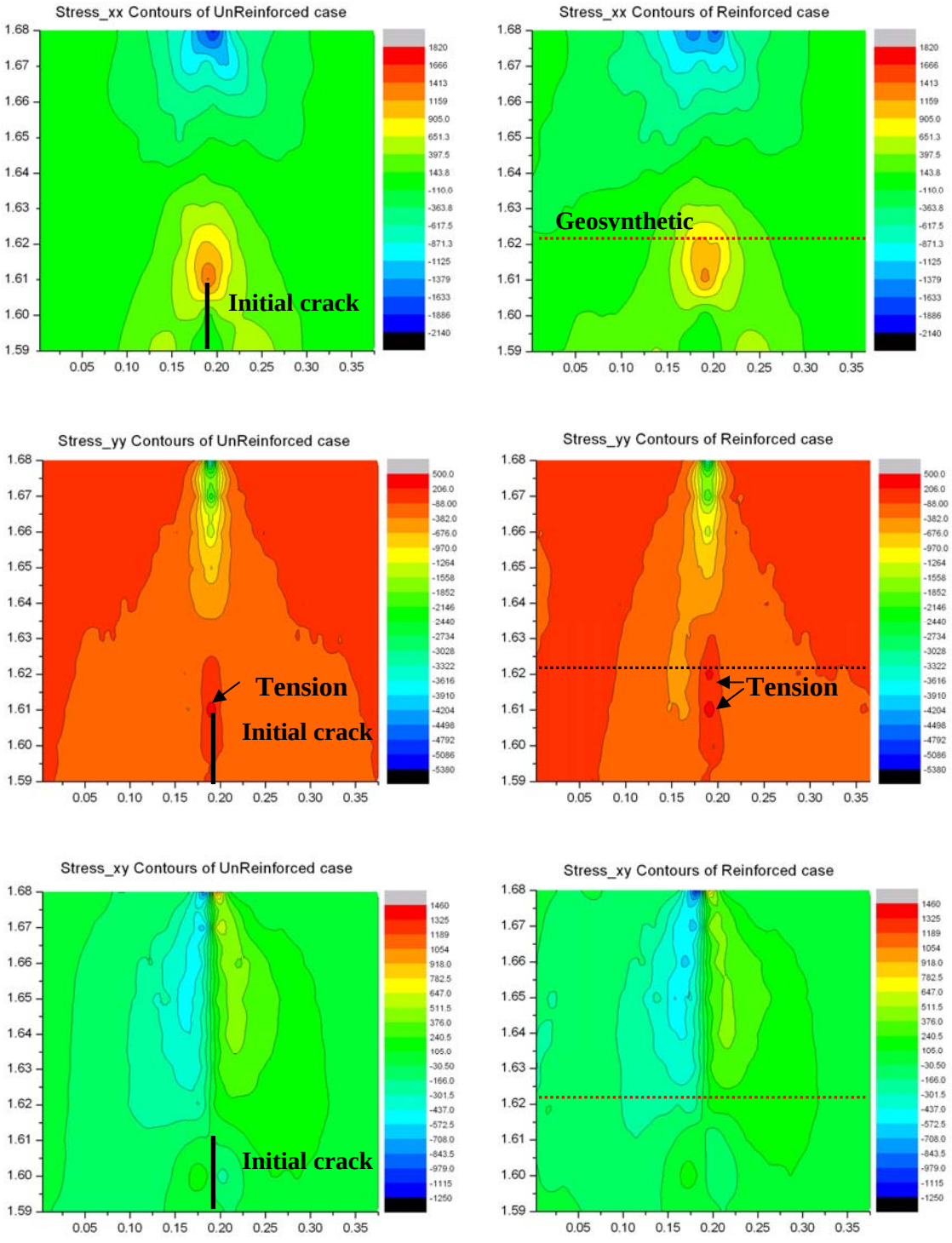

Figure 5.17 Stress contours of AC overlay with initial crack

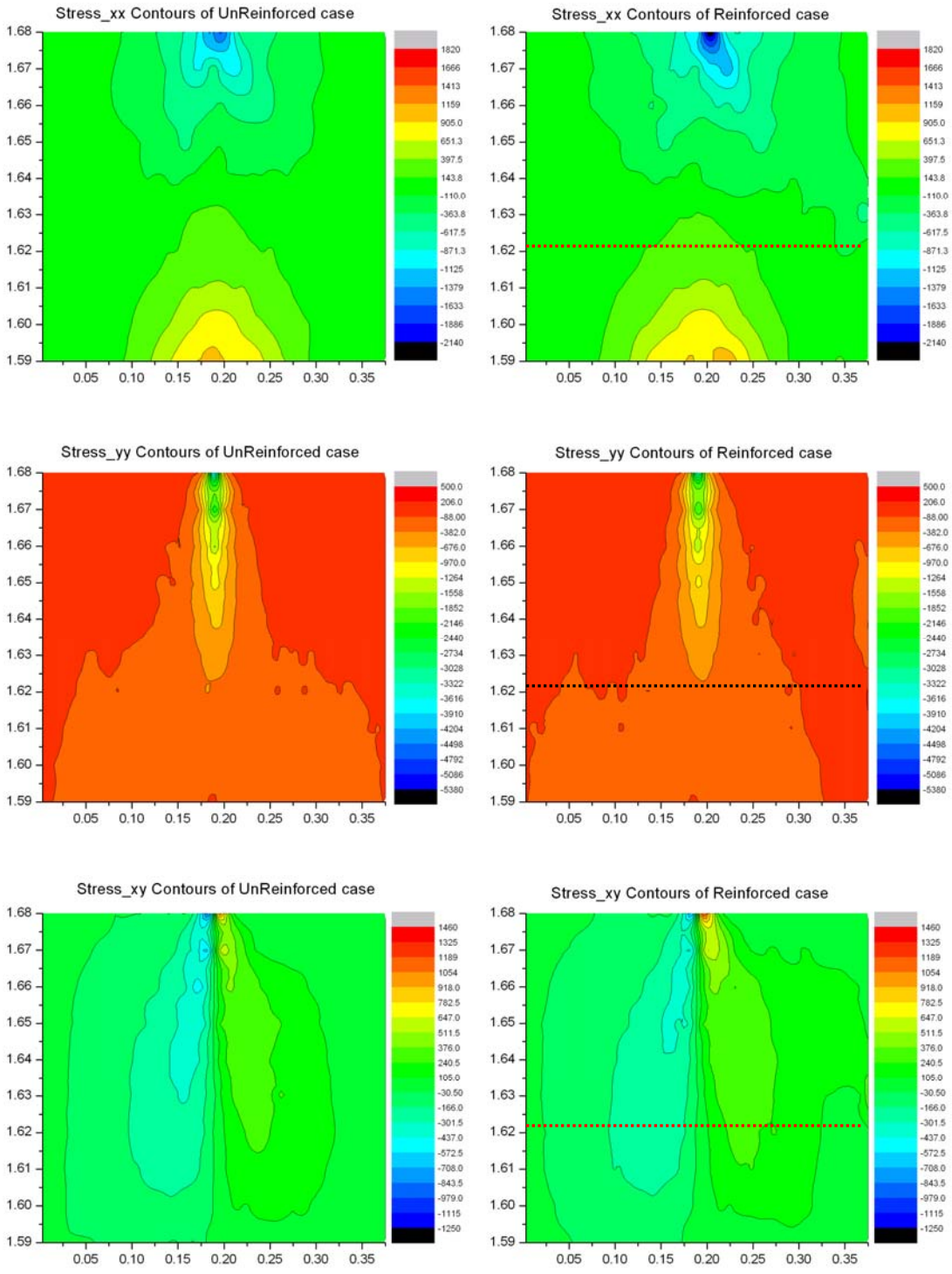

Figure 5.18 Stress contours of AC overlay without initial crack

Figure 5.19 shows the contours of porosity, which is the ratio of void volume to total volume after loading, with initial crack in overlay. To facilitate the visual comparison, the same scale range, 0.1890 to 0.1935, is applied in both cases even though the exact porosity values are not presented. High density is shown in the vicinity of the crack in both cases. It means that maximum strain is occurring around that area, which is in accordance with strain results addressed before. In reinforced overlay, the upper part of the reinforcement is relatively looser than the lower part. Displacement under the reinforcement is occurs relatively evenly except around the crack.

Porosity contours without initial crack are shown in Figure 5.20. Again, the facilitate visual comparison, the same scale is applied in both cases, ranging from 0.1915 to 0.1920, which is a relatively narrower range than that used with initial-cracked overlay. When using this scale, porosity of the reinforced overlay is displayed very roughly. Therefore, a different scale, ranging from 0.1876 to 0.1939, is applied in order to see the details as shown in Figure 5.20(b). Figures show that most porosity changes occur around the point of loading where there is no reinforcement. However, in reinforced overlay, porosity changes mainly under the reinforcement and at the bottom.

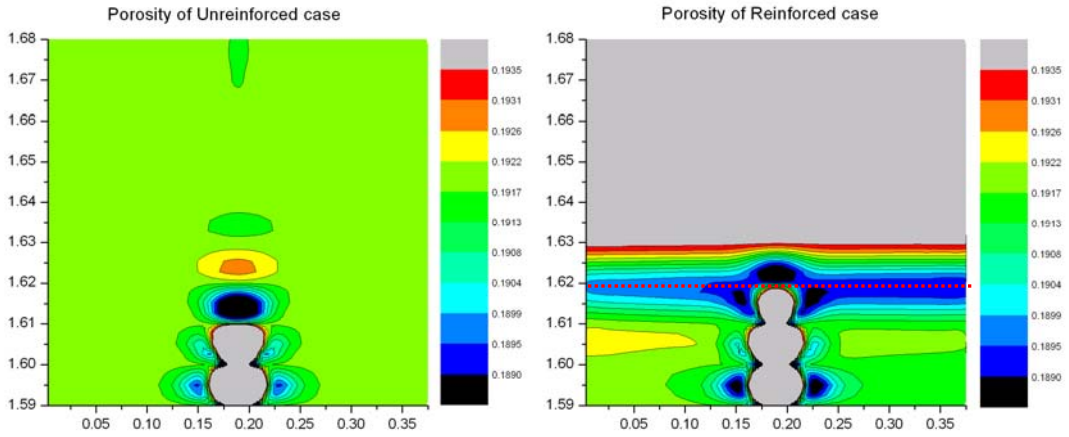

Figure 5.19 Porosity of AC overlay with initial crack

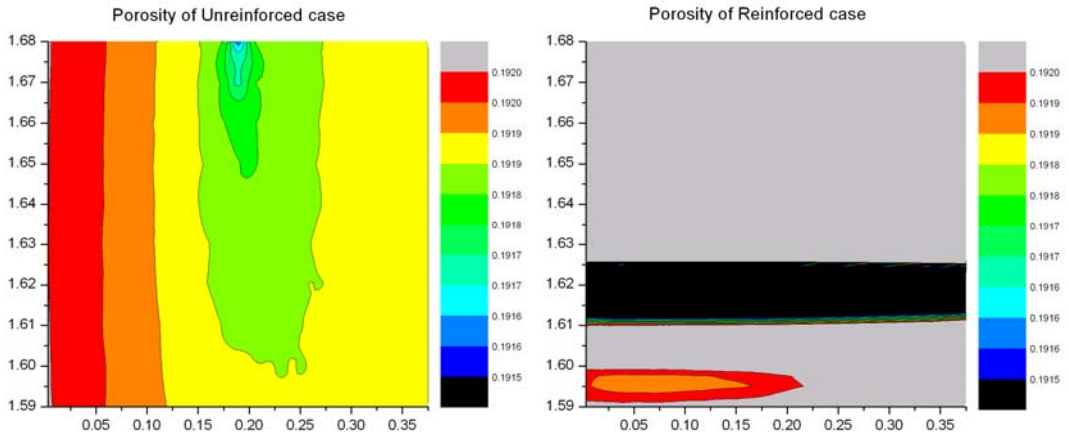

(a)

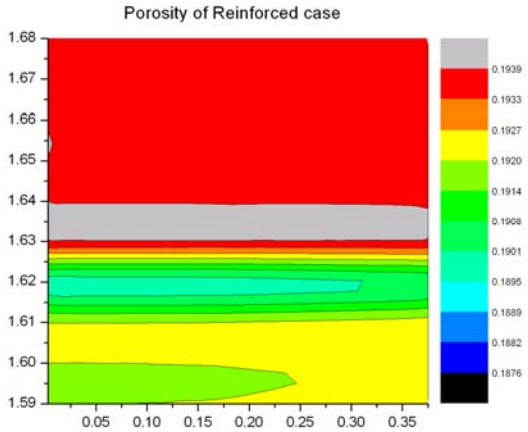

(b)

Figure 5.20 Porosity of AC overlay without initial crack

5.3.2 Effect of Geosynthetic Properties

5.3.2.1 Displacement and Strain

Geosynthetic reinforcement is an effective way to reduce or retard the reflective cracking and its effectiveness according to the different types of geosynthetic used has been studied by several researchers (Maurer and Malashekie, 1989; Hughes and Somers, 2000). To investigate the effect of reinforcement according to geosynthetic types in this study, the properties of two different geotextiles are used. These are denoted GT_01 and GT_02 herein, and their respective properties are presented in Table 5.3. GT_01 is used for the whole of this study and its properties are illustrated minutely in a previous section. The higher normal and shear stiffness values than asphalt aggregate are used for the geosynthetic properties of GT_02.

Table 5.3 Geosynthetics Parameters of DEM pavement model

Parameters selected for the geosynthetics	GT_01	GT_02
Normal stiffness, k_n^{gg} (N/m)	4×10^7	4×10^{11}
Shear stiffness, k_{gg} (N/m)	5×10^7	5×10^{11}
Tensile strength (N)	3×10^4	3×10^4
Shear strength (N)	3×10^4	3×10^4
Friction angle, μ_{gg}	0	0

AC overlay and PCC layers are generated with cubic packing and most displacement occurs at the base/subgrade layers generated by irregular packing. Cubic packing is denser than irregular packing, thus, the change in porosity, *n*, according to the DEM pavement

model, is very small, from 0.192 to 0.1918. Moreover, the differences in displacement between the reinforced and unreinforced overlays range from 0.218 mm to 0.274 mm with a similar porosity of 0.1926; this is according to Bhandari et al.'s study (2008) by DEM, even though these simulations used irregular packing. In this study, displacement changes are minor according to different reinforcement locations but marginal differences surely exist. Thus, this study is focused on recognizing trends, rather than on evaluating values of displacement.

Results of displacement at the top of the pavement are presented in Figure 5.21. Results indicate that the displacement of GT_01 is a little bit higher than that of GT_02; the difference of 0.03 mm is so small as to be negligible. It is inferred that because this model is using constant loading stress (80 psi), there is no displacement change after reaching a certain time (around 0.06 sec); therefore, displacement is not a significant indicator in evaluating the effect of geosynthetic properties under constant loading. Still, the marginal effect of geosynthetic properties can be seen.

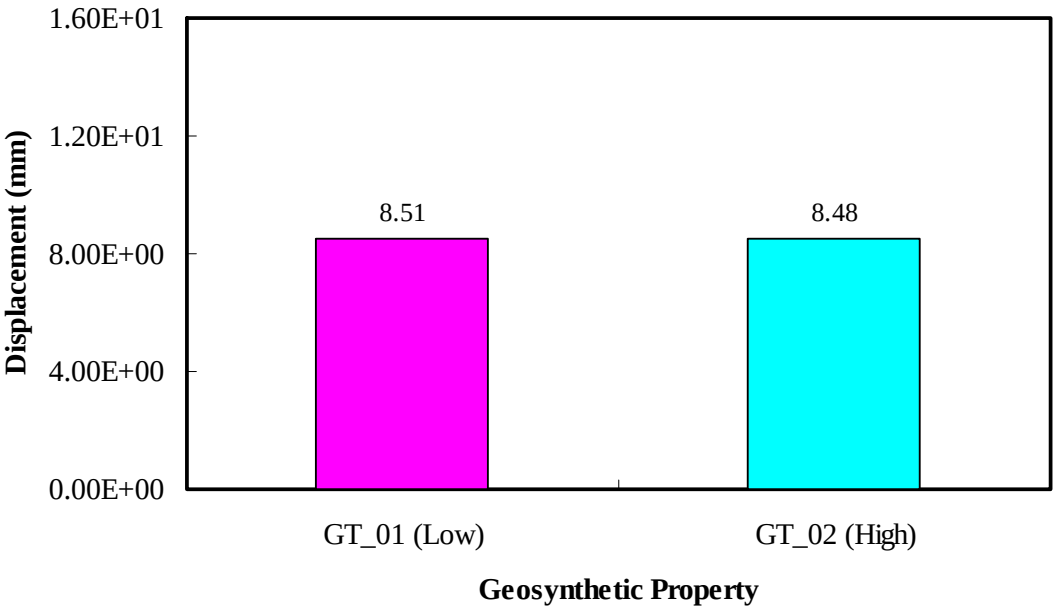

Figure 5.21 Displacement on top for overlays reinforced at different locations

Figure 5.22 shows horizontal strain in overlay with initial crack under the reinforcement. Analyses indicate that as the geosynthetic modulus increases, the predicted strains effectively decrease by around 2% below the geosynthetic and by around 10% above the geosynthetic. This shows that the benefit of geosynthetic reinforcement is increased by using stiffer geosynthetics.

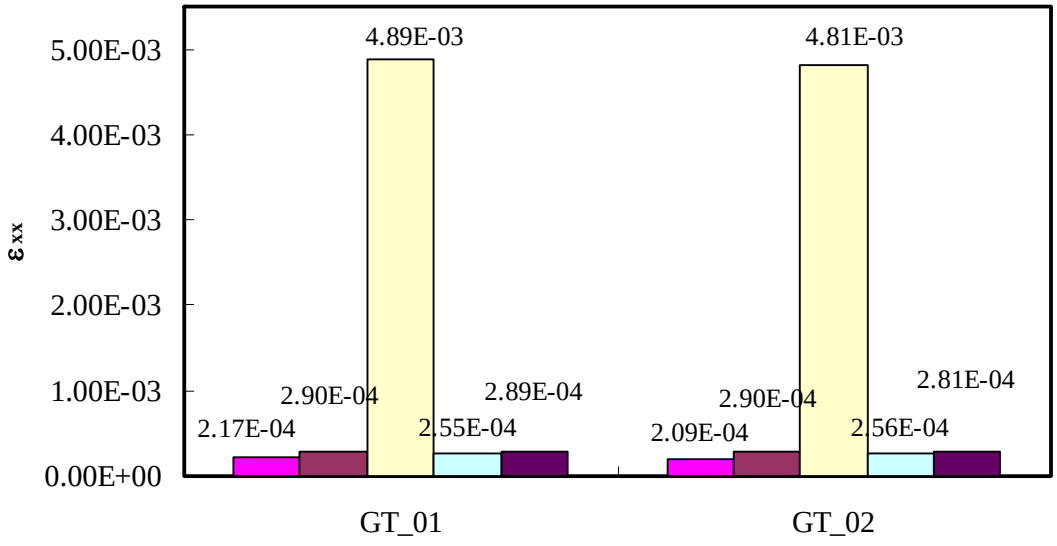

(a) Geosynthetic Properties (Under Geosynthetic)

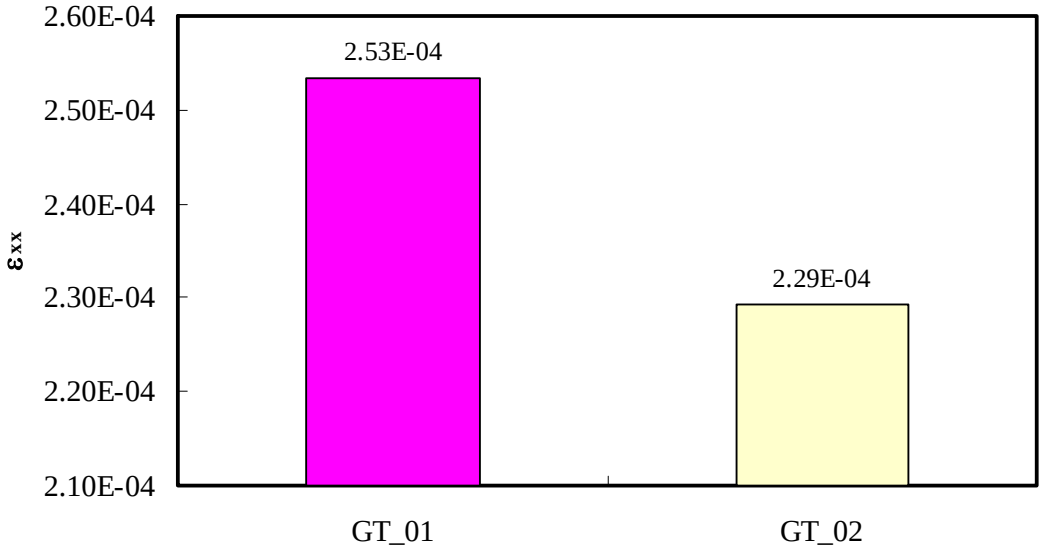

(b) Geosynthetic Properties (Above Geosynthetic)

Figure 5.22 Horizontal strains according to geosynthetic properties

5.3.2.2 Stresses and Porosity

To investigate geosynthetic effect according to geosynthetic types, two different sets of geosynthetic properties are used in this study and stress curves are combined in order to make comparisons easier. Results of observed stress distribution in the vicinity of initial crack tip are presented in Figures 5.23 to 5.25. Figures show that maximum horizontal stress generated in the vicinity of the crack is considerably decreased by 820 kPa when using stiffer geosynthetic (i.e. GT_02), while stress in the surrounding area is not significantly different. Also in the vicinity of the crack, vertical stress is decreased by around 128 kPa and shear stress is reduced by around 100 kPa. Overall, analyses indicate that stresses shown in GT_02, including horizontal, vertical, and shear stresses, are relatively lower than those in GT_01. This means that a higher modulus lead to decreased stress, therefore, a stiffer geosynthetic is more effective for reinforcement.

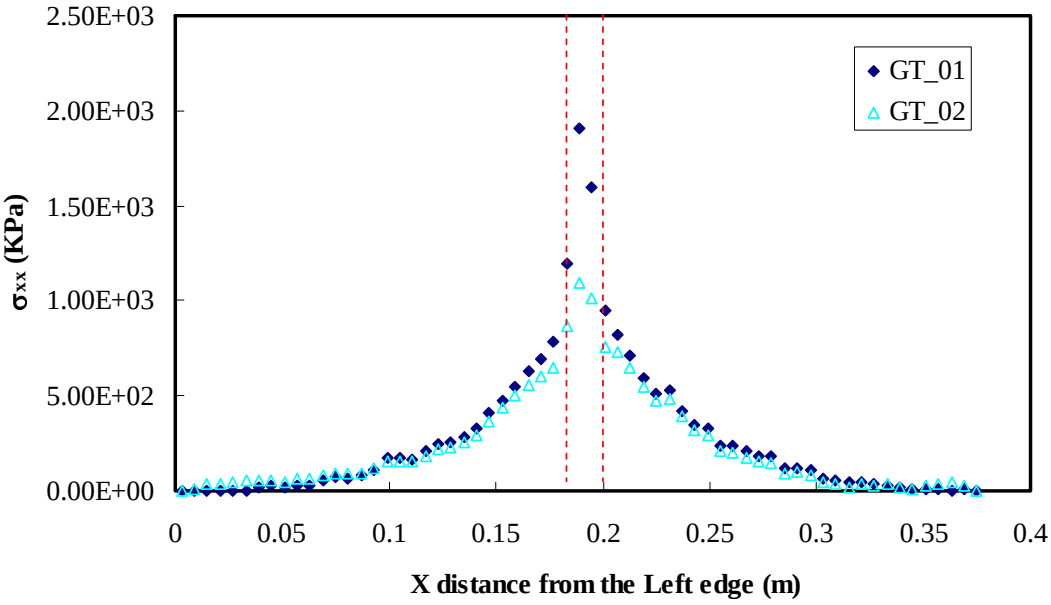

Figure 5.23 Horizontal stress distributions according to geosynthetic properties

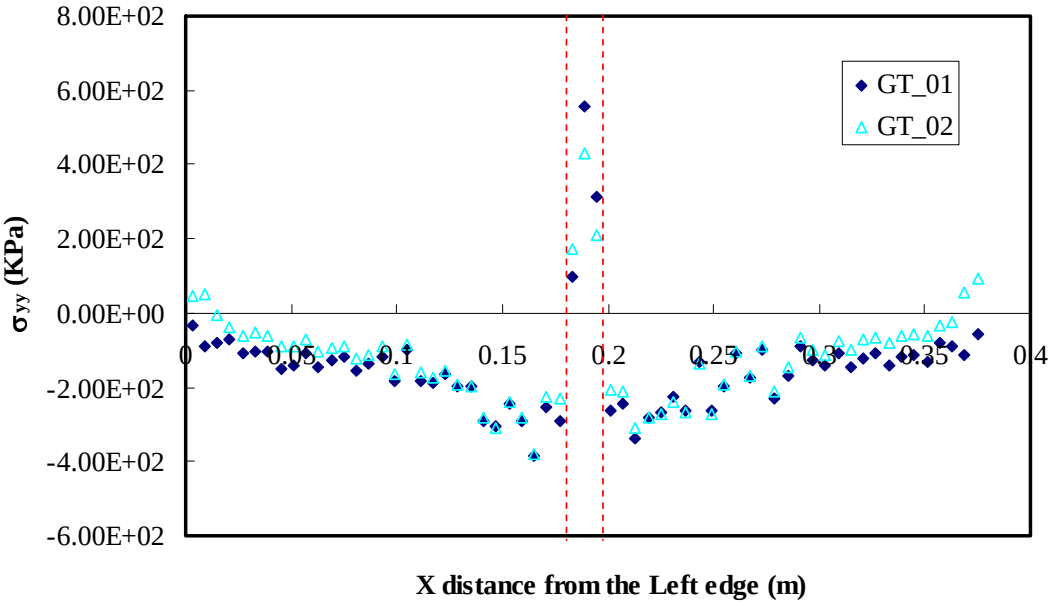

Figure 5.24 Vertical stress distributions according to geosynthetic properties

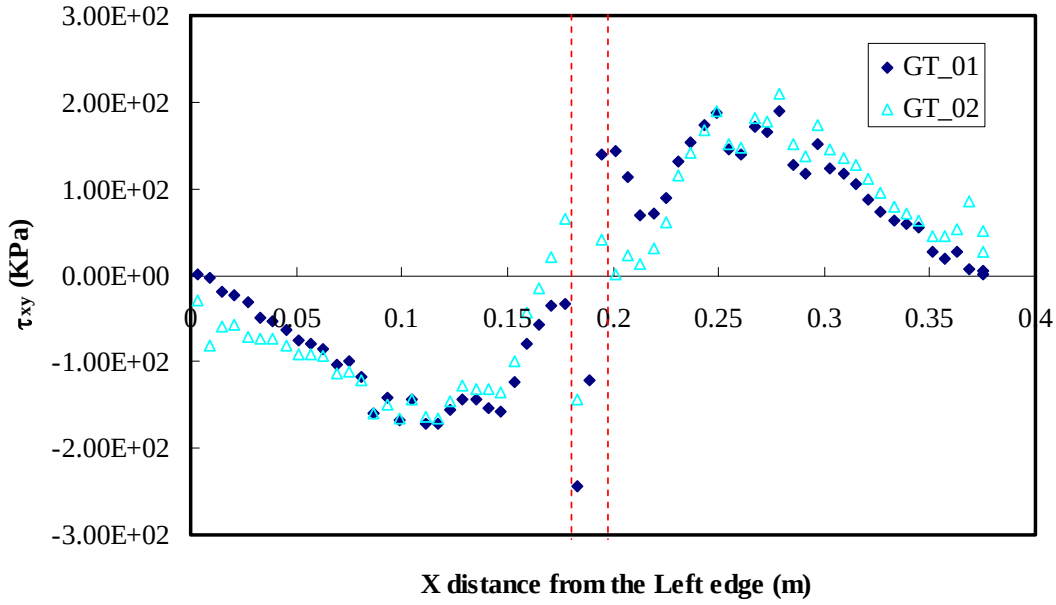

Figure 5.25 Shear stress distributions according to geosynthetic properties

Stress contour images are displayed for different geosynthetic properties in Figure 5.26. These images show that there are slight differences between the two cases around the crack and beneath the loaded area. Stresses for GT_02 at those areas appear to be less converged, indicating that GT_02 provides more effective reinforcement.

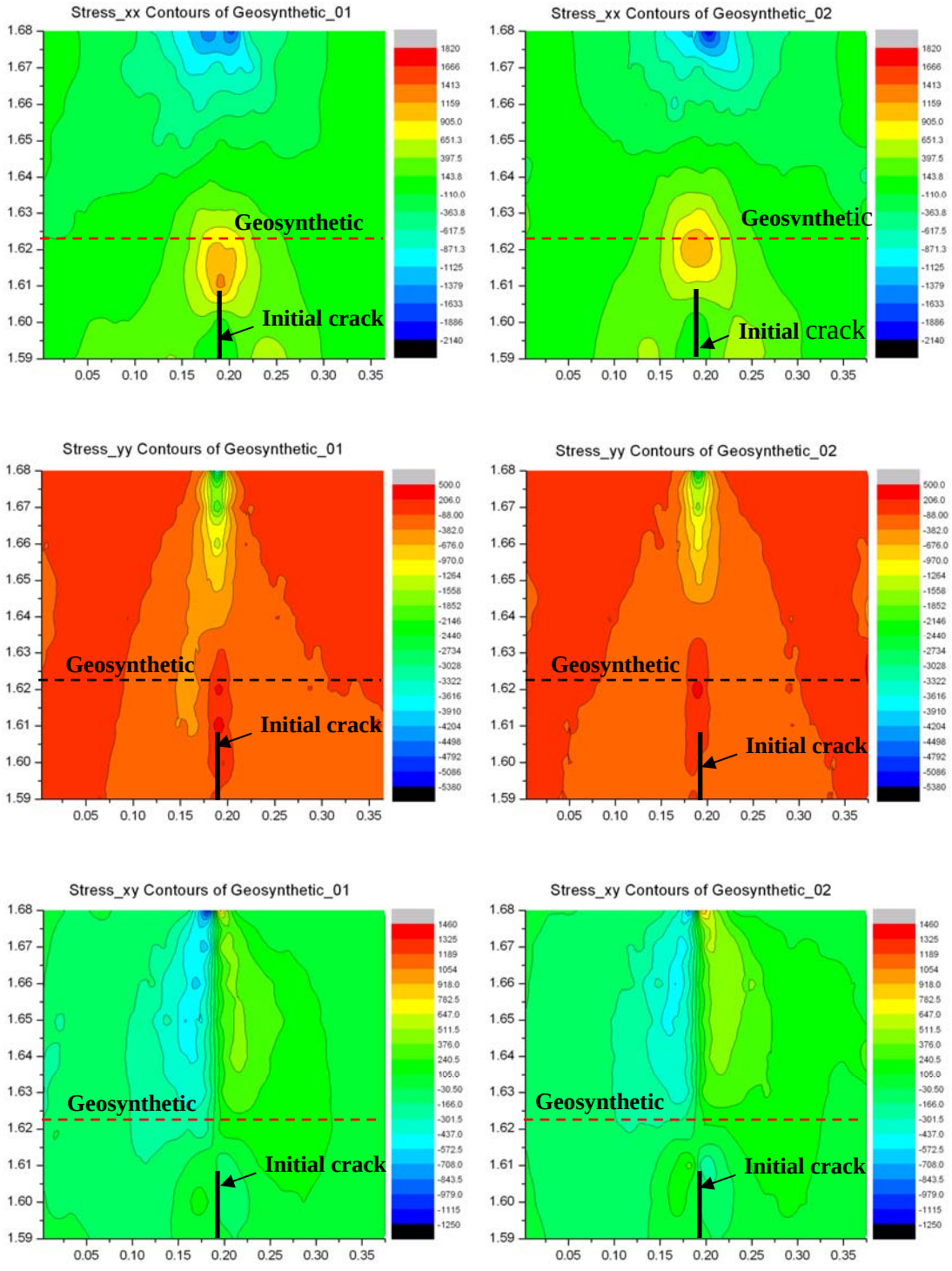

Figure 5.26 Stress contours according to geosynthetic properties

Porosity contours are presented in Figure 5.27 and an obvious difference can be seen there as well. For visual comparison, the same scale range of 0.1860 to 0.1940 is applied. The main difference between the two materials is shown under reinforcement and around initial crack. When a geosynthetic having a high modulus is used, it relatively prevents porosity change from focusing in the vicinity of the crack.

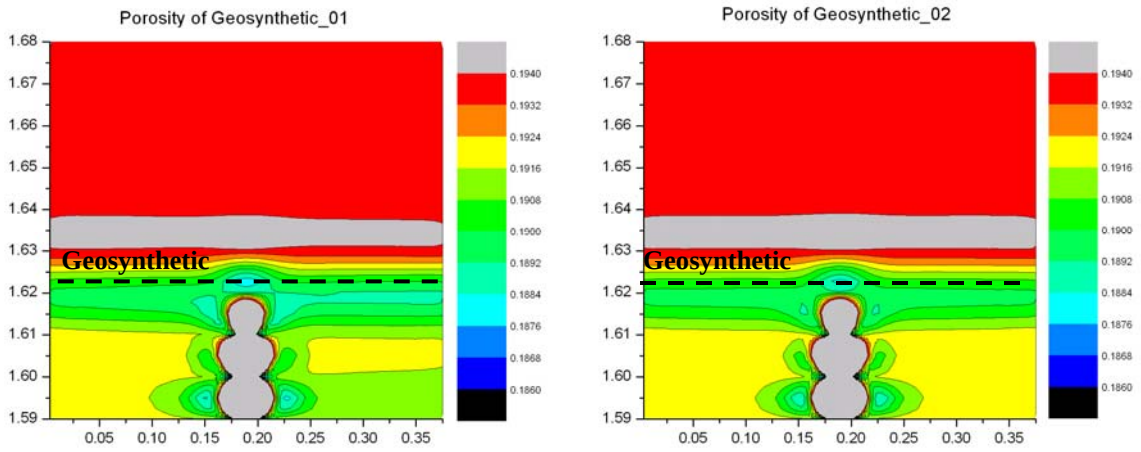

Figure 5.27 Porosity of AC overlay according to geosynthetic properties

5.3.3 Effect of Geosynthetic Location

5.3.3.1 Displacement and Strain

It is important to determine the best placement of the geosynthetic layer to maximize the reinforcement effect on reducing/retarding reflective cracking. Studies on the optimum placement of reinforcement were conducted by several researchers (Brown et al., 2001; Kuo and Hsu, 2003; Sobhan et al., 2005; Khodaii et al., 2009). In this study, to investigate the most effective place, geosynthetics are placed in four different locations relative to the overlay layer: at the bottom (or beneath the overlay), and at 1/3H, 1/2H, and 2/3H from the bottom, where H equals the thickness of the AC overlay layer, as seen in Figure 5.28.

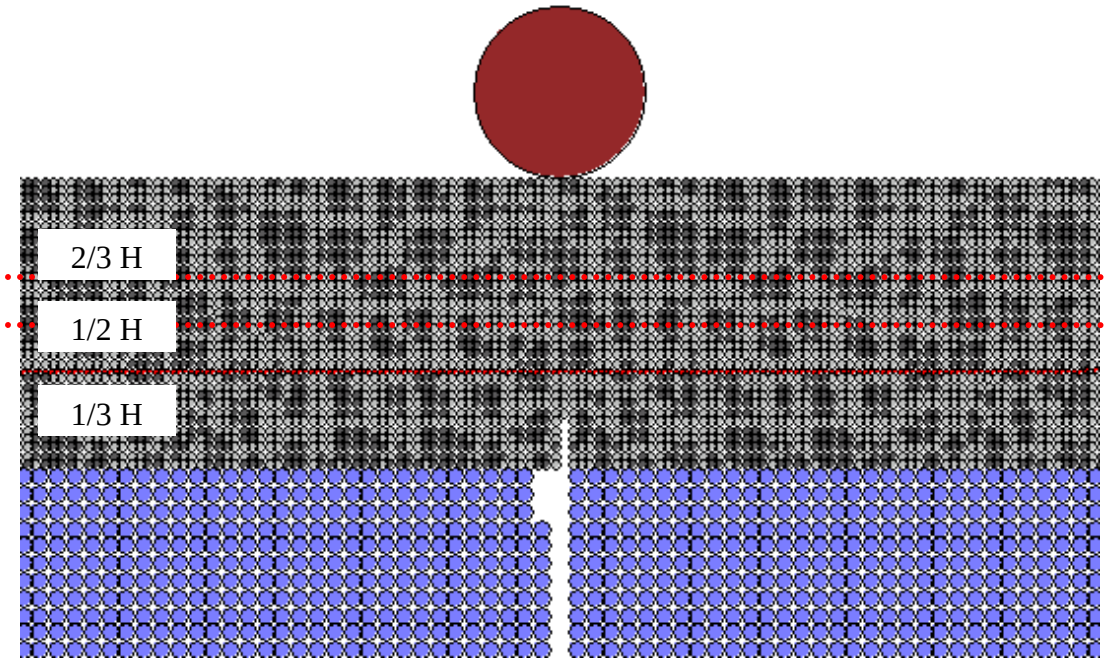

Figure 5.28 Geosynthetics locations in the Asphalt Concrete

Displacements are assessed on the top of the pavement section. Displacements at 1/3H are 8.5 mm, and at 1/2H and 2/3H of the overlay are 8.6 mm as shown in Figure 5.29. The analyses show that the differences are slight but reinforcements placed at 1/2H and 1/3H are more effective than when placed at 2/3H. With 2/3H reinforcement, the displacement is almost the same as that of unreinforced overlay; therefore, reinforcement at 2/3H can be considered to have virtually no effect. Results indicate the importance of the location of geosynthetics within the pavement structure in order to improve pavement performance. This improvement comes from the ability of the geosynthetics to confine lateral movement of the aggregate, resulting in wider load spread throughout the aggregate and a corresponding drop in normal stress on the pavement layers.

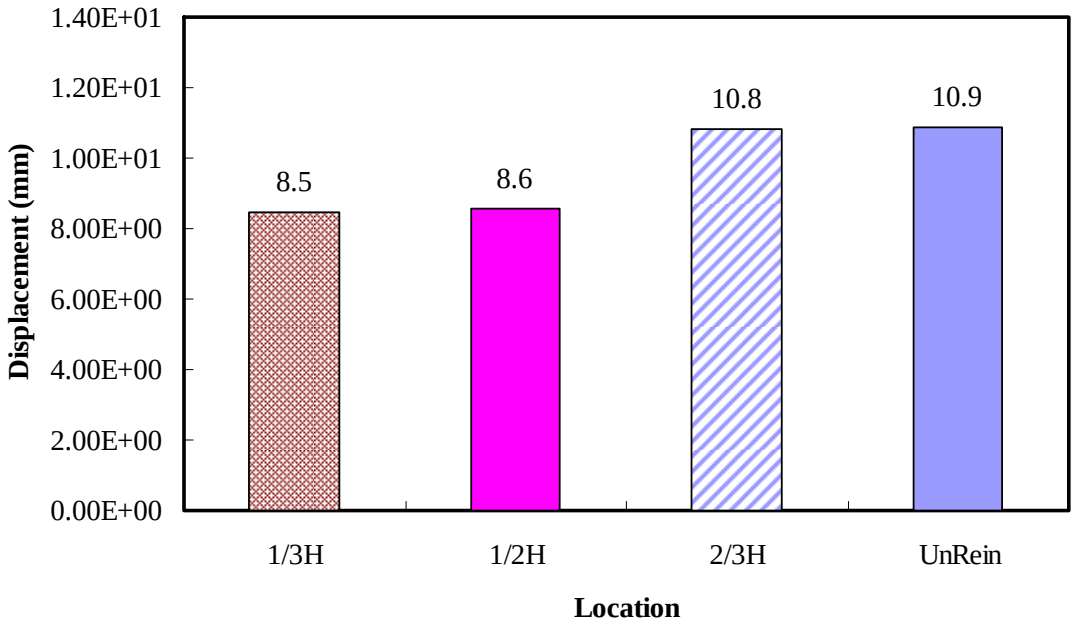

Figure 5.29 Displacement on top for cracked overlays at different locations

To see more of the effect of location on the performance of geosynthetic, other simulations are conducted to exclude the effect of an initial crack in the asphalt concrete. A section with the reinforcement placed at the bottom is added to compare with reinforcement at 1/3H of overlay. The results for these different geosynthetic locations can be seen in Figure 5.30. It is observed that geosynthetic reinforcement at 1/3H from the bottom is the most effective compared with geosynthetic embedded at other locations, though differences in displacements are small. The analyses show that the difference in displacements between reinforcement at the bottom and at 1/3H is 0.1 mm, and a difference of 1.6 mm is shown between reinforcement at 1/3H and at 1/2H. Again, it seems that placing the geosynthetic reinforcement at 2/3H of overlay is no more effective than unreinforced pavement. Khodaii et al. (2009) observed that samples with reinforcement at 1/3H lasted longer than other reinforced locations. It has been demonstrated that an initial crack in the AC overlay can affect the strain and stress distribution, thus, results in affecting total displacement as shown above results.

Figure 5.31 shows horizontal strain measurements in overlay with an initial crack above the reinforcement. Analyses show that the measured strain at 1/3H is effectively decreased by around 14% and 41% over that at 1/2H and 2/3H, respectively. This indicates that 1/3H is the optimum location for reinforcement.

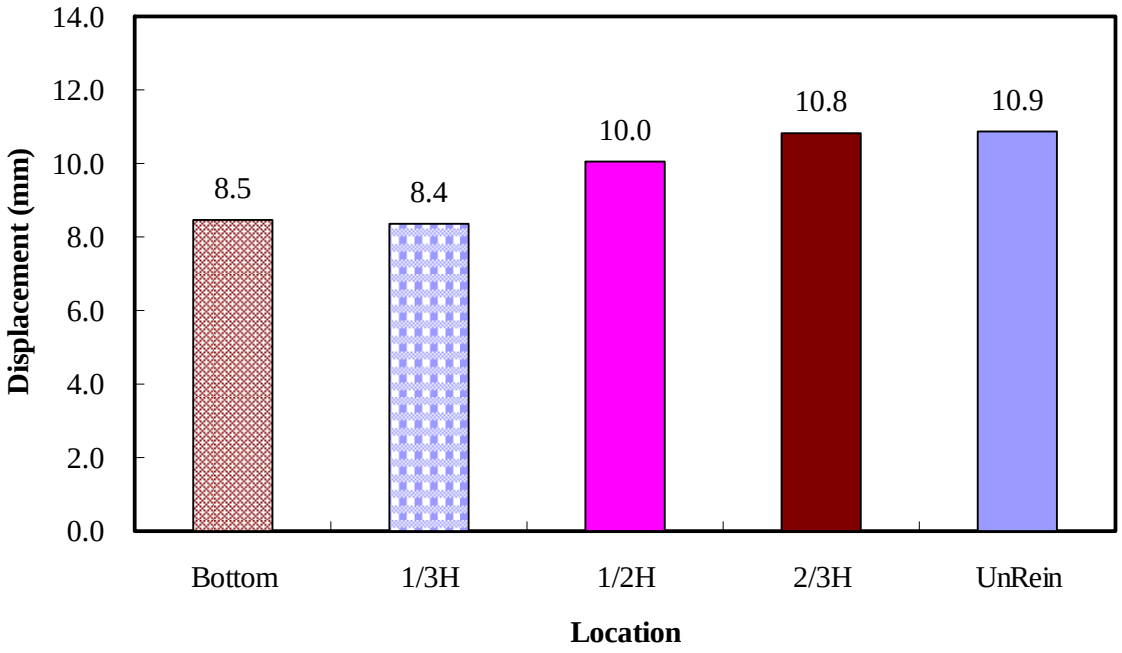

Figure 5.30 Displacement for reinforced overlays at different locations without initial crack

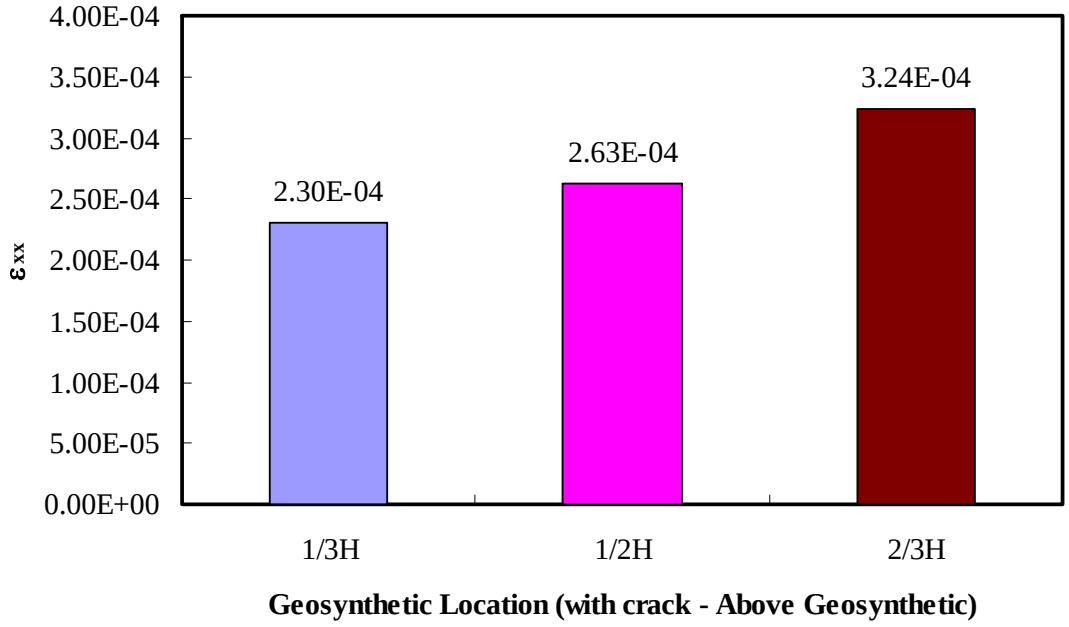

Figure 5.31 Horizontal strains with crack above geosynthetic

Results for tensile strains without initial crack are presented in Figure 5.32, with the result for bottom reinforcement added in for comparison with strain at 1/3H reinforcement. Tensile strains are significantly decreased compared with those of overlay without an initial crack because the presence of a crack promoted horizontal movement. Analyses indicate that when the geosynthetic is placed at 1/3H, tensile strain is reduced by 25% compared with that of reinforcement at the bottom; and reduced by around 86% and 100% compared to reinforcement at 1/2H and 2/3H, respectively. Therefore, strain results also support that 1/3H reinforcement is the most effective. These results correspond with those of Kuo and Hsu (2003), who found that placing the geogrid at 1/3H gave the reinforced overlay maximum fatigue life, due to the minimum tensile strain as compared with bottom-reinforced and 1/2H-reinforced AC overlay.

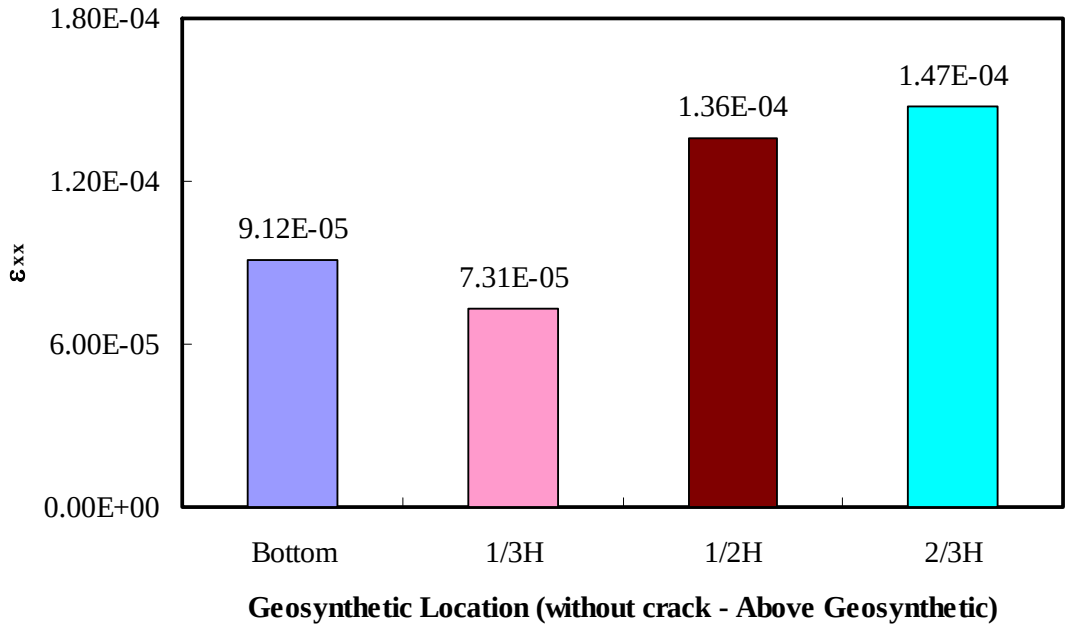

Figure 5.32 Horizontal strains without crack above geosynthetic

5.3.3.2 Stresses and Porosity

Stress distributions around the initial crack tip for different geosynthetic locations (1/3H, 1/2H and 2/3H) are presented in Figures 5.33 to 5.35. Because stress behaviors are the same as explained previously, stress differences according to reinforcement locations are addressed herein. At 0.18 m and 0.2 m of overlay length, maximum stresses are observed for all reinforcement locations, and results show that the closer the geosynthetic is placed to the top, the greater the increase in stress, as well. Analyses indicate that maximum horizontal stress is 1,660 kPa, 1,520 kPa and 1,240 kPa at 2/3H, 1/2H and 1/3H reinforcement, respectively, as shown in Figure 5.33. Similarly, maximum vertical and shear stresses show the same order, but differences between 2/3H and 1/3H are 140 kPa for vertical and 172 kPa for shear, which are relatively smaller than with horizontal stress. This means, again, that geosynthetic reinforcement at 1/3H is the most effective, in comparison with 2/3H and 1/2H reinforcement. Results indicate the importance of the location of geosynthetic within the pavement structure in order to improve pavement performance.

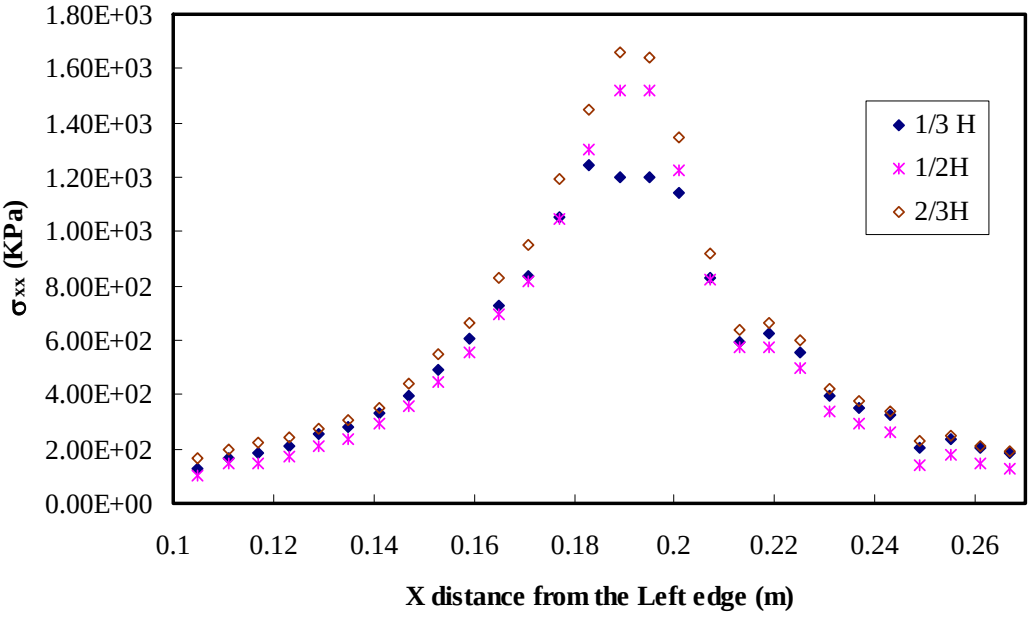

Figure 5.33 Horizontal stress distributions according to geosynthetic locations

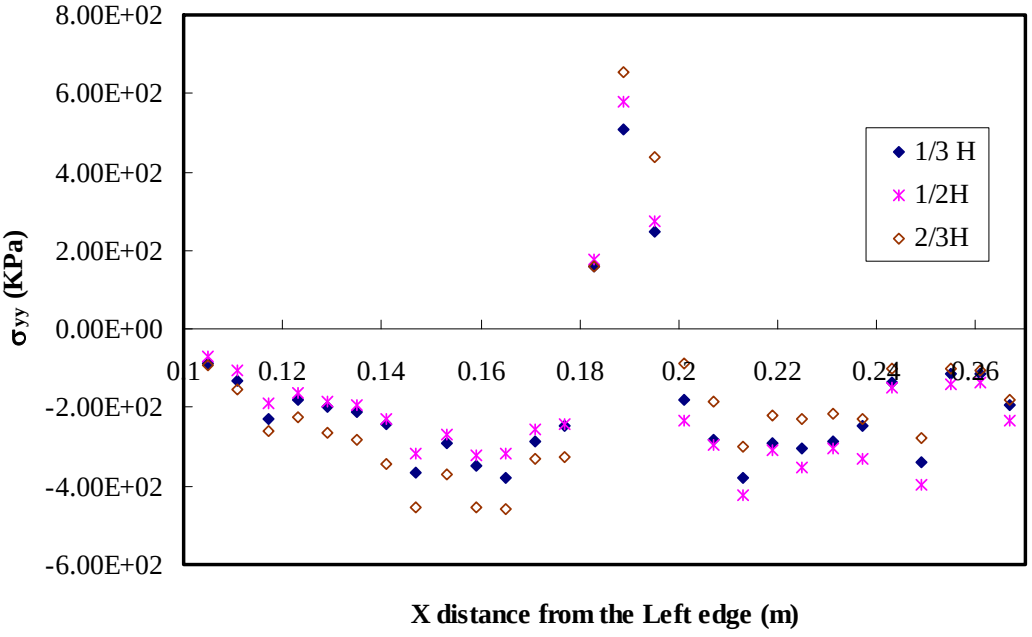

Figure 5.34 Vertical stress distributions according to geosynthetic locations

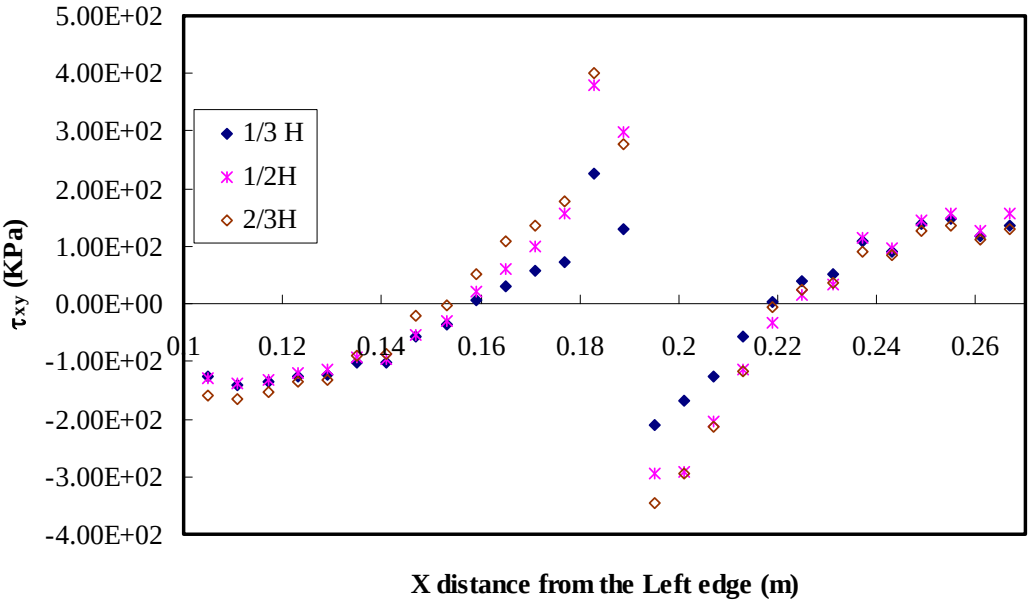

Figure 5.35 Shear stress distributions according to geosynthetic locations

Stress contours for reinforcement have already been shown above. However, it is not easy to make detailed comparisons when values change from negative to positive, so in this section absolute values are used for displaying contours. The stress contours of vertical, horizontal, and shear stress for the whole overlay are presented in Figure 5.36.

Horizontal stress contours are largely divided into two sections which show the greatest concentration of stresses at the initial crack tip and at the point of applied loading. From the figure, it can be seen that there is a lesser concentration of stresses for 1/3H reinforced pavement, especially under the geosynthetic in the vicinity of the crack. This is because 1/3H is the most effective location for reinforcement as already explained above.

Vertical stress contour imaging shows that most differences are in the lower portion of the overlay. The closer the reinforcement is placed to the top of the overlay, the more stress is concentrated in the vicinity of the crack. Similarly, shear stress contour images show maximum stress at the bottom of overlay around the crack. These stress contours show that 1/3H is the best location for geosynthetic reinforcement, as this placement shows the least stress concentrations.

In addition, in order to compare bottom reinforcement and 1/3H reinforcement, stress contours without initial crack are shown in Figure 5.37. Comparing this with Figure 5.36, it can be seen clearly that the initial crack affects the stress field in the vicinity of the crack, and that heavy stress concentrations are not found near the bottom of the overlay, as they are where an initial crack is present. As highlighted by the dotted circle, 1/3H reinforced overlay has lower stress values compared with bottom reinforced overlay. Thus, 1/3H is the optimum location for geosynthetic reinforcement, a conclusion which is in agreement with Kuo and Hsu (2003), Sobhan et al. (2005) and Khodaii et al. (2009).

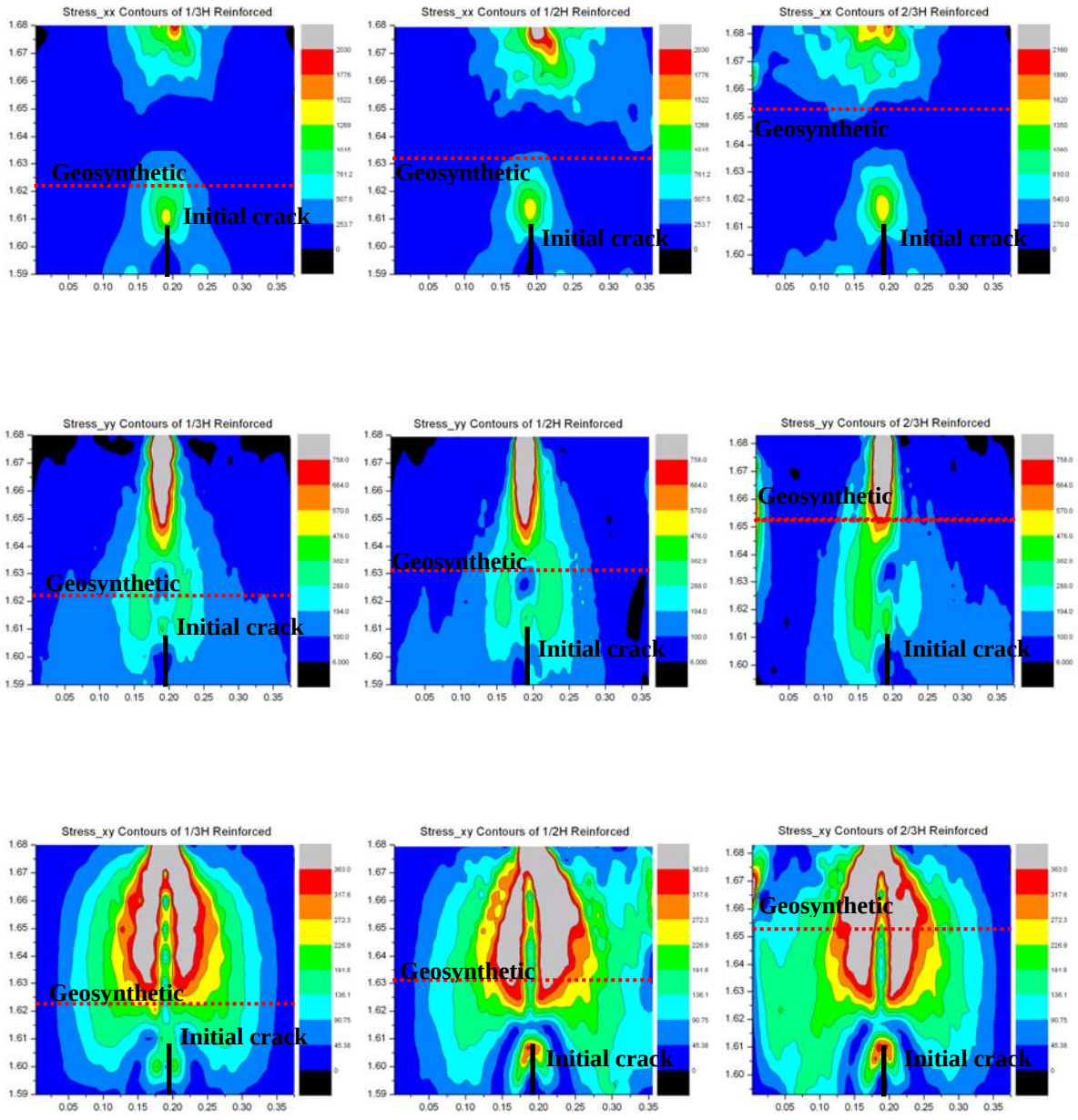

Figure 5.36 Stress Contours for geosynthetic locations with initial crack

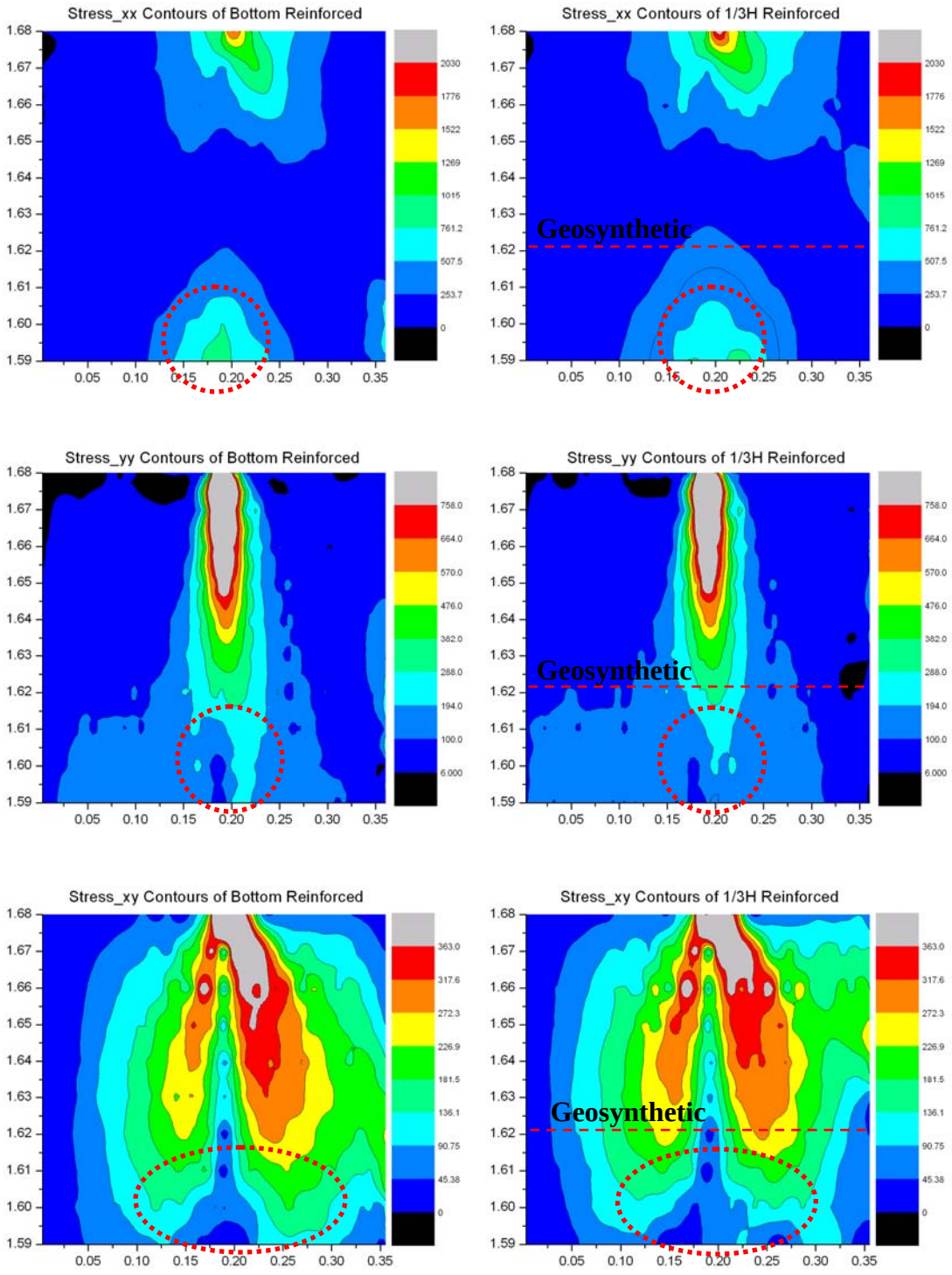

Figure 5.37 Stress Contours for geosynthetic locations without initial crack

Porosity contours are presented in Figure 5.38. For visual comparison, the porosity of all cases is scaled with a range of 0.1860 to 0.1940. The main difference among the three cases is the location of the major change of porosity. In the case of 1/3H reinforcement, porosity changes mainly in the vicinity of the crack because the geosynthetic is located near the initial crack. In the other reinforced overlays, most change of porosity occurs right below the geosynthetic reinforcement.

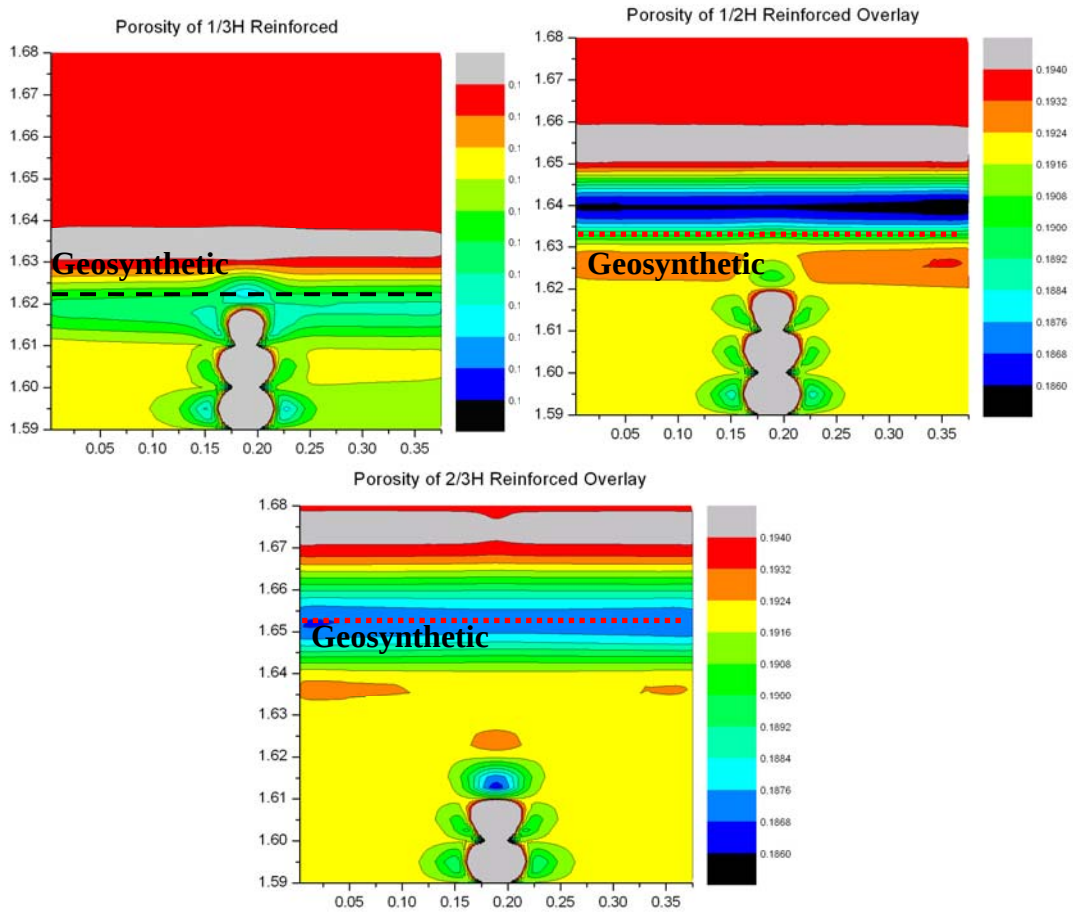

Figure 5.38 Porosity Contours for geosynthetic locations with initial crack

In addition, porosity contours for overlay without initial crack are presented in Figure 5.39. All porosities are scaled with a range of 0.1876 to 0.1939. As in those cases with an initial crack, change of porosity occurs mostly right below the geosynthetic reinforcement. However, porosity changes horizontally, as if the geosynthetic acts as a plate.

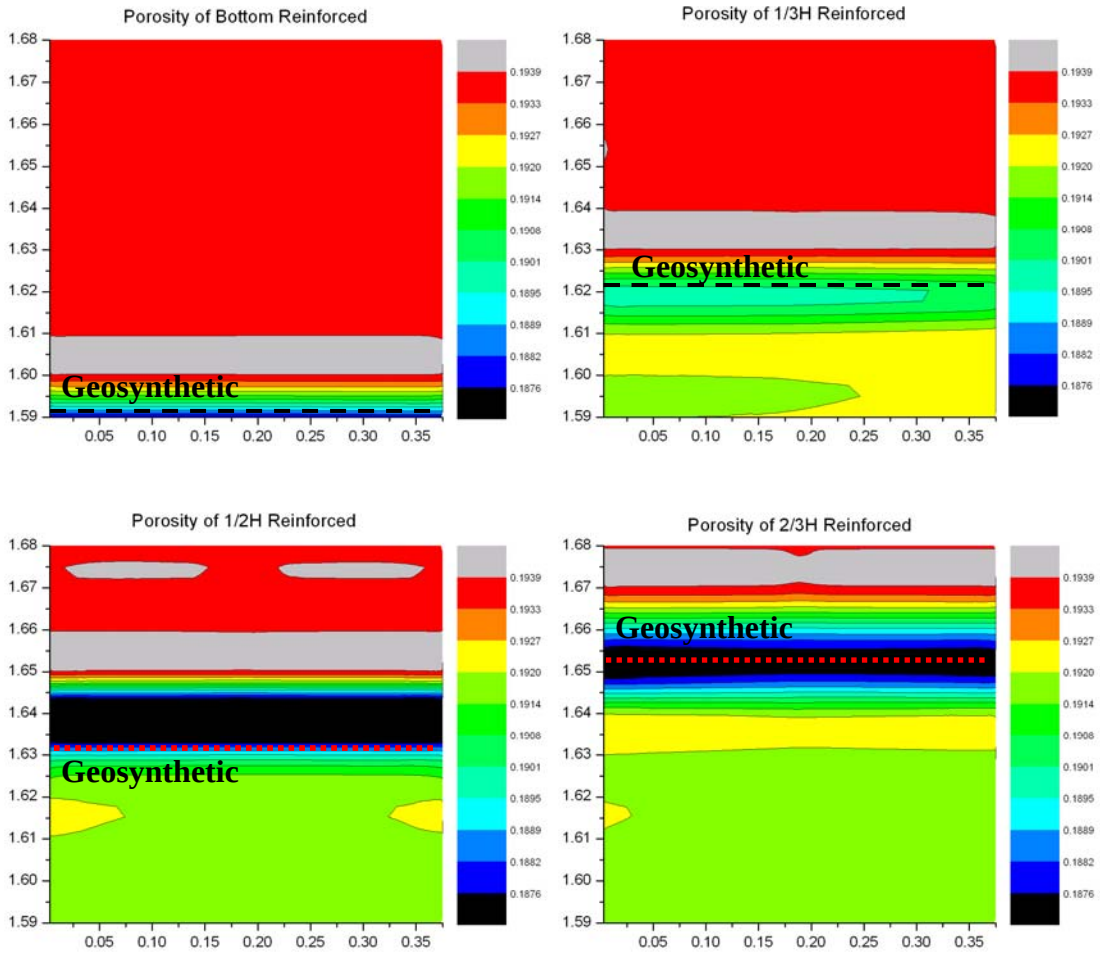

Figure 5.39 Porosity Contours for geosynthetic locations without initial crack

5.3.4 Effect of Aggregate pattern of AC

To investigate the effect of the aggregate pattern of the asphalt concrete, two different aggregate patterns are used. Aggregate_01 is original pattern and Aggregate_02 is rotated by 180° from Aggregate_01 as shown in Figure 5.40. Simulations are conducted on two AC overlays, with and without reinforcement.

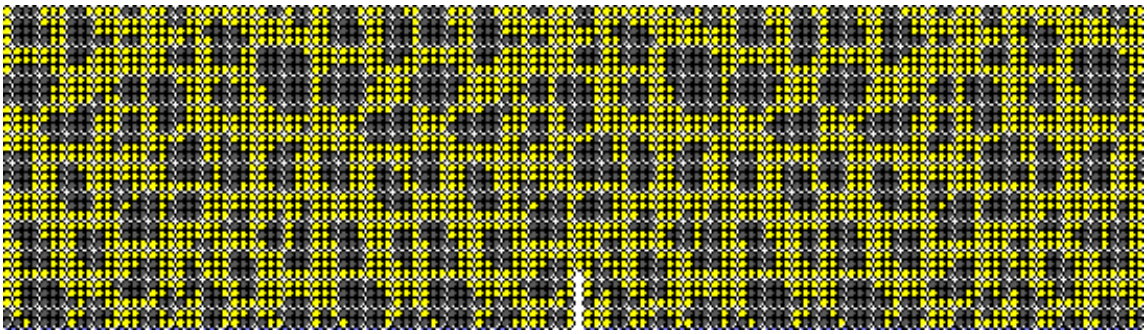

(a) Aggregate_01

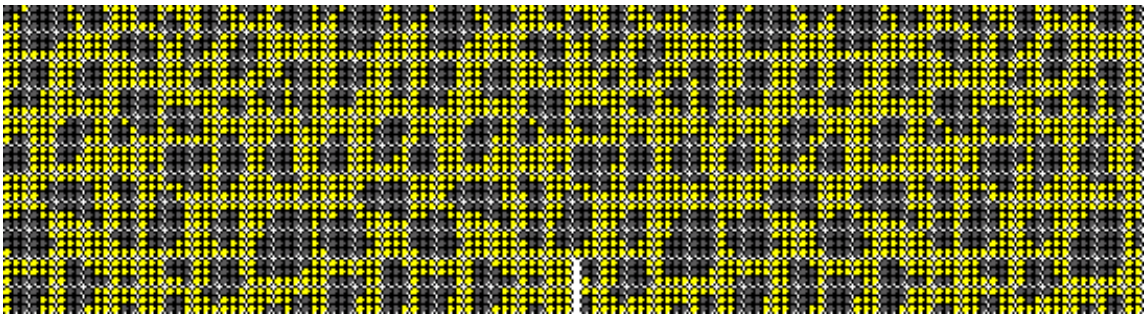

(b) Aggregate_02

Figure 5.40 Different Aggregate patterns on AC layer

5.3.4.1 Displacement and Strain

Results are presented in Figure 5.41 for displacement at the top, showing only a marginal difference. Analyses show that displacement differences at the top for both patterns, with and without reinforcement, are 0.1 mm. This is because, for Aggregate_02, there is one more particle of aggregate along the inserted crack line where loading is applied. It indicates that the particle geometry may affect the behavior of the asphalt. The greater the concentration of the aggregate, the higher the modulus; consequently, the more effectively the aggregate is restrained from sliding and rotation, the less displacement is caused. The effects of strain and stress will be addressed in the next section.

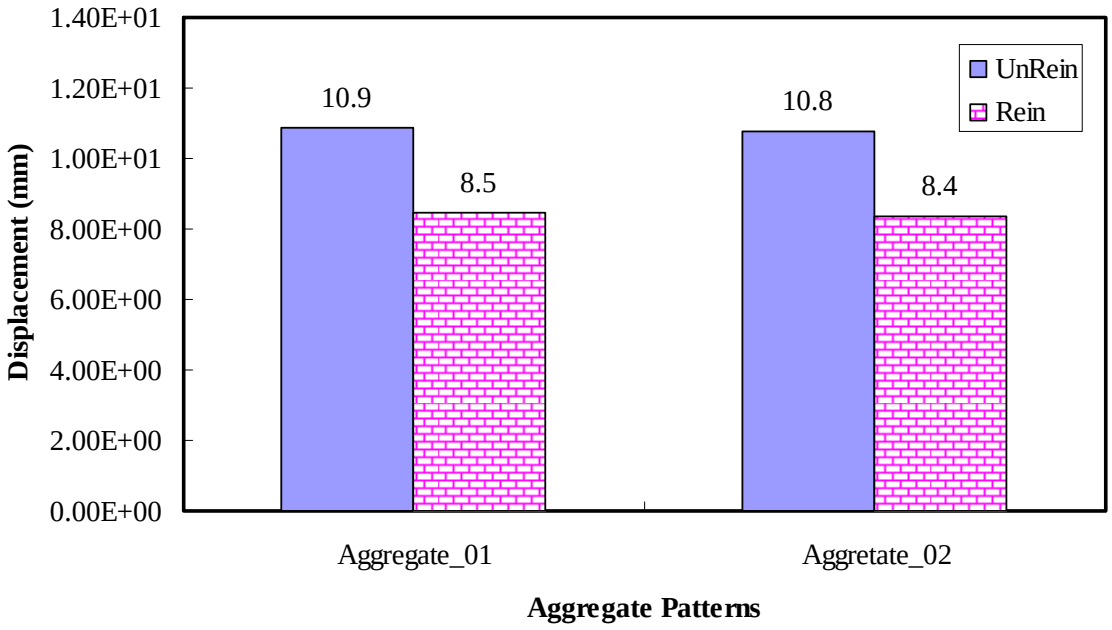

Figure 5.41 Displacements according to aggregate patterns

With reference to Figure 5.42, tensile strains which are measured from 5 measurement circles for overlay without reinforcement at the bottom are distributed in the shape of an arch, both with and without reinforcement. Results show that strains within Aggregate_02 are relatively smaller that those of Aggregate_01 and tensile strain is decreased by around 11% compared with Aggregate_01; thus, aggregate patterns surely affect behavior of the asphalt overlay. Also, Figure 5.43 shows the results of tensile strain distribution for overlay with reinforcement. Analyses indicate that tensile strain in Aggregate_02 is decreased by around 20% as compared with strain in Aggregate_01. Moreover, analyses indicate that when reinforcement is placed in initial-cracked AC overlay with different aggregate distributions, tensile strain under geosynthetic increases by 18.5% over that without reinforcement with Aggregate_01, as well as tensile strain increases only 6% over that without reinforcement with Aggregate_02. However, tensile strain above the reinforcement decreases by around 8% with Aggregate_01 and 23% with Aggregate_02 compared to without reinforcement as seen in Figure 5.44. It means that greater strain reduction occurs because the geosynthetic works more effectively with Aggregate_02.

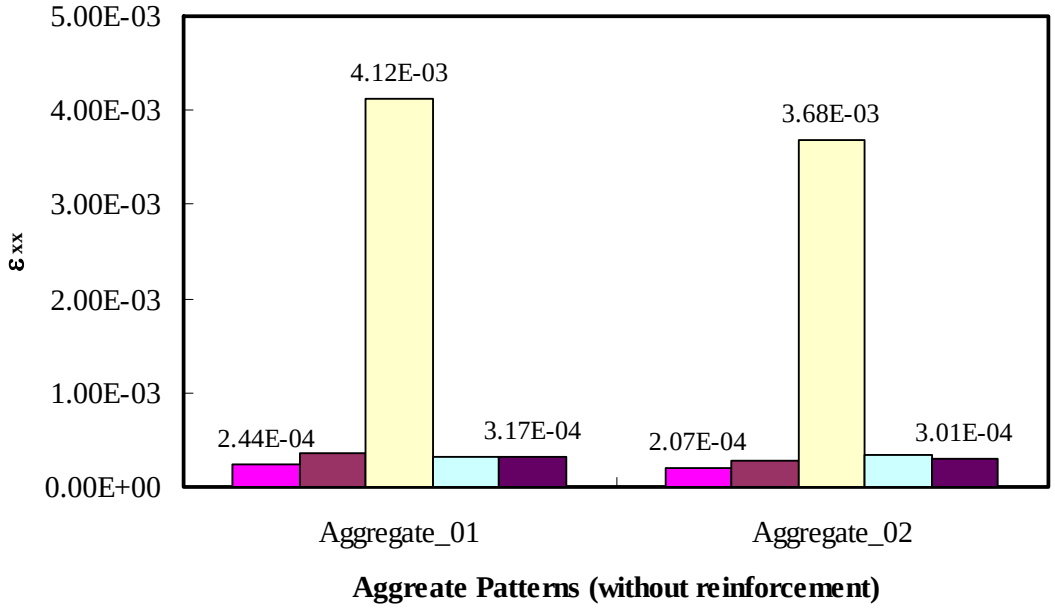

Figure 5.42 Strain distributions without reinforcement under geosynthetic

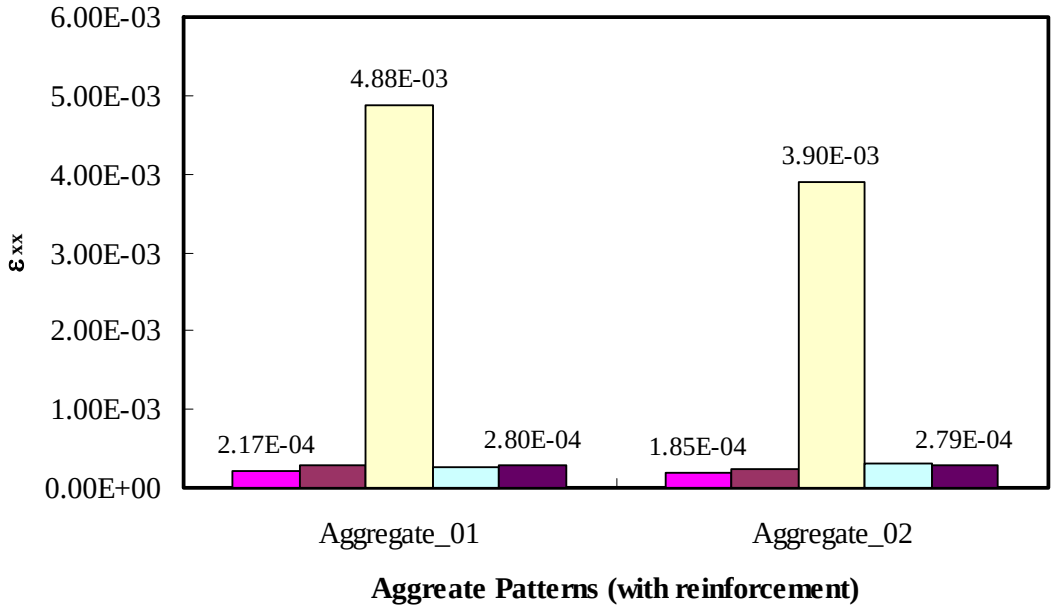

Figure 5.43 Strain distributions with reinforcement under geosynthetic

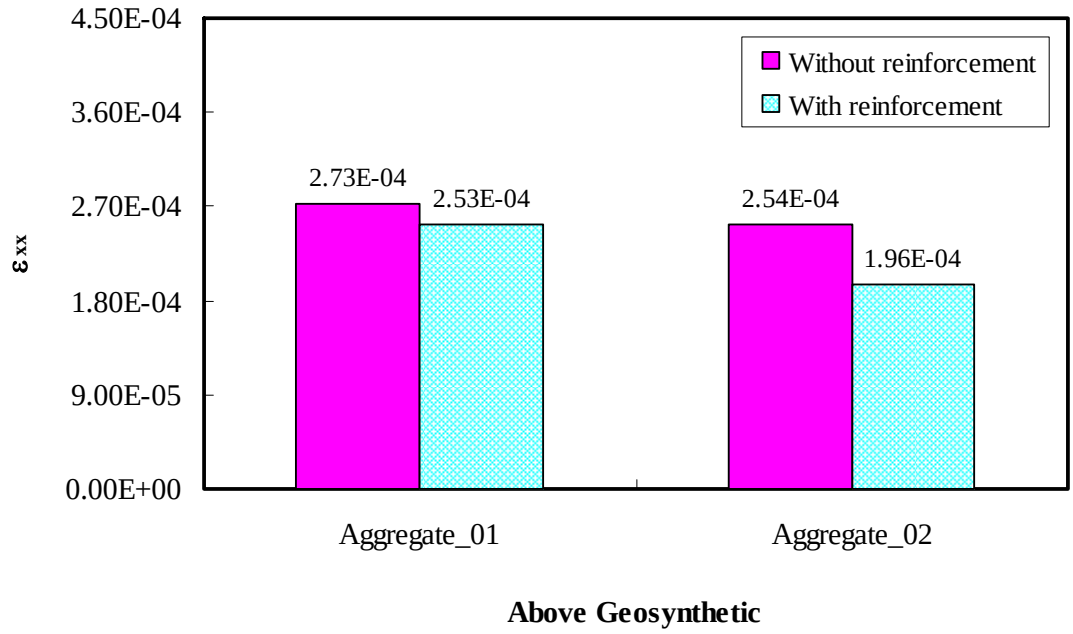

Figure 5.44 Strain distributions with and without reinforcement above geosynthetic

5.3.4.2 Stresses and Porosity

Combined results of horizontal stress analyses in the vicinity of the crack tip are presented in Figure 5.45. These results indicate that maximum horizontal stresses are 1,170 kPa for Aggregate_01 and 1,370 kPa for Aggregate_02, and stresses of Aggregate_02 are higher than those of Aggregate_01. This result is not in accordance with displacement and strains results. Because the aggregate pattern is changed, measurement circles have different compositions of aggregates and FAM, unlike previous cases which had the same compositions. Thus, stress is affected by both modulus (E) and strain (ε). Results for vertical stress are shown in Figure 5.46. Similarly, maximum vertical stress difference is 193 kPa with the same order as horizontal stress values. But it is noted that the other two values

observed around the initial crack for Aggregate_01 are higher than that of Aggregate_02. Figure 5.47 shows the result of shear stress analysis, which indicates that maximum shear stresses are 200 kPa for Aggregate_02 and 193 kPa for Aggregate_01; however, the orders of higher value are mixed, like the results for vertical stress. In addition, combined results for horizontal, vertical and shear stresses with reinforcement in the vicinity of the crack tip are presented in Figures 5.48 to 5.50. These results show the same tendency as in the unreinforced overlay, though not the same values.

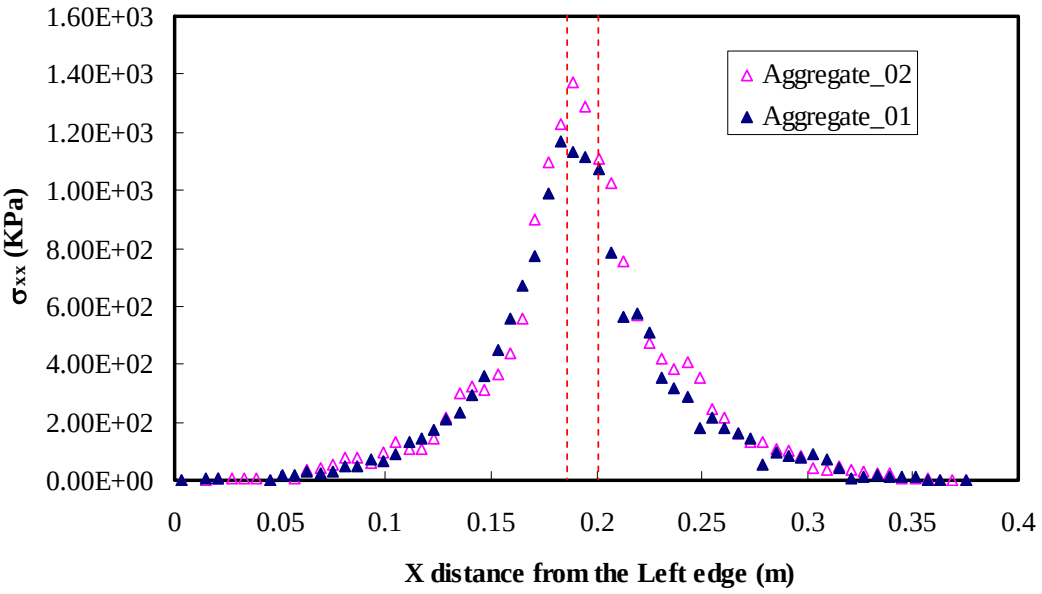

Figure 5.45 Horizontal stress distributions according to different aggregate distribution

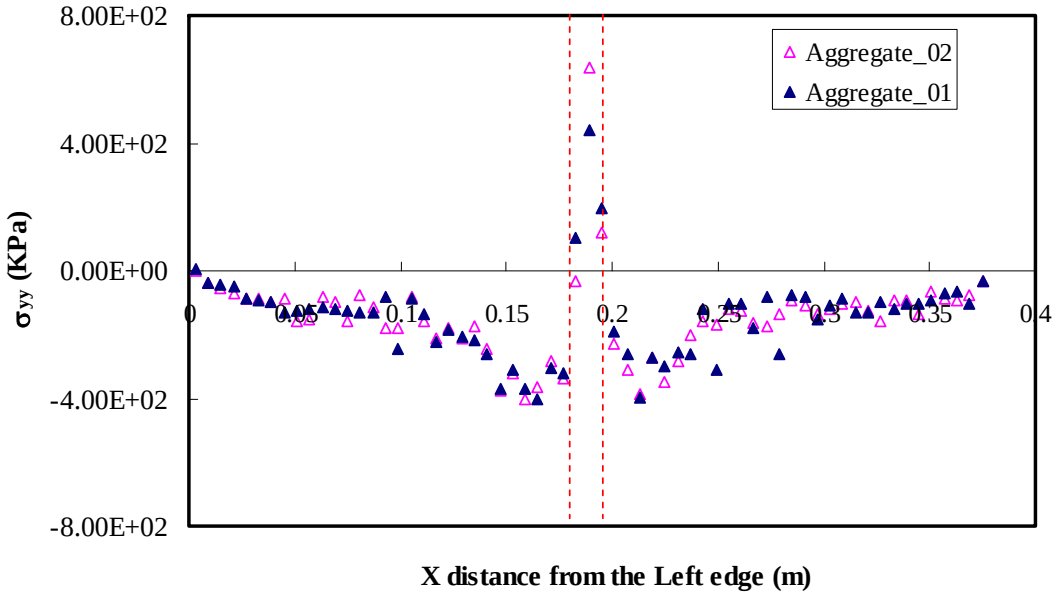

Figure 5.46 Vertical stress distributions according to different aggregate distribution

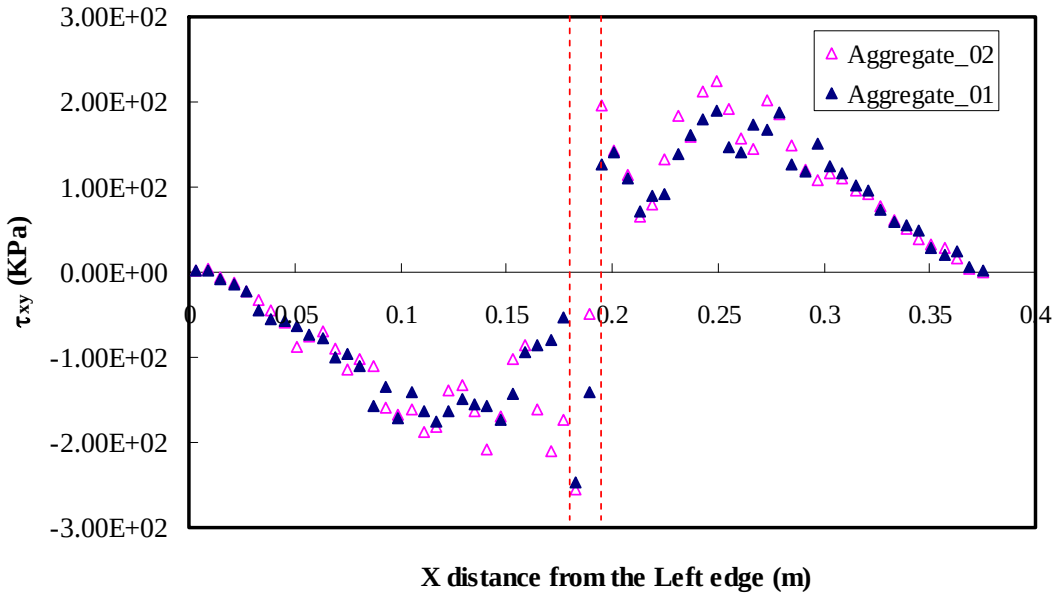

Figure 5.47 Shear stress distributions according to different aggregate distribution

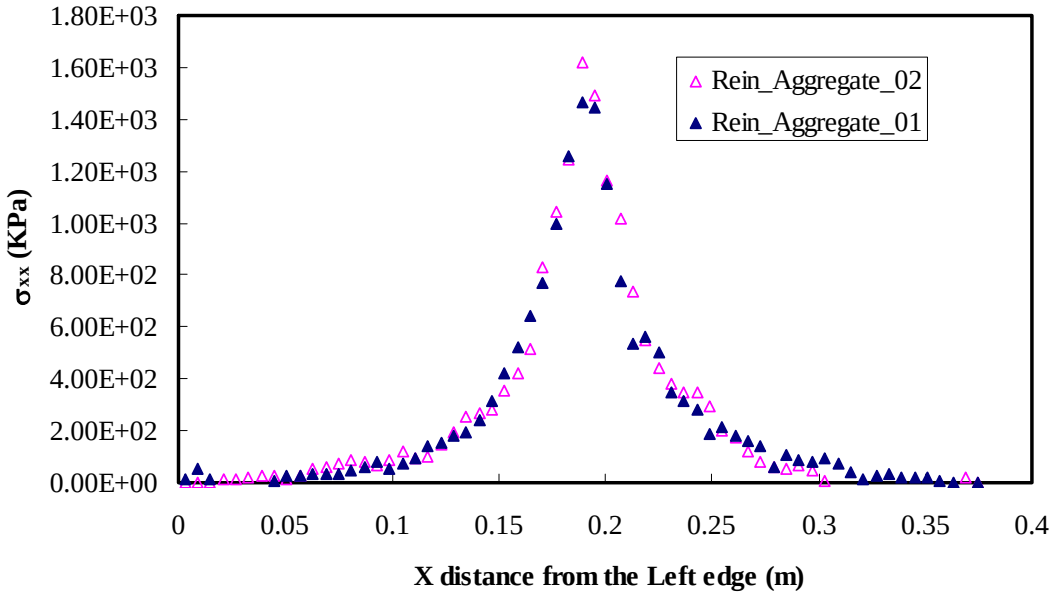

Figure 5.48 Horizontal stress distributions according to different aggregate distribution with reinforcement

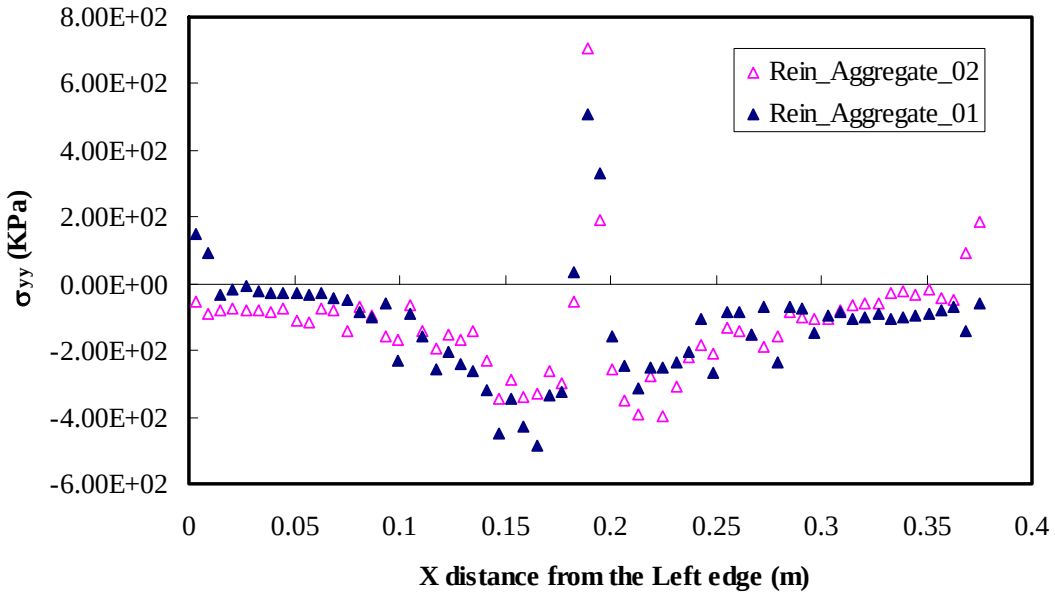

Figure 5.49 Vertical stress distributions according to different aggregate distribution with reinforcement

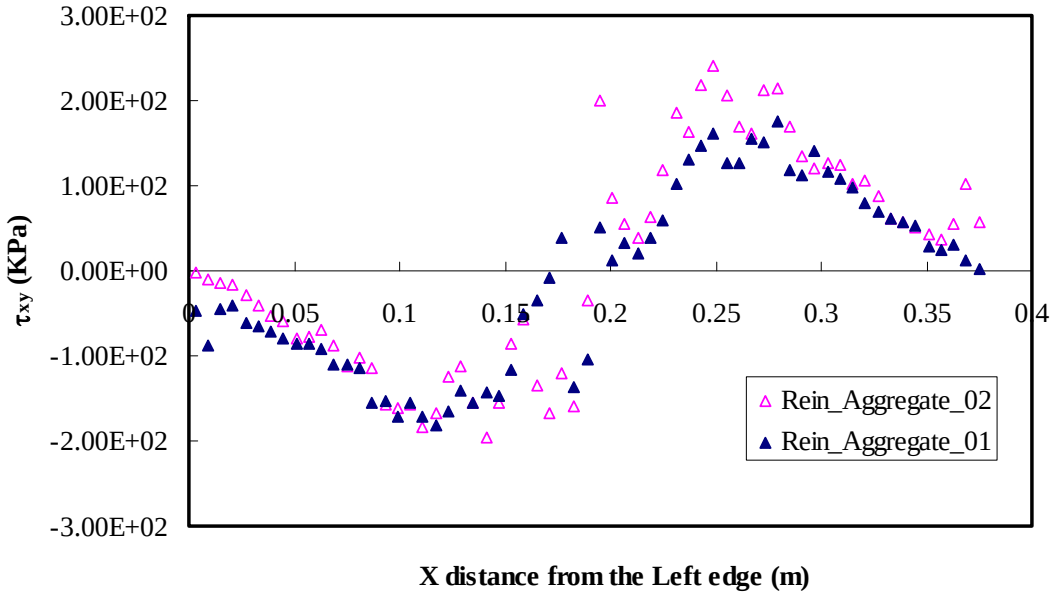

Figure 5.50 Shear stress distributions according to different aggregate distribution with reinforcement

Stress contours without and with reinforcement are displayed for the different aggregate patterns in Figures 5.51 to 5.52. Stress contours show that while there are no major differences between the cases, roughly speaking, minor differences do exist around the crack and beneath the loaded area. In the reinforced overlay, the differences can be seen clearly in Figure 5.52. In the case of Aggregate_01, stresses are relatively more distributed on the left side, while stresses of Aggregate_02 are more concentrated on the right side.

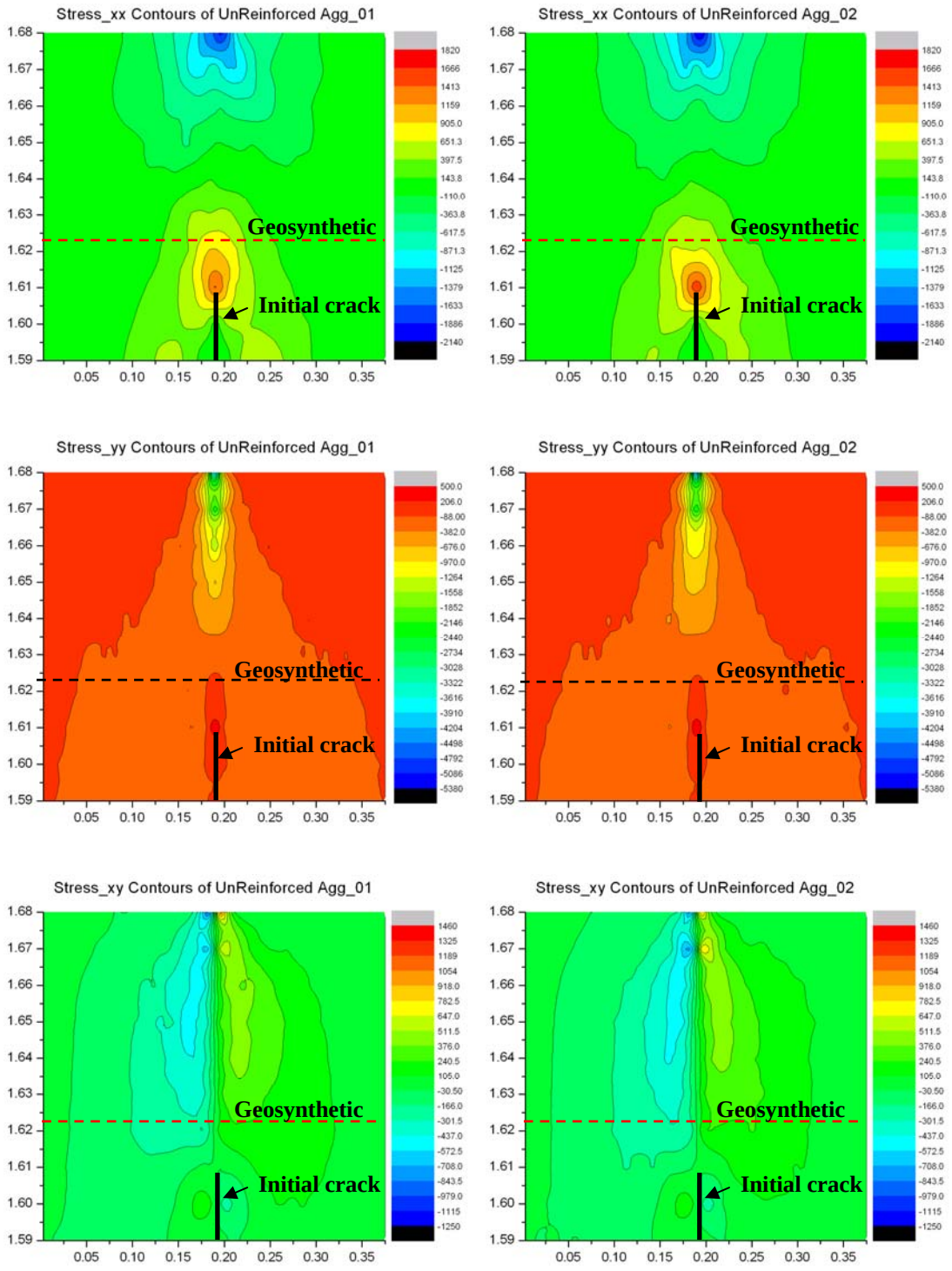

Figure 5.51 Stress contours without reinforcement according to different aggregate distribution

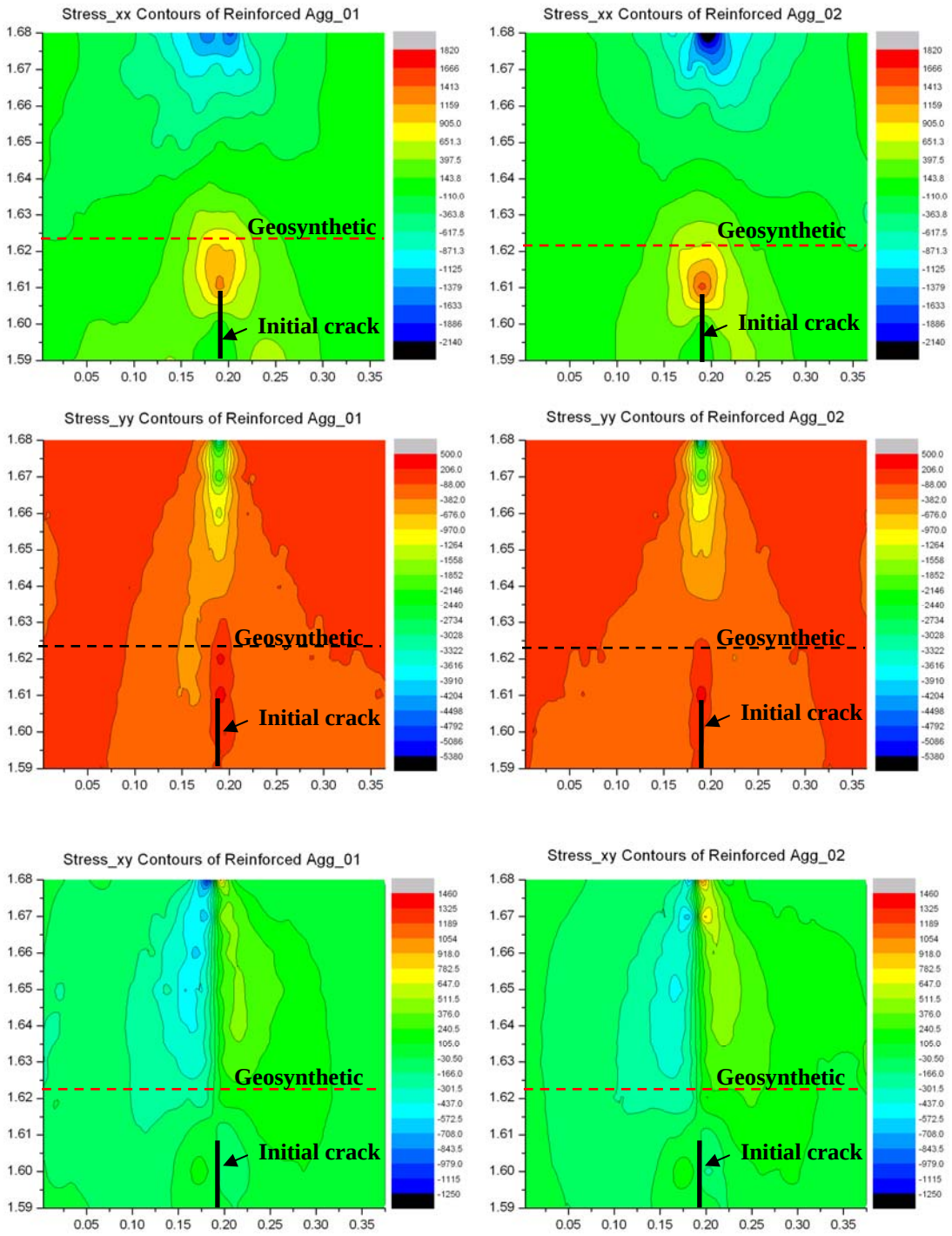

Figure 5.52 Stress contours with reinforcement according to different aggregate distribution

Porosity contours without reinforcement are presented in Figure 5.53. Both porosities are scaled ranging from 0.1915 to 0.1921. The two porosity contours are almost the same except for the areas pointed out with dotted-line circles. Relatively more changes are seen in the vicinity of the crack for Aggregate_01, while more changes are shown beneath the loading point for Aggregate_02.

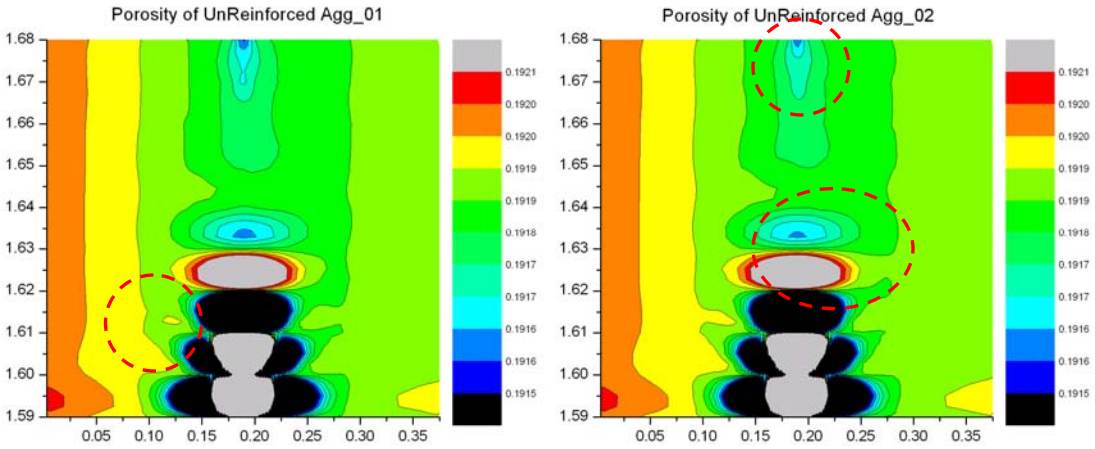

Figure 5.53 Porosity contours without reinforcement according to aggregate distribution

Figure 5.54 shows the porosity contours with reinforcement. Both porosities are scaled ranging from 0.1840 to 0.1940. Analyses show that changes mostly occur on the right side under reinforcement for Aggregate_01, while the porosity of Aggregate_02 changes more on the left side.

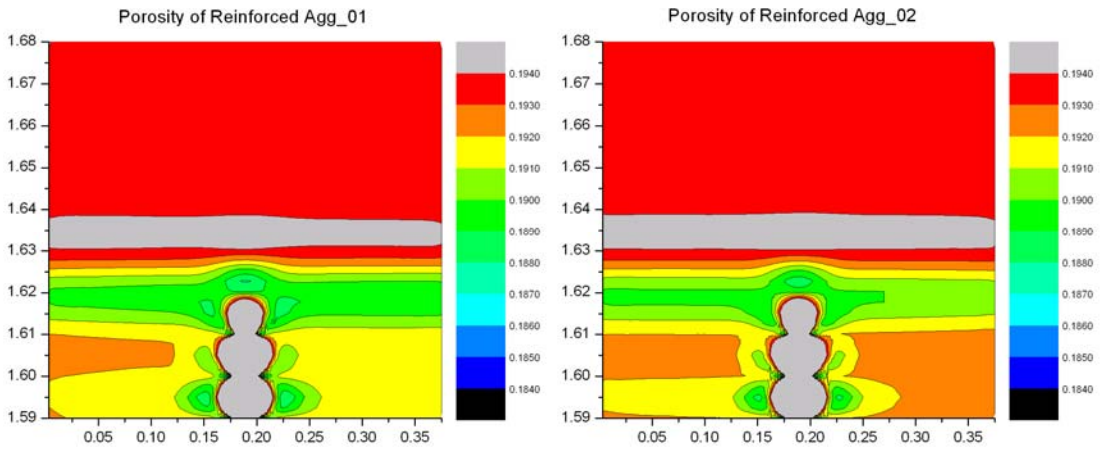

Figure 5.54 Porosity contours with reinforcement according to aggregate distribution

5.4 Effect of existing PCC Pavement Condition

5.4.1 Effect of PCC properties

5.4.1.1 Displacement and Strain

It is important to first quantify the severity and extent of distress in the existing pavement as part of the rehabilitation design process. To investigate the effect of the existing concrete condition, two modulus values are used. The low modulus value represents a deteriorated concrete condition with an initial crack (i.e. soft layer). The high modulus value represents an original concrete condition with no initial crack (i.e. stiff layer). Figure 5.55 shows displacement according to these different PCC properties. Analyses indicate that displacement at the top is 10.9 mm with high modulus and 9.5 mm with low modulus, resulting in a difference of 1.4 mm for overlay without reinforcement. It can be explained that the soft layer (AC) with stiff PCC layer is more effective for the deformation than the stiff layer (AC) with soft PCC layer. However, displacement is increased by 0.1 mm in the

case of reinforced overlay, accompanied by increased tensile strain at the bottom of the overlay as seen in the next paragraph.

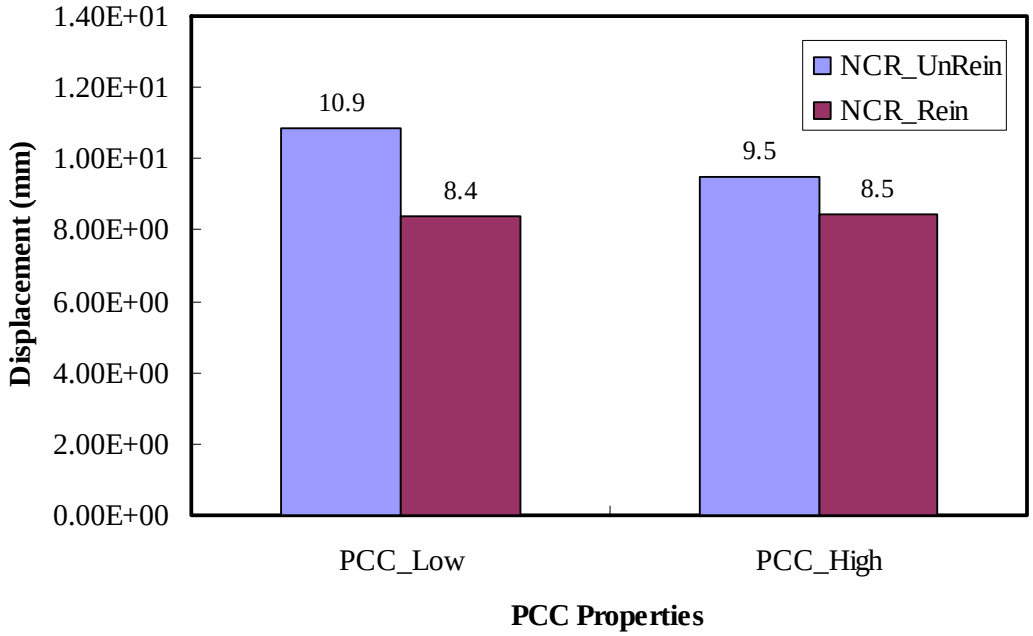

Figure 5.55 Displacement at the top according to PCC properties

Figure 5.56 shows tensile strains at the bottom of the overlay for PCC with high modulus and with low modulus, with and without reinforcement. Strains are distributed in the shape of an arch in both cases. Analyses indicate that PCC with high modulus leads to decreased lateral strain by around 53% in the middle for unreinforced overlay, as shown in Figure 5.56(a). It can be explained that PCC with high modulus performs as tensile reinforcement by preventing lateral spreading of the AC overlay. High modulus develops a stiffer layer associated with an interlocking action. In addition, tensile strains are presented in

Figure 5.56(b) for both low and high modulus with reinforcement. Analysis indicates that tensile strain in the middle is decreased by around 36%, which is smaller than the decrease found in unreinforced overlay. It can be explained that the stiffer layer developed by high modulus PCC promotes lateral movement when a geosynthetic is in place because the geosynthetic is less effective laterally, thus, larger tensile strain occurs and this results in increased displacement of pavement.

Figure 5.57 shows vertical strains at the bottom of the overlay for PCC with high modulus and low modulus, with and without reinforcement. Strains are distributed in the shape of a reversed arch in both cases, unlike the results for horizontal strain. Analyses indicate that vertical strains in PCC with high modulus are increased by around 47% in the middle without reinforcement and 52% with reinforcement. This means that high modulus PCC is less effective vertically. The increase in vertical strain also has an effect on stress behavior, as will be discussed in the next section.

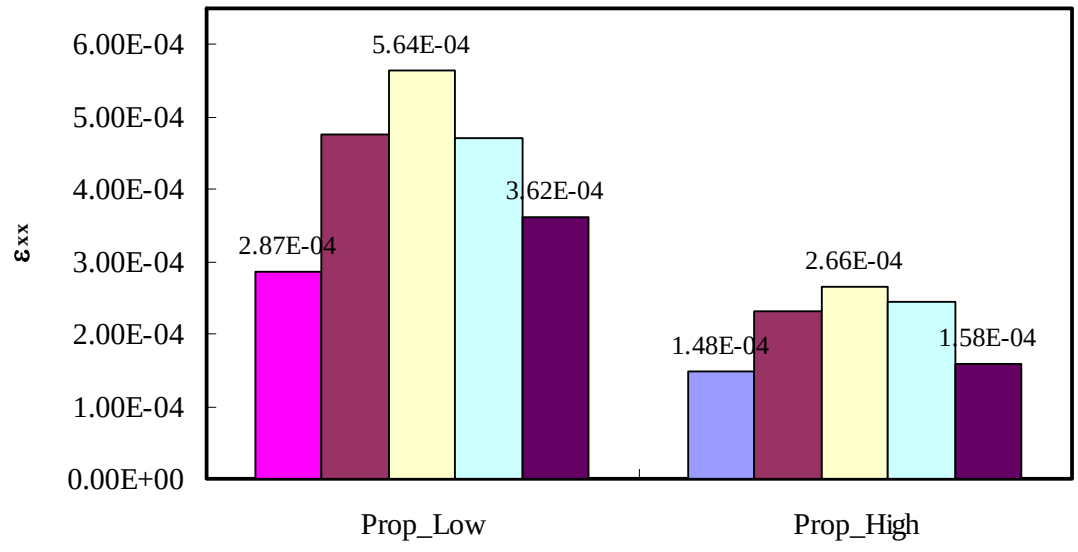

(a) PCC Properties (NCR_Unrein)

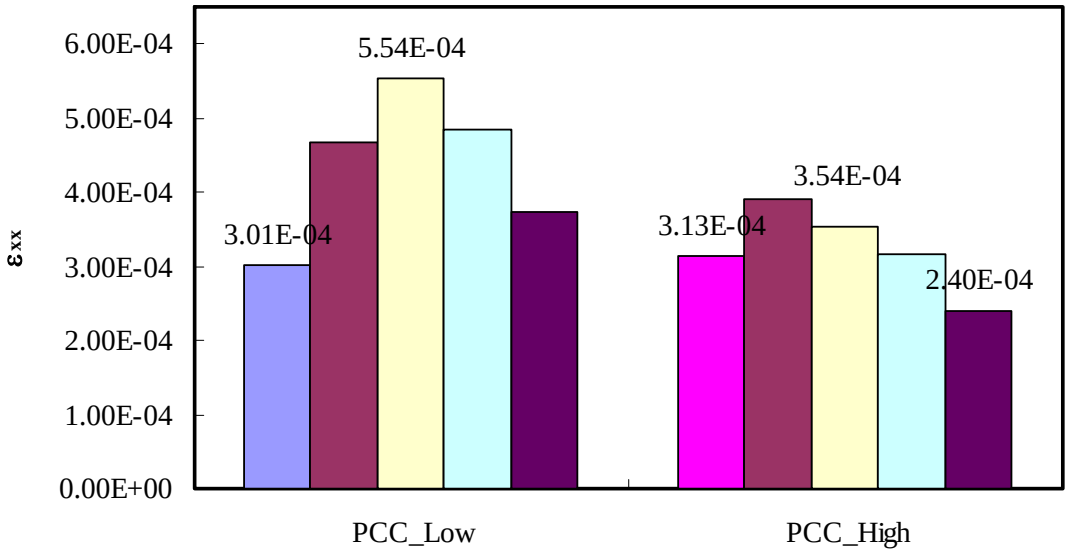

(b) PCC Properties (NCR_Rein)

Figure 5.56 Horizontal strain distributions at the bottom of overlay.

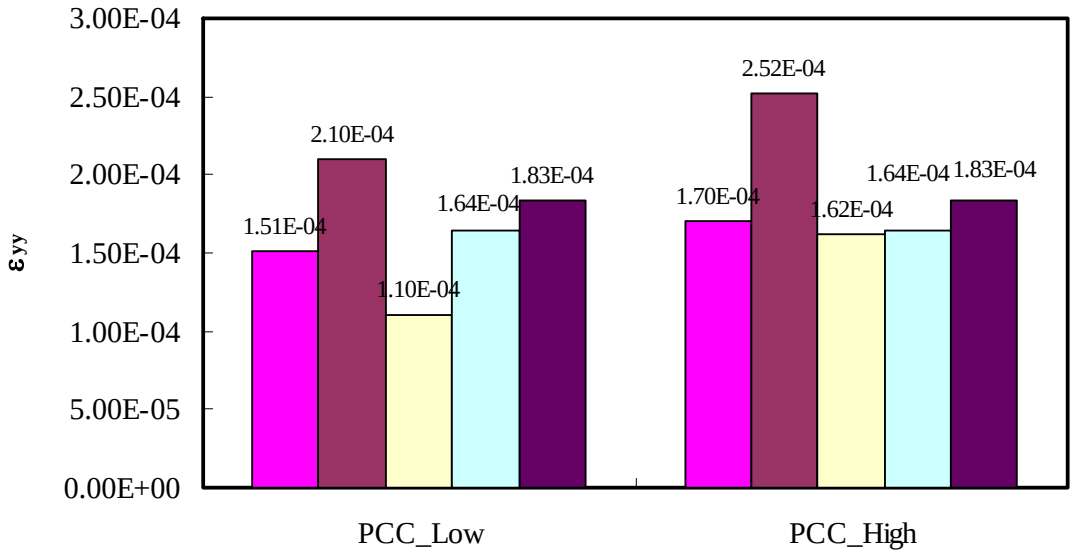

(a) PCC Properties (NCR_Unrein)

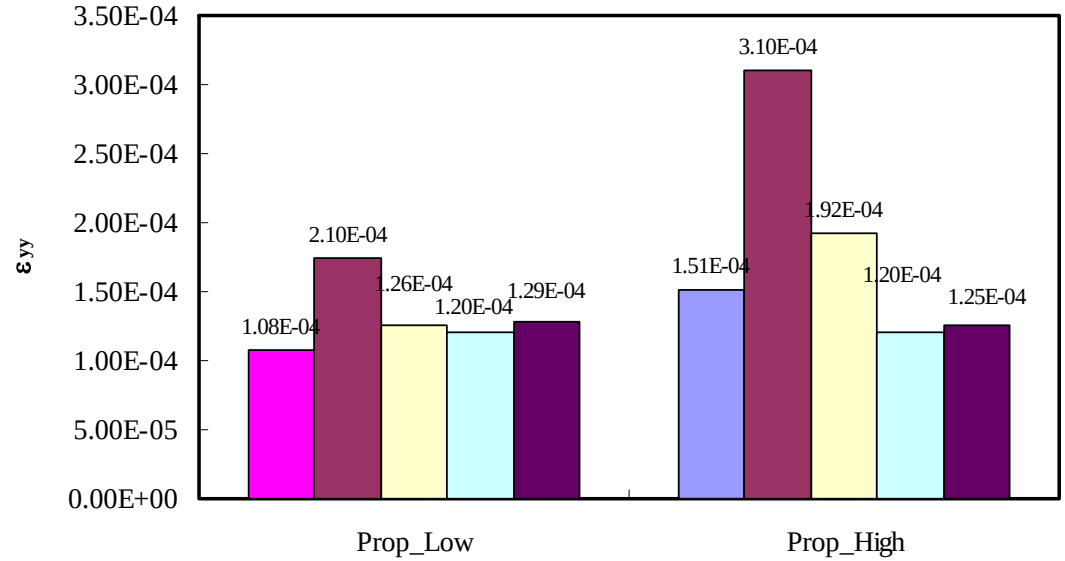

(b) PCC Properties (NCR_Rein)

Figure 5.57 Vertical strain distributions at the bottom of overlay

5.4.1.2 Stresses and Porosity

To further investigate the effect of the two different PCC properties used in this study, stress curves were determined and combined for comparison. Results for stress distribution at the bottom of unreinforced overlay are presented in Figures 5.58 to 5.60. Figure 5.58 shows that maximum horizontal stress is developed in the middle of the overlay in both cases. Also, stresses in the PCC with low modulus are higher than those in the PCC with high modulus. Analysis indicates that horizontal stress is decreased by around 230 kPa. However, vertical stress behavior is not like that of horizontal stress. As shown in Figure 5.59, in the middle of the overlay, vertical stresses in PCC with high modulus are relatively higher than those in PCC with low modulus, but the reverse is true at both sides of the overlay. Analysis indicates an increase of vertical stress of around 115 kPa in PCC with high modulus, which is related to the vertical strain behavior explained before. Figure 5.60 shows the combined results for shear stress distribution. Unlike horizontal and vertical stress behaviors, negative stresses are converted to positive ones through the middle of the overlay. Maximum stresses are shown at right before and after mid-point of overlay. Results show that stresses in PCC with high modulus are relatively smaller than those in PCC with low modulus, but the values are small when compared with horizontal and vertical stresses.

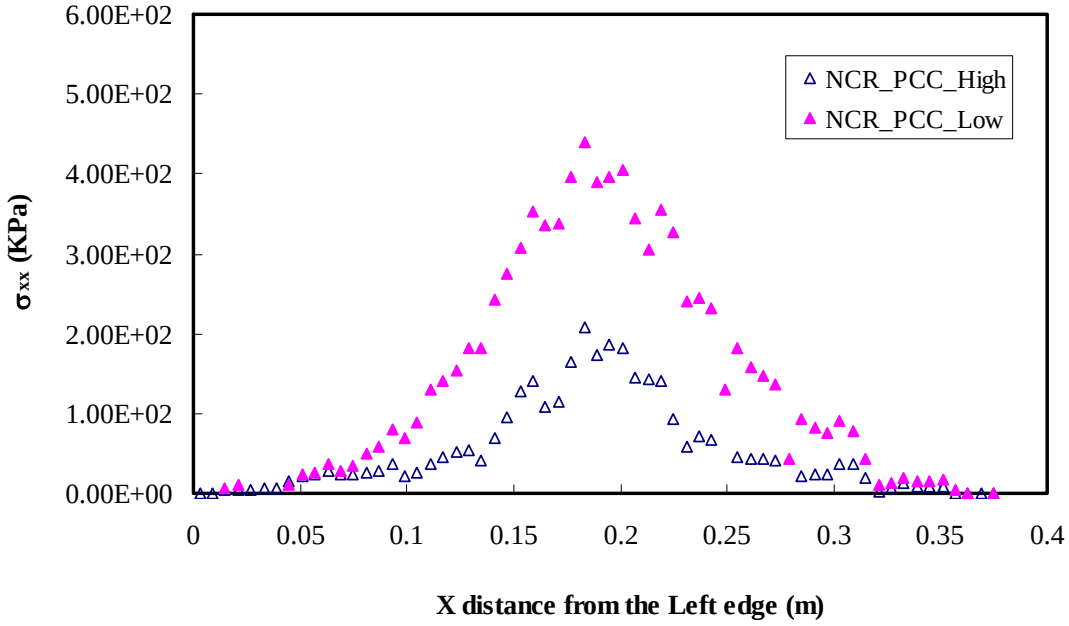

Figure 5.58 Horizontal stress distributions according to PCC properties for unreinforced overlays

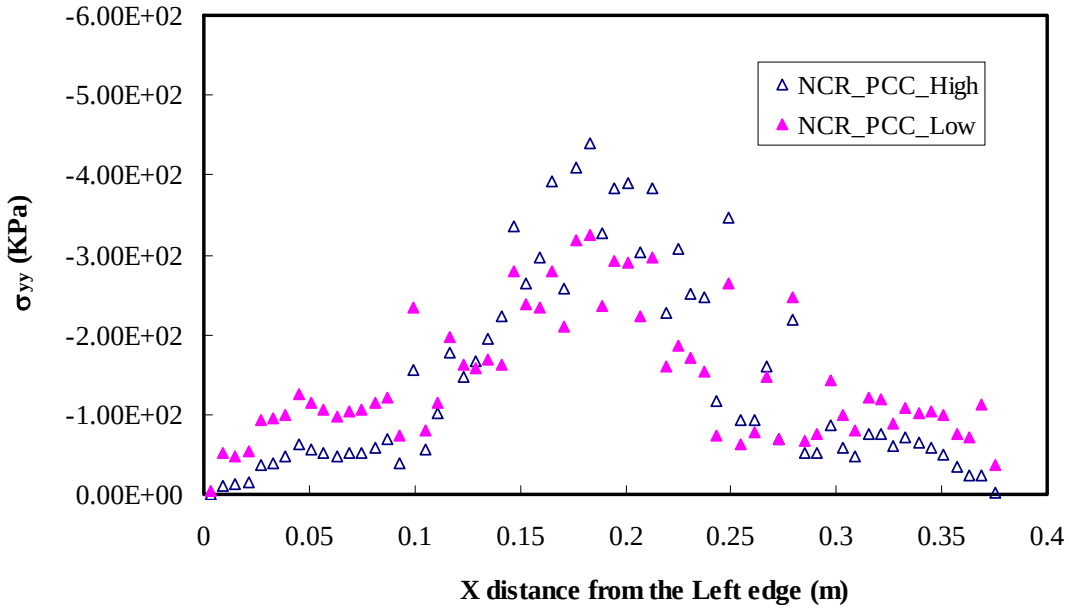

Figure 5.59 Vertical stress distributions according to PCC properties for unreinforced overlays

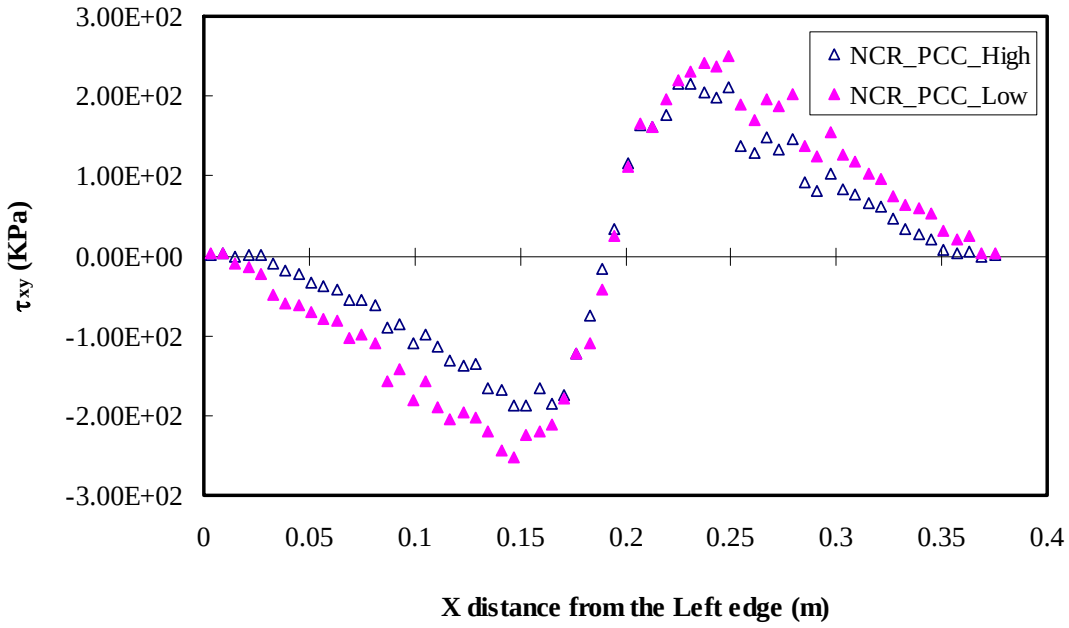

Figure 5.60 Shear stress distributions according to PCC properties for unreinforced overlays

Analysis results for stress distribution at the bottom of reinforced overlay are presented in Figures 5.61 to 5.63. Stress behaviors are generally similar to those of reinforced overlays except for the maximum values. Figure 5.61 shows that maximum horizontal stress is developed in the middle of overlay in both cases. Stresses in PCC with low modulus are higher than those in PCC with high modulus. Analysis indicates that, with reinforcement, maximum horizontal stress is decreased by around 13 kPa, compared to overlay without reinforcement. However, tensile stress is increased by 140 kPa when reinforcement is in place. This corresponds with tensile strain, and results in increased displacement. Figure 5.62 shows the vertical stress behavior. As in the case of unreinforced overlay, vertical stresses in the middle of the overlay are relatively higher in PCC with high modulus than those in PCC

with low modulus. Figure 5.63 shows the combined results for shear stress distribution analyses. Shear stress behavior is the same as in unreinforced overlay. Results show that shear stresses in PCC with high modulus are relatively smaller than those in PCC with low modulus, but the differences are relatively small when compared with horizontal and vertical stresses.

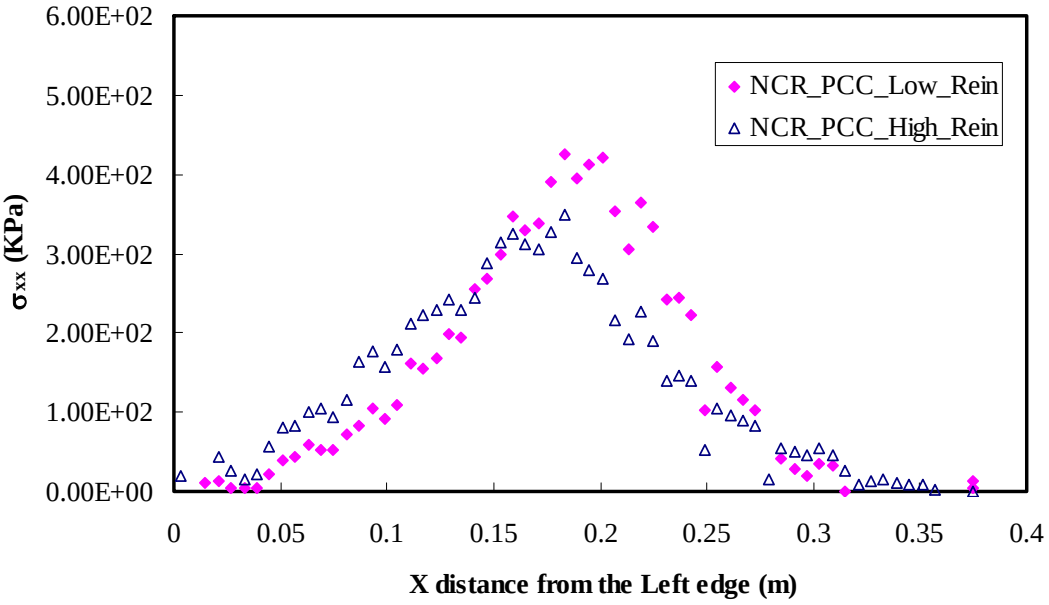

Figure 5.61 Horizontal stress distributions according to PCC properties for reinforced overlays

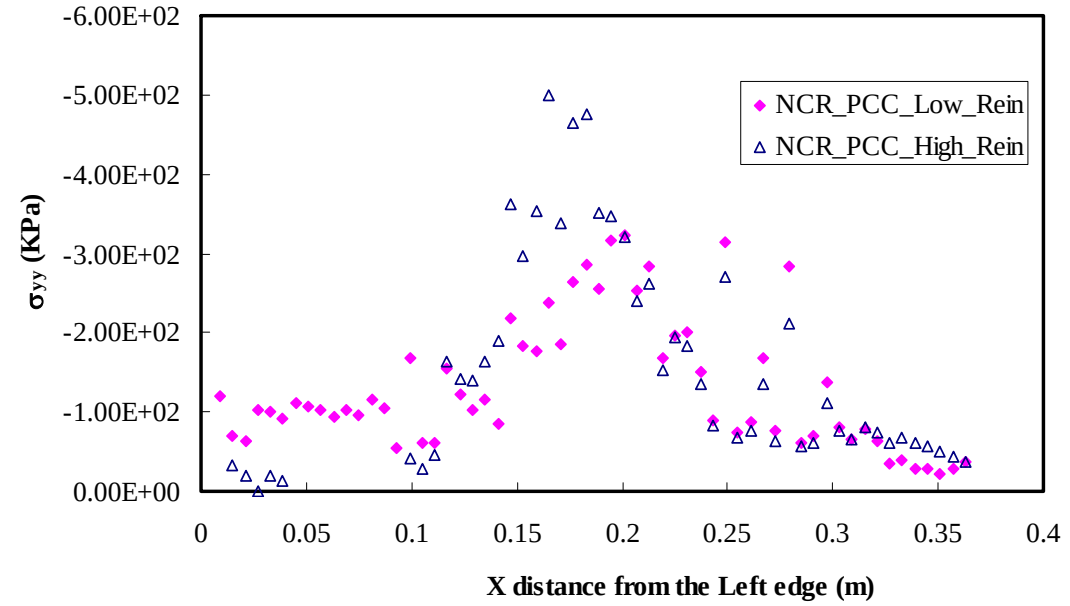

Figure 5.62 Vertical stress distributions according to PCC properties for reinforced overlays

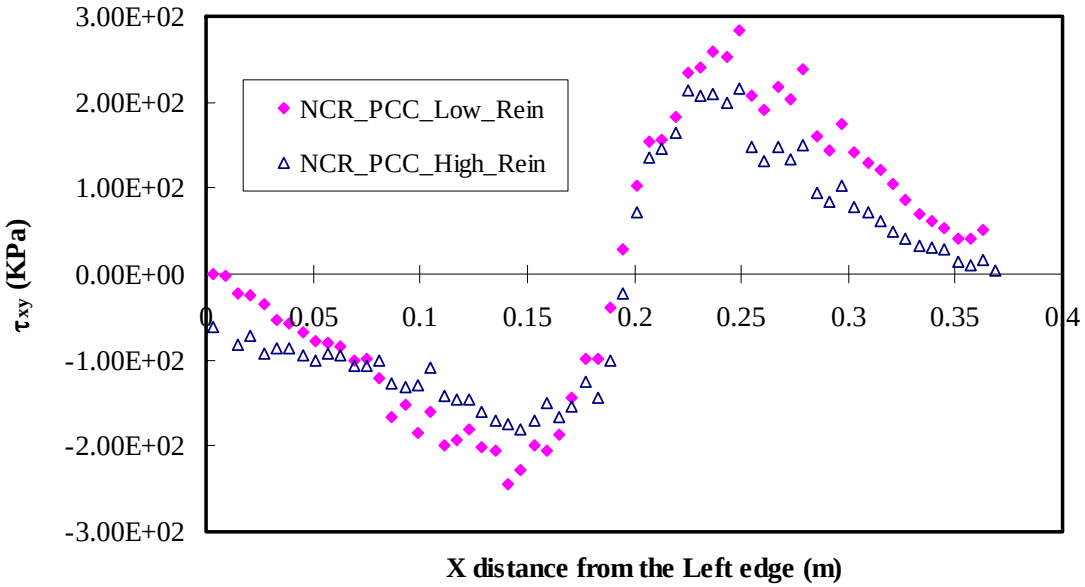

Figure 5.63 Shear stress distributions according to PCC properties for reinforced overlays

The stress contours of vertical, horizontal, and shear stress for the unreinforced overlay are presented in Figure 5.64. Because high modulus PCC means having a soft overlay, thus, result in more vertical stress in overlay. in other hand, low modulus PCC stands for having a stiff overlay, therefore, leads to less vertical stress in overlay. In the case of PCC with low modulus, the vertical stress contour is more widely distributed than in high-modulus PCC, which is more concentrated in the middle. Shear stress contours show that the left section of overlay is governed by negative but positive value exists mostly on the right. Moreover, the contour for low modulus PCC is widely distributed and shows relatively higher stress, compared with high modulus PCC. The stress contours for reinforced overlay are shown in Figure 5.65. Horizontal stress contours show that focused stresses appear at the top and the bottom of the overlay, and higher stresses are shown in PCC with low modulus. In addition, reinforced overlay displays more concentrated tensile stress contours compared with unreinforced overlay, which is in accordance with horizontal strain results. As in the unreinforced overlay, vertical contours in PCC with low modulus are distributed more widely and lower stresses are shown in the middle compared with high-modulus PCC. Shear stress values are relatively higher throughout the whole layer for PCC with low modulus than those of PCC with high modulus.

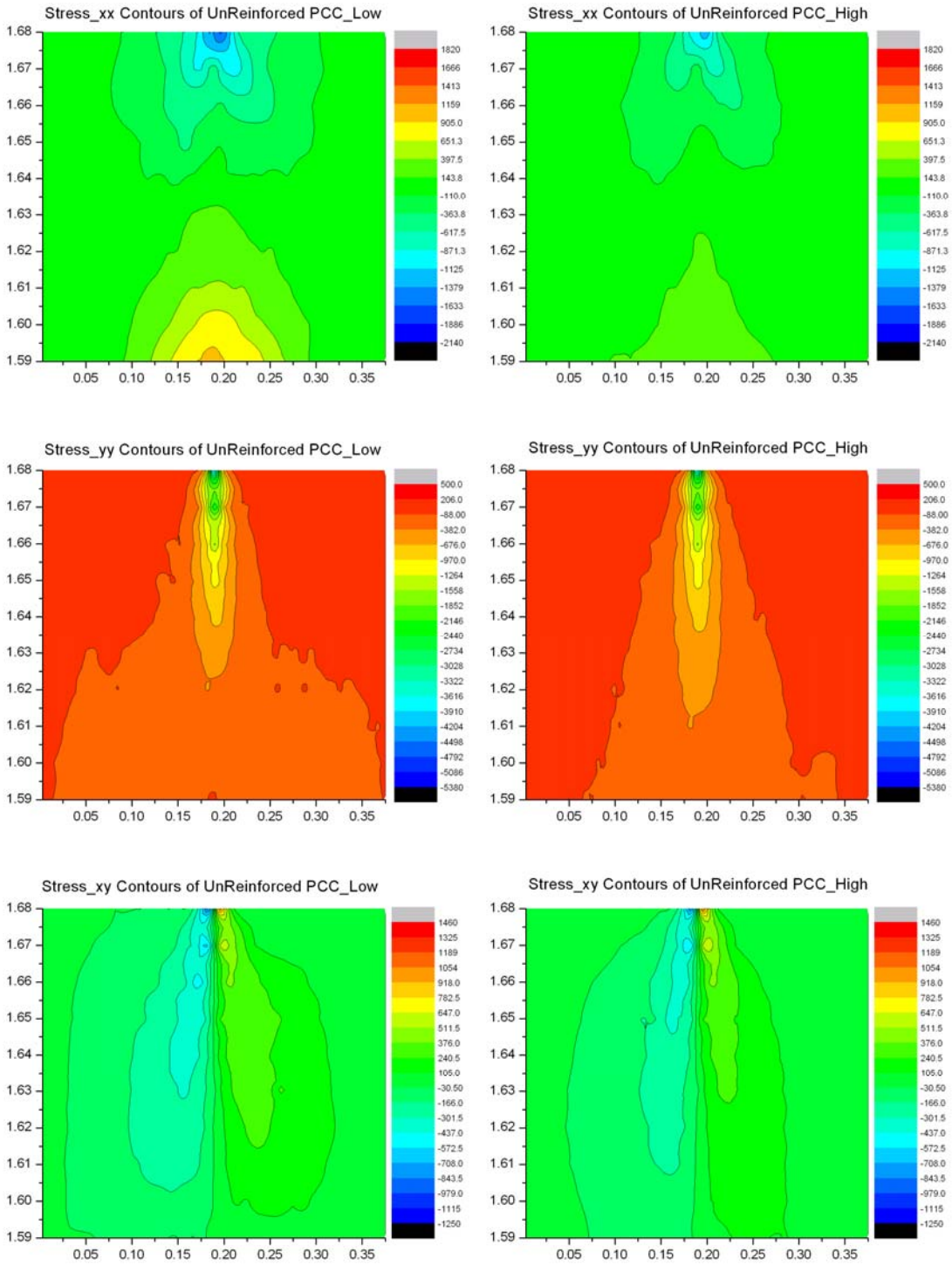

Figure 5.64 Stress contours according to PCC properties without reinforcement

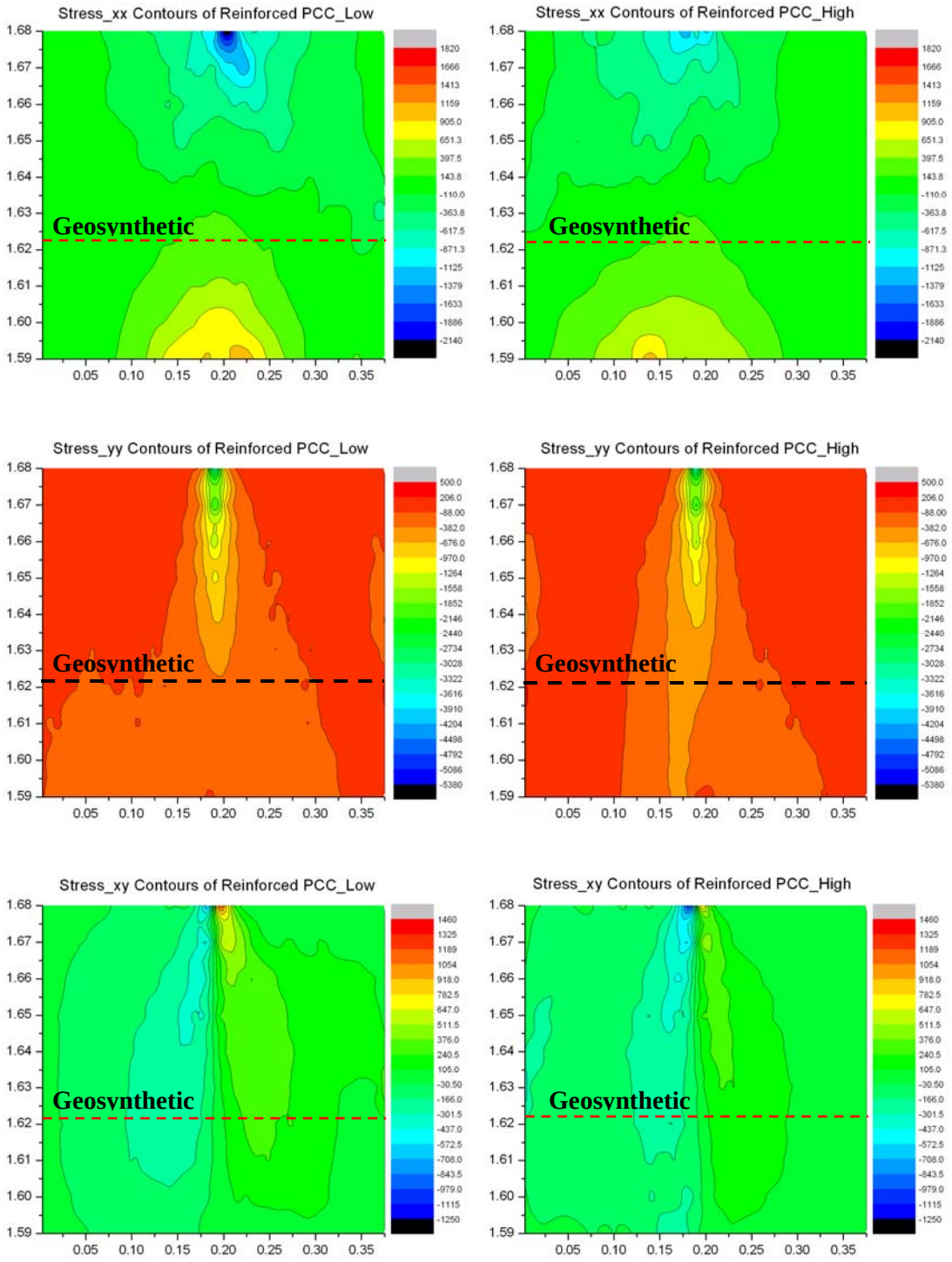

Figure 5.65 Stress contours according to PCC properties with reinforcement

Figure 5.66 shows the porosity contours without reinforcement. Both porosities are scaled by ranging from 0.1915 to 0.1921. These contours show that porosity in low-modulus PCC changes mostly in the middle and is lower than that of high-modulus PCC, which corresponds with displacement results.

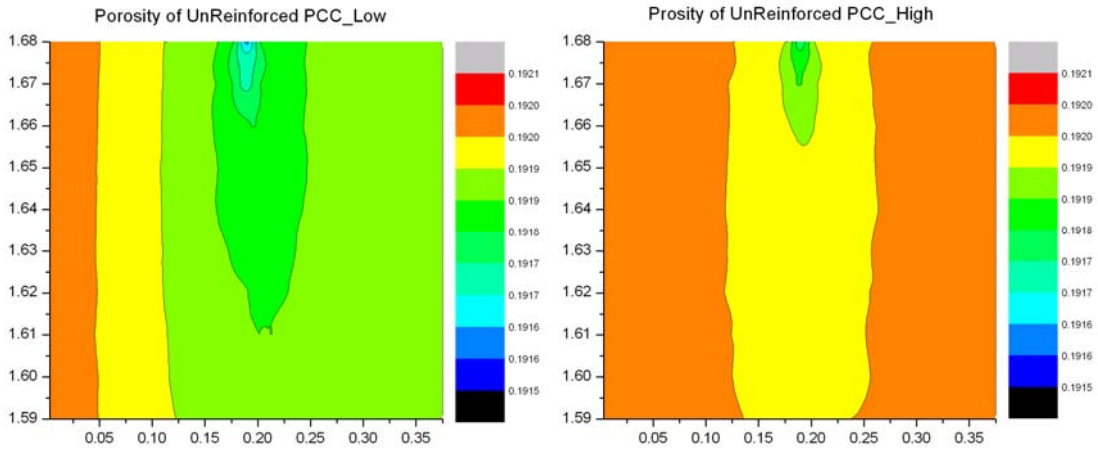

Figure 5.66 Porosity of according to PCC properties without reinforcement

In addition, the porosity contours with reinforcement are displayed in Figure 5.67. Both porosities are ranged from 0.1870 to 0.1940. Analysis indicates that porosity with reinforcement shows more change around the bottom of the overlay and beneath the reinforcement when compared with unreinforced overlay, thus resulting in more displacement. This is accordance with displacement results.

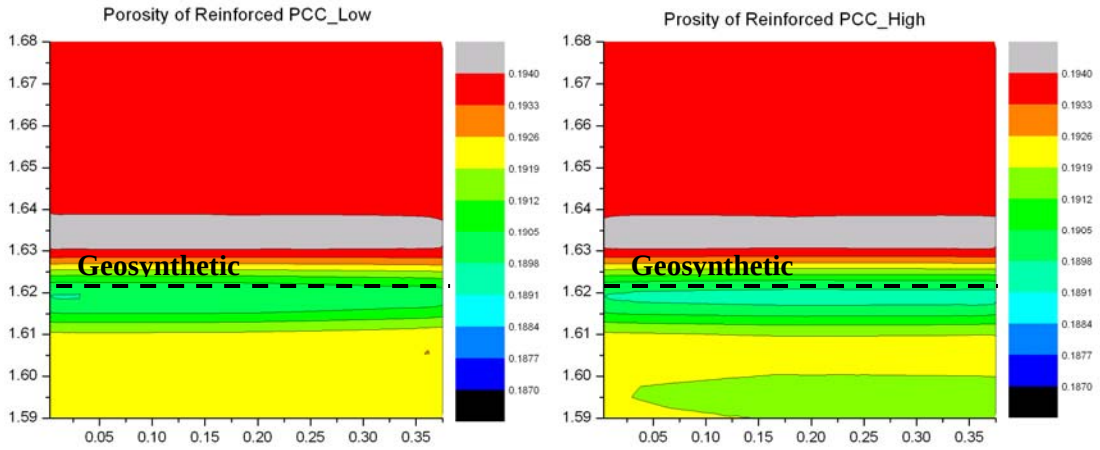

Figure 5.67 Porosity of according to PCC properties with reinforcement

5.4.2 Effect of PCC crack width

5.4.2.1 Displacement and Strain

Unreinforced and reinforced sections with different gap intervals in the PCC layer are made to simulate the effect of an existing crack or joint. Three crack widths are selected: 12 mm, 18 mm, and 24 mm. Total displacement on the top pavement section is obtained according to the width of the concrete gap, as shown in Figure 5.68. Analysis shows that displacements for the 12 mm and 18 mm crack widths are not significantly different and there is an increase of only 1 mm with the 24 mm gap. All displacements are reduced when geosynthetic reinforcement is embedded in the AC overlay.

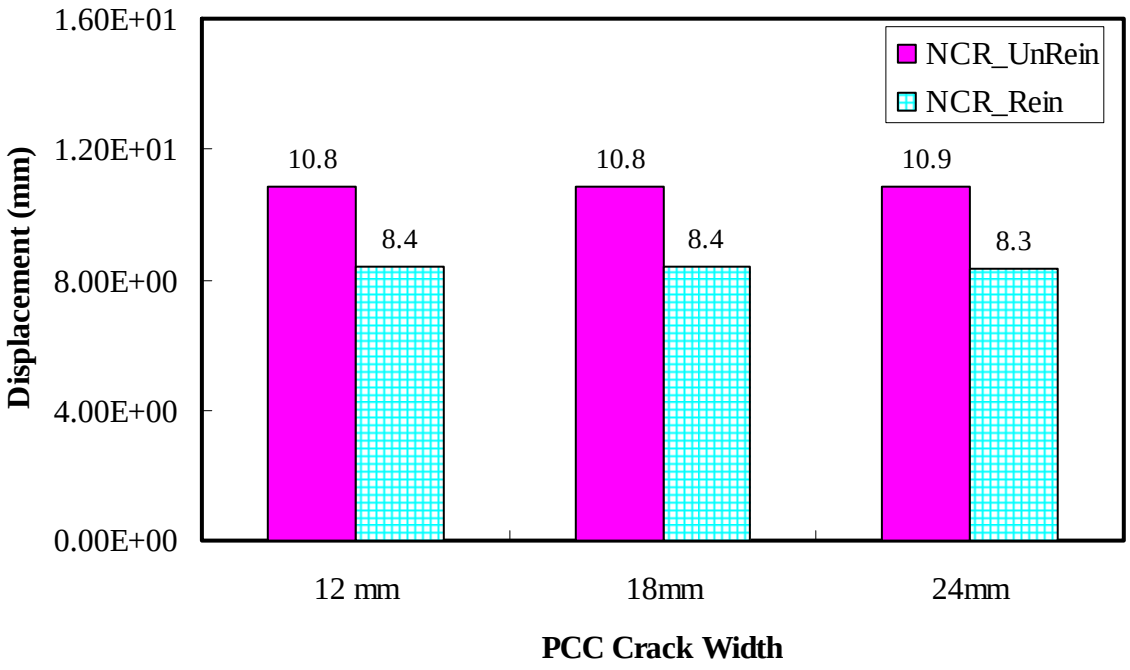

Figure 5.68 Displacement on the top varying with PCC crack widths with and without reinforcement

Figure 5.69 shows tensile strains at the bottom of overlay for varying PCC crack widths without reinforcement. Strain distributions take the shape of an arch in all cases. As the width of the gap in the PCC increases, lateral strain also increases. Analyses indicate that increasing crack widths of 18 mm and 24 mm lead to increase lateral strain by around 2% to 6% for unreinforced overlay. Tensile strains with reinforcement are presented in Figure 5.70. Analyses indicate that increasing crack widths of 18 mm and 24 mm again lead to increased lateral strain, but by around 3% to 5%, as lateral strain is decreased when a geosynthetic is placed in the AC overlay. It can be explained that as the width of a crack or joint increases, stresses are more concentrated around it and consequently, more lateral strain occurs.

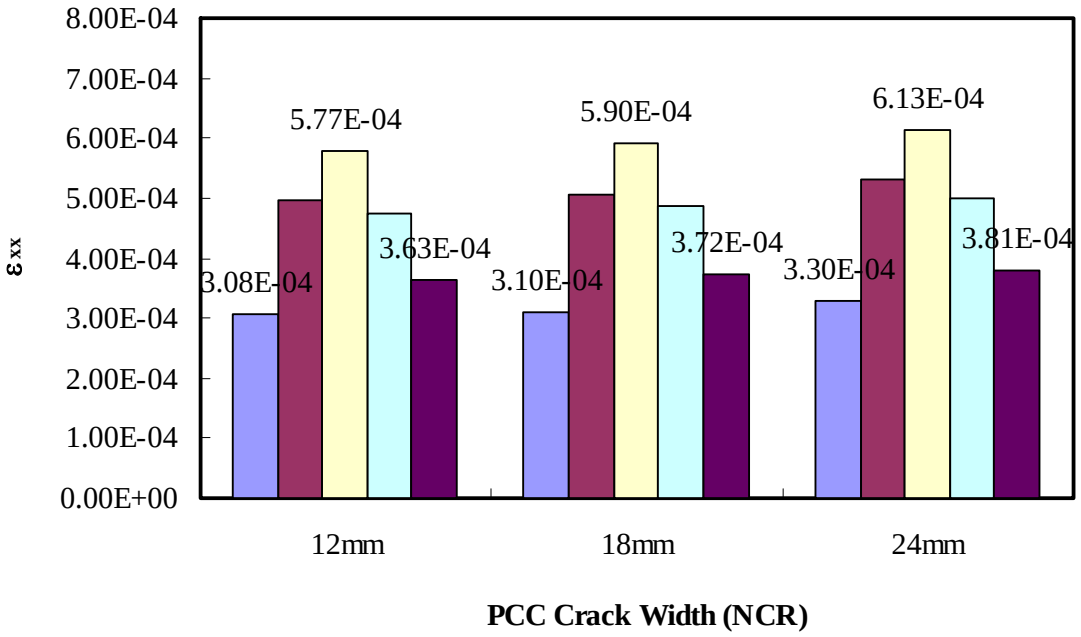

Figure 5.69 Strain distributions according to PCC crack widths without reinforcement

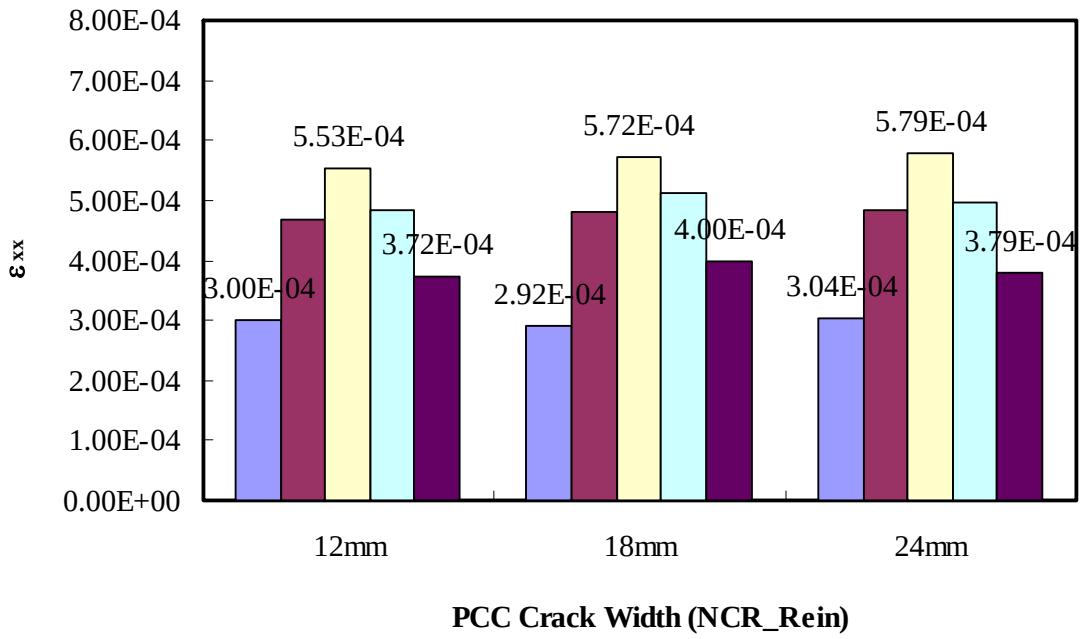

Figure 5.70 Strain distributions according to PCC crack widths with reinforcement

5.4.2.2 Stresses and Porosity

Combined results for horizontal stresses at the bottom of the overlay are presented in Figure 5.71. Maximum stress can be seen around 0.2 m from the left edge of overlay. And analyses indicate that maximum horizontal stress increases from 101 kPa to 111 kPa as the gap interval increases from 12 mm to 24 mm. Combined results for vertical stresses are shown in Figure 5.72. Higher stress is shown where the PCC crack is larger. However, unlike horizontal stress, vertical stress is reduced to tension above the PCC crack. This behavior is similar to that in an overlay layer with initial crack; therefore, a crack in the PCC layer affects stress behavior. Combined results for shear stresses are presented in Figure 5.73. Most stresses are not notably different, though a difference in stress appears above the PCC crack. As with horizontal stress, the maximum stress of (-) 106 kPa is obtained from the 24 mm gap and differences among three cases are not significant.

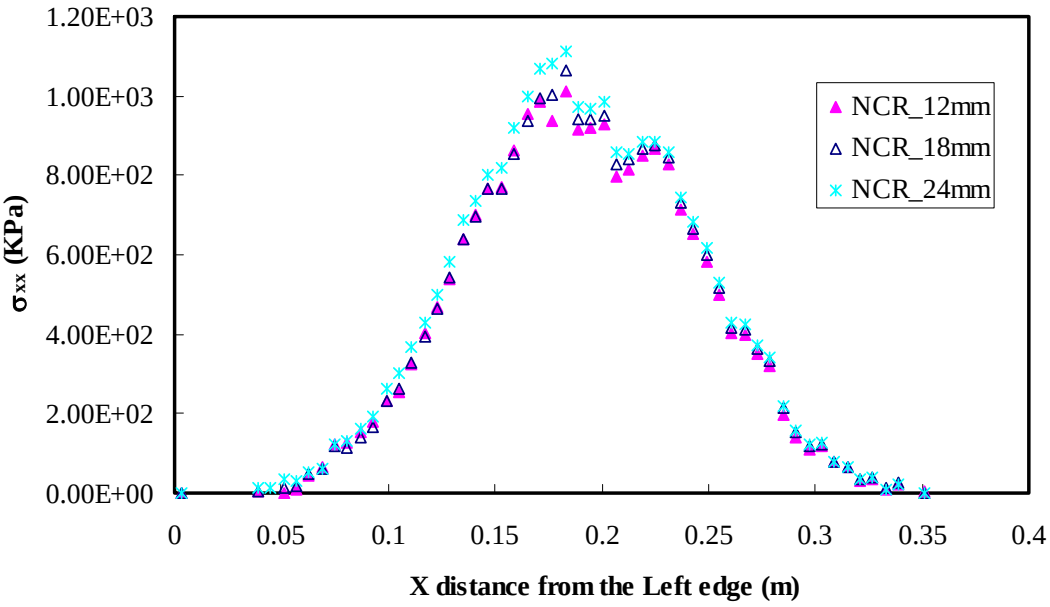

Figure 5.71 Horizontal stress distributions according to PCC crack widths without reinforcement

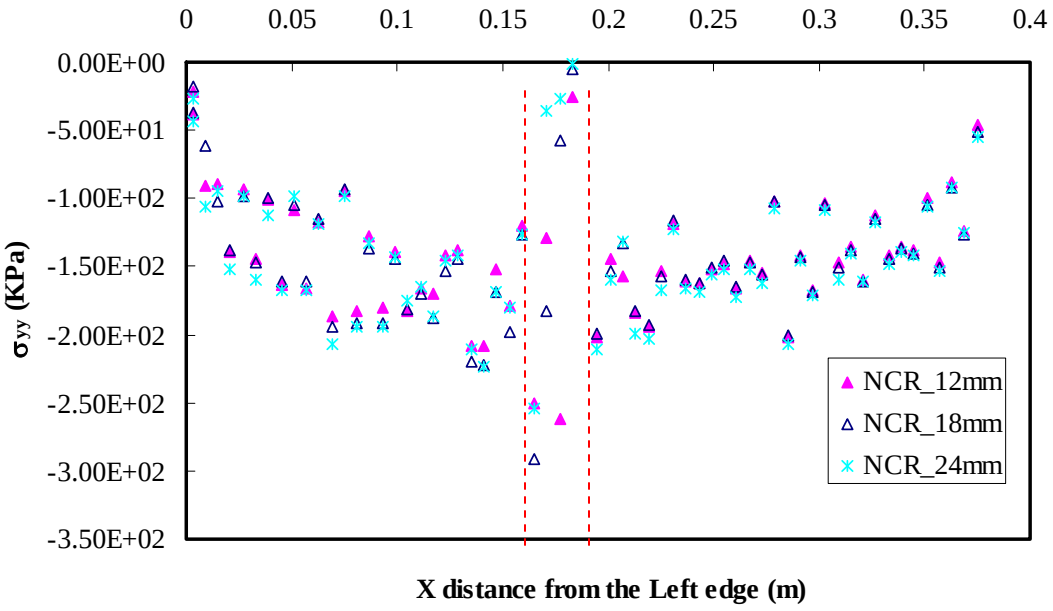

Figure 5.72 Vertical stress distributions according to PCC crack widths without reinforcement

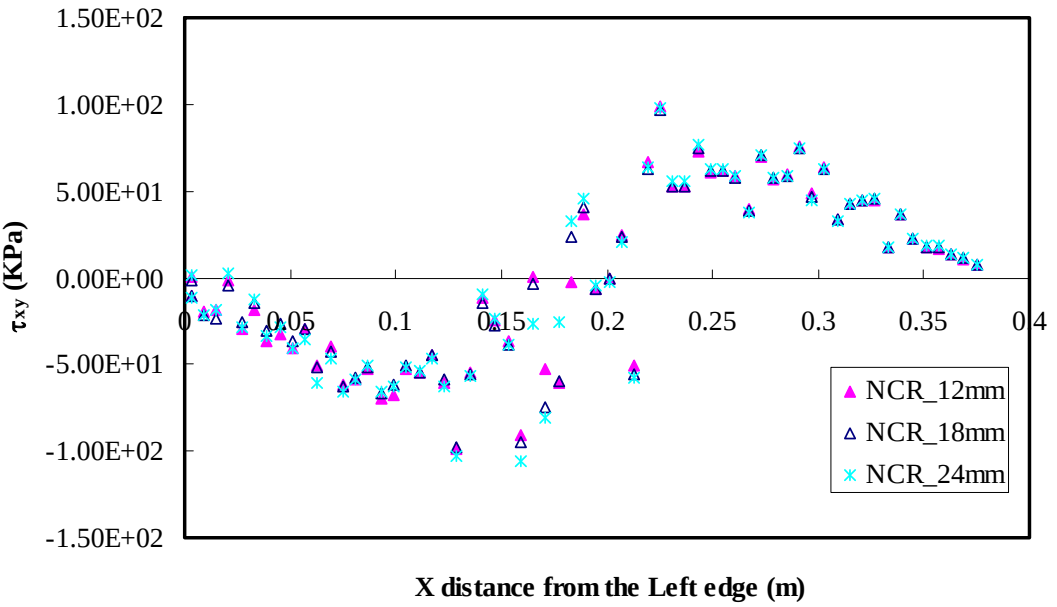

Figure 5.73 Shear stress distributions according to PCC crack widths without reinforcement

Combined stress distributions according to PCC crack widths, with reinforcement, are presented in Figures 5.74 to 5.76. All stresses are measured beneath the reinforcement instead of at the bottom of the overlay. Stress behaviors are similar to those observed where there is no reinforcement. Analyses indicate that maximum horizontal stress increases from 496 kPa to 530 kPa as the gap interval increases from 12 mm to 24 mm (Figure 5.74). However, the order of vertical stresses is changed above the PCC crack, as seen in Figure 5.75, because the crack in the PCC layer affects the stress field. Also, higher stress is shown in the case of the 24 mm gap even though the change of shear stress is minor as seen in Figure 5.76.

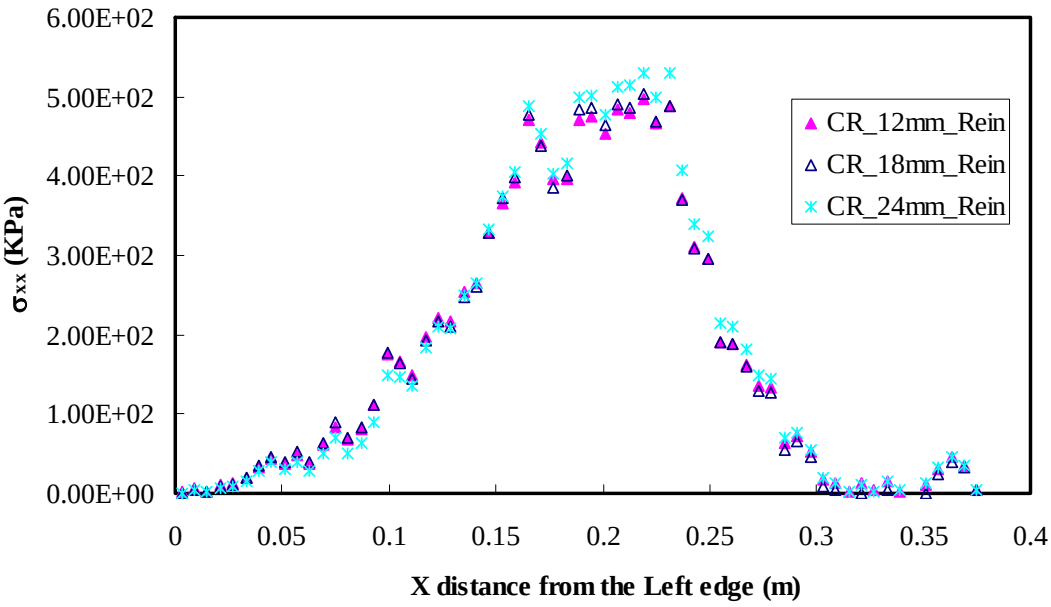

Figure 5.74 Horizontal stress distributions according to PCC crack widths with reinforcement

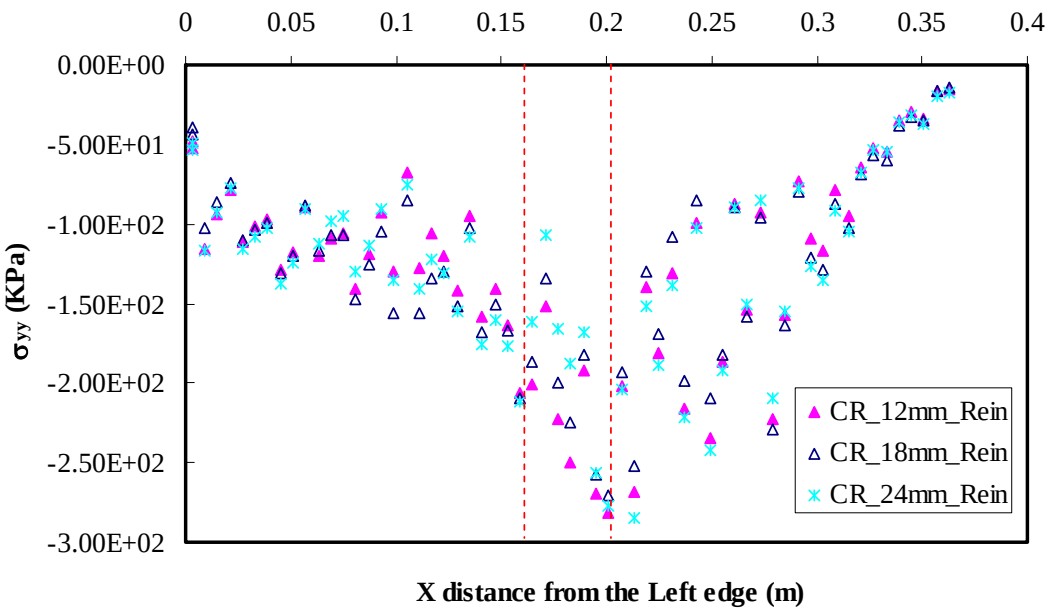

Figure 5.75 Vertical stress distributions according to PCC crack widths with reinforcement

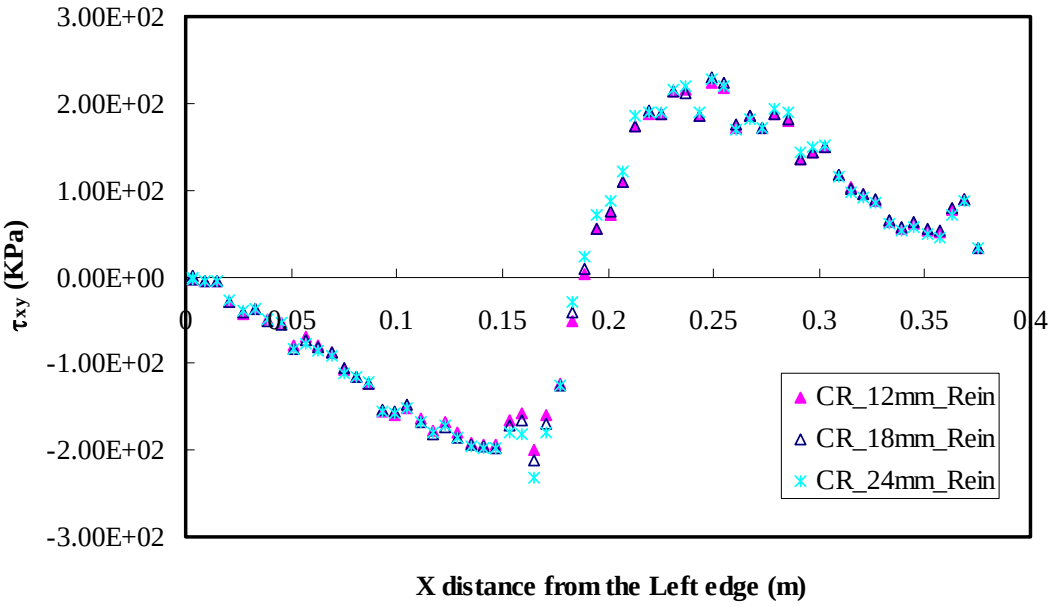

Figure 5.76 Shear stress distributions according to PCC crack widths with reinforcement

The stress contours of vertical, horizontal, and shear stress for the whole overlay, with and without reinforcement, are presented in Figures 5.77 to 5.79. For horizontal stress, as shown in Figure in 5.77, contours show that stresses are focused in the top and bottom of the overlay, and reinforcement affects the right side of the overlay. In addition, as the PCC cracks widen, stresses are also increased at the bottom of the overlay. Stress is relatively higher at the bottom of the overlay without reinforcement than it is with reinforcement, but it is lower than stress observed at the top of reinforced overlay. Vertical stress contours are presented in Figure 5.78. Stress contours without and with reinforcement are similar for the three different gap widths, except for a marginal difference at the bottom as pointed out with a dotted circle. As the crack is getting larger, this difference is also getting larger. Also, stress is higher without reinforcement than with reinforcement. Figure 5.79 shows the shear stress contours. Stress contours without and with reinforcement seem to be similar for the three different gaps. The greatest differences between the reinforced and unreinforced cases are shown at the top of the overlay. Higher shear stress shows on the left side of unreinforced overlay and on the right side of reinforced overlay.

In addition, Figure 5.80 shows the porosity contours according to the three different PCC crack widths, without and with reinforcement. For unreinforced overlays, porosity is scaled from 0.1915 to 0.1921. This contour shows that porosity change in the middle section of overlay increases as crack width gets larger. For reinforced overlay, porosity ranges from 0.1875 to 0.1934. This contour shows that porosity changes occur mostly under the reinforcement and are intensified by increasing crack width.

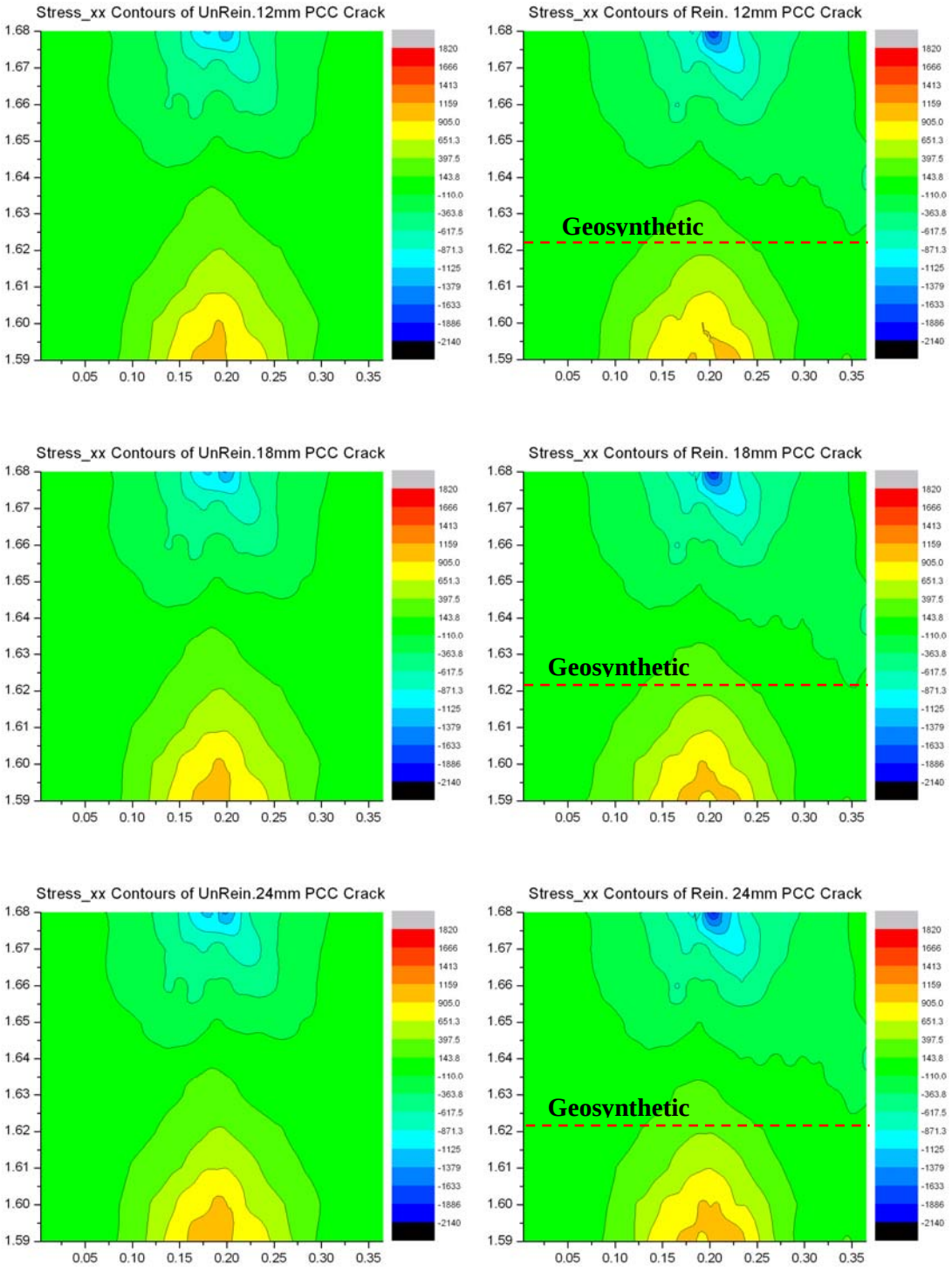

Figure 5.77 Horizontal stress contours according to PCC crack widths

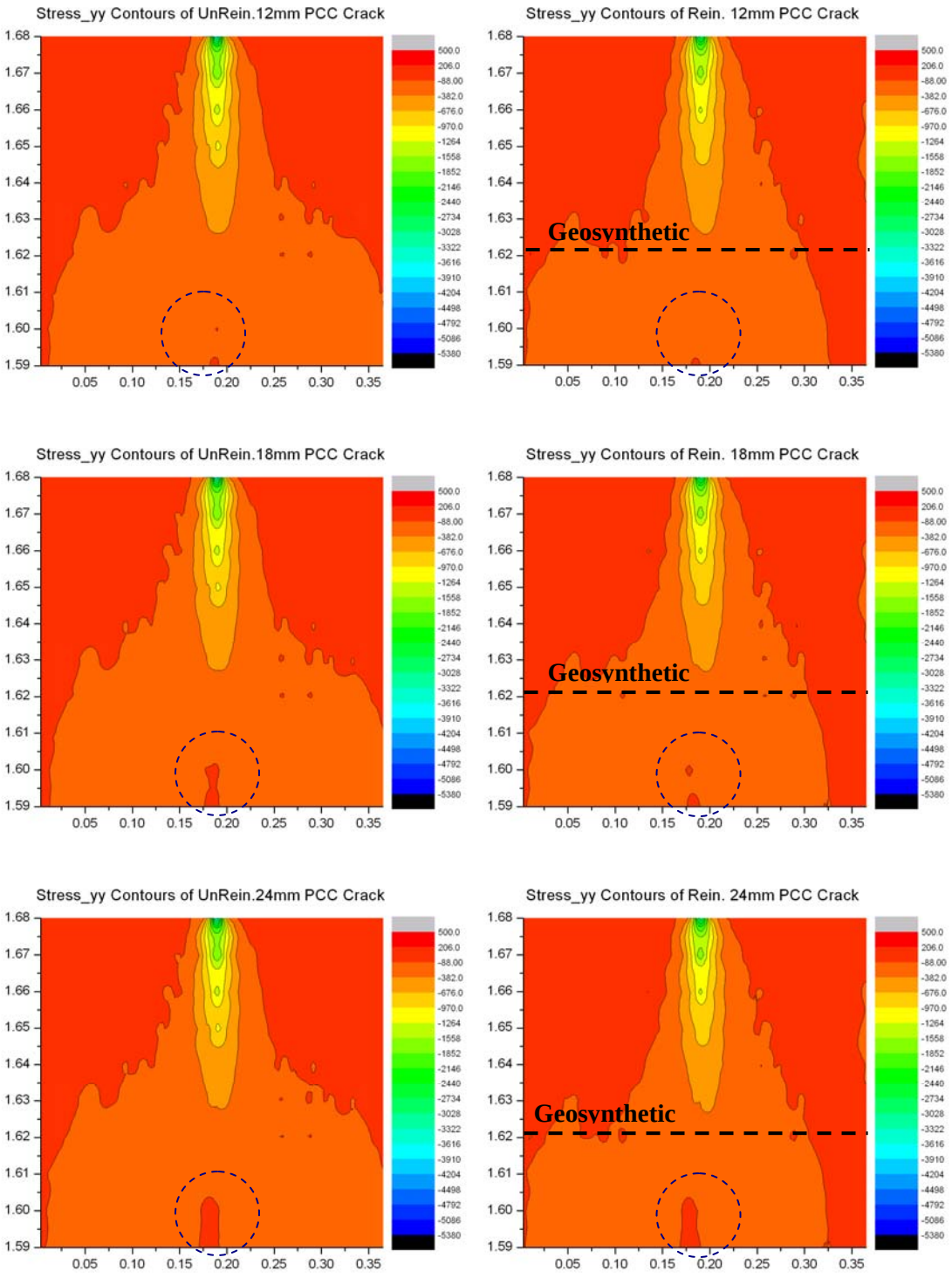

Figure 5.78 Vertical stress contours according to PCC crack widths

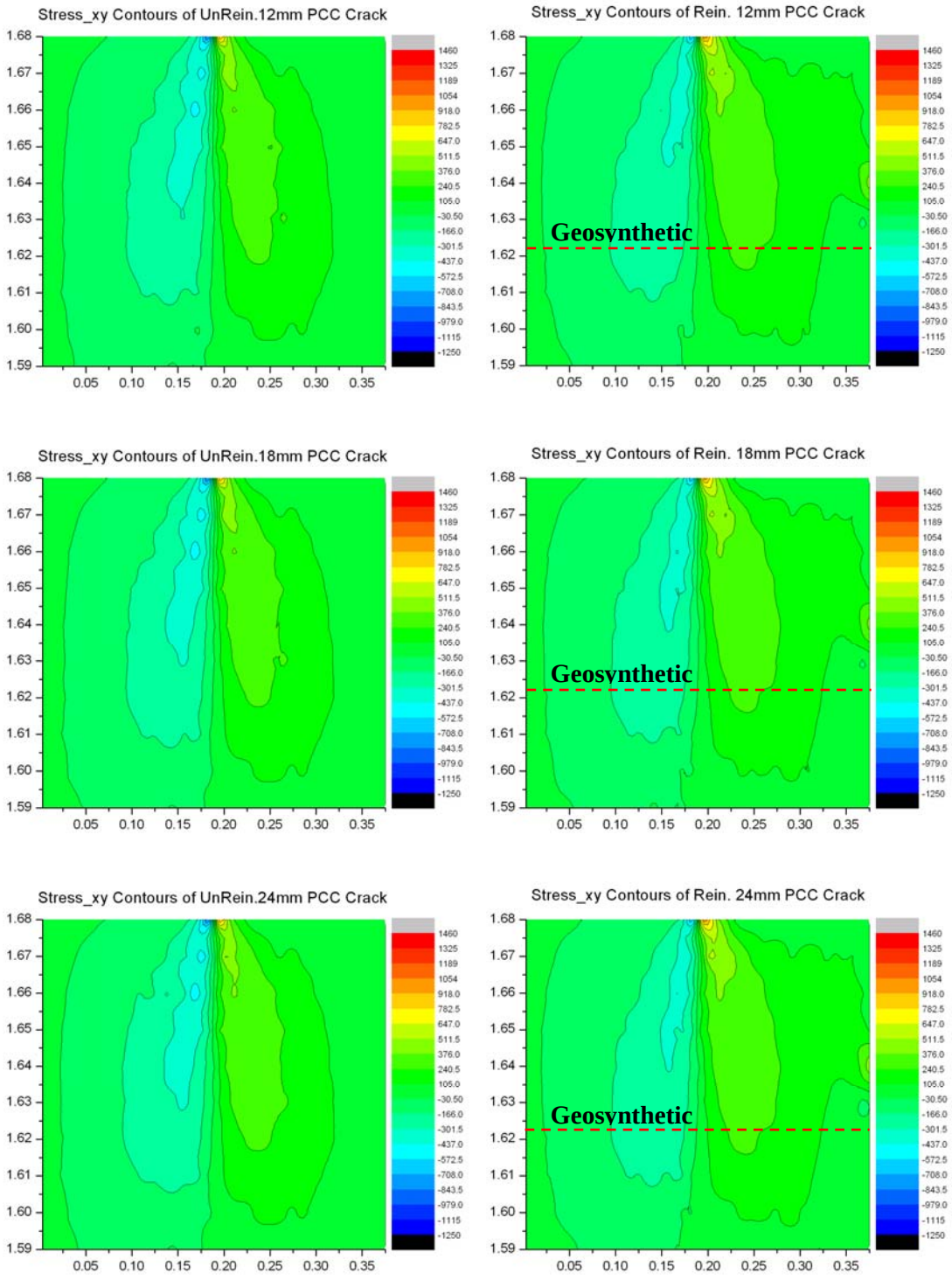

Figure 5.79 Shear stress contours according to PCC crack widths

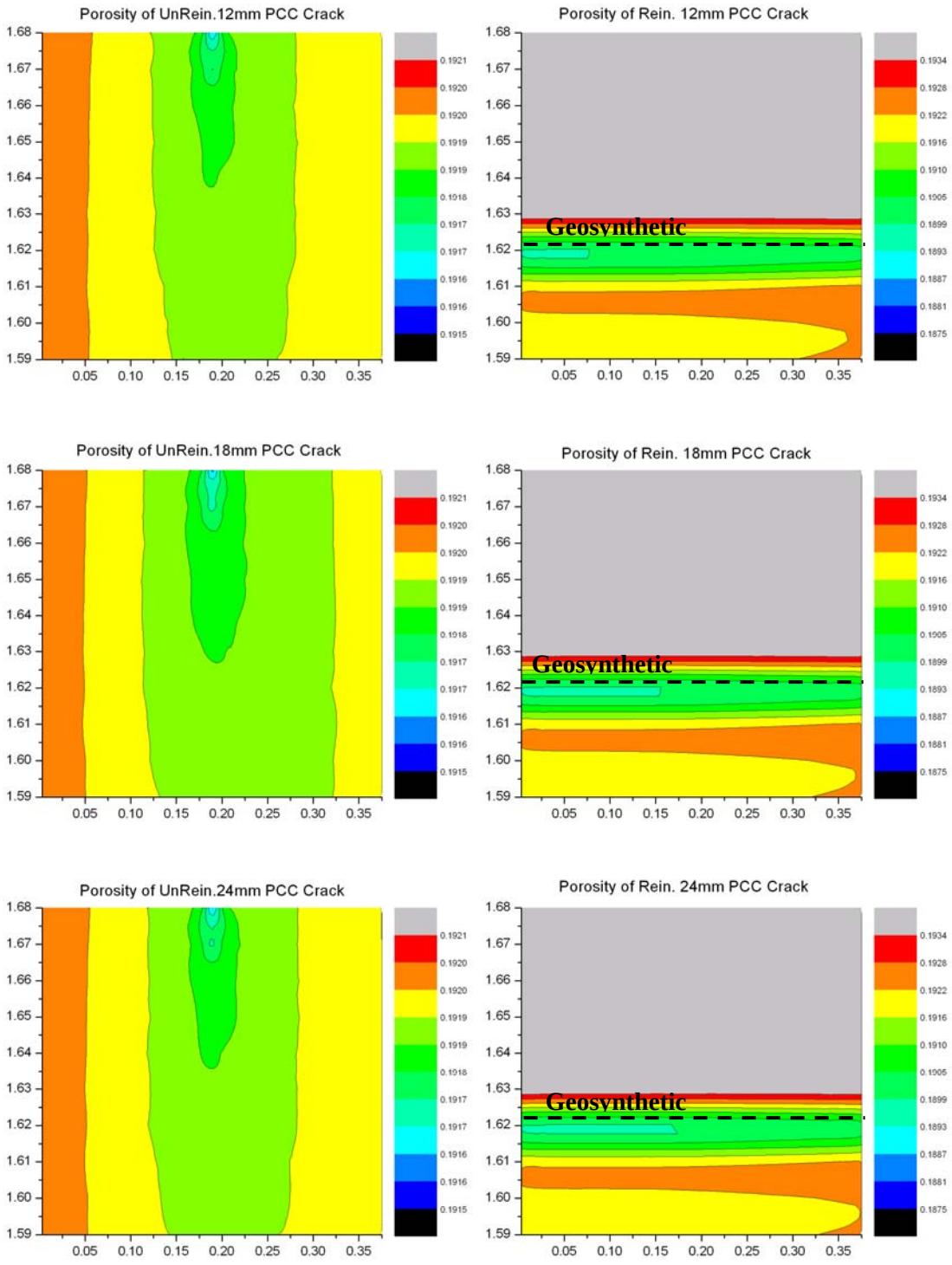

Figure 5.80 Porosity contours according to PCC crack widths

5.5 Effect of Overlay Thickness

5.5.1 Effect of Reinforcement

5.5.1.1 Displacement and Strain

One of the effective ways to minimize reflective cracking is to increase overlay thickness. To investigate the effect of overlay thickness, three cases – 3", 4", and 6" – of overlay thickness are used, with and without reinforcement. Geosynthetic is embedded at 1/3H of each overlay (where H equals total overlay thickness, from the bottom up) and an initial crack is inserted. The results of displacement analyses according to the three different overlay thicknesses, without and with reinforcement, are presented in Figure 5.81. Displacement numbers for the 3" (75 mm) and 4" (100 mm) overlays without reinforcement are the same at 10.9 mm, while the 6" (150 mm) overlay showed displacement of 11.1 mm; thus, thicker overlay causes more pavement deflections. With reinforcement, displacements for the 3" (75 mm), 4" (100 mm), and 6" (150 mm) overlays are 8.46 mm, 8.48 mm, and 8.50 mm, respectively; thus, displacement is reduced as a benefit of geosynthetic reinforcement. Because the differences in displacement among the three thicknesses of overlay are very small, they do little to explain the effect of overlay thickness on reflective cracking. However, the effect of overlay thickness becomes more obvious in terms of strain and stress behaviors which are addressed next.

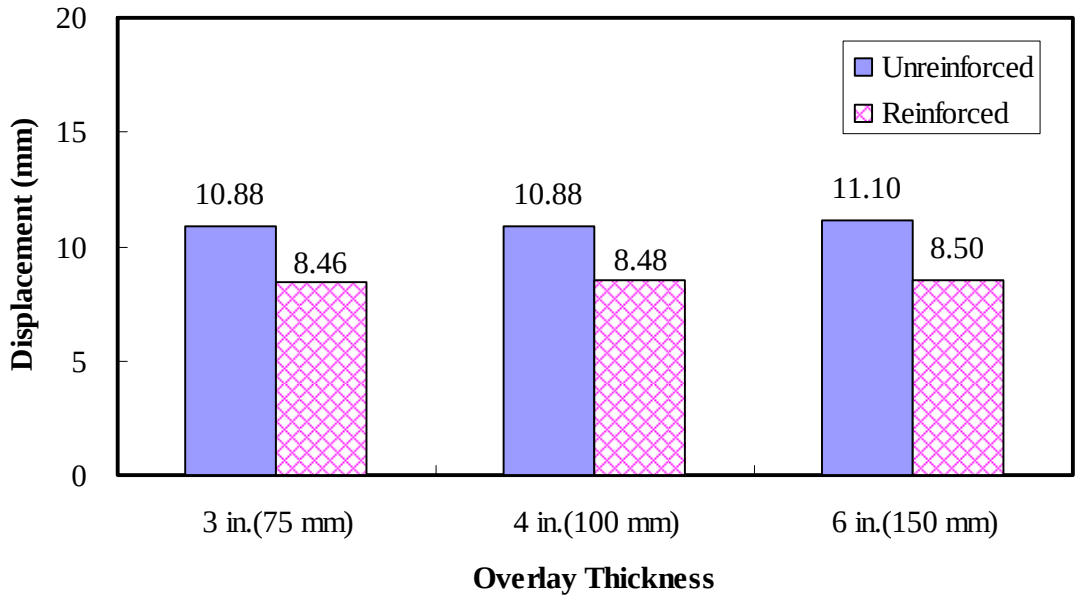

Figure 5.81 Displacement on the top with varying Overlay thickness

Figure 5.82 shows tensile strains at the bottom of the overlay for varying overlay thickness without reinforcement. Strain distributions are shown as arching below the reinforcement. Analyses indicate that when overlay thickness increases to 4" and 6", tensile strain decreases by 73% and 89%, compared with 3" overlay. It appears that the increased overlay thickness also has a strong effect on decreasing the tensile strain at the bottom of the overlay. It can be explained that increased overlay thickness can dissipate the energy generated in the vicinity of the crack tip (Elseifi and Al-Qadi, 2005).

However, except for the 6" overlay, tensile strain is increased when geosynthetic is placed in the overlay, as seen in Figure 5.83. Analyses indicate that when reinforcement is placed in initial-cracked AC overlay, tensile strain increases in the 3" and 4" overlays by 16% and 19%, respectively. As explained before, the use of a soft interlayer causes an

increase in pavement deformations, which leads to larger tensile strain at the bottom of the overlay based on the crack state of stresses (Elseifi and Al-Qadi, 2005). However, with reinforcement, tensile strain in the 6" overlay decreases by 4% compared to without reinforcement. This means that an overlay thickness of 6" is sufficient to avoid premature failure of the pavement through a fatigue-related mechanism. Moreover, it is noted that tensile strains above the reinforcement in 4" and 6" overlay thicknesses are reduced by around 16% and 11%, respectively, as a benefit of the geosynthetic, when compared with strains in unreinforced overlays. This result is presented in Figure 5.84.

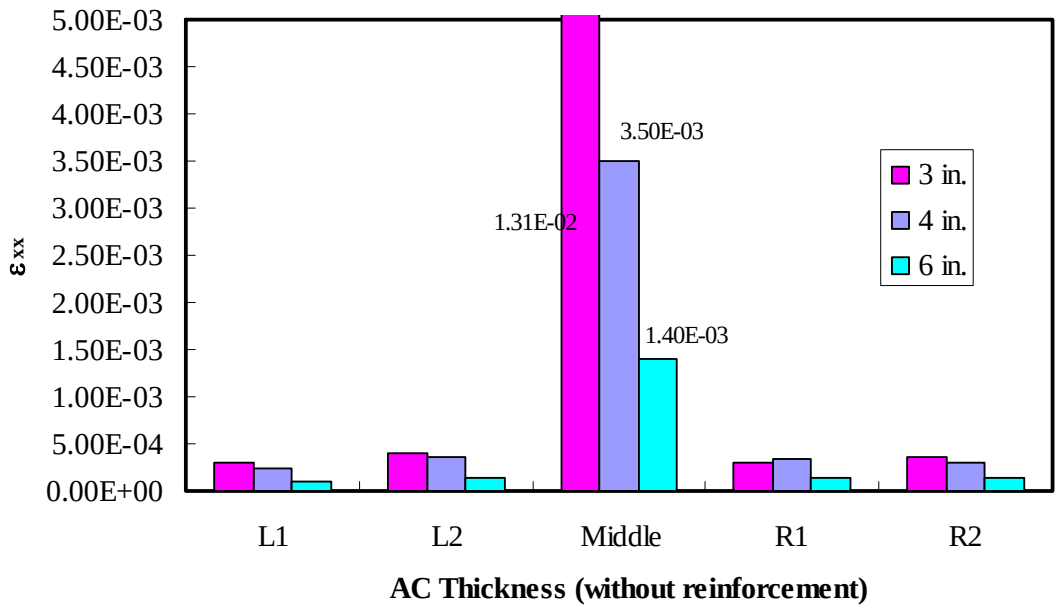

Figure 5.82 Tensile strains at bottom of the unreinforced overlay for different overlay thickness

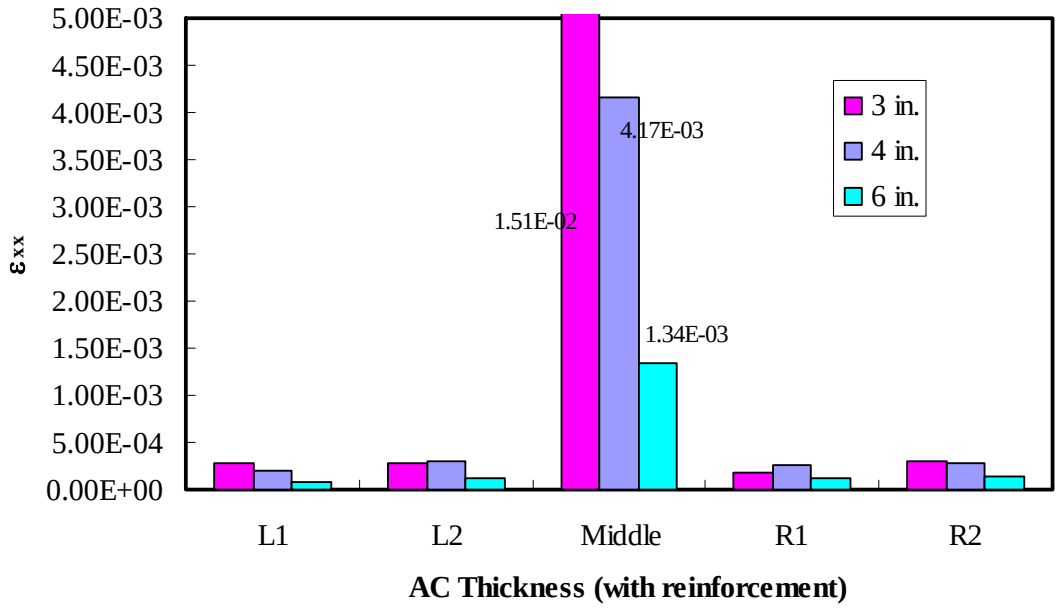

Figure 5.83 Tensile strains at bottom of the reinforced overlay for different overlay thickness

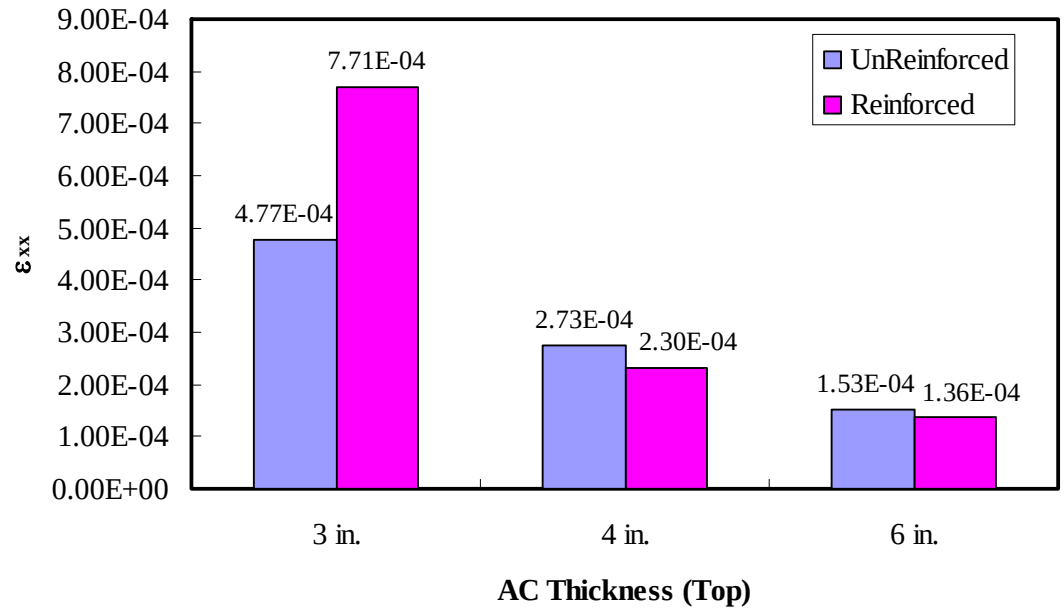

Figure 5.84 Tensile strains over geosynthetic for different overlay thickness

5.5.1.2 Stresses and Porosity

Combined results for horizontal stresses in the vicinity of the crack are presented in Figure 5.85. Analyses indicate that maximum horizontal stresses of 3”, 4”, and 6” overlays are 2,290 kPa, 1,170 kPa, and 437 kPa, respectively thus, horizontal stress decreases more than 80% when the overlay thickness is increased from 3” to 6”. As is the case with strain, increasing the overlay thickness has a strong benefit in reducing horizontal stress. Figure 5.86 combines the results for vertical stresses in the three thicknesses of overlay without reinforcement. Analysis indicates that vertical stresses around the crack in the 3”, 4”, and 6” overlays are 841 kPa, 443 kPa, and 79.3 kPa, respectively; demonstrating a decrease in vertical stress of more than 90% when overlay thickness is increased from 3” to 6”. In addition, results of combined shear stresses are shown in Figure 5.87. Analysis indicates that the maximum shear stresses of the 3”, 4”, and 6” overlays are calculated at 646 kPa, 199 kPa, and 92.4 kPa, respectively. It shows a greater than 80% decrease in shear stress when increasing the overlay thickness from 3” to 6”. Therefore, increasing overlay thickness works to reduce strain and stress as if the overlay were reinforced.

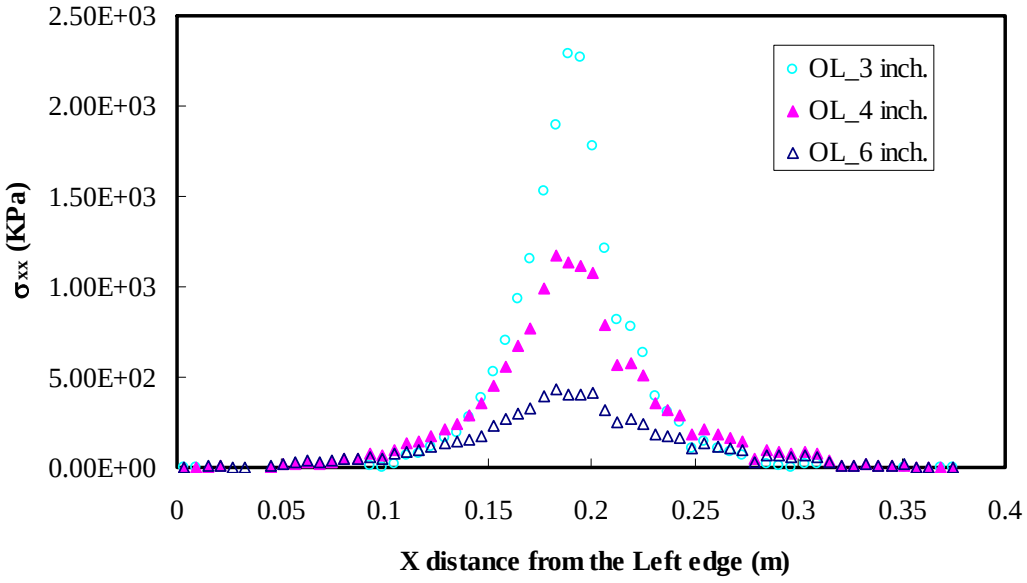

Figure 5.85 Horizontal stress without reinforcement for overlay thickness

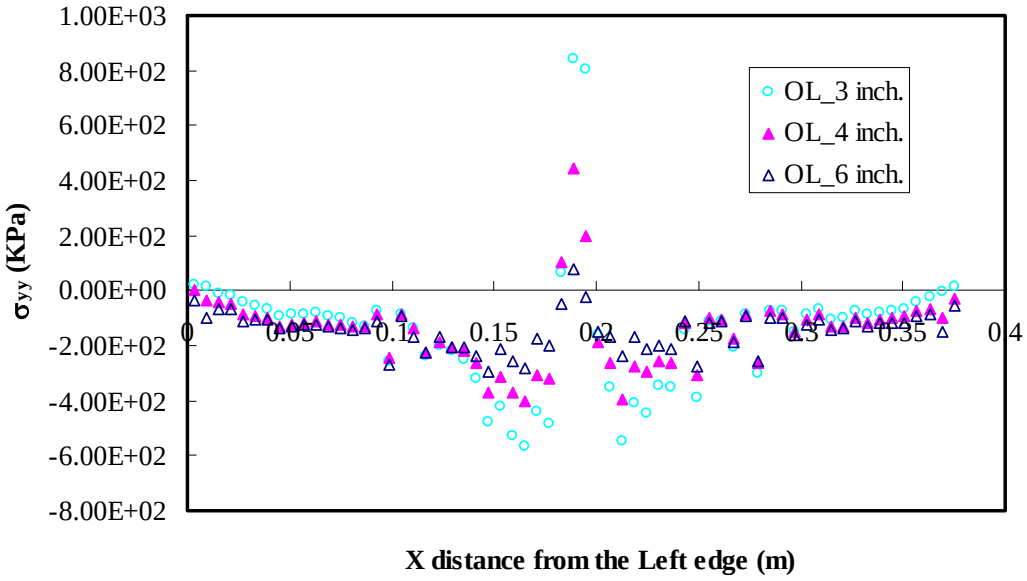

Figure 5.86 Vertical stress without reinforcement for overlay thickness

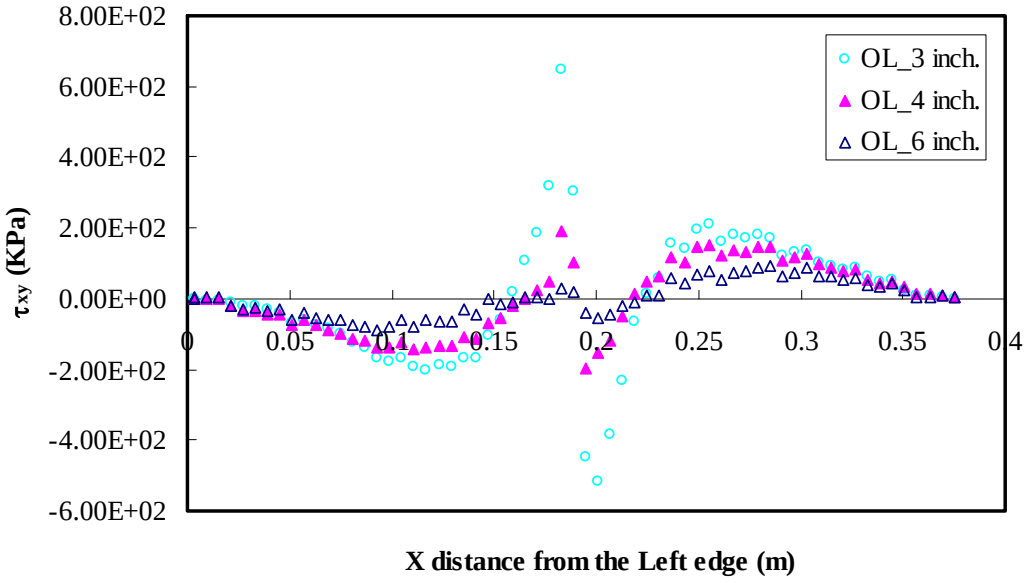

Figure 5.87 Shear stress without reinforcement for overlay thickness

Combined results for horizontal, vertical and shear stresses in the vicinity of the crack, with geosynthetic reinforcement in place, are presented in Figures 5.88 to 5.90. Maximum values for horizontal, vertical and shear stresses are lower as an effect of reinforcement. The horizontal stress distribution is presented in Figure 5.88. Analyses indicate that maximum horizontal stress is reduced from 1,910 kPa to 390 kPa, a decrease of around 80%, when the overlay thickness is increased from 3" to 6". Combined vertical stresses are shown in Figure 5.89, which shows that vertical stress, too, is reduced in the vicinity of the crack from 713 kPa to 61.2 kPa, more than 90%, when overlay thickness is increased from 3" to 6". In addition, results for combined shear stresses are shown in Figure 5.90. Analyses indicate that

when the overlay is increased from 3” to 6”, the maximum shear stress is reduced from 600 kPa to 91.2 kPa, a decrease of around 80%.

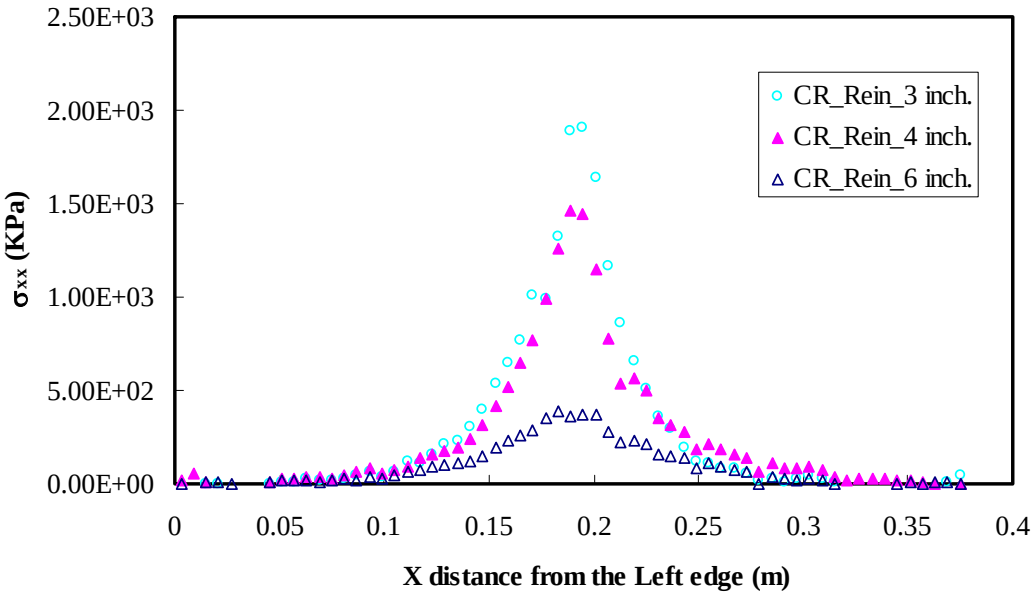

Figure 5.88 Horizontal stress with reinforcement for overlay thickness

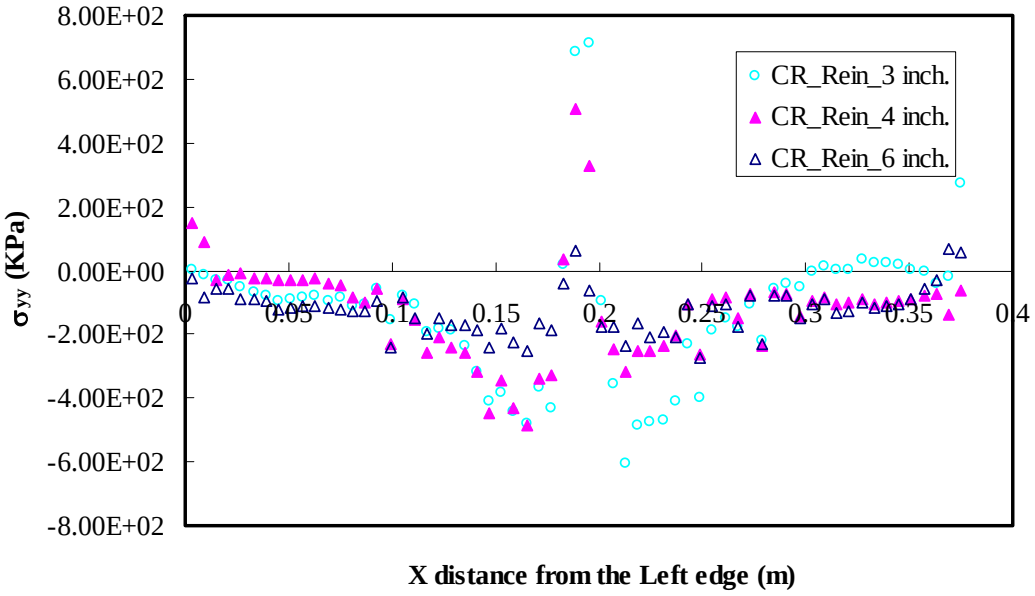

Figure 5.89 Vertical stress with reinforcement for overlay thickness

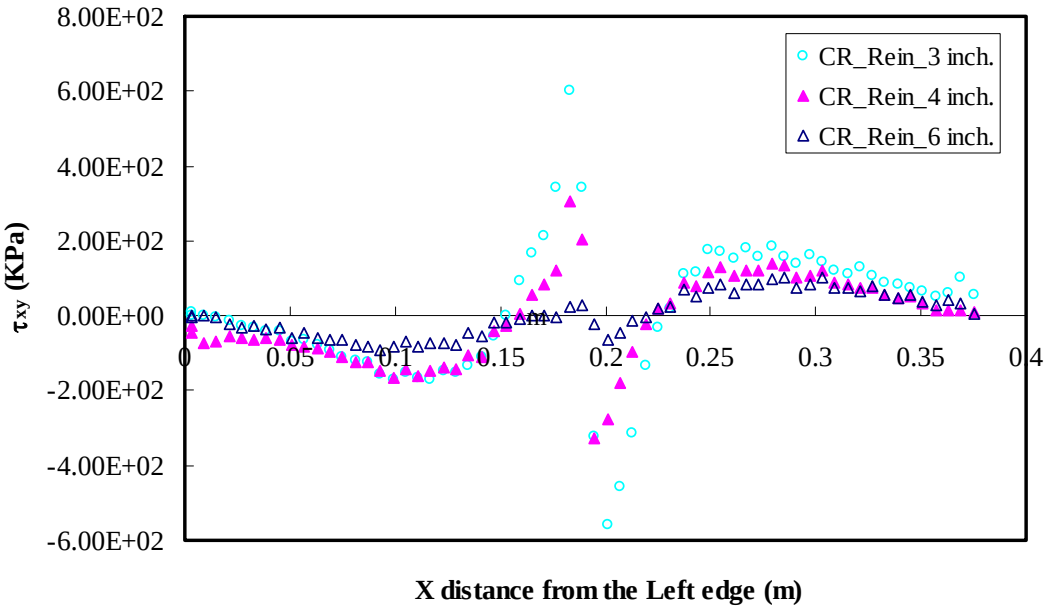

Figure 5.90 Shear stress with reinforcement for overlay thickness

The stress contours according to overlay thicknesses, including tensile, shear and vertical stress, without and with reinforcement, are presented in Figures 5.91 to 5.93. The tensile stress contours show stresses focused in the vicinity of the crack and beneath loading as shown in Figure 5.91. Higher stress values are shown in the vicinity of the crack in overlay without reinforcement, and also appeared beneath loading in the reinforced overlay. Stresses are less concentrated with increasing overlay thickness both without and with reinforcement. Both vertical stress and shear stress contours show that increasing overlay thickness is more effective in reducing stress in the vicinity of the crack. This is due to the ability of the fairly thick overlay with geosynthetic reinforcement to absorb some of the movement of the old, cracked pavement and thus to help protect the AC overlay from those stresses from below (Marienfield and Guram, 1999).

Figure 5.94 shows the porosity contours according to the three different initially cracked overlay thicknesses without and with reinforcement. Both with and without reinforcement, all porosity contours are scaled from 0.1860 to 0.1940 in order to facilitate comparison. As always, most changes of porosity occur in the vicinity of the crack; however, the contour of the 3” overlay shows most porosity changes occurring on top of the overlay beneath loading. And lower porosity values can be seen above the crack in overlays without reinforcement. This is because geosynthetic reinforcement prevents some particle movements. The contours also show that porosity change gets bigger at the bottom of the overlay as overlay thickness increases.

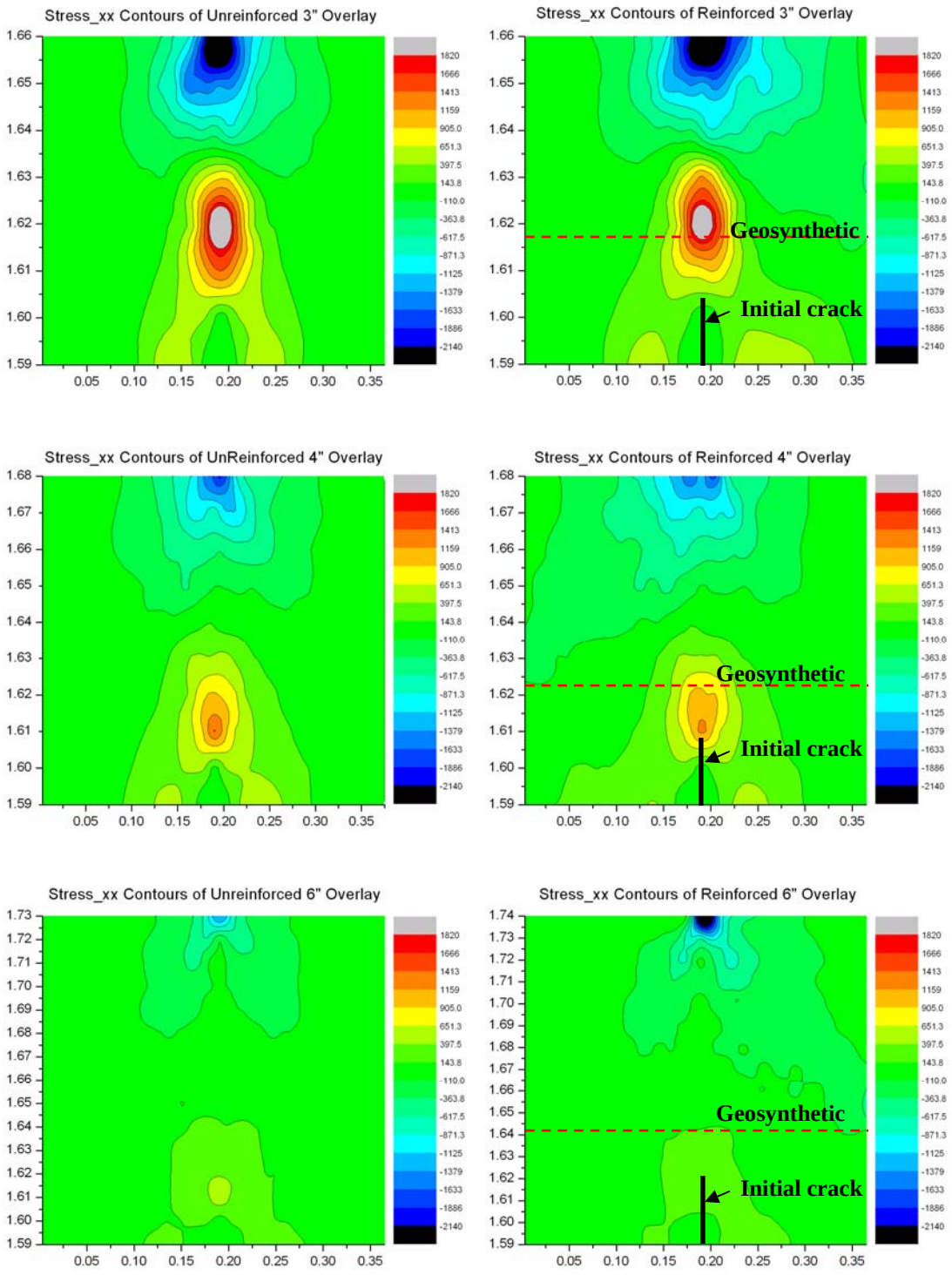

Figure 5.91 Horizontal stress contours for overlay thickness

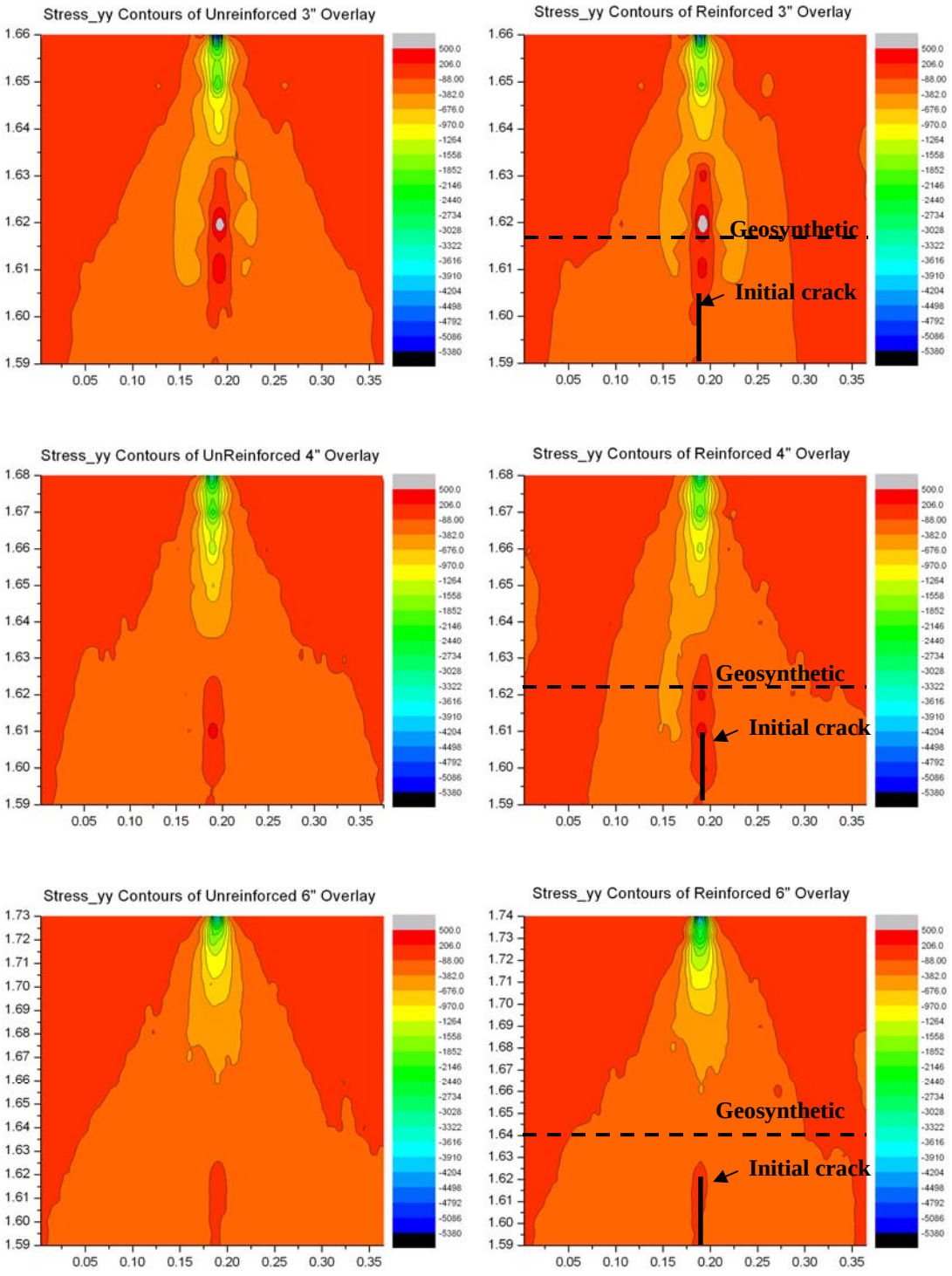

Figure 5.92 Vertical stress contours for overlay thickness

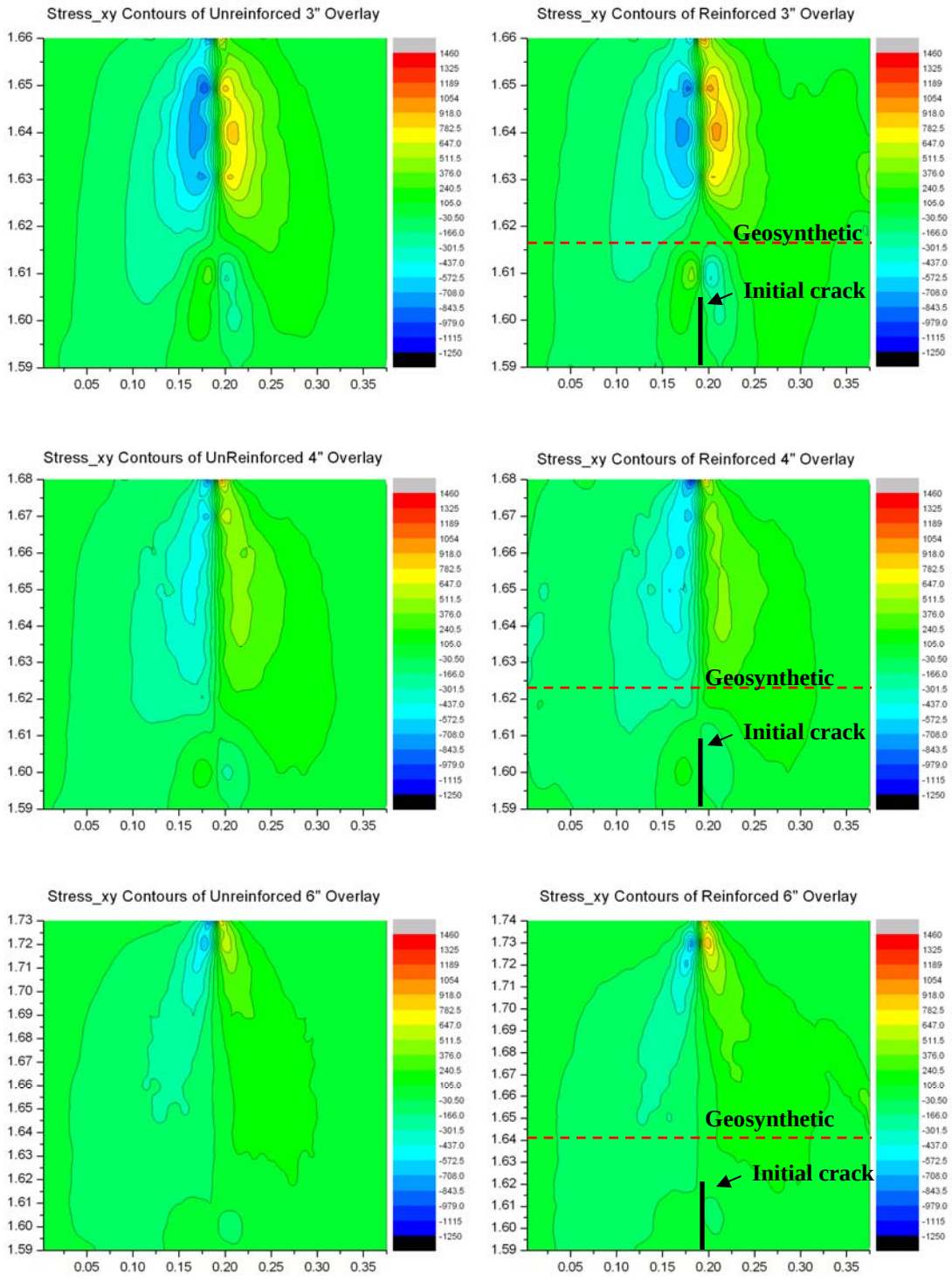

Figure 5.93 Shear stress contours for overlay thickness

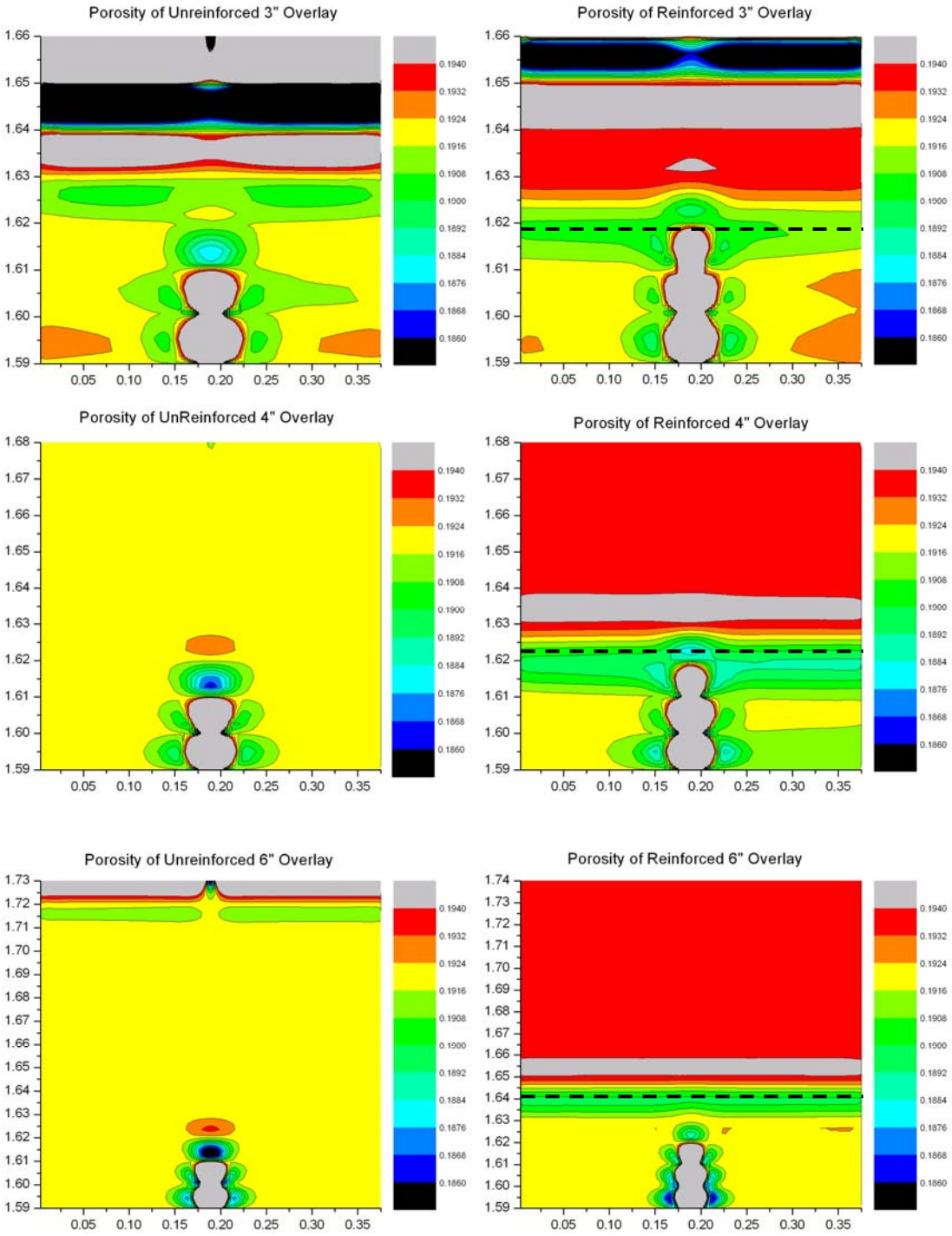

Figure 5.94 Porosity for overlay thickness

5.6 Summary

In this chapter, the DEM pavement model was developed and conducted under constant loading. Analyses including displacement on top of asphalt concrete and strain and stress distributions were studied in AC overlay both without and with reinforcement. In addition, stress and porosity contours of overlay were displayed for visual evaluations. To evaluate the effects of the geosynthetic, the following conditions were considered, without and with reinforcement.

- Effect of initial crack of overlay: geosynthetic properties, geosynthetic location, and aggregate distribution
- Effect of existing pavement conditions: PCC properties, PCC crack widths, and
- Effect of overlay thickness

Throughout the results, it was found that (a) displacement, strain, and stress were reduced if geosynthetic reinforcement was embedded in the asphalt concrete overlay, and (b) the presence of an initial crack affected the strain and stress fields. Also, it was demonstrated that the most effective location for geosynthetic reinforcement was at one-third depth (from the bottom) of the AC overlay.

CHAPTER 6 DEM Model with Fracture

6.1 Introduction

Reflective cracking, which is one of the most serious problems associated with the use of thin overlays, may be induced by shear and tensile stresses created by traffic loading and/or thermal loading (Cleveland et al., 2002). The external wheel loading contributes to high stress and strain levels in the overlay above the existing crack. While a previous chapter investigates the geosynthetic-soil interaction under constant loading, this chapter is focused on the geosynthetic-soil interaction under fracture which is controlled y-velocity to make cracks on AC overlay.

The main object of this study is to evaluate the effectiveness of geosynthetic reinforcement in controlling reflective cracking of asphalt concrete overlays according to different geosynthetic properties under fracture. This study includes the comparisons of maximum stress and maximum strain in a local level, and macro- and micro-cracks are displayed to allow visual comparison of reflective cracking.

6.2 Model Description

The DEM pavement model uses the same dimensions as demonstrated in Chapter 5 and the same loading conditions as in Chapter 4, as shown in Figure 6.1. Details of the model description and model properties are illustrated in Chapters 4 and 5. In this study, wheel load controlled by y-velocity of 7 mm/sec is applied. Also, boundary conditions of the right and left side edges are assigned to free as in Chapter 4. Stress and strain variations will be monitored using measurement circles at assigned points.

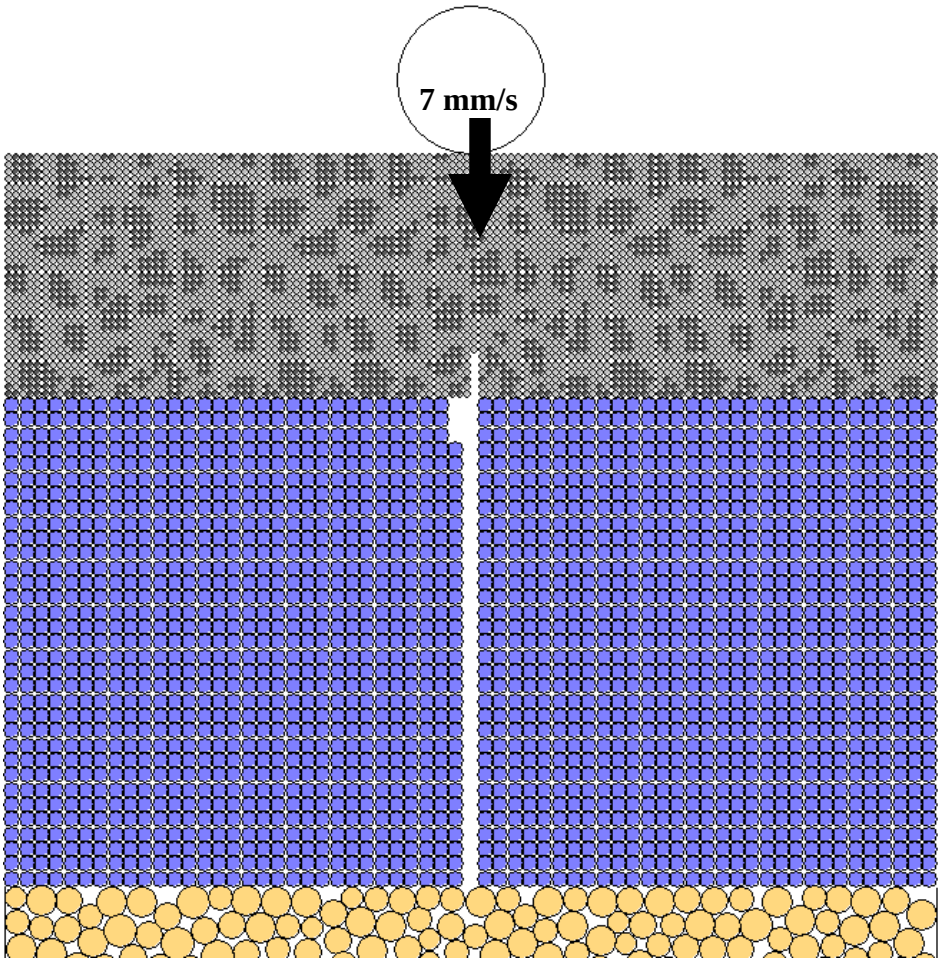

Figure 6.1 Schematic of DEM Fracture Model and loading condition

6.3 Results and Analyses

Stresses and strains are monitored in 5 measurement circles which are located above the initial crack as shown in Figure 6.2. Details of geosynthetic properties are presented in Chapters 4 and 5.

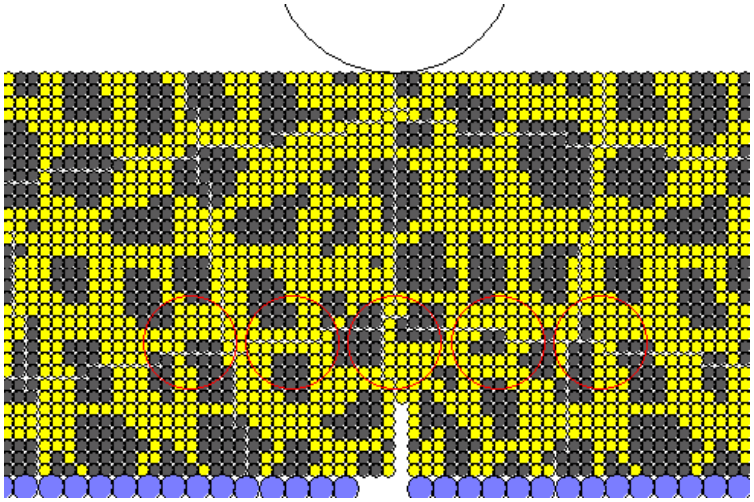

Figure 6.2 Measurement circle locations

6.3.1 DEM fracture model without reinforcement

Figure 6.3 shows the maximum stress distribution monitored from measurement circles after reflective cracking. Stress in tension is distributed in an arching shape. The highest value shows in the middle and then stresses are lowered toward both sides. Analysis indicates that the highest value in the middle is 889 kPa. The vertical stress distribution pattern is same as the horizontal one, but vertical stress is governed by compression and its highest value in the middle is 2,590 kPa, as shown in Figure 6.4. Also, shear stress distribution is presented in Figure 6.5. Shear stresses in the left side and middle are in compression, and stress of 435 kPa is the lowest in the middle, then stress is converted to tension in the right side.

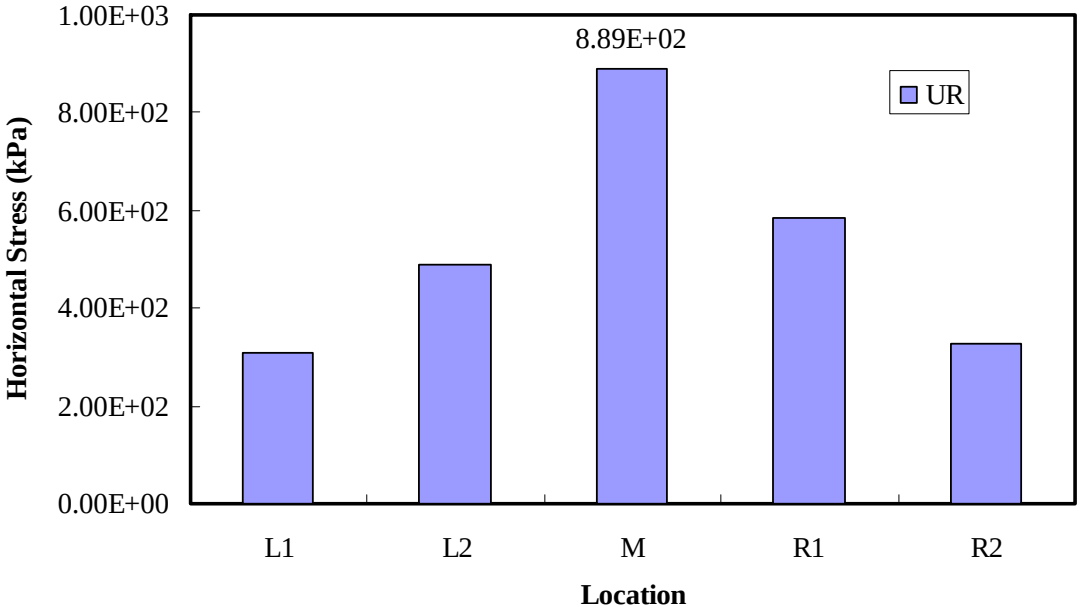

Figure 6.3 Maximum horizontal stress distribution without reinforcement

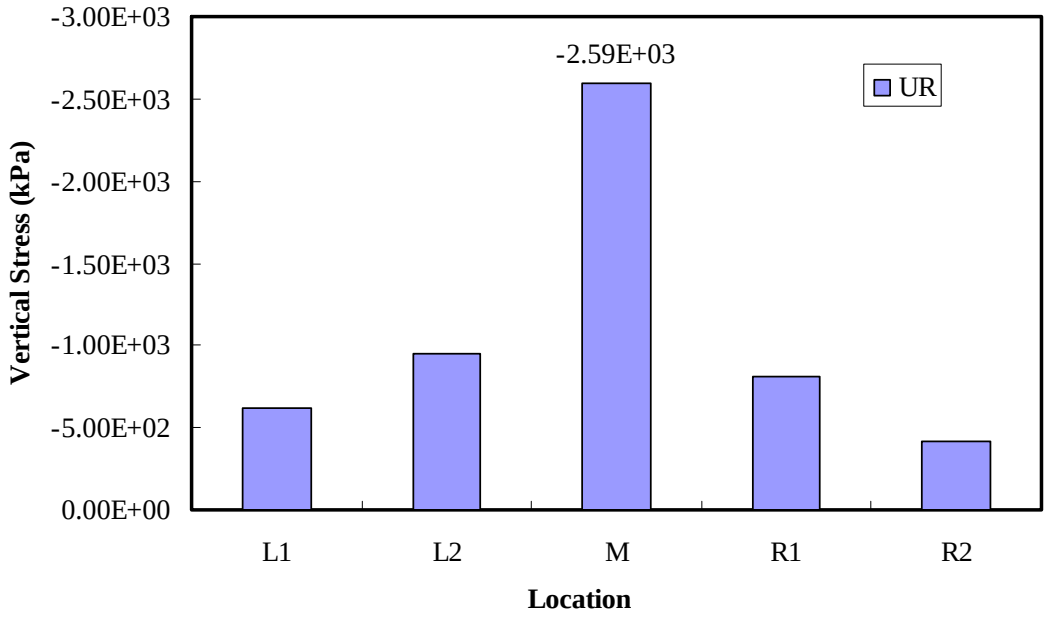

Figure 6.4 Maximum vertical stress distribution without reinforcement

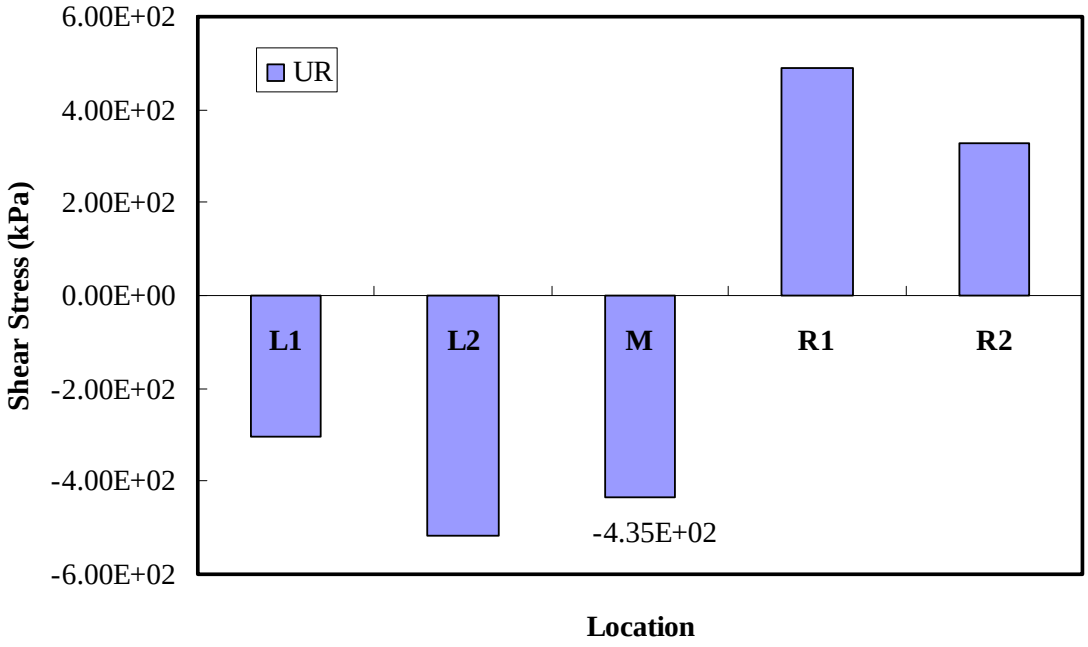

Figure 6.5 Maximum shear stress distribution without reinforcement

Distributions of the maximum horizontal, vertical and shear strain without reinforcement after reflective cracking are presented in Figures 6.6 to 6.8. The maximum horizontal strain of 0.534 is obtained in the middle; the rest of the values are very small in comparison with that middle value, as shown in Figure 6.6. This means that most strain is occurring in the middle due to the loading. Figure 6.7 shows the results of vertical strain. Like the horizontal strain results, the maximum vertical strain of 0.129 is obtained in the middle and values at the rest of the locations are very small. Also, the maximum shear strains at each location are presented in Figure 6.8. Again, the maximum shear strain of 0.148 is measured in the middle. Analyses indicate that horizontal strain is relatively high compared

with vertical and shear strain results. This means that horizontal strain is related to the initiation and propagation of the crack into the overlay.

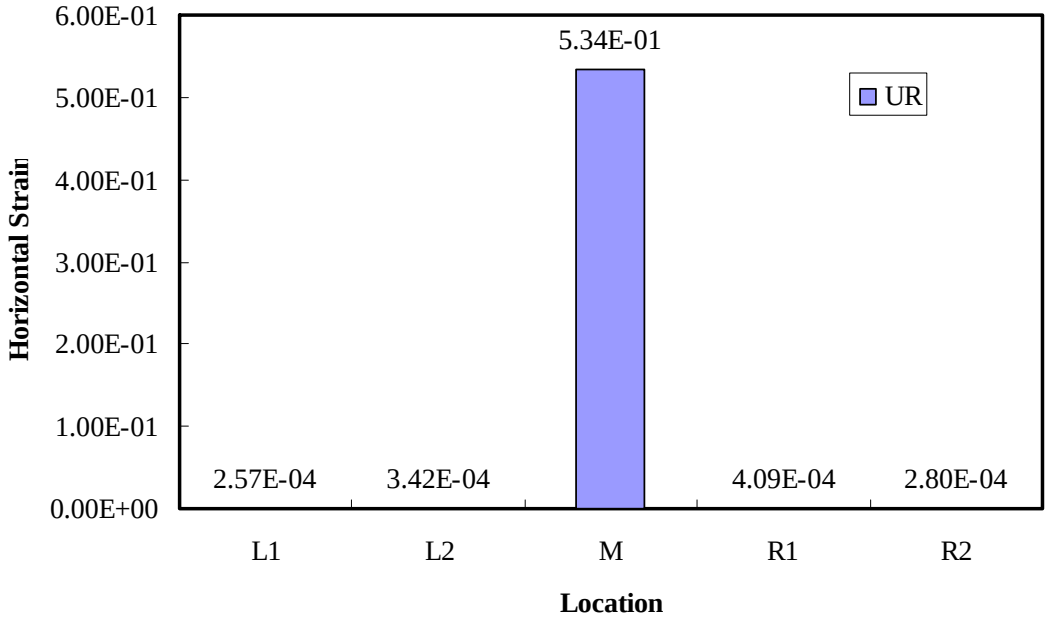

Figure 6.6 Maximum horizontal strain distribution without reinforcement

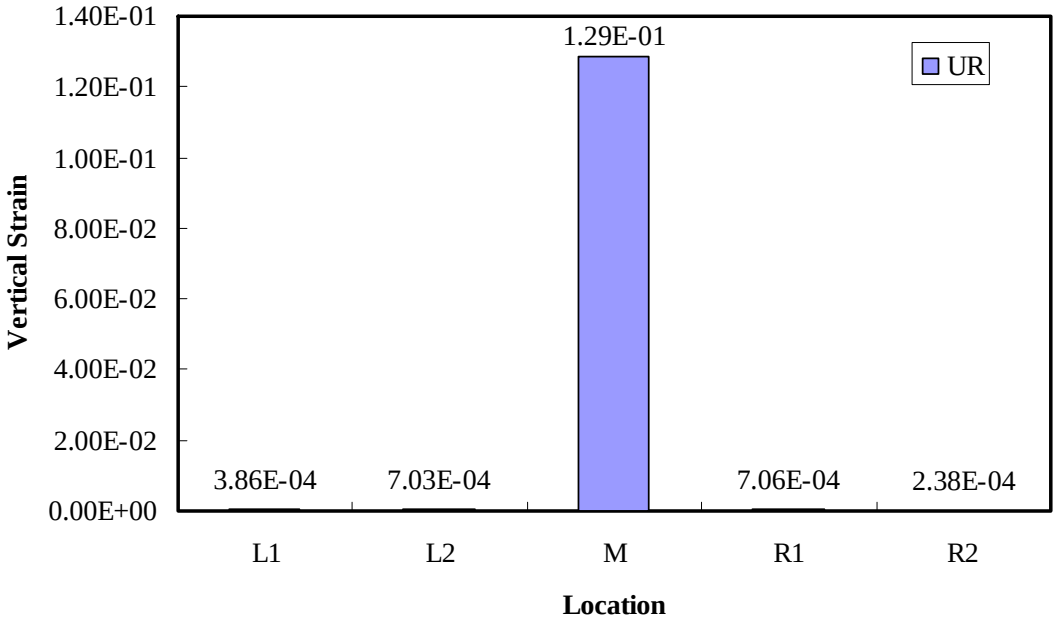

Figure 6.7 Maximum vertical strain distribution without reinforcement

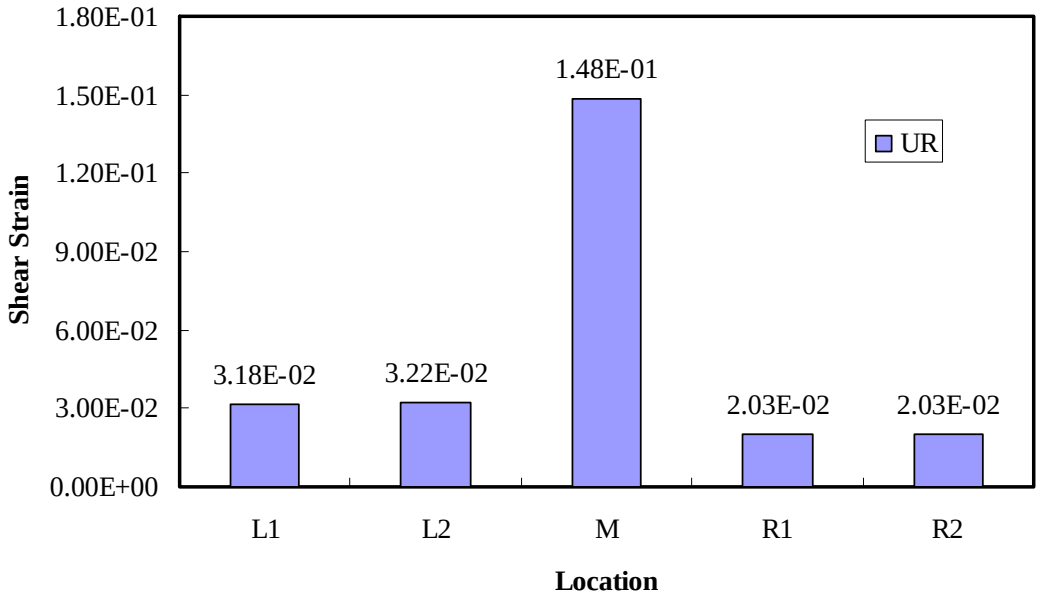

Figure 6.8 Maximum shear strain distribution without reinforcement

6.3.2 DEM fracture model with reinforcement

To investigate the effect of reinforcement, the geosynthetic is placed in the AC overlay at 1/3H. The geosynthetic properties used in the DEM model are presented in Table 6.1. Properties of GT_P1 are the same as detailed in a previous chapter. To represent the very stiff geosynthetic, GT_P2 is assigned a parallel-bond model which does not preclude the possibility of slip, unlike a contact-bond model and describes the constitutive behavior for cementatious material existing between the two balls. Therefore, GT_P2 is much stronger and stiffer than AC and PCC.

Table 6.1 Geosynthetics Parameters of DEM Fracture model

Parameters selected for the geosynthetics	GT_P1 (Contact Bond)	GT_P2 (Parallel Bond)
Normal stiffness, k_n^{gg} (N/m)	4.0×10^7	5.0×10^{12}
Shear stiffness, k_{gg} (N/m)	5.0×10^7	1.3×10^{13}
Tensile strength (N)	3.0×10^4	1.0×10^{10}
Shear strength (N)	3.0×10^4	1.0×10^{10}
Friction angle, μ_{gg}	0	0

Results for maximum stress with GT_P1 reinforcement after reflective cracking are presented in Figures 6.9 to 6.11. Figure 6.9 shows the stress distribution monitored from measurement circles. Stress behaviors are the same as without reinforcement. Analysis indicates that the highest value in the middle is 796 kPa. The vertical stress distribution pattern is the same as the horizontal one, but vertical stress is governed by compression and its highest value in the middle is 2,280 kPa as shown in Figure 6.10. Shear stress distribution is presented in Figure 6.11. Shear stresses in the left sides are in compression and stress is converted to tension in the middle and right sides. In addition, maximum stress of 424 kPa in the middle is obtained. Stresses are reduced as an effect of reinforcement and comparisons are addressed next.

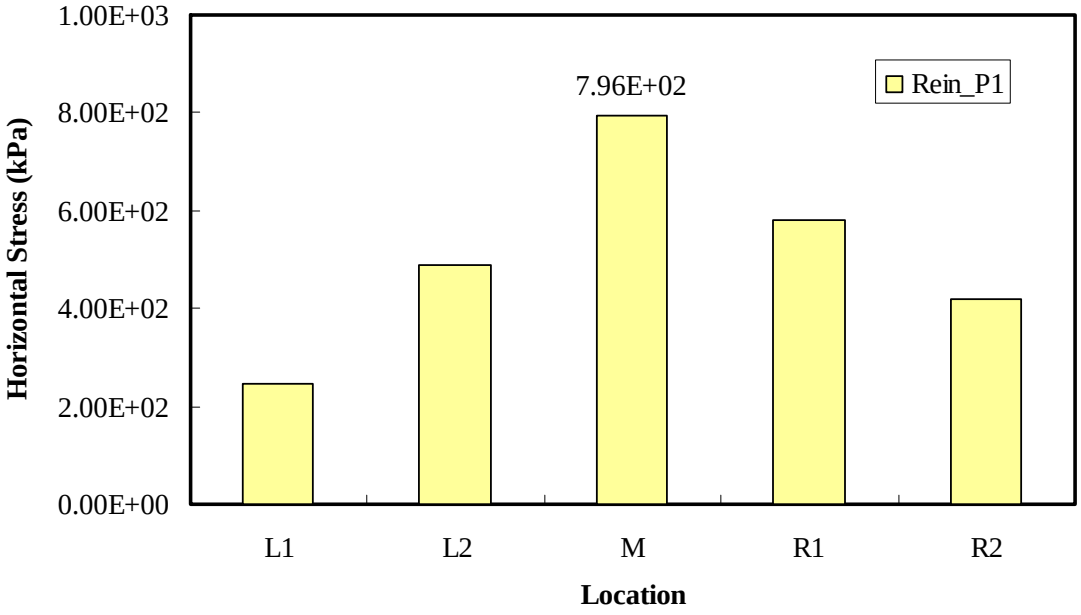

Figure 6.9 Maximum horizontal stress distribution with reinforcement

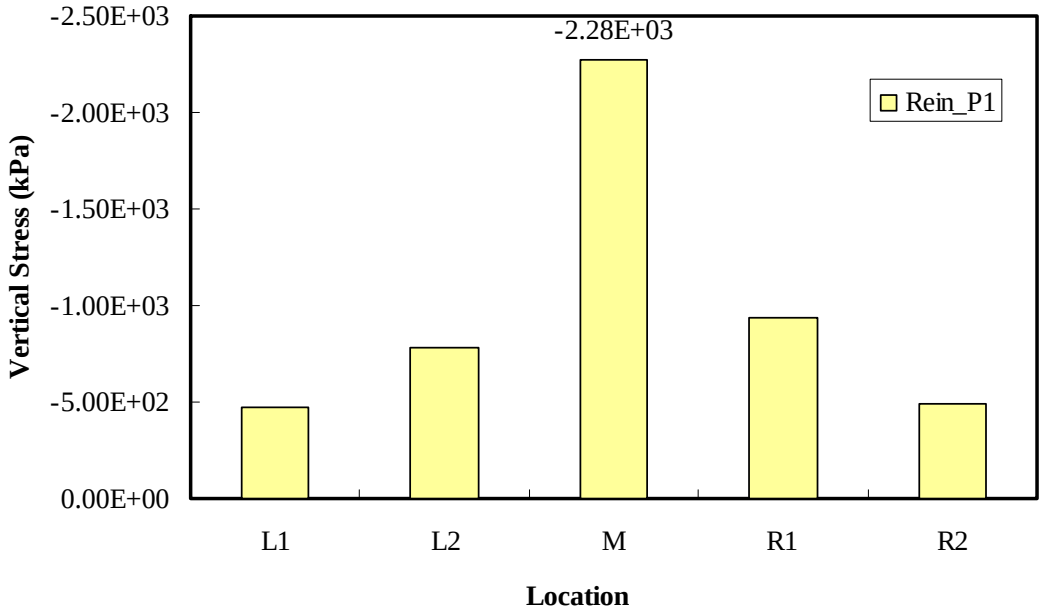

Figure 6.10 Maximum vertical stress distribution with reinforcement

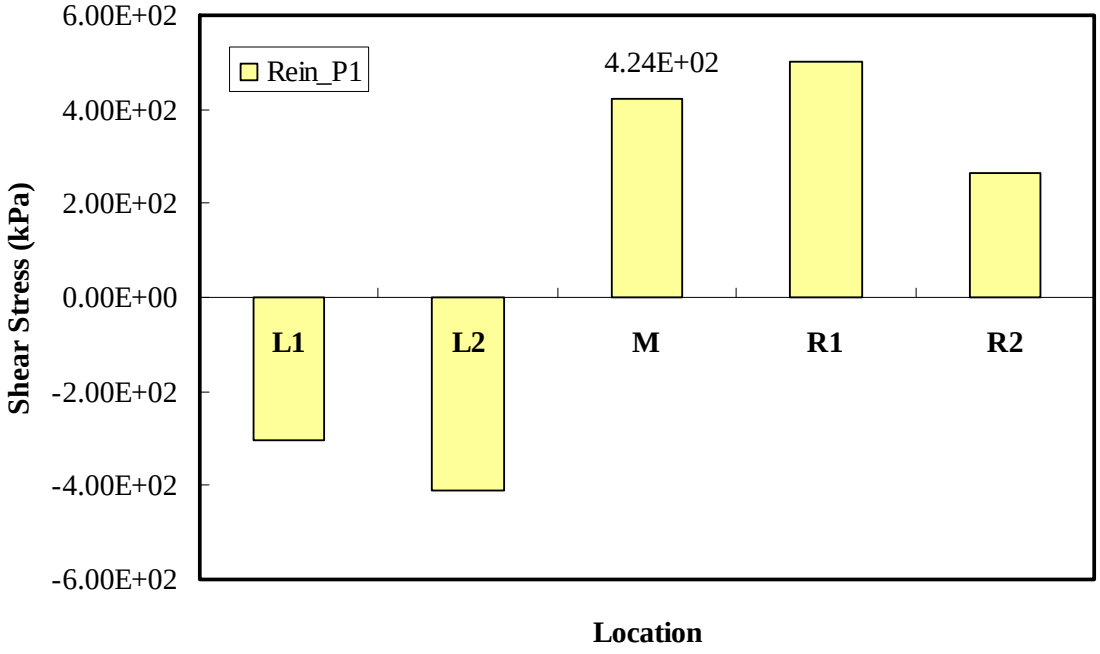

Figure 6.11 Maximum shear stress distribution with reinforcement

To allow comparison without and with reinforcement, combined results of maximum stress in the middle are presented in Figures 6.12 to 6.14. Maximum values for horizontal, vertical and shear stresses in the middle are decreased as an effect of reinforcement. Horizontal stress is presented in Figure 6.12. Analyses indicate that maximum horizontal stress is reduced from 889 kPa to 796 kPa and 631 kPa, around 10% to 30% decrease in horizontal stress when GT_P1 and GT_P2, respectively, are placed in the overlay. Combined vertical stresses are shown in Figure 6.13. Analyses indicate that maximum horizontal stress is reduced from 2,590 kPa to 2,280 kPa and 1,060 kPa, a decrease of around 10% to 60% in horizontal stress when GT_P1 and GT_P2 are placed in the overlay. In addition, results of combined shear stresses are shown in Figure 6.14. Analyses indicate that maximum shear

stress is reduced from 435 kPa to 424 kPa and 50.7 kPa, showing a decrease of around 3% to 88% in shear stress when GT_P1 and GT_P2 are placed in the overlay. this means that reinforcement significantly affects the stress field in the vicinity of the crack tip, especially, and that the stiffer material is much more effective in reducing shear stress. It can be explained that the geosynthetic works as a stress-absorbing layer around the crack tip.

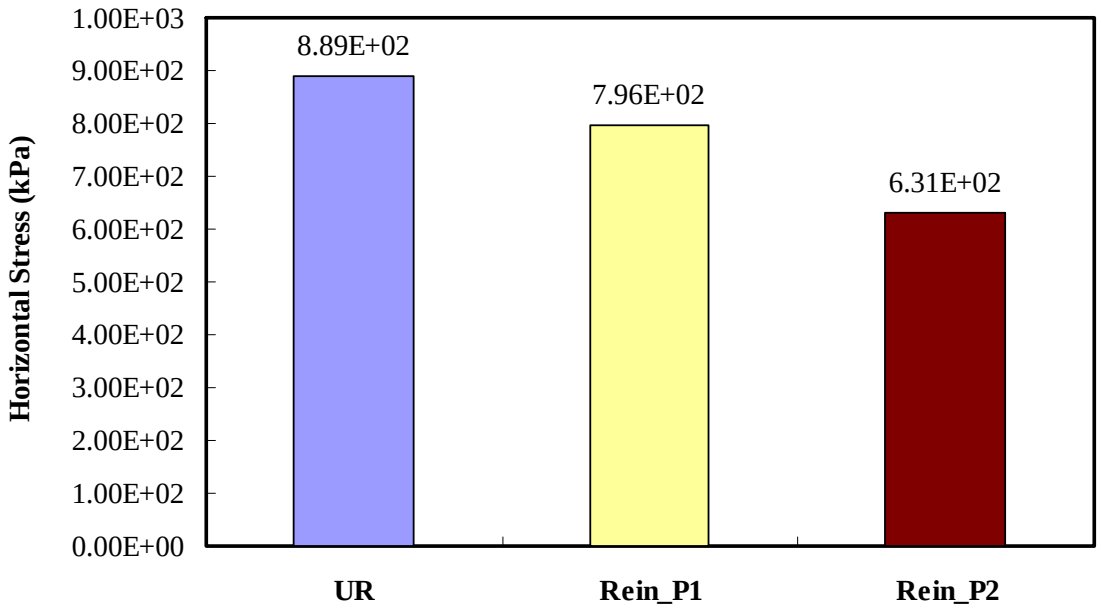

Figure 6.12 Combined maximum horizontal stresses in the middle

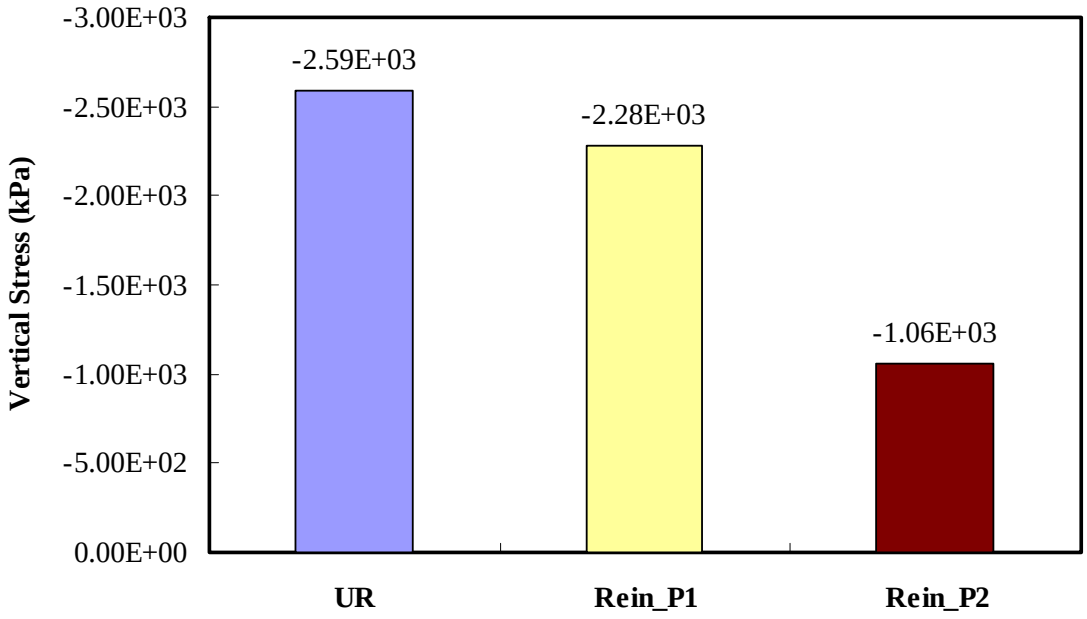

Figure 6.13 Combined maximum vertical stresses in the middle

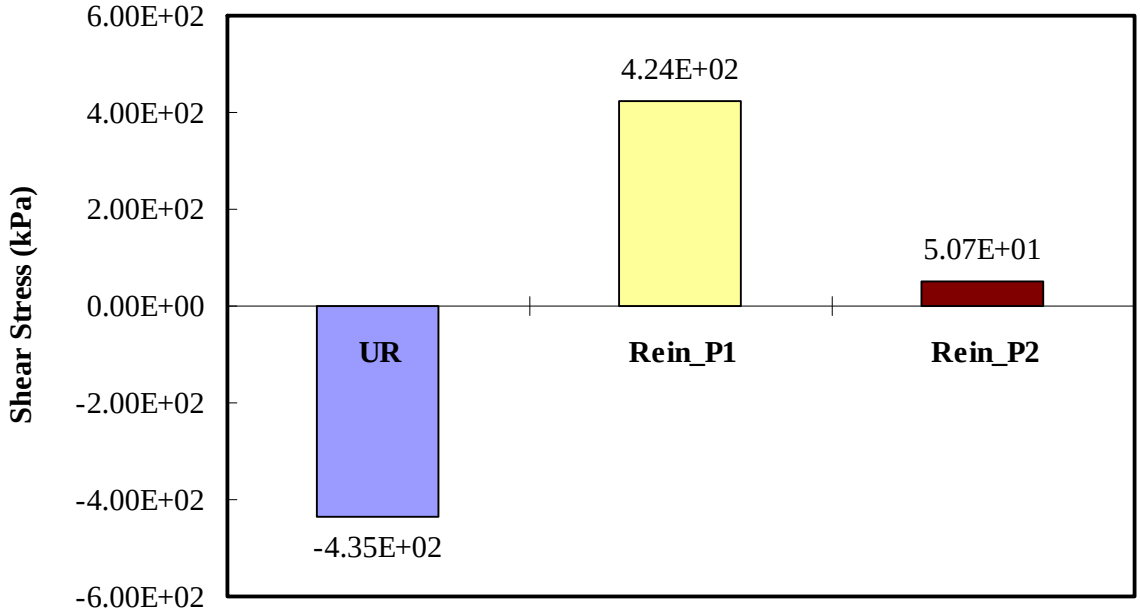

Figure 6.14 Combined maximum shear stresses in the middle

In addition, distributions of horizontal, vertical and shear strain with GT_P1 reinforcement are presented in Figures 6.15 to 6.17. Strain behaviors are also similar to those in overlay without reinforcement. Analysis indicates that the maximum horizontal strain of 0.384 is obtained in the middle and the rest of the measurements are very small compared with value in the middle as shown in Figure 6.15. Figure 6.16 shows the results of vertical strain. The maximum vertical strain of 0.0496 is also calculated in the middle and most vertical and horizontal strains are apparent in the middle. Shear strain is presented in Figure 6.17. Analysis indicates that the maximum shear strain of 0.037 is measured in the middle.

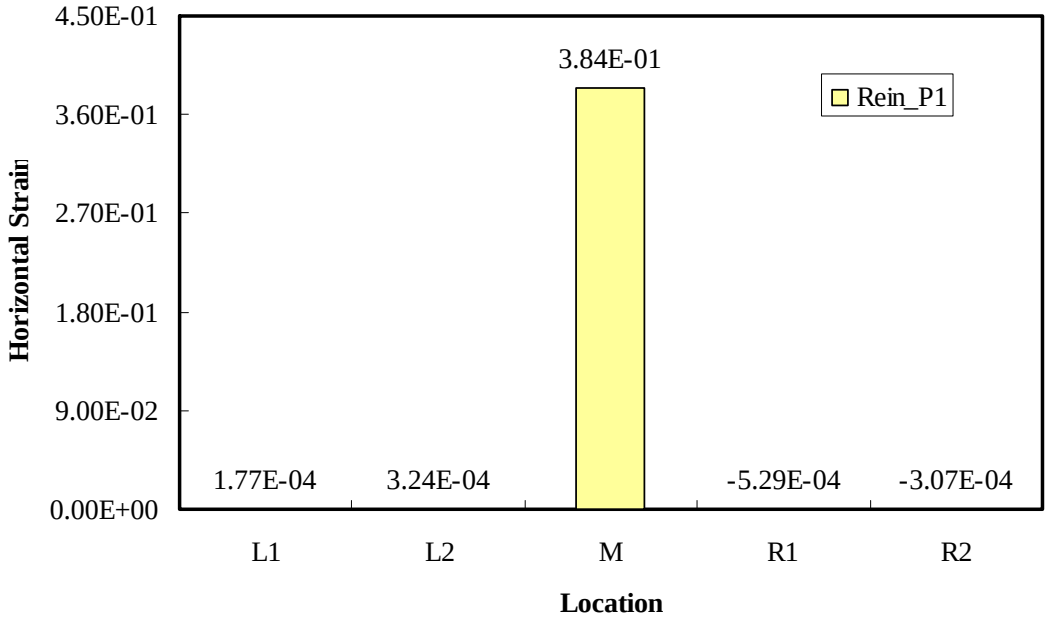

Figure 6.15 Maximum horizontal strain distribution with reinforcement

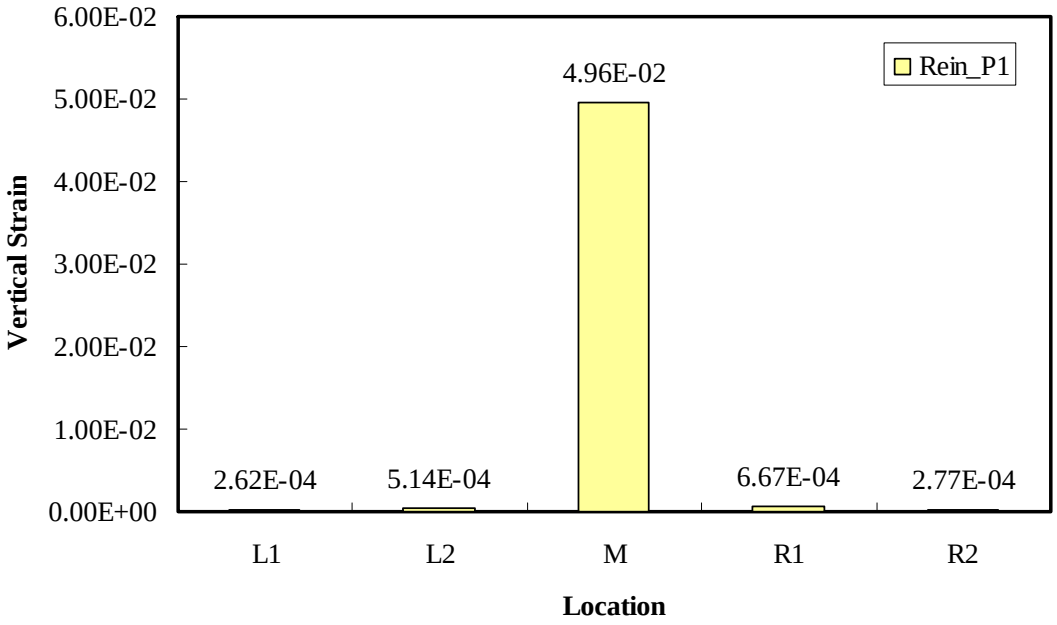

Figure 6.16 Maximum vertical strain distribution with reinforcement

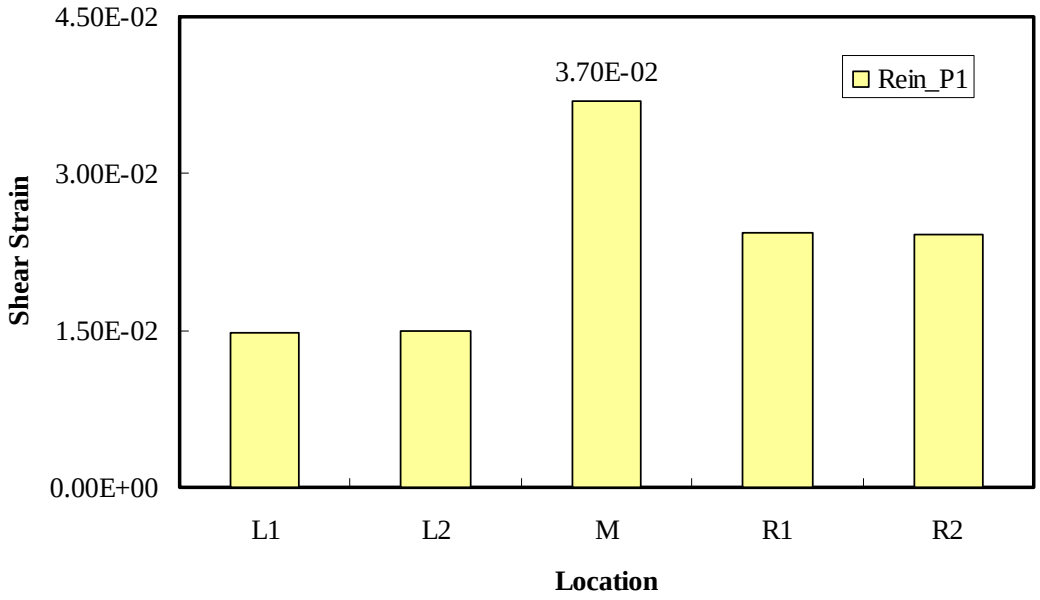

Figure 6.17 Maximum shear strain distribution with reinforcement

In addition, combined results of strain values are presented in Figures 6.18 to 6.20. Maximum values for horizontal, vertical and shear strains in the middle are decreased as a benefit of geosynthetic reinforcement and the most effective reduction in strain can be seen in the stiffer material. Maximum horizontal strains in the middle are presented in Figure 6.18. Analyses indicate that maximum horizontal strain is reduced from 0.534 to 0.384 and 0.0156, thus, more than 25% to 85% decrease in horizontal strain when GT_P1 and GT_P2 are placed in the overlay. Results of combined vertical strains are shown in Figure 6.19. Analyses indicate that maximum vertical strain is reduced from 0.129 to 0.0496 and 0.000567, showing more than 60% to 95% decrease in vertical strain when GT_P1 and GT_P2 are embedded in the overlay. In addition, results of combined shear strains are shown in Figure 6.20. Analyses indicate that maximum shear strain is reduced from 0.148 to 0.0370 and 0.00404, a decrease of more than 75% to 95% in shear strain when GT_P1 and GT_P2 are placed in the overlay. This indicates that geosynthetics work effectively by preventing lateral movement of particles when placed in the AC layer.

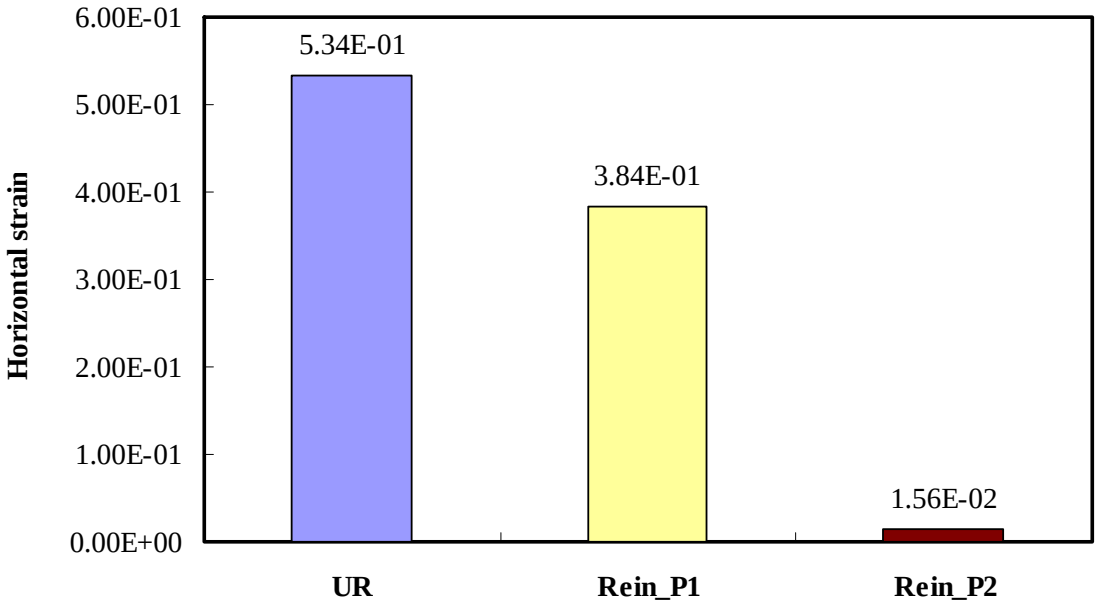

Figure 6.18 Combined maximum horizontal strains in the middle

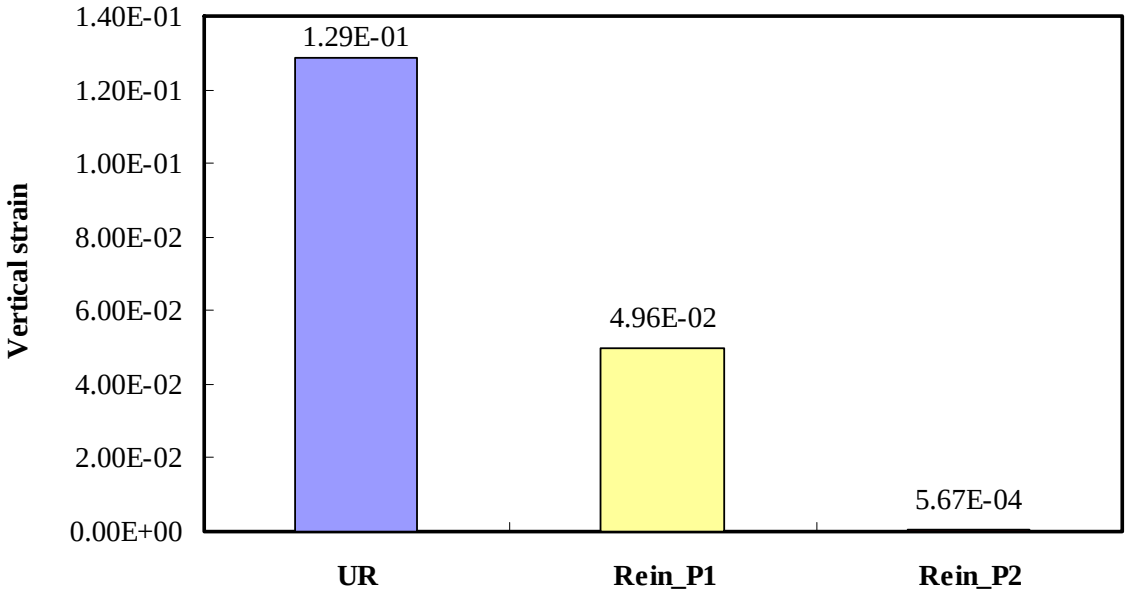

Figure 6.19 Combined maximum vertical strains in the middle

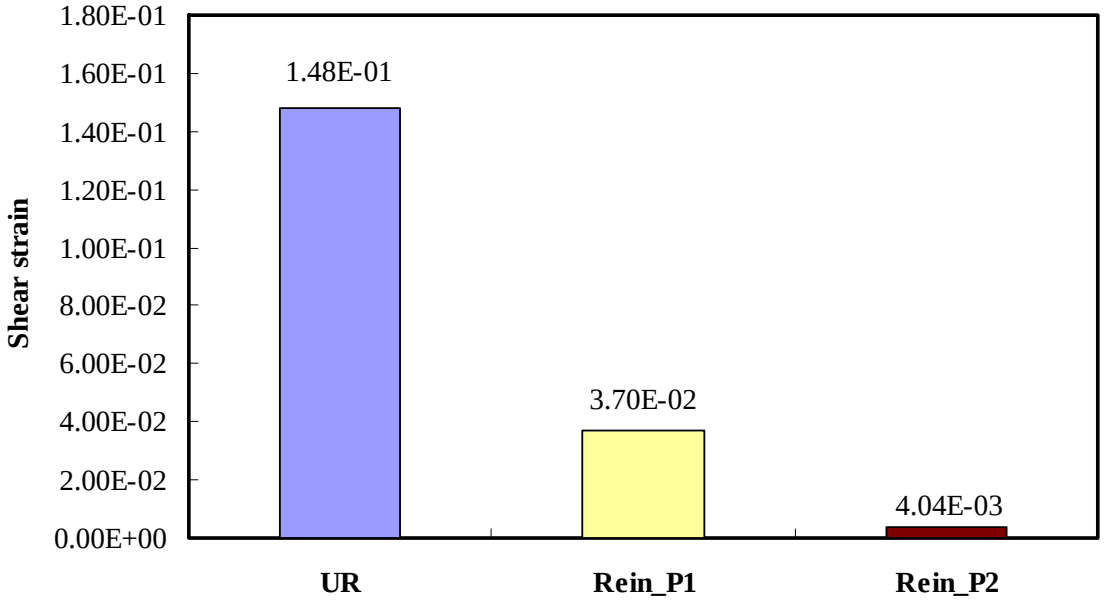

Figure 6.20 Combined maximum shear strains in the middle

6.3.3 Macro and Micro cracks in Overlays with and without reinforcement

Figure 6.21 shows the macro- and micro-cracks of overlay without reinforcement. Macro cracks developed by loading start from an existing initial crack and continue to penetrate the entire overlay and reach the top of the overlay as seen in Figure 6.21 (a). In addition, Figure 6.21 (b) shows the micro-cracks which are formed along the macro-cracks and distributed within a narrow range.

Figure 6.22 shows the macro- and micro-cracks of overlay reinforced with GT_P1. While macro-cracks develop from the initial crack without reinforcement, with GT_P1 macro-cracks develop through the whole overlay. Because of the geosynthetic reinforcement, macro-cracks progress not only upward but also downward from the reinforcement as seen in Figure 6.22 (a). This is confirmed by the micro-cracks shown in Figure 6.22 (b).

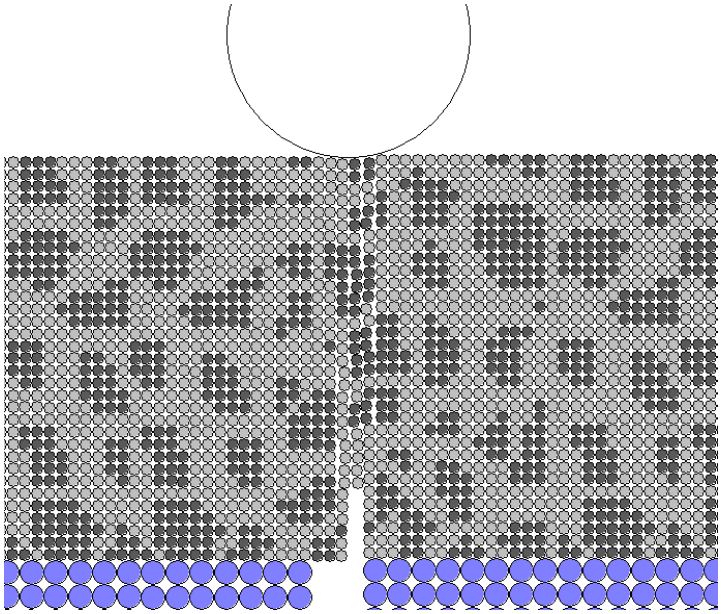

(a) Macro-cracks

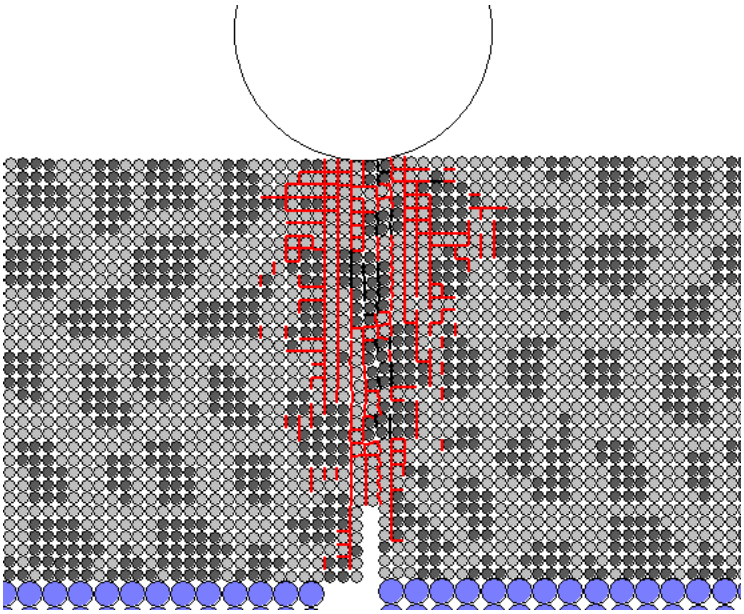

(b) Micro-cracks

Figure 6.21 Crack in AC overlay without reinforcement

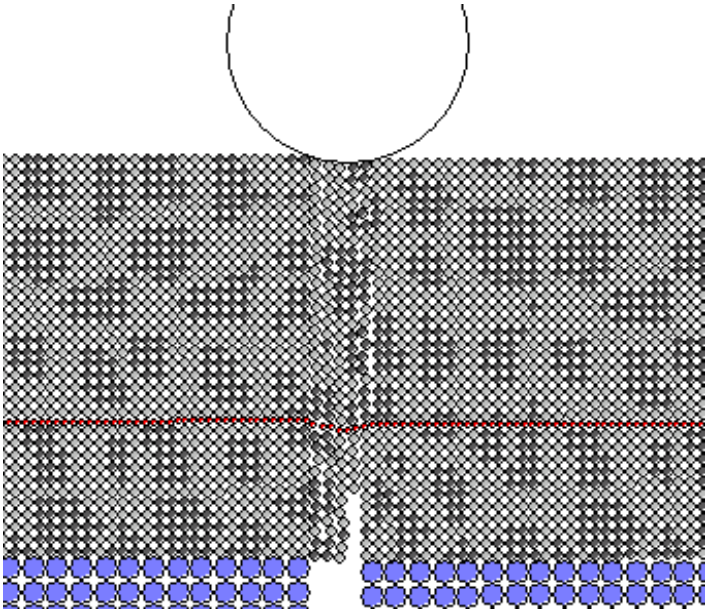

(a) Macro-cracks

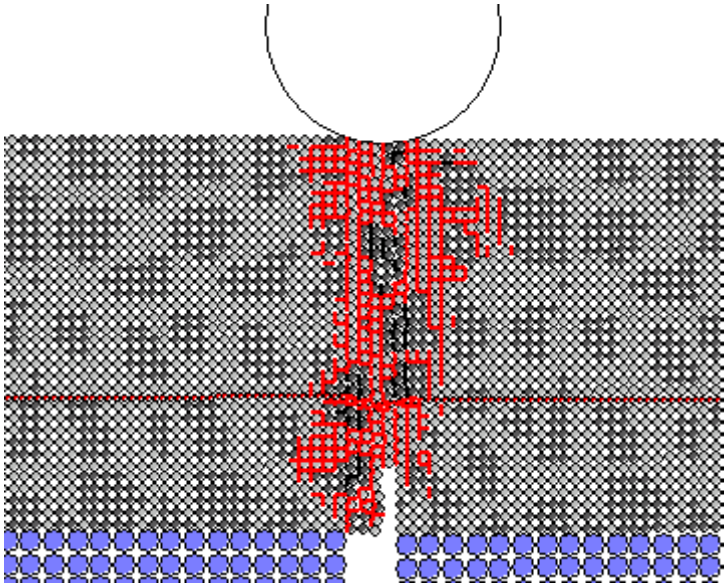

(b) Micro-cracks

Figure 6.22 Crack in AC overlay with GT_P1 reinforcement

Figure 6.23 shows the macro- and micro-cracks of overlay that is reinforced with GT_P2. Unlike without reinforcement, macro-cracks cannot penetrate the overlay because the geosynthetic is very stiff; instead, cracks exist not only in the vicinity of the crack under the reinforcement but also along the geosynthetic. This can be verified from the micro-cracks as shown in Figure 6.23 (b). Micro-cracks develop along the geosynthetic reinforcement, and cover a wider range in comparison to both unreinforced overlay and overlay reinforced with GT_P1.

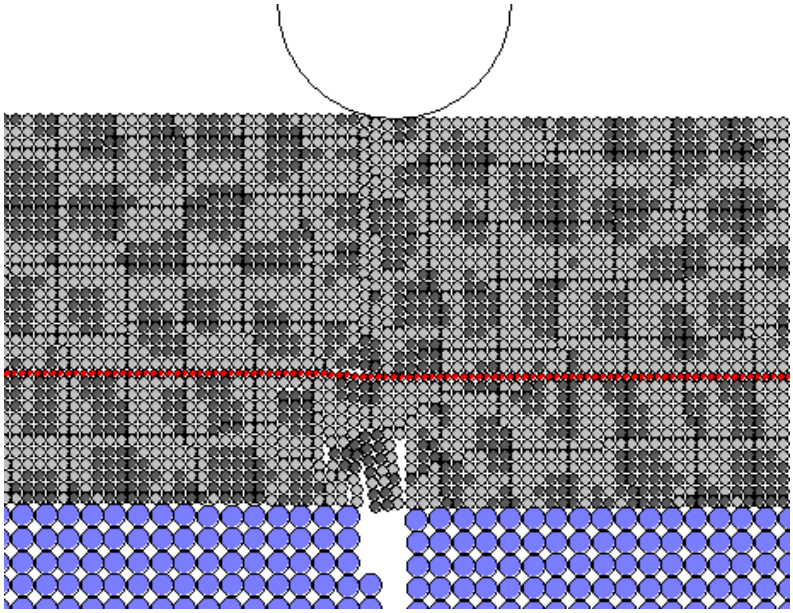

(a) Macro-cracks

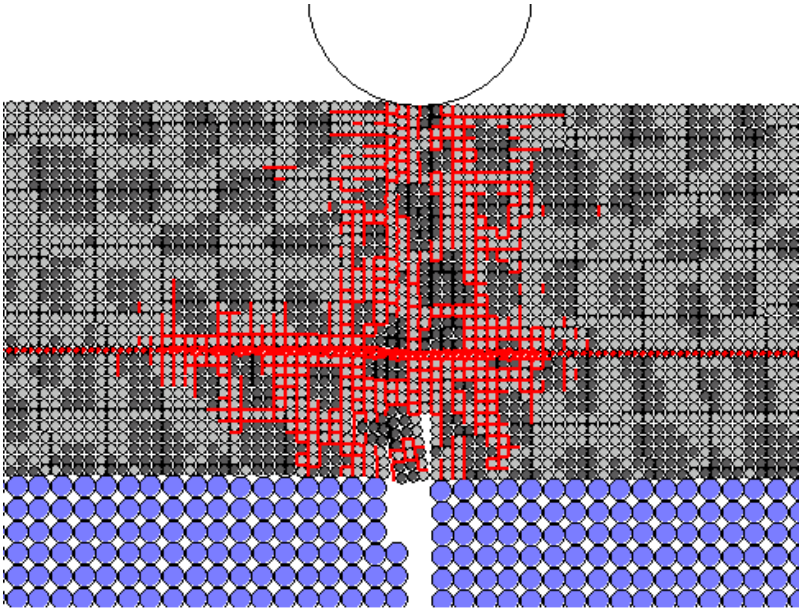

(b) Micro-cracks

Figure 6.23 Crack in AC overlay with GT_P2 reinforcement

6.2 Summary

In this chapter, the DEM fracture model was developed and conducted under controlled y-velocity as one of the loading conditions, with and without reinforcement. Wheel load controlled by y-velocity of 7 mm/sec was applied. Two different geosynthetic reinforcements were used, one very much stiffer than the other, to investigate the effect of geosynthetic properties. Stress and strain were monitored from measurement circles at 5 different positions, and then compared. Results showed that the reinforcements both showed benefit in decreasing stress and strain; the stiffer one worked most effectively. In addition, macro- and micro-cracks were investigated. Reflective cracking was shown between the areas under loading and above the initial crack, both in overlay without reinforcement and in overlay reinforced with the less-stiff geosynthetic. However, in overlay which was reinforced with stiffer geosynthetic, macro-cracks mainly occurred below the reinforcement; micro-cracks were also shown along the geosynthetic, and covered a wider range than in the other two cases.

CHAPTER 7 DEM Model under Moving Wheel Loading

7.1 Introduction

Many researchers have studied and attempted to evaluate the effects of geosynthetic-soil confinement using such means as the bending stiffness test (Sprague et al., 2004), push tests (Matys and Baslik, 2004), cyclic plate load test (Haas et al., 1998), accelerated pavement tests, and field trafficking tests. Numerical computations have also been used to evaluate the geosynthetic-soil interaction, and both the continuum method (i.e., FEM) and discontinuum method (i.e., DEM) have been commonly used, as addressed in a previous chapter. Notably, Han et al. (2008) proposed a performance-based test to evaluate the effect of geosynthetic reinforcement in base courses under moving wheel loading in the laboratory. Furthermore, they (2008) developed a DEM model to investigate the reduction of rut depth for geotextile-reinforced bases under moving wheel loading because DEM is suitable to handle geosynthetic-soil interaction problems.

In this study, the DEM model is developed and extended to a whole pavement section including AC overlays, unlike Han's model which was composed of only the base layer. Stress and strain will be monitored from measurement circles which are assigned to 5 different locations. Moreover, contours of stress and air void ratio (porosity) after moving wheel loading will displayed as well.

7.2 Model Description

The same DEM pavement model is used as demonstrated in Chapter 5 except for loading condition. The detailed model description and model properties are illustrated in

Chapter 5. In this study, both moving wheel load controlled by x-velocity and also vertical loading are applied. The x-velocity of 0.7 m/sec and vertical loading of 18 kip (80 kN) single axle, which satisfy the ratio maximum unbalance force (MUF) to maximum contact force (MCF) of 0.01 or less, are applied as moving wheel loading conditions both with and without reinforcement. Unlike the previous model, the boundary conditions of the right and left side edges are assigned to be fixed to prevent the layers from separating and slipping due to the moving wheel load. The wheel moves from the left to the right side only one time because of time constraints. Stress and strain variations according to wheel location are monitored using measurement circle at assigned points. Details will be addressed in the next section.

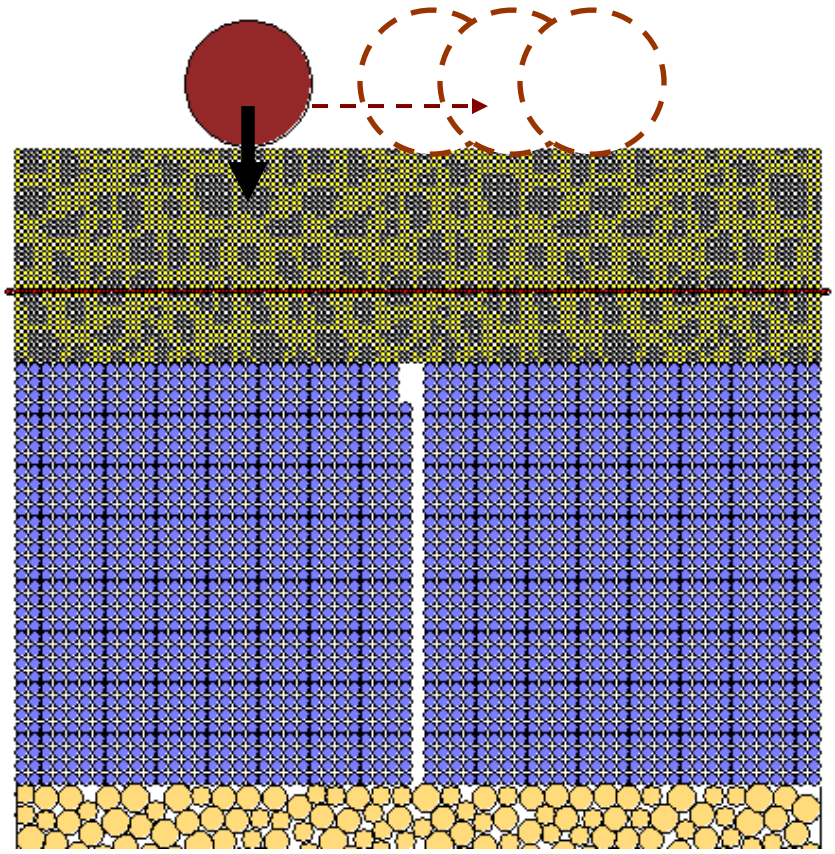

Figure 7.1 Geometry of Pavement DEM model for Reinforced section

7.3 Results of Moving wheel load

7.3.1 Stress distribution during wheel movement

As mentioned in the above section, stresses of x, y, and xy directions are monitored at the 5 measurement circles located under the reinforcement during the movement of the wheel. Stresses are monitored according to wheel locations while the wheel moves from the left side to right side as shown in Figure 7.2.

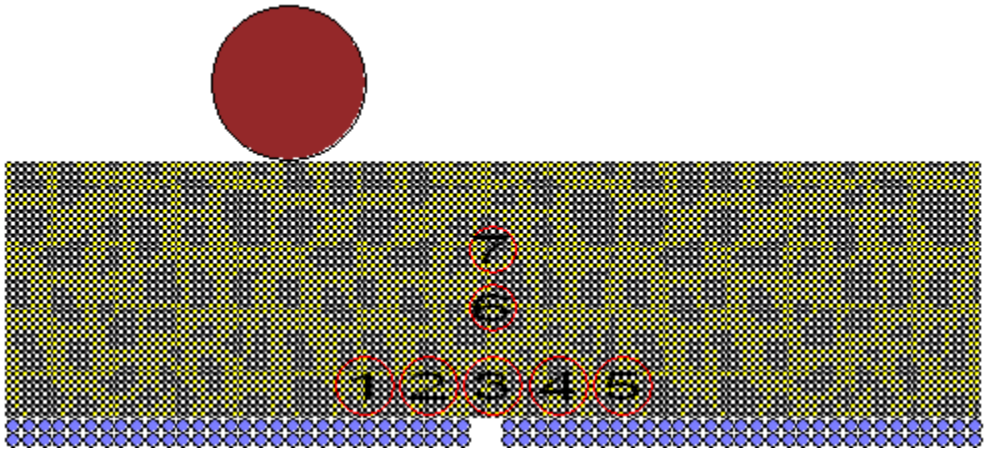

Figure 7.2 Measurement circles for monitoring

Horizontal stress curves monitored from the measurement circles in the unreinforced overlay are presented in Figure 7.3. Measurement circles numbered 1 to 5 are identified as Left 1, Left 2, Middle, Right 1, and Right 2, respectively, according to their locations. Positive stresses indicate tension and negative stresses indicate compression. Horizontal stress gradually increases in the approach to each measurement circle. When the wheel is located above each measurement circle, horizontal stress at that point shows the maximum

values (i.e., tension), and then stress goes down (i.e., compression) gradually as the wheel moves to next measurement circle. Stresses at Left 1 and Right 2, which are located on each side, are more variable compared to other locations because their positions affect the amount of time it takes to reach maximum stress level. Analysis indicates that stress changes vary from around 440 kPa to (-)340 kPa.

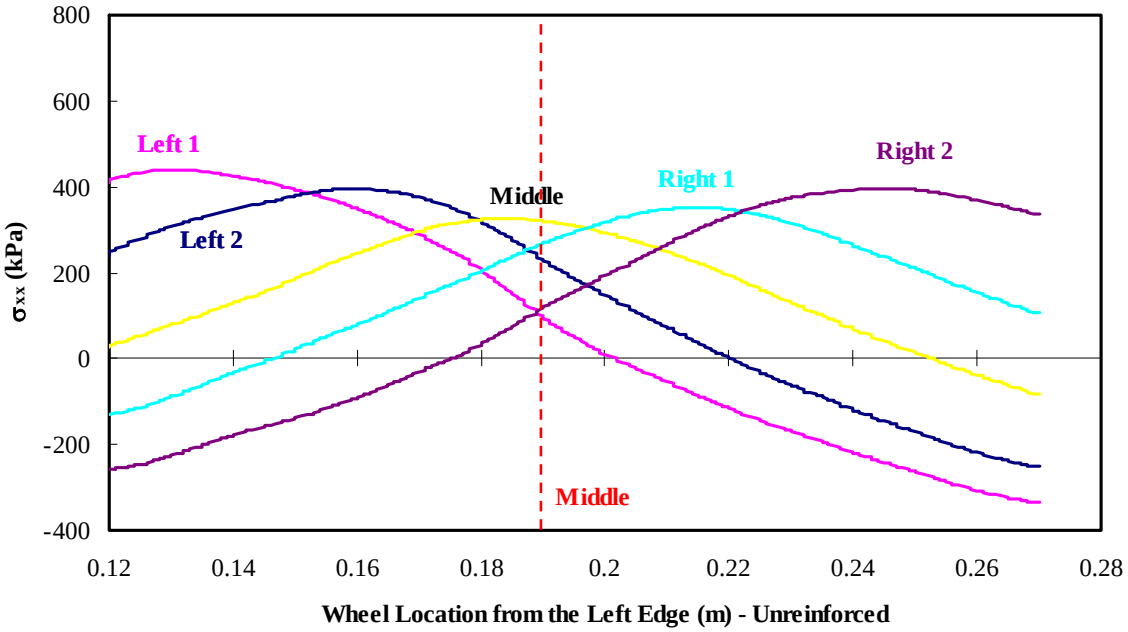

Figure 7.3 σ_{xx} variations according to moving wheel locations for unreinforced overlay

Vertical stress curves monitored from the measurement circles in unreinforced overlays are presented in Figure 7.4. Like horizontal stress curves, maximum stress is produced when the wheel is passing over each measurement circle. However, stresses vary

from around 100 kPa to 300 kPa in compression with relatively slight change compared to that of horizontal stress.

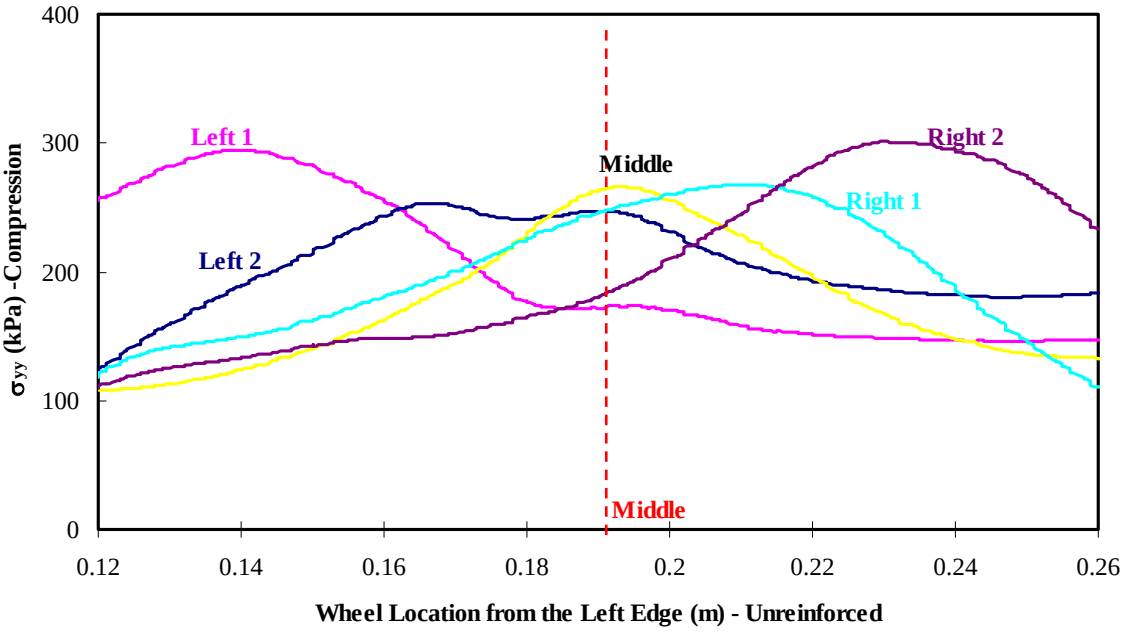

Figure 7.4 σ_{yy} variations according to moving wheel locations for unreinforced overlay

Shear stress curves monitored from the measurements for unreinforced overlays are presented in Figure 7.5. All shear stresses are curves converted from positive if moving wheel is located on measurement circle to negative if wheel move to the next position in turn. Shear stress values are observed from around 260 kPa to (-)380 kPa.

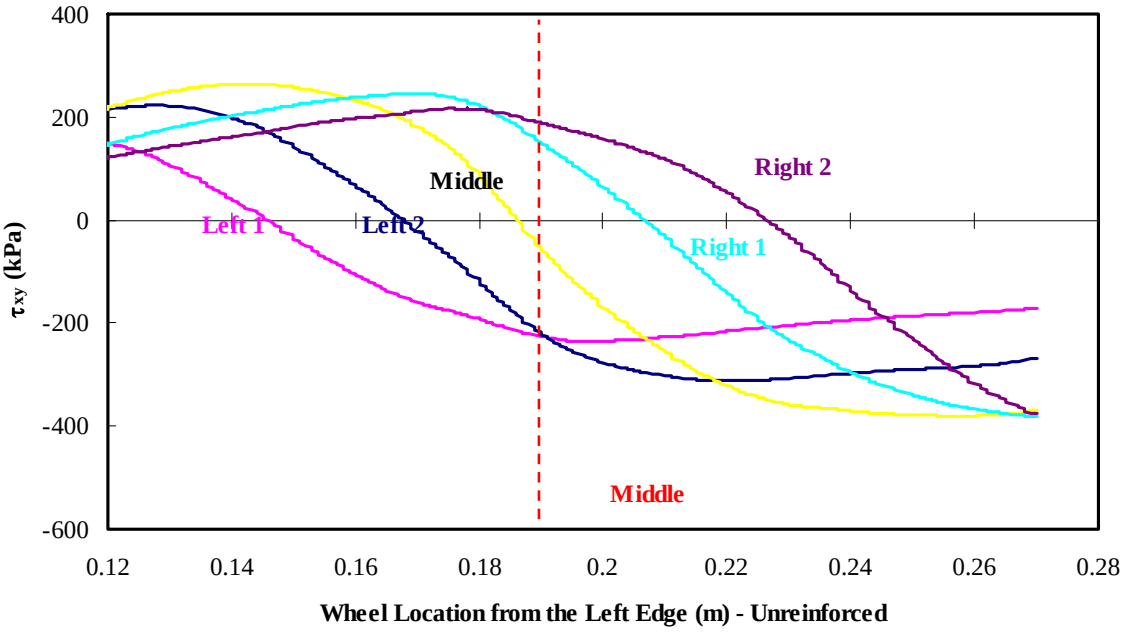

Figure 7.5 τ_{xy} variations according to moving wheel locations for unreinforced overlay

In addition to these, the horizontal, vertical, and shear stress curves monitored from the measurement circles for reinforced overlays are presented in Figures 7.6 to 7.8. With reference to Figures, stress behaviors are the same as in the unreinforced overlays.

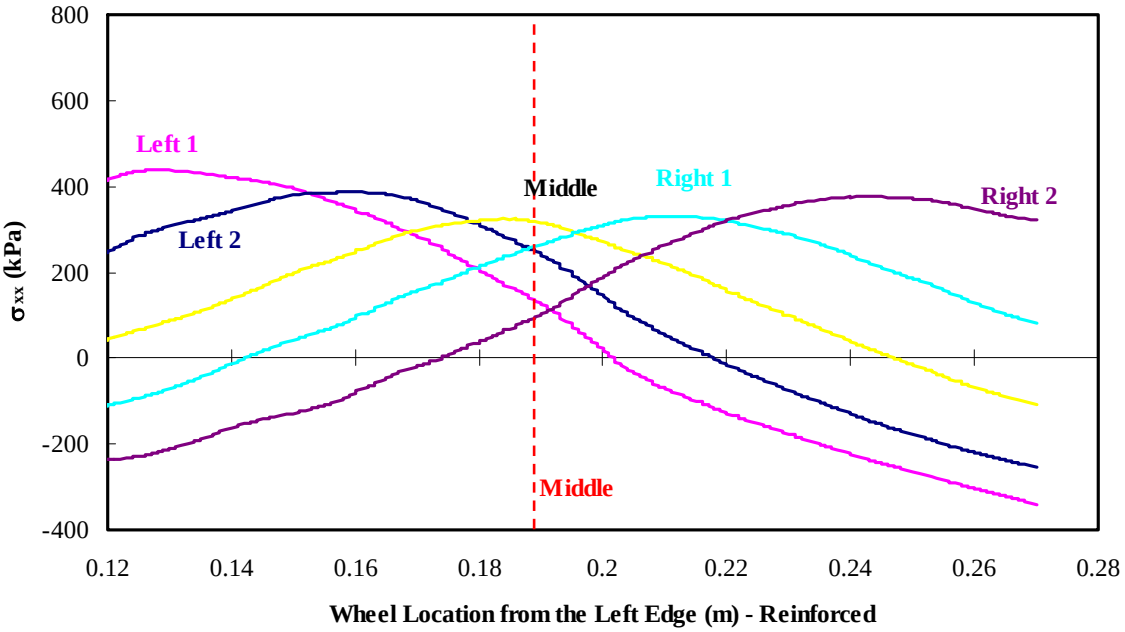

Figure 7.6 σ_{xx} variations according to moving wheel locations for reinforced overlay

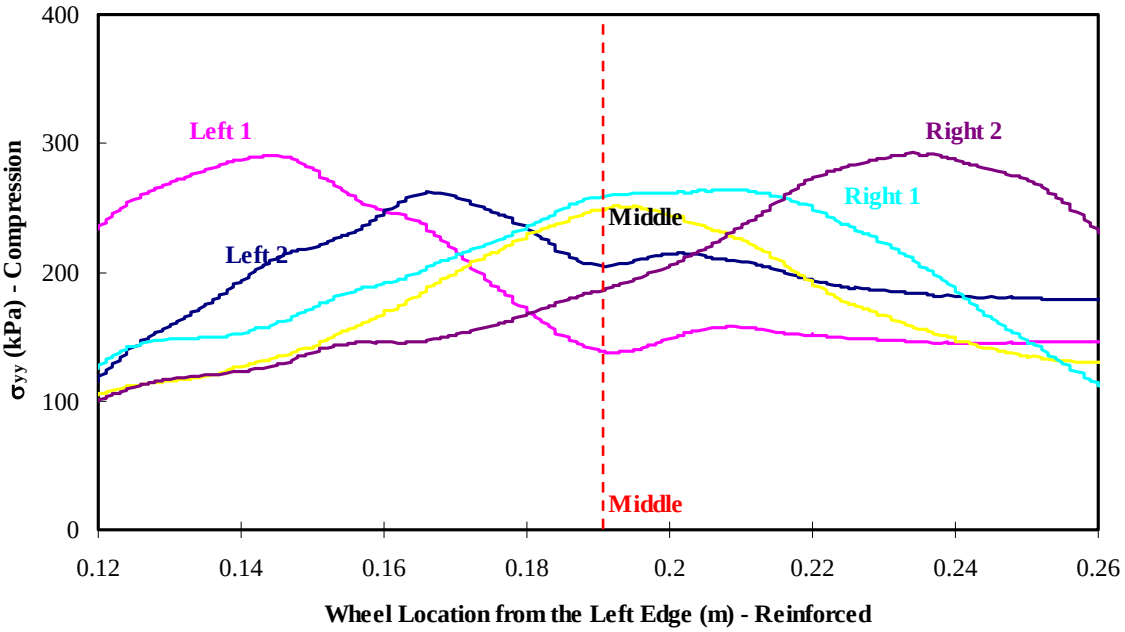

Figure 7.7 σ_{yy} variations according to moving wheel locations for reinforced overlay

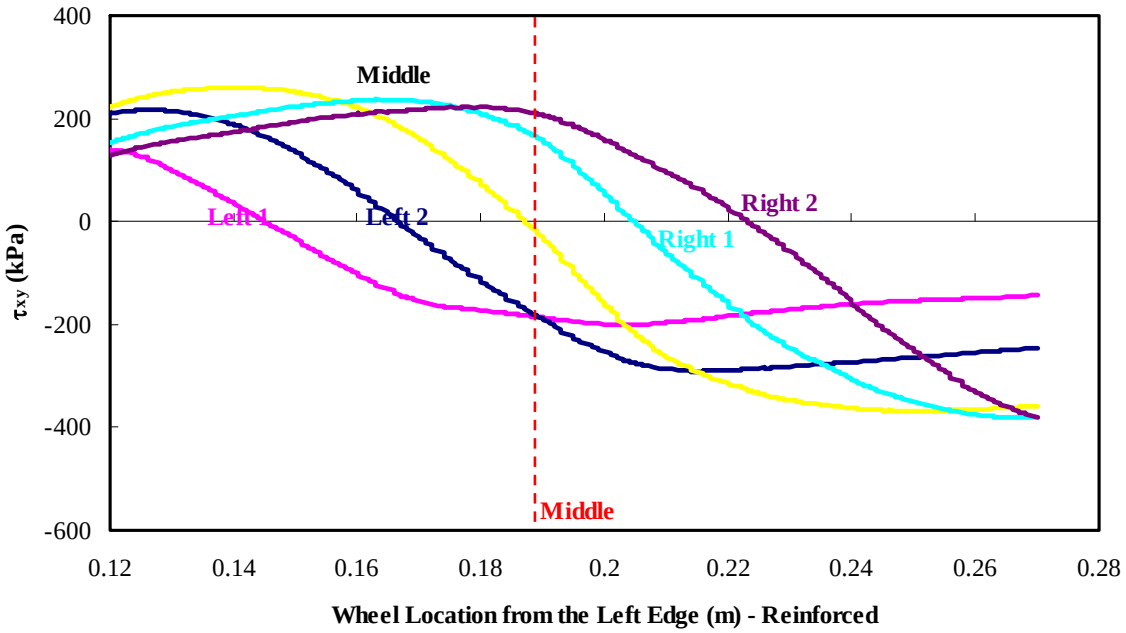

Figure 7.8 τ_{xy} variations according to moving wheel locations for reinforced overlay

To compare the results for both unreinforced and reinforced overlays, combined stress curves are showed in Figures 7.9 to 7.11. Horizontal stress curves are combined in Figure 7.9. Solid lines stand for reinforced overlays and dotted lines for unreinforced overlays. On the whole, stress readings from reinforced overlays are less pronounced than from unreinforced overlays because of geosynthetic reinforcement, but the stress differences are marginal. Figure 7.10 shows the combined vertical stress curves for both cases. The Figure shows a more remarkable geosynthetic reinforcement effect than is seen in the horizontal stress curves because geosynthetic reinforcement is more effective in vertical confinement. Most differences are shown in the middle for Left 1 (i.e., 45 kPa) and Left 2 (i.e., 35 kPa). For the combined shear stress curves as seen in Figure 7.11, the geosynthetic

reinforcement effect is more noticeable for the Left 1 (difference of 41kPa) and Left 2 (difference of 32 kPa) due to the initial crack of PCC layer.

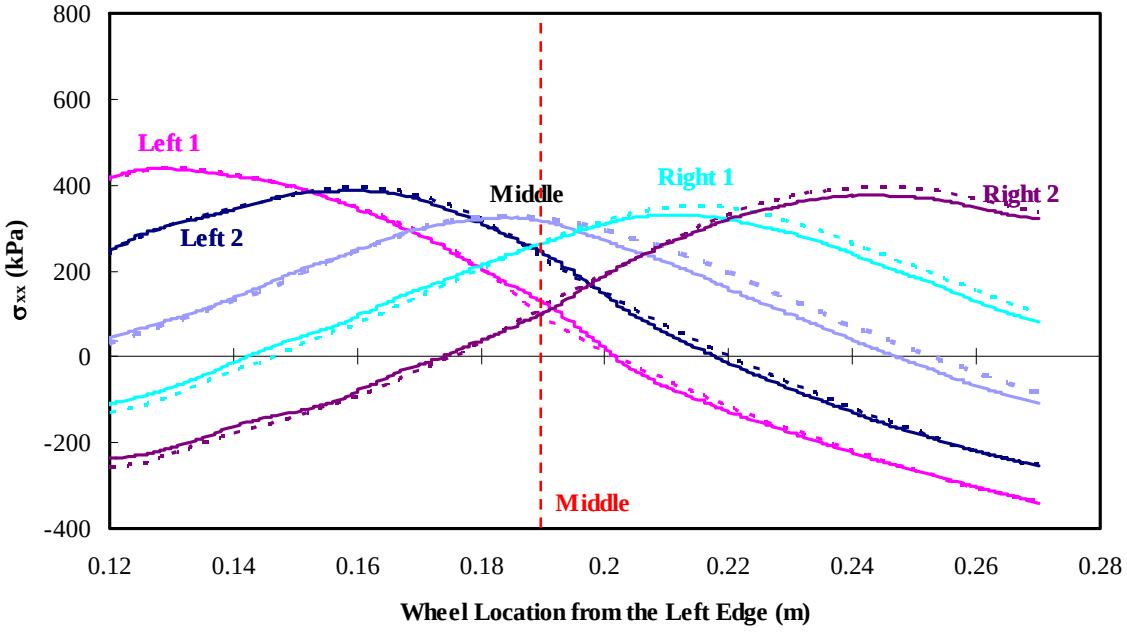

Figure 7.9 Combined σ_{xx} variations according to moving wheel locations for both cases

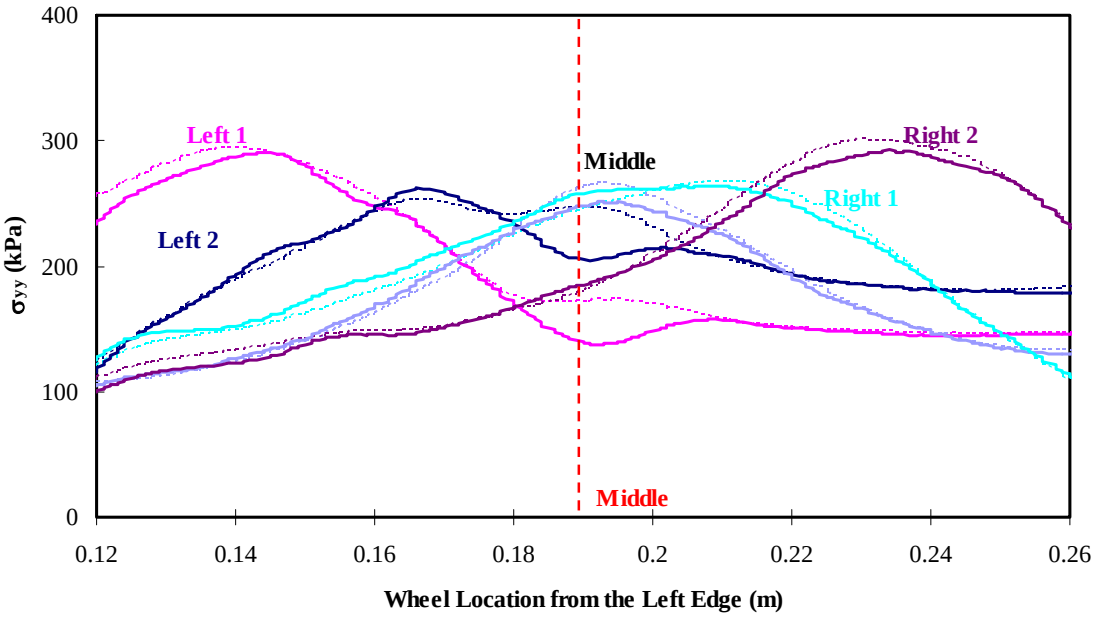

Figure 7.10 Combined σ_{yy} variations according to moving wheel locations for both cases

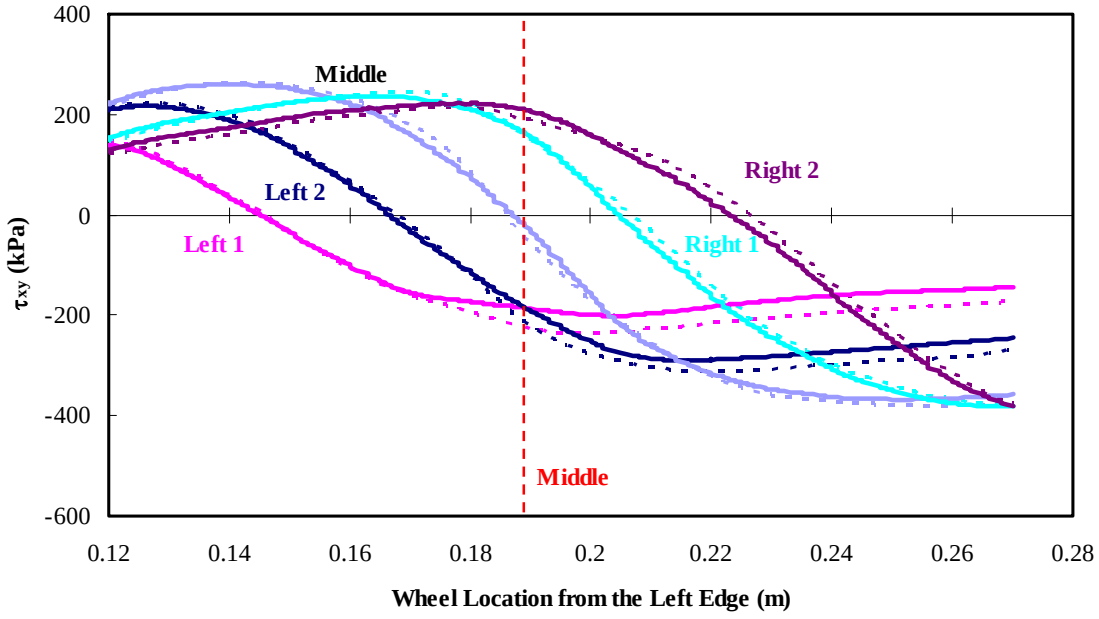

Figure 7.11 Combined τ_{xy} variations according to moving wheel locations for both cases

As further illustration, the contours of horizontal, vertical, and shear stresses are displayed in Figure 7.12. These contours are obtained after finishing the moving wheel loading. The red dotted line in the figure represents the location of the geosynthetic reinforcement. Overall, significant differences between the two cases are not apparent; however, the reinforcement effect of the geosynthetic can be seen beneath loading and around the reinforcement area.

For horizontal stress contours, stresses change from positive to negative in the upper part of the pavement overlay as the wheel moves left to right. It shows that compression converts to tension after the wheel passes by, unlike compression during loading. Conversely, stresses switch from compression to tension in the lower part of the pavement overlay. In other words, if loading is applied, the upper part undergoes compression and tension is produced in the reaction in the lower part. For vertical stress contours, overlays mostly display compression after the wheel moves away, unlike horizontal stress. In the shear stress contours, stresses are changed from positive to negative gradually according to wheel movement. Moreover, negative and positive coexist when loading is applied. In addition, the geosynthetic reinforcement effect can be seen mostly in the upper part of the overlay.

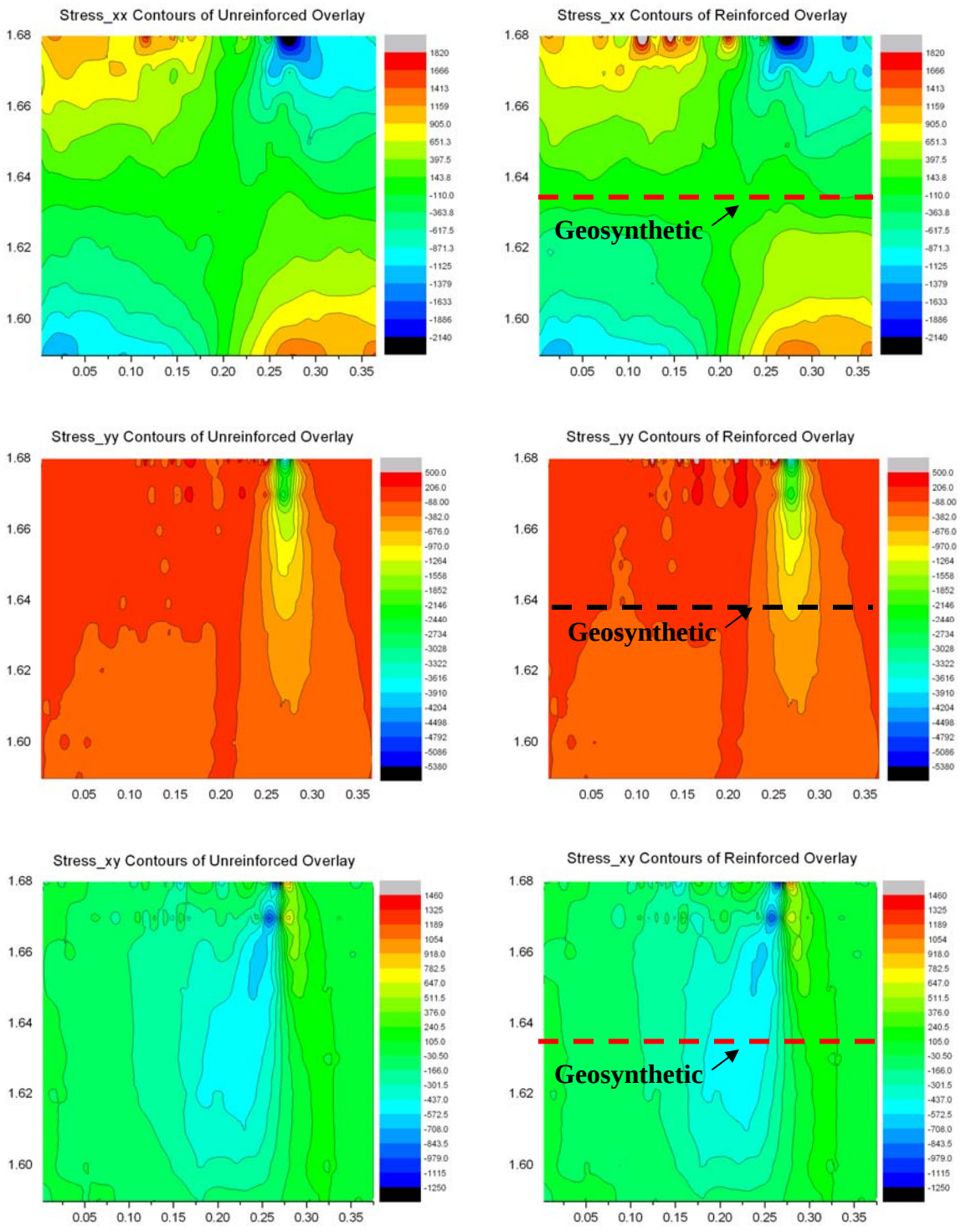

Figure 7.12 Stress contours after finishing wheel movement

7.3.2 Strain variations during wheel movement

Strain also can be obtained from measurement circles. And the sign convention is analogous to that of stress. Horizontal strain curves according to moving wheel locations for unreinforced overlay are presented in Figure 7.13. Similar to the horizontal stress curves, strain gradually increases, reaching maximum strain level at each measurement circle as the wheel is moving over it from left to right, and then strain decreases by degrees as the wheel moves to next measurement circle. Induced strain due to the external wheel loading vanishes gradually if the applied loading is moved. Figure 7.14 presents the vertical strain curves for unreinforced overlay according to moving wheel locations. Variations are relatively smaller than those of horizontal strain; in other words, more strain occurs in x-direction than in y-direction. Like horizontal strain behavior, after reaching maximum strain level due to external wheel loading, vertical strain gradually comes back its initial condition. In addition to these, horizontal strain and vertical strain behaviors according to moving wheel locations for reinforced overlay are presented in Figures 7.15 and 7.16. Strain curves in x and y directions seem to be the same as those of unreinforced overlays.

To check failure condition, the maximum strain level that is produced by one pass of the moving wheel load is compared with the DEM fracture model results addressed in Chapter 4. Horizontal strain and vertical strain at failure were 0.16% and 0.15%, respectively. Maximum horizontal and vertical strains generated by moving wheel loading are just 0.04% and 0.02% respectively, much less than 0.16% and 0.15%. This indicates that cracking cannot be induced by a single instance of moving wheel loading. It is also confirmed by stress-strain relationship in later.

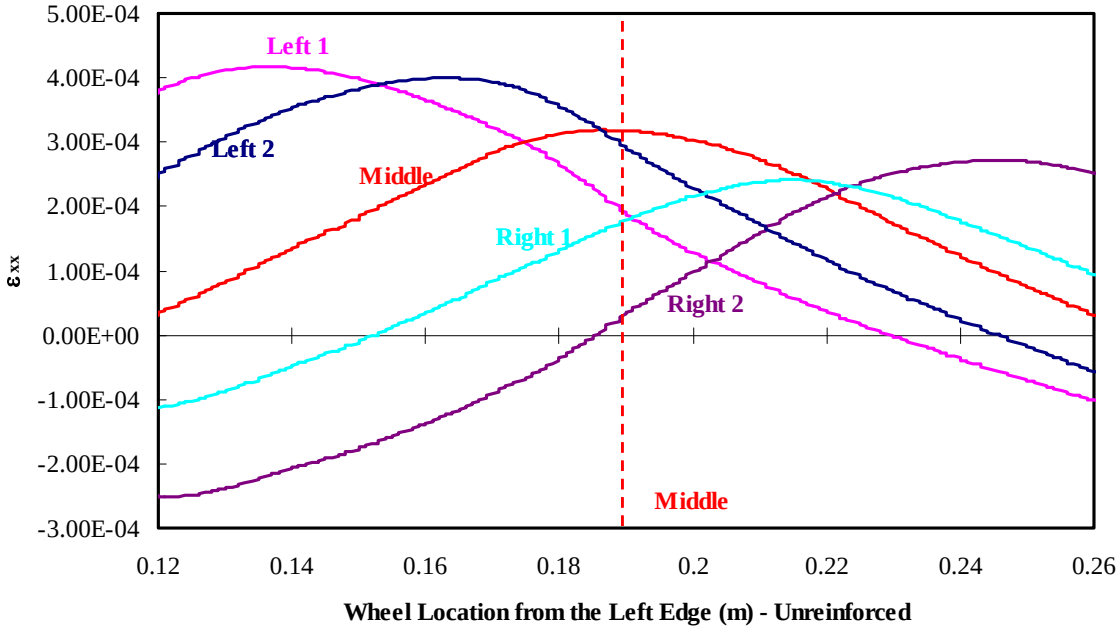

Figure 7.13 ε_{xx} variations according to moving wheel locations for unreinforced overlay

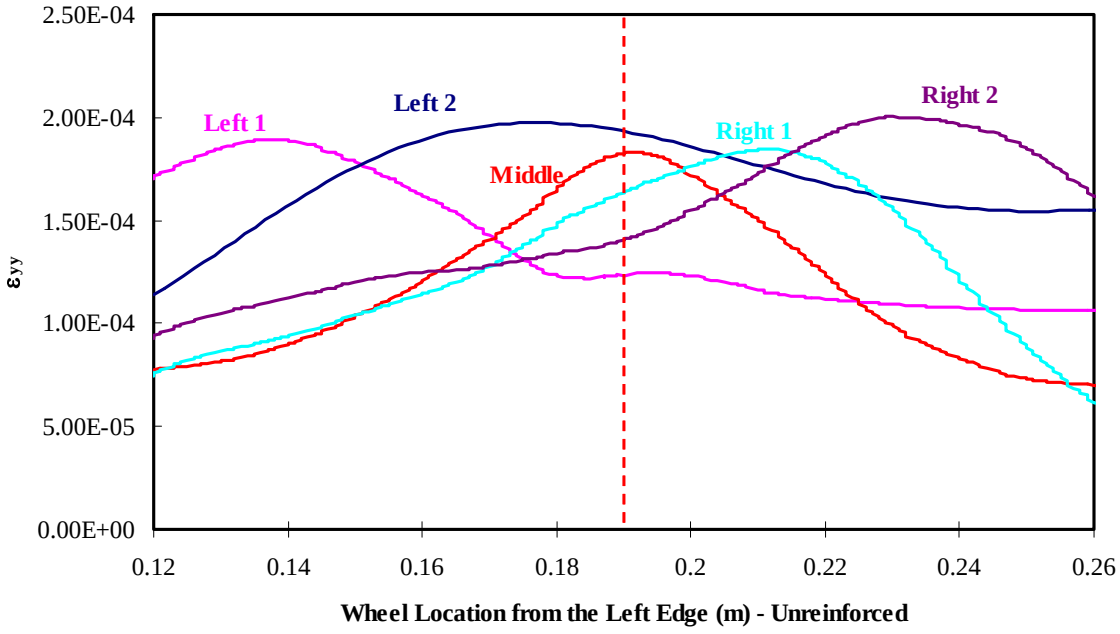

Figure 7.14 ε_{yy} variations according to moving wheel locations for unreinforced overlay

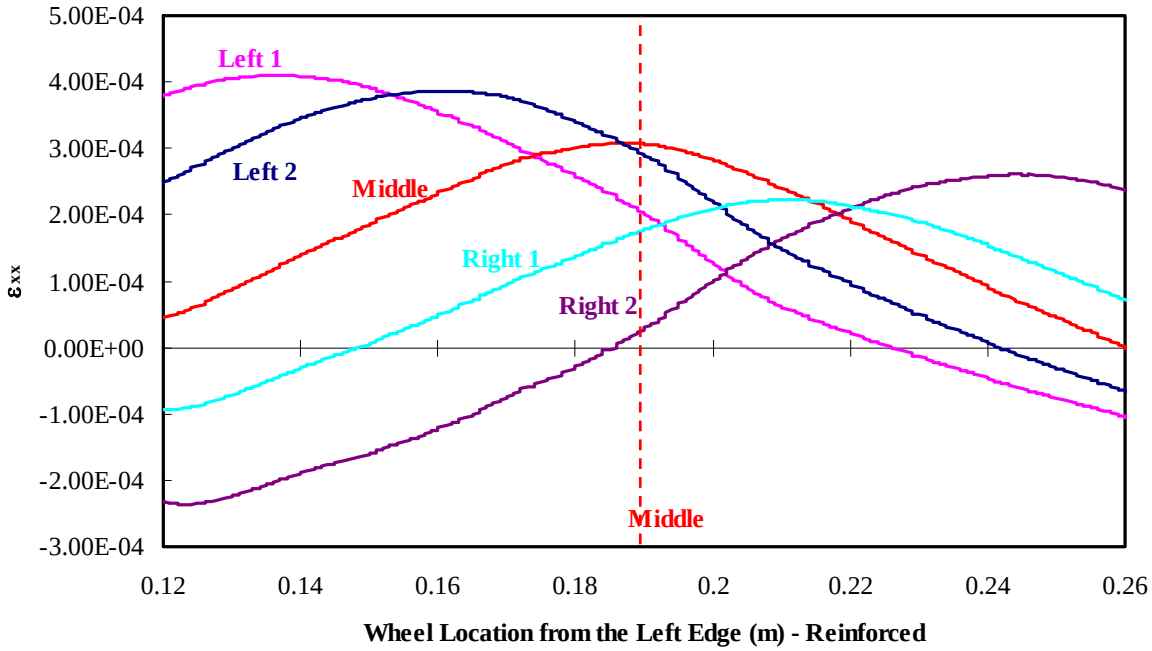

Figure 7.15 ε_{xx} variations according to moving wheel locations for reinforced overlay

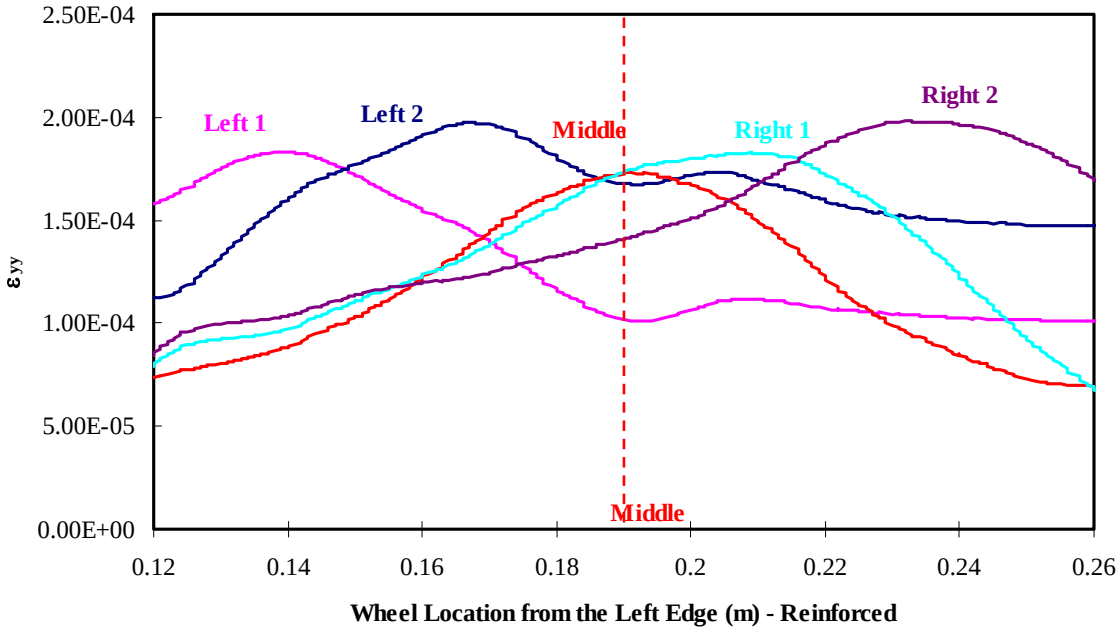

Figure 7.16 ε_{yy} variations according to moving wheel locations for reinforced overlay

Figure 7.17 shows the vertical strain distribution according to overlay depth (3, 6 and 7 measurement circles) with and without reinforcement. Vertical strain decreases by approaching geosynthetic reinforced area, and then gradually increases as approaching bottom of overlay. The significant geosynthetic effect is shown in over reinforced area, however, the effect decreases as approaching interface of overlay and PCC layer.

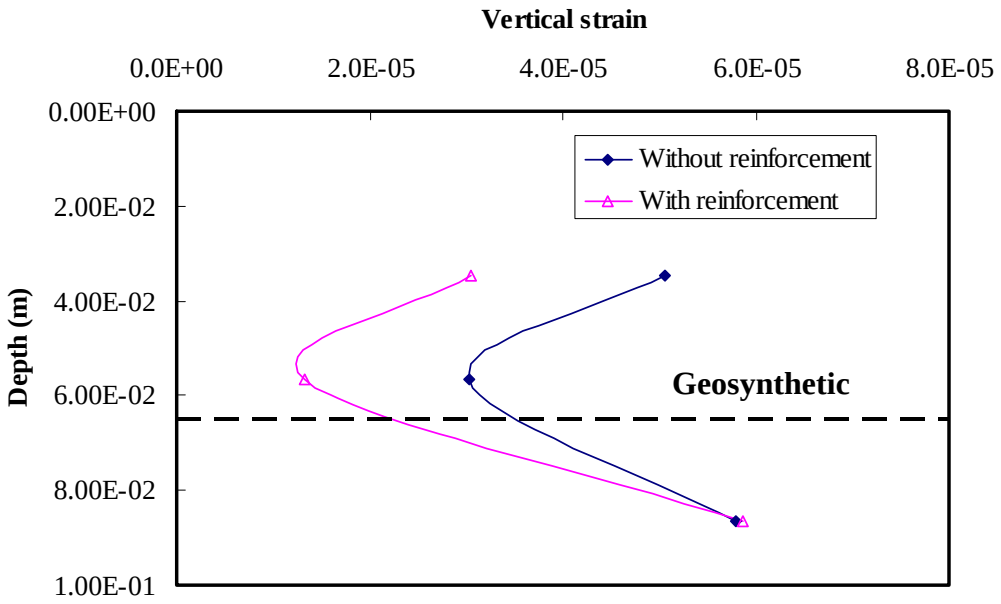

Figure 7.17 ε_{yy} variations according to overlay depth

To facilitate visual comparison of both results, combined horizontal strain curves and vertical strain curves are presented in Figures 7.18 and 7.19, respectively. With reference to Figures, geosynthetic reinforcement helps to reduce strain actions, and it seems to be more effective in the vertical direction than the horizontal direction because geosynthetic reinforcement affords vertical confinement, while it produces lateral sliding. Most vertical strain reductions of around 20% are showing in the middle for Left 1 and Left 2.

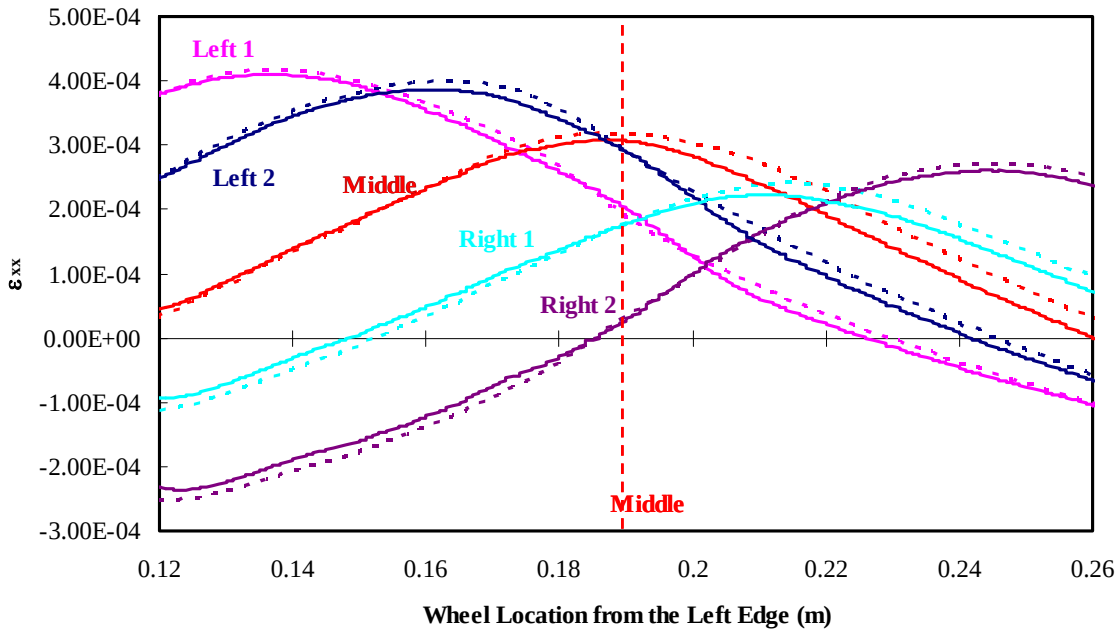

Figure 7.18 Combined ε_{xx} variations according to moving wheel locations for both cases

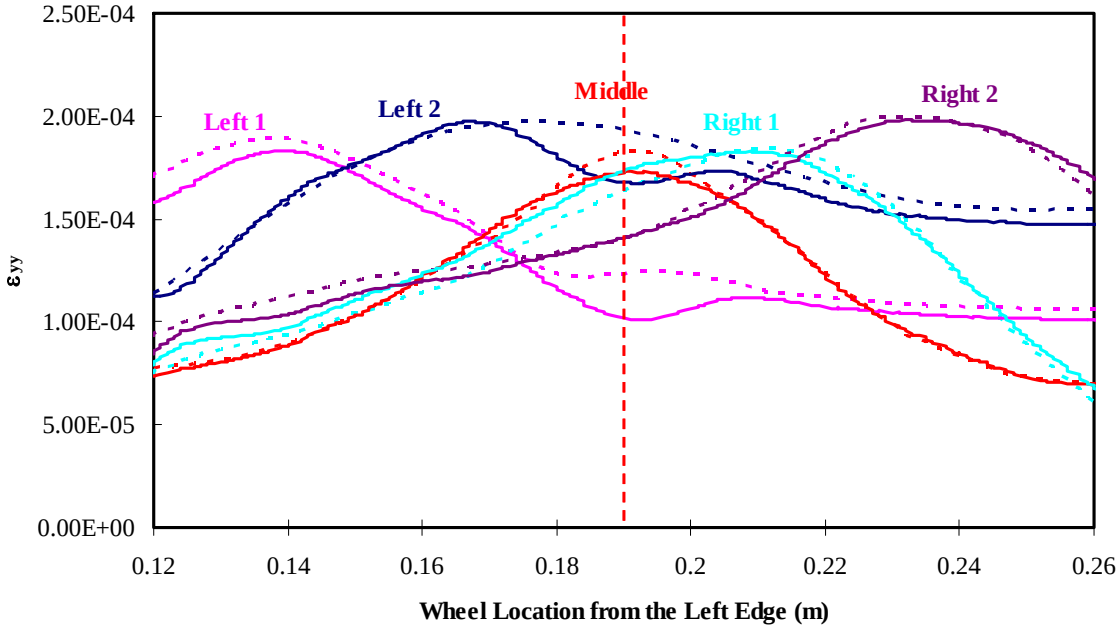

Figure 7.19 Combined ε_{yy} variations according to moving wheel locations for both cases

Figure 7.20 shows the stress-strain behavior for three different locations in AC overlay. Stresses and strains are obtained from measurement circles of 3, 6 and 7 (see Figure 7.2). Stress-strain behavior is shown differently according to the measuring locations. As location is closer to the bottom of overlay, an elastic property is lowered. And any one among three locations is not showing the failure condition. It is corresponding with strain results as addressed in before.

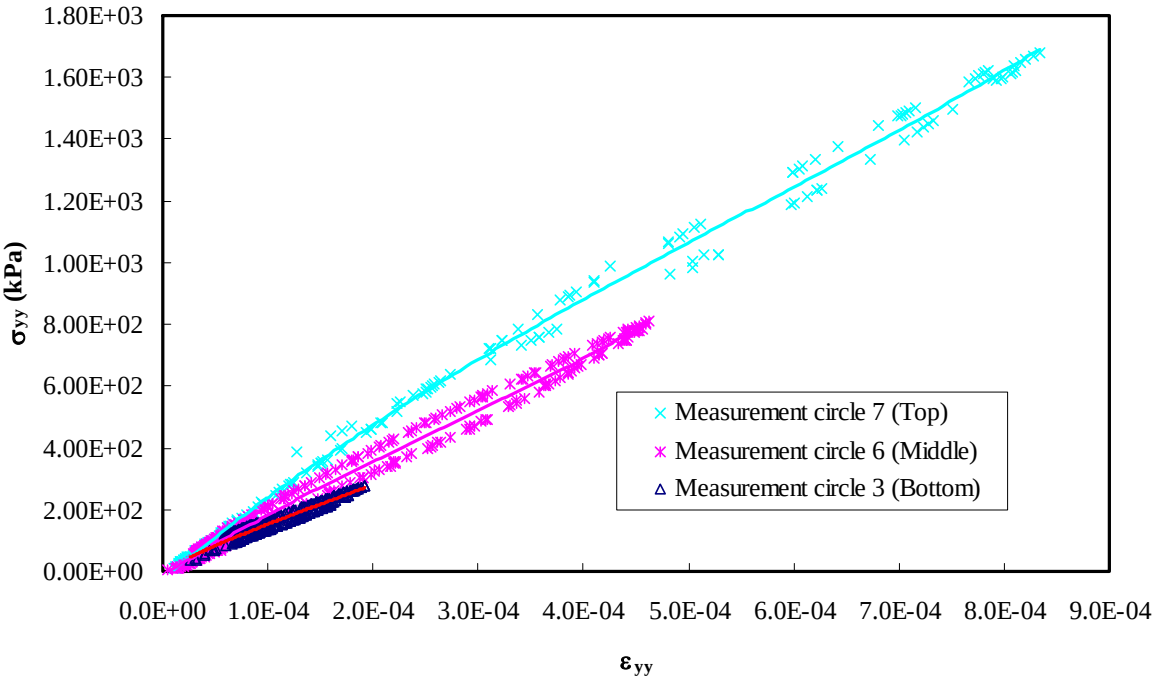

Figure 7.20 Stress-strain curves at the different locations

Porosity contours of unreinforced and reinforced overlays after moving wheel loading are presented in Figure 7.21. In the case of unreinforced overlay, porosity is divided into several vertical lines showing different porosity from loose to dense as the wheel moves from

left to right. On the other hand, the contour of porosity for reinforced overlay is divided transversely because of the geosynthetic reinforcement. The part above the reinforcement is loose but the lower part, below the reinforcement, is relatively dense. The left part is looser than the right because the wheel is moving from left to right.

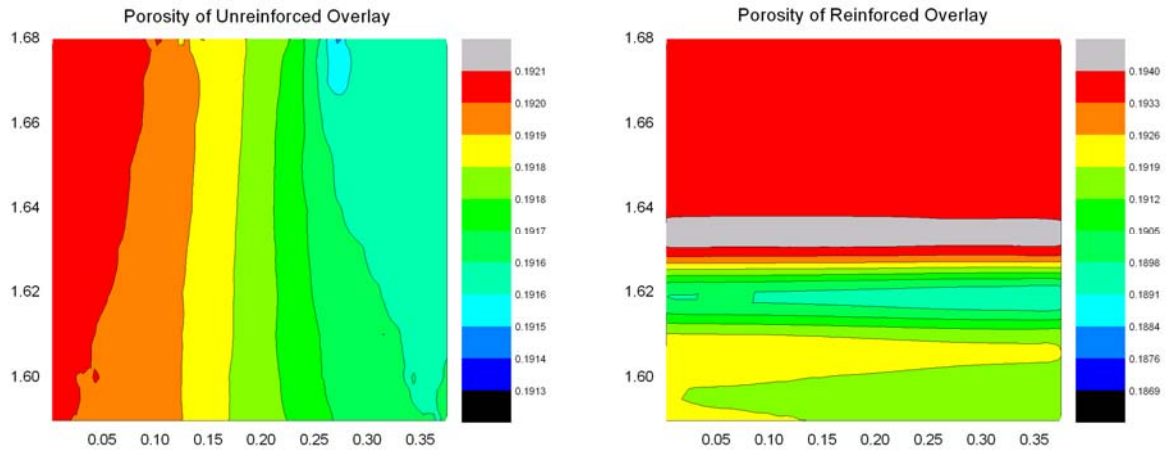

Figure 7.21 Porosity after moving wheel loading

7.4 Summary

Moving wheel load tests, as one of the different loading conditions for unreinforced and reinforced overlays, were conducted using the DEM model developed in a previous Chapter. The wheel moved from the left to right side of overlay one time because of time constraints. Stress and strain were monitored from measurement circles at 5 different positions along the path of the moving wheel. Horizontal and vertical stress curves showed relatively similar trends, except for different stress variation. Stresses in both cases were gradually increased and reached maximum stress level as the wheel moved over each

measurement circle, decreasing by degrees as the wheel passed by. However, shear stress curves showed positive at the left side of overlay and were changed to negative at the right side in turn regardless of the positions of their measurement circles. Strain behaviors were similar to those of stress. Geosynthetic reinforcement was more effective in the vertical direction than the horizontal direction because geosynthetics have the ability to confine movement vertically but induce sliding in a horizontal direction. In addition to these findings, stress contours after wheel loading were displayed for both cases and contours of air void ratio (porosity) were presented as well. Both horizontal and vertical strain levels under moving wheel loading were lower than failure strain levels which were obtained from fracture modeling in Chapter 4; thus, reflective cracking was not induced under this loading condition.

CHAPTER 8 Conclusions and Recommendations

8.1 Conclusions

This dissertation presents the results of discrete numerical investigations for the effects of geosynthetic reinforcement in overlays, applying three different loading conditions: constant pressure loading, constant loading rate for fracture, and moving wheel loading. A DEM pavement model was developed to investigate 1) the effect of an initial crack, including geosynthetic properties, geosynthetic locations, and aggregate distribution, 2) the effect of the existing pavement condition, including PCC properties and different PCC crack widths, and 3) the effect of overlay thickness with and without reinforcement embedded in the overlays. Displacement at the top of the pavement, as well as stress and strain distributions in the vicinity of the initial crack were assessed. In addition to these, not only contours for tensile, shear, and vertical stresses but also porosity contours of AC overlay were displayed. Sensitive analyses were conducted for the factor of safety, effect of particle sizes, and effect of stiffness and particle friction of asphalt concrete as well. A bilinear cohesive softening model was implemented into heterogeneous DEM pavement models and compared with field case studies for the model calibration. So far, works for comparing the results of field with DEM modeling for the whole pavement section were rarely conducted. The findings outlined in this paper contribute significantly to our better understanding of mechanisms that governs the response of overlays reinforced with geosynthetics under different loading conditions, quantifying effect of geosynthetics including initial crack, old pavement conditions and overlay thickness effects.

8.1.1 DEM model Calibration

Reflective cracking was investigated under a constant loading rate of 7 mm/sec and the results were compared with data from field case studies. The following conclusions were drawn from the results.

- The thicker overlays have more service life than the thinner overlays, and crack patterns and crack initiation locations are different according to overlay thickness under the same loading condition. Also, as overlay thickness is increased, the PCC layer is less affected by compression because of that overlay thickness.
- The geosynthetic reinforcement of AC overlay considerably improves the service life by reducing reflective cracking. The performance trends of the DEM model results and the case studies, with and without fabric, are basically the same; this is because the geosynthetic reinforcement helps distribute the contact forces more widely beneath the reinforced layer.
- A 3” reinforced overlay is very similar to the 4” AC control overlay rather than the 2” reinforced overlay of the Georgia case study because the Georgia environment is not considered in the DEM simulations. However, basic findings that geosynthetics can retard or reduce reflective cracking are the same.
- Geosynthetic reinforcement placed at a one-third depth from the bottom is more effective than geosynthetic embedded at the bottom of the overlay. This result is in good agreement with a previous chapter and with the works of Kuo and Hsu (2003) and Khodaii et al. (2009) as well.

- Geosynthetics have the benefit of reducing reflective cracking according to the geosynthetic types. Also, DEM simulation results can be varied by factors of environments such as geosynthetic properties, loading conditions, and regional conditions.
- Calibration factors of 7.9 and 9.5 (8.2) are calculated at two different sites. These factors are not significantly different; thus, it can be seen that the DEM model is an appropriate method for analyzing the pavement section.

8.1.2 DEM model under Constant loading

The following conclusions were drawn by DEM pavement modeling under constant loading pressure.

- Geosynthetics have the benefit of reducing displacement, stress, and strain. It can be explained that the geosynthetic layer performs as tensile reinforcement by preventing lateral spreading of AC overlay when placed in the AC layer (Kwon et al., 2008).
- An initial crack in the AC overlay affects pavement behaviors for tensile strain and stress field according to different geosynthetic properties, geosynthetic locations, and aggregate distributions. Significantly more tensile strain occurs with initial crack than without initial crack because the presence of a crack promotes horizontal movement. Moreover, when reinforcement is placed in initial cracked AC overlay, tensile strain increases by 18.5% over that in unreinforced overlay. However, it is noted that, as a benefit of the geosynthetic,

tensile strain decreases by around 8% above the reinforcement compared to overlay without reinforcement.

- Geosynthetic reinforcement is more effective at decreasing stress and strain both when a stiffer geosynthetic is used and when the geosynthetic is located at one-third depth of the overlay (from the bottom up). As geosynthetic modulus increases, the predicted strains effectively decrease by around 2% below the reinforcement and by around 10% above the reinforcement. Moreover, when geosynthetic is placed at 1/3H, tensile strain is decreased by 25 % compared with that of reinforcement at the bottom of the overlay.
- PCC with high modulus performs as tensile reinforcement by preventing lateral spreading of AC overlay. The high modulus develops a stiffer layer associated with interlocking action. Also, high modulus of PCC is less effective vertically and increased vertical strain affects the stress behavior.
- As crack width on PCC increases, total displacement on the top pavement section for both unreinforced and reinforced overlays also increases, though the difference is marginal. In addition, lateral strain and stress are decreased when geosynthetic is placed in the AC overlay. It can be explained that as the width of the crack/joint increases, stresses are more concentrated around it; consequently, more lateral strain is induced.
- The effect of overlay thickness on displacement is very small, but strain and stress behaviors show an obvious effect. The increased overlay thickness has a strong effect on decreasing tensile strain at the bottom of the overlay. Therefore,

increasing overlay thickness works to reduce strain and stress as if geosynthetic reinforcement were used.

- Because this model uses constant loading stress (80 psi), there is no displacement change after reaching a certain time (around 0.06 sec); therefore, displacement is not a sufficient indicator for investigating the effect of geosynthetic properties under constant loading, though marginal differences exist.

8.1.3 DEM Model with Fracture

The following conclusions were drawn from DEM fracture under constant loading rate.

- Reinforcement significantly affects the stress field in the vicinity of the crack tip, and a stiffer reinforcement material is much more effective on reducing stress and strain. For example, maximum shear stress is reduced by around 3% to 88% when GT_P1 and GT_P2 are placed in the overlay. Also, a more than 75% to 95% decrease in shear strain occurs when GT_P1 and GT_P2 are placed in the overlay.
- Reflective cracking is shown between the points under loading and above the initial crack both in unreinforced overlay and in overlay reinforced with a less stiff geosynthetic. Meanwhile, macro-cracks in overlay which is reinforced with much stiffer geosynthetic are mainly seen below the geosynthetic, and micro-cracks are also shown along the geosynthetic, covering a wider range than in the other two cases.

8.1.4 DEM model under moving wheel loading

The following conclusions were drawn from conducting the DEM model under moving wheel loading.

- Horizontal and vertical stress curves show relatively similar trends except for different stress variations. Stresses for in both cases are increased gradually and reach maximum stress level as the wheel is placed over each measurement circle; after that, stresses decrease by degrees as the wheel passes by. However, shear stress curves converted from positive if moving wheel is located on measurement circle to negative if wheel move to the next position in turn.
- The geosynthetic reinforcement stress reduction effect is more noticeable for the Left 1 (difference of 41kPa) and Left 2 (difference of 32 kPa) due to the initial crack of PCC layer. Also, most vertical strain reductions of around 20% are showing in the middle for Left 1 and Left 2.
- Stress-strain behavior is shown differently according to the measuring locations. And any one among three locations is not showing the failure condition.

8.2 Recommendations

In this study, the DEM pavement model was developed and the results were analyzed under different loading conditions. Based on the findings and limitations in this study, some recommendations are proposed as follows:

- Some model properties such as particle size distribution need to be improved to make more realistic simulations; however, it should be carefully employed

because although an increased number of particles would make it possible to capture more micro-scale properties and behaviors, the computational time would be increased dramatically.

- Hexagonal packing arrangements should be used to investigate Poisson's ratio of soil rather than cubic packing. However, Poisson's ratio still has a limitation within a certain range (e.g., maximum value of 0.33 for plane stress and 0.25 for plane strain) unless random packing arrangements are used.
- Additional, different loading conditions should be considered, such as thermal and fatigue loading.
- Pore water pressure should be considered because it can have a considerable effect on the behavior of the pavement section.
- This study is limited for rigid pavement systems, thus, it would need to be enlarged for investigating flexible pavement systems as well.
- This two dimensional simulation is simplified from the real three dimensional problems. The two dimensional plane assembly undergoes dilation at a higher rate than the three dimensional one because the two dimensional assembly can dilate in one direction only. Also, the two-dimensional Poisson's ratio is different from the three-dimensional one. Therefore, for realistic results, three dimensional assembly should be considered.
- Irregular particle shapes such as clumps (Lu and McDowell, 2007; Zhao, 2009) or ellipses (Rothenburg and Bathurst, 1992, 1993) can be simulated.

The DEM modeling in this study has unique capabilities to investigate the crack behavior of asphalt concrete as compared to continuum approaches by directly accounting for the contribution and modeling of the material's heterogeneity (discrete aggregate particles and asphalt-aggregate binder) although there should be more work needed. These very detailed geometrical representations of elements and the numerical calibrations allowed for well-founded investigation of the geosynthetic-aggregate interaction under loading.

REFERENCES

AASHTO (1993). *AASHTO Guide for Design of Pavement Structures.* American Association of State Highway and Transportation Officials, Washington, DC.

AASHTO (2002). *Standard Specifications for Highway Bridges*, 16th Edition, American Association of State Highway and Transportation Officials, Washington, DC.

Abbas, A., Masad, E., Papagiannakis, T. and Shenoy, A. (2005), "Modelling asphalt mastic stiffness using discrete element analysis and micromechanics-based models", *The Internatioal Journal of Pavement Engineering*, Vol.6, No.2, pp. 137-146

Abbas, A., Masad, E., Papagiannakis, T. and Harman, T. (2007), "Micromechanical Modeling of the Viscoelastic Behavior of Ashphat Mixtures Using the Discrete-Element Method", *International Journal of Geomechanics* ⓒASCE, March/April

Ahlrich, R. C. (1986), "Evaluation of Asphalt Rubber and Engineering Fabrics as Pavement Interlayers," Final Report, Miscellaneous Paper GL-86-34, U.S. Army Corps of Engineers, Waterways Experiment Station, Vicksburg, MS, Nov.

Aldea, C. M. and Darling, J. R. (2004), "Effect of Coating on Fiberglass Geogrid Performance", 5th International RILEM Conference, Limoges, France, 5-7 May 2004.

Allison, R.E. (1989), "Fabric Reinforcement to Prevent Reflective Cracking", Washington State Department of Transportation, Olympia, Washington.

Amini, F. (2005), "Potential Applications of Paving Fabrics to Reduce Reflective Cracking", Report, No. FHWA/MSDOT-RD-05-174, Federal Highway Administration, 39 pgs.

Anderson, T. L. (1995), *Fracture Mechanics: Fundamental and Applications*, CRC Press, Boca Raton.

Baek, J. and Al-Qadi, I.L. (2006), "Finite Element Method Modeling of Reflective Cracking Initiation and Propagation", *Journal of the Transportation Research Board*, No. 1949, pp. 32-42.

Bagi, K. (2003), "Statistical analysis of contact force components in random granular assemblies", *Granular Matter*, 5, 45-54.

Barenblatt, G.I. (1962), "Mathematical Theory of Equilibrium Cracks in Brittle Fracture", *Advances in Applied Mechanics*, Vol. 7, pp. 55-129.

Barksdale, R. D. (1991). "Fabrics in Asphalt Overlays and Pavement Maintenance." *National Cooperative Highway Research Program Report 171*, Transportation Research Board, National Research Council, Washington, DC, 72 pgs.

Barksdale, R.D. and Alba, J.L. (1993), "Laboratory determination of resilient modulus for flexible pavement design", *Interim Report No. 2*, Prepared for NCHRP, 1993 (Transportation Research Board, National Research Council: Washington, DC).

Barnhart, V. T. (1989), "Field Evaluation of Experimental Fabrics to Prevent Reflective Cracking in Bituminous Resurfacing," Final Report, Research Project 80-NM-617, Research Report No. R-1300, Research Laboratory Section, Materials and Technology Division, Michigan Transportation Commission, Lansing, July.

Bhandari, A., Han, J., Parsons, R.L. (2008), "DEM analysis of geotextile–soil interaction under wheel loading", *In: Paper Accepted for Presentation and Publication at the Research Symposium on the Characterization and Behavior of Interfaces (CBI), Atlanta.*

Bhandari, A. and Han, J. (2010), "Investigation of geotextile-soil interaction under a cyclic wheel load using the discrete element method", *Geotextiles and Geomembranes*, 28, 33-43.

Broek, D. (1984), "Elementary Engineering Fracture Mechanics", Martinus Nijhoff Publishers, The Hague, Netherlands, pp. 16, 132, 328.

Brown, S.F., N.H. Thom, and P. J. Sanders (2001), "A Study of Grid Reinforced Asphalt to Combat Reflection Cracking", *In Proceedings, Association of Asphalt Paving Technologists*, Volume 70, 2001.

Budkowska, B.B. and Yu, J. (2003), "Mitigation of short term rutting by interlocking layer developed around a geogrid-sensitivity analysis", *Comput. Geotech.*, 30, 61–79.

Buttlar, W. G., Bozkurt, D. and Dempsey, B. J. (2000), "Cost-Effectiveness of Paving Fabrics Used to Control Reflective Cracking," Transportation Research Record, Transportation Research Board, No. 1730, pp. 139-149.

Buttlar, W. G., and Roque, R. (1996), "Evaluation of Empirical and Theoretical Models to Determine Asphalt Mixture Stiffnesses at Low Temperatures", *Journal of the Association of Asphalt Paving Technologists*, 65, 99–141.

Buttlar, W.G. and You, Z. (2001), "Discrete Element Modeling of Asphalt Concrete: a Micro-fabric Approach", *Transportation Research Record*, No. 1757.

Button, J.W. (1989a), "Overlay Construction and Performance Using Geotextiles", In *Transportation Research Record 1248*, TRB, National Research Council, Washington, D.C., pp. 24-33.

Button, J.W. (1989b), "Engineering Fabrics and Asphalt Overlay Performance", Report No. 187-17. Texas Transportation Institute, Texas A&M University, College Station, Texas.

Button, J.W., C.K. Estakhri, and D.N. Little (1994), "NCHRP Synthesis of Highway Practice 193: Hot In-Place Recycling of Asphalt Concrete", *TRB*, National Research Council, Washington, D.C., 69 pp.

Button, J.W. and R.L. Lytton (1987), "Evaluation of Fabrics, Fibers, and Grids in Overlays", *In Proceedings, Sixth International Conference on Structural Design of Asphalt Pavements*, Volume 1, Ann Arbor, Michigan, July, pp. 925-934.

Button, Joe W and Lytton, Robert L. (2007), "Guidelines For Using Geosynthetics With Hot Mix Asphalt Overlays To Reduce reflective Cracking", *Transportation Research Board* For publication and presentation at the 86th Annual Meeting, January.

Camacho, G.T. and Ortiz, M. (1996), "Computational Modeling of Impact Damage in Brittle Materials", *International Journal of Solids and Structure*, Vol. 33, pp. 2899- 2938.

Carino, N. J. and Clifton J. R. (1005), "Prediction of Cracking in Reinforced Concrete Structures", Report NISTIR 5634.

Carmichael, R.F. and M.L. Marienfeld (1999), "Synthesis and Literature Review of Nonwoven Paving Fabrics Performance in Overlays", *In Transportation Research Record 1687*, TRB, National Research Council, Washington, D.C., pp. 112-124.

Carver, C. and C.J. Sprague (2000), "Asphalt Overlay Reinforcement", *Geotechnical Fabrics Report*, Industrial Fabrics Association International, St. Paul, Minnesota, March.

Chandra, S. Viladkar, M. N., Nagrale, P. P. (2008), "Mechanistic Approach for Fiber-Reinforced Flexible Pavements", *Journal of Transportation Engineering*, Vol. 134, No. 1.

Chang, C. S., Wang, T. K., Sluys, L. J. and Mier, J. G. M. (2002), "Fracture modeling using a micro-structural mechanics approach-I. Theory and formulation", *Engineering Fracture Mechanics* 69, 1941-1958

Chang, K.G. and Meegoda, J.N. (1997), "Micromechanical Simulation of Hot Mix asphalt", *Journal of Engineering Mechanics*, Vol. 123, No. 5, May, pp. 495-503.

Chareyre, B., Briançon, L., and Villard, P. (2002), "Theoretical Versus Experimental Modeling of the Anchorage Capacity of Geotextiles in Trenches", *Geosynthetics International*, Vol. 9, No. 2, pp. 97-123.

Chareyre, B., Villard, P. (2002), "Discrete element modeling of curved geosynthetic anchorages with known macro-properties", In: Paper Presented at the Numerical Modeling in Micromechanics Via Particle Methods, Gelsenkirchen, Germany.

Camacho, G. T., and Ortiz, M. (1996), ‘‘Computational Modeling of Impact Damage in Brittle Materials,’’ *Int. J. Solids Struct.*, **33**, pp. 2899–2938.

Chen, T., Mao, K., Huang, X., and Wang, M. Y., “Dissipation mechanisms of non-obstructive particle damping using discrete element method”, Smart Structures and Materials 2001: Damping and Isolation, Proceedings of SPIE Vol. 4331.

Christensen, R.M. and Lo, K.H. (1979), “Solutions for Effective Shear Properties in Three Phase Sphere and Cylinder Models”, *Journal of Mechanics in Physics and Solids*, Vol. 27, pp. 315-330.

Cleveland, G.S., Button, J.W. and Lytton, R. L. (2002), “Geosynthetics in Flexible and Rigid Pavement Overlay Systems to reduce Reflection Cracking”, FHWA/TX-02/1777-1.

Collop, A. C., McDowell, G. R., and Lee, Y. (2004), “Use of the Distinct Element Method to Model the Deformation Behavior of an Idealized Asphalt Mixture”, *International Journal of Pavement Engineering*, Volume 5, Issue 1.

Counto, V.J. (1964), “The Effect of the Elastic Modulus of the Aggregate on the Elastic Modulus, Creep, and Creep Recovery of Concrete”, *Magazine of Concrete Research*, Vol.62, No. 48, pp. 129-138.

Cui, L. and O’Sullivan, C. (2006), “Exploring the macro- and micro-scale response characteristics of an idealized granular material in the direct shear apparatus” *Geotechnique* **56**(7), 455-468.

Cundall, P.A., and Strack, O.D.L. (1979), “Discrete numerical model for granular assemblies”, *Geotechnique*, 29(1).

Cundall, P.A. and Potyondy, D.O. (2004), “A bonded-particle model for rock”, *International Journal of Rock Mechanics & Mining Sciences* 41.

Daniel, I. M. (1993), ‘‘Composite Materials,’’ A. S. Kobayashi, ed., *Handbook on Experimental Mechanics*, Society for Experimental Mechanics, Bethel, CT.

Delmas, P. (1979), “Sols renforcés par géotextiles. Premières études”, The. Doct. Ing. IRIGM Uni. Grenoble, p. 202.

Deresiewicz, H. (1958), “Mechanics of granular material”, *Advd. Appl. Mech.* 5, 233-306.

Duffy, J., and Mindlin, R. D. (1957), “Stress-strain relations of a granular medium”, *J. Appl. Mech.*, 24(4), 585-593.

Dugdale D. (1960), “Yielding of Steel Sheets Containing Slits”, *Journal of Mechanics and Physics of Solids*, Vol. 8, pp. 100-104.

Einstein, A. (1911), “Eine Neue Bestimmung der Molekuldimensionen”, *Annalen der Physik*. Vol. 34, pp. 591-592.

Eltahan, A. A and Lytton, R. L. (2000), “A Mechanistic-Empirical Approach for Modeling Reflection Cracking”, *Transportation Research Board*

Elseifi, M. A. and Al-Qadi, I. L. (2005), “Modeling of Strain Energy Absorbers for Rehabilitated Cracked Flexible Pavements”, *Journal of Transportation Engineering*, p 653-661.

Elseifi, M. M. and Al-Qadi, I. L. (2003), “A Simplified Overlay Design Model against Reflective Cracking Utilizing Service Life Prediction”, *Transportation Research Board.*

Evans, T. M., and J. D. Frost. (2007). “Shear Banding and Microstructure Evolution in 2D Numerical Experiments.” *Proceeding of GeoDenver 2007: New Peaks in Geotechnics*, February 18-21. Denver, CO.

Evans, T. M., Mojarrad, H., Cunningham, C., and Tayebali, A. A. (2009), “Grain Size Distribution Effects in 2D Discrete Numerical Experiments”, Proceedings of Selected Sessions of the 2009 International Foundation Congress and Equipment Expo.

Finn, F.N., and C.L. Monismith (1984), " *NCHRP Synthesis of Highway Practice 116: Asphalt Overlay Design Procedures*. TRB, National Research Council, Washington, D.C., 1984, 66pp.

Finn, W. D. L. (1963), "Boundary Value Problems of Soil Mechanics", *Journal of the Soil Mechanics and Foundation Division*, ASCE. Vol. 89, No. SM5, pp. 39-72.

Germann, F.P., and R.L. Lytton (1979), "Methodology for Predicting the Reflection Cracking Life of Asphalt Concrete Overlays", Report No. FHWA-TX-79-09 + 207-5. Texas State Department of Highways and Public Transportation, Austin, Texas

Guo, Z.K., Kobayashi, A.S., and Hawkins, N.M. (1995), "Dynamic Mixed Mode Fracture of Concrete," *International Journal of Solids and Structures*, Vol. 32, No. 17/18, pp. 2591-2607

Gurjar, A.H., T.Tang, and D.G. Zollinger (1997), "Evaluation of Joint Sealants of Concrete Pavements", Report No. 187-27. Texas Transportation Institute, College Station, Texas.

Haas, R., Walls, J., and Carrol, R. G. (1998), "Geogrid reinforcement of granular base in flexible pavements", *Transportation Research Board*, 1188, pp 19-27.

Hainbuchner, E., Potthoff, S., Koneitzky, H., and te Kamp, L. (2002), "Particle based modeling of shear box tests and stability problems for shallow foundations in sand", 1st International PFC Symposium on Numerical Modeling in Micromechanics via Particle Methods, Gelsenkirchen, Germany, pp 151-156.

Han, J., Bhandari, A., and Wang, F. (2011), "DEM analysis of stresses and deformations of geogrid-reinforced embankments over piles", *International Journal of Geomechanics*, ASCE, in press.

Han, J., Zhang, Y.Z., and Parsons, R.L. (2008), "Development of a performance-based laboratory test method for evaluating geosynthetics-soil confinement", CD-Rom Publication, *the 87th TRB Annual Meeting*, January, Washington, DC.

Hashin, Z. (1965), "Viscoelastic Behaviour of Heterogeneous Media", *Journal of Applied Mechanics, Trans. ASME*, No. 9, pp. 630-636.

Heins, D. (1989), "A Study of the Use of Fabric to Retard Reflective Cracking Over Widening Joints", Iowa Department of Transportation, Ames, Iowa, July.

Hermann, F.V., B.J. Dempsey, and M.T. Mukhtar (1997), "Interlayer Stress Absorbing Composite in AC Overlays", Aircraft Pavement Technology Conference: In the Midst of Change, American Society of Civil Engineers, Seattle, Washington.

Hirsh, T.J. (1962), "Modulus of Elasticity of Concrete Affected by Elastic Modulus of Cement Paste Matrix and Aggregate." *Journal of the American Concrete Institute*, Vol. 59, No. 3, pp. 427-452.

Holtz, R.D., Christopher, B. R., and Berg, R. R. (1998). "Geosynthetic Design and Construction Guidelines", Publication No. FHWA HI-95-038. Federal Highway Administration, Washington, DC, 459 pgs.

Huang, Yang H. (1993), "PAVEMENT ANALYSIS AND DESIGN", Prentice Hall, Second Edition

Ince, R., Arslan, A., and Karihaloo, B. L. (2003), "Lattice Modeling of Size Effect in Concrete Strength", *Engineering Fracture Mechanics*, Vol. 70, 2307-2320.

ITASCA Consulting Group, Inc. (2004), *PFC 2D version 3.1*, Minneapolis, Minnesota, 55415, USA.

Jackson, R.D. (1980), "Use of Fabrics and Other Measures For Retarding Reflective Cracking of Asphaltic Concrete Overlays", Report No. FAA-RD-80-8. WES-MP-GL-80-2, Waterways Experiment Station.

Jayawicrama, P.W. and R.L. Lytton (1987), "Methodology for Predicting Asphalt Concrete Overlay Life Against Reflection Cracking", *In Proceedings, Sixth International Conference on Structural Design of Asphalt Pavements*, Vol.1, Michigan, July, pp.912-924.

Jin, Z. H., Paulino, G. H., and Dodds Jr., R. H. (2003), "Cohesive fracture modeling of elastic–plastic crack growth in functionally graded materials", *Engineering Fracture Mechanics*, Volume 70, Issue 14, September 2003, Pages 1885-1912.

Khodaii, A., Fallah, S. and Nejad, F. M. (2009), "Effects of geosynthetics and reduction of reflection cracking in asphalt overlays", *Geotextiles and Geomembranes*, 27, 1-8.

Kim, J. and Buttlar W.G. (2002), "Analysis of Reflective Crack Control System Involving Reinforcing Grid over Base-Isolating Interlayer Mixture", *Journal of Transportation Engineering*, pp. 375-384

Kim, H., and Buttlar W.G. (2005), "Micromechanical Fracture Modeling of Asphalt Mixture Using the Discrete element Method", Geotechnical Special Publication, n 130-142, *Geo-Frontiers 200*5.

Kim, H., Wagoner, M.P. and Buttlar, W.G. (2005), "Toward Realistic Heterogeneous Fracture Modeling of Asphalt Mixture Using Disk-Shaped Compact Tension Test Based on Discontinuum Approach", *Transportation Research Board*, January

Kim, H. (2007), Investigation of Toughening Mechanisms in the Facture of Asphalt Concrete using the clustered Discrete Element Method, Ph.D Dissertation, University of Illinois at Urbana-Champaign

Kohutek, G.L. (1983), "The Development of Regional Overlay Design Equations to Consider Reflection Cracking," Master's Thesis, Texas A&M University.

Konietzky, H. and Keip, M.-A (2005), "PFC3D discrete element modeling of geogrid pullout tests", *Interim Progress Report*, Prepared for Tensar Earth Technologies, Inc., ITASCA Consultants GmbH, Gelsenkirchen, Germany.

Konietzky, H., te Kamp, L. and Hainbuchner, E. (2000), "Tensar geogrid modeling part II: interaction of the geogrid with soil (pullout test)", *Progress Report*, Prepared for Tensar International, ITASCA Consultants GmbH, Gelsenkirchen, Germany, 30p.

Konietzky, H., te Kamp, L., Gro¨ger, T. and Jenner, C. (2004), “Use of DEM to model the interlocking effect of geogrids under static and cyclic loading”, *In Numerical Modeling in Micromechanics via Particle Methods*, edited by Y. Shimizu, R. Hart and P. Cundall, pp. 3–12 (A.A. Balkema: Rotterdam).

Kose, S., Guler, M., Bahia, H.U., and Masad, E., (2000), “Distribution of Strains within Asphalt Binders in HMA Using Image and Finite Element Techniques”, *Transportation Research Record*, No. 1728, pp. 21-27.

Kuo Ch. M., Hsu T. R. (2003), “Traffic induced reflective cracking on pavements with geogrid reinforced asphalt concrete overlay”, 82nd Annual TRB Meeting, pp. 1-23.

Kwon, J., E. Tutumluer and H. Konietzky (2008). "Aggregate base residual stresses affecting geogrid reinforced flexible pavement response". *The international journal of pavement engineering (1029-8436)*, 9 (4), p. 275.

Kwon, J., Tutumluer, E. and Kim, M. (2005a), “Development of a mechanistic model for geosynthetic-reinforced flexible pavements”, *Geosynth. Int*., 12(6), 310–320.

Lobo-Guerrero, S., Vallejo, L.E.; Vesga, L.F. (2006). “Visualization of crushing evolution in granular materials under compression using DEM.” *International Journal of Geomechanics*, 6(3), pp. 195-200.

Lytton, Robert L. (1989), “Use of Geotextiles for Reinforcement and Strain relief in Asphalt Concrete”, *Geotextiles and Geomembrane*s *vol.*8, 217-237.

Magnier, S. A., and Donzé, F. V. (1998), “Numerical simulations of impacts using a discrete element method”, *Mechanics of Cohesive-frictional Materials*, Volume 3, Issue 3, pages 257–276, July 1998.

Marienfeld, M.L. and T.L. Baker (1999), “Paving Fabric Interlayer System as a Pavement Moisture Barrier”, *In Transportation Research Circular Number E-C006*, TRB, National Reseach Council, Washington, D.C., March.

Masad, E., Tashman, L., Somedavan, N. and Dallas Little, D. (2002), "Micromechanics-Based Analysis of Stiffness Anisotropy in Asphalt Mixtures", *Journal of Materials in Civil Engineering*, Vol. 14, Issue 5, TECHNICAL PAPERS.

Mascunana, I. (1981). "An Evaluation of Engineering Fabric in Pavement Rehabilitation (IHD-21)," Final Report, Physical Research Report No. 88, Illinois Department of Transportation.

Masson, S. and Martinez, J. (2001), "Micromechanical analysis of the shear behavior of a granular material", *Journal of Engineering Mechanics*, V.127, n10, October, 2001, the static and flow aof dense granular systems, pp.1007-1016.

Masuya H, Kajukawa Y, Nakata Y. (1994), "Application of the distinct element method to the analysis of concrete members under impact", *Nuclear Engineering and Design*; 6(2): 283-294.

Matys, M. and Baslik, R. (2004), "Study of interlocking effect by the push test", Proceedings of Asian Regional Conference on Geosynthetics (GeoAsia'04), Seoul, Korea, pp 341-347.

Maurer, D.A. and G.J. Malasheskie (1989), "Field Performance of Fabrics and Fibers to Retard Reflective Cracking", *In Transportation Research Record 1248*, TRB, National Research Council, Washington, D.C., pp. 13-23.

Maxim Technologies, Inc. (1997), "NONWOVEN PAVING FABRICS STUDY FINAL REPORT", *Industrial Fabrics Association International Geotextile Division*, December.

McDowell, G. R. (2002), "On the Yielding and Plastic Compression of Sand", *SOILS AND FOUNDATIONS -TOKYO-*, 42(1), 139-146.

McDowell, G. R. and Amon, A. (2000), "Yielding of granular materials", *Soils and Foundations* 40(5), p. 133.

McDowell, G.R., Harireche, O., Konietzky, H., Brown, S.F. and Thom, N.H. (2006), "Discrete element modelling of geogrid-reinforced aggregates", *In Proceedings of the*

Institution of Civil Engineers, Geotechnical Engineering 159, January, pp. 35–48.

McLaughlin, A.L. (1979), "Reflection Cracking of Bituminous Overlays for Airport Pavements, A State of the Art", Report No. FAA-RD-79-57. Federal Aviation Administration.

Mosalam, Khalid M., and Paulino, Glaucio H. (1997), "Evolutionary characteristic length method for smeared cracking finite element models", *Finite Elements in Analysis and Design*, Volume 27, Issue 1, 30 September 1997, Pages 99-108.

Mustoe, GGW., and Griffiths, DV. (1998), "An Equivalent Continuum Model Using the Discrete Element Method", *Proceedings of the 12th ASCE Engineering Mechanics Conference*, pp. 989-992.

Olovsson L., Simonsson K. and Unosson M. (2005), "Selective mass scaling for explicit finite element analyses", *International Journal for Numerical Methods in Engineering*, **63**, No 10, 1496-1505

Ord, A., Hobbs, B., Regenauer-Lieb, K. (2007). "Shear band emergence in granular materials - a numerical study", *International Journal for Numerical and Analytical Methods in Geomechanics*, 31(3) pp. 373-393.

Ortiz, M., and Pandolfi, A. (1999), "Finite-deformation irreversible cohesive elements for three-dimensional crack-propagation analysis", *Int. J. Numer. Meth. Engng*. 44, pp.1267-1282.

O'Sullivan, C., and Bray, J.D. (2004), "Selecting a suitable time step for discrete element simulations that use the central difference time integration scheme", *Engineering Computations*, v 21, n 2, p 278-303.

Papagiannakis, A. T., Abbas, A. and Masad, E. (2002), "Micromechanical Analysis of Viscoelastic Properties of Asphalt Concretes", *Transportation Research Record: Journal of the Transportation Research Board*, Volume 1789.

Paris, P.C. and F.A. Erdogan (1963), "Critical Analysis of Crack Propagation Laws", Transactions of the ASME, *Journal of Basic Engineering*, Vol. 85, Series D, No. 4.

Pickett, D.L. and R.L. Lytton (1983), "Laboratory Evaluation of Selected Fabrics for Reinforcement of Asphalt Concrete Overlays", Report No. FHWA-TX-84+261-1. Texas Transportation Institute, College Station, Texas.

Perkins, S.W. (2001), "Numerical Modelling of Geosynthetic Reinforced Flexible Pavements", Report No. FHWA/MT-01-003/99160-2, Federal Highway Administration, USA, 97 pp.

Perkins, S.W., Bowders, J.J., Christopher, B.R. and R.R. Berg (2005), "Geosynthetic Reinforcement for Pavement Systems: US Perspectives", Geotechnical Special Publication, n 130-142, *Geo-Frontiers 200*5

Perkins, S.W., Cuelho, E.V. (1999), "Soil–geosynthetic interface strength and stiffness relationships from pullout tests", *Geosynthetics International* 6 (5), 321–346.

Perkins, S.W. and Svano, G. (2004), "Assessment of interface shear growth from measured geosynthetic strains in a reinforced pavement subject to repeated loads", In Compendium of Papers CD-ROM, 83rd *Transportation Research Board (TRB) Annual Meeting*, Washington, DC.

Poe Jr, C.C. (1983), **"**A unifying strain criterion for fracture of fibrous composite laminates", *Engineering Fracture Mechanics*, Volume 17, Issue 2, pp 153-171.

Potyondy, D. O., and P. A. Cundall (2004), "A Bonded-Particle Model for Rock," *Int. J. Rock Mech. & Min. Sci.*, ***41***(8), 1329-1364.

Qian, Y., Han, J., and Pokharel, S.K., and Parsons, R.L. (2011), "Stress analysis on triangular aperture geogrid-reinforced bases over weak subgrade under cyclic loading - an experimental study", *Journal of the Transportation Research Board*, No. 2204, *Low-Volume Roads*, Vol. 2, 83-91.

Rice, J.R. (1968), "A Path Independent Integral and Approximate Analysis of Strain Concentration by Notches and Cracks", *ASME Journal of Applied Mechanics*, 35, pp.379-386.

Roberts, F.L., P.S. Kandhal, E.R. Brown, D.Y. Lee, and T.W. Kennedy (1996), "Hot Mix Asphalt Materials, Mixture Design and Construction", NAPA Research and Education Foundation, Lanham, Maryland.

Routhenburg, L., Bogobowicz, A., and Hass, R. (1992), "Micromechanical Modeling of Asphalt Concrete in Connection with Pavement Rutting Problems", *7th International Conference on Asphalt Pavements*, Vol. 1, pp. 230-245.

Ruiz, J M, Schindler, Anton K., Rasmussen, R. O., Nelson, P. K., and Chang, G. K. (2001), "Concrete Temperature Modeling and Strength Prediction Using Maturity Concepts in the FHWA HIPERPAV Software", *Transportation Research Board.*

Santamarina, J.C., Klein, K.A., and Fam, M.A. (2001), *Soils and Waves*, J. Wiley and Sons, Chichester, p.488.

Schapery, R. A. (1973), "A theory of crack growth in viscoelastic media", Report NN-2764-73-1, Mechanics and Materials Research Center, Texas A&M University, 1973.

Schapery, R. A. (1982), "Models for damage growth and fracture in nonlinear viscoelastic particulate composites", In *Proceedings, 9th US Congress of Applied Mechanics,* American Society of Mechanical Engineers, Book No. H00228.

Shet, C. and Chandra, N. (2002), "Analysis of Energy Balance When Using Cohesive Zone Models to Simulate Fracture Processes", *Journal of Engineering Materials and Technology,* Vol. 124

Seif, M.A. and Shanjahan, M. (2001). "Mixed-mode failure of graphite/epoxy composites", *Journal of Engineering Materials and Technology, Transactions of the ASME,* v 123, n 3, July, p 371-376

Seif, M.A. and Dasari, N.B. (2001), "Effect of combined loading on cracks in graphite\epoxy composites", *Composite Structures*, v 52, n 3-4, May/June, *Design and Manufacturing of Composite Structures*, p 539-544

Sherman, G. (1982), "NCHRP Synthesis of Highway Practice 92: Minimizing Reflection Cracking of Pavement Overlays, *Transportation Research Board*, National Research Council, Washington, D.C., 38 pp.

Shuler, S. and Harmelink, D. (2004), "Reducing Reflection Cracking in Asphalt Pavements", 5th International RILEM Conference, Limoges, France, 5-7 May 2004.

Siegmund, T., and Needleman, A.(1997), "A numerical study of dynamic crack growth in elastic-viscoplastic solids", *International Journal of Solids and Structures*, v 34, n 7, 769-87, March 1997.

Smith, R.D. (1984), "Laboratory Testing of Fabric Interlayers for Asphalt Concrete Paving", Report No. FHWA/CA/TL-84/06. California Department of Transportation, Translab, June.

Smith, R.D (1983), "Laboratory Testing of Fabric Interlayers for Asphalt Concrete Paving: Interim Report", *In Transportation Research Record 916*, TRB, National Research Council, Washington, D.C., pp.6-18.

Sobhan, K., Genduso, M., Tandon, V., (2005), "Effects of geosynthetic reinforcement on the propagation of reflection cracking and accumulation of permanent deformation in asphalt overlays", Third LACCET International Latin American and Caribbean Conference for Engineering and Technology (LACCET 2005), *Advances in Engineering and Technology*: A Global Perspective 8-10, June 2005, Cartegena, Columbia, pp. 1-9.

Song, S.H., Paulino, G.H. and Buttlar, W.G. (2005), "Cohesive zone simulation of mode I and mixed-mode crack propagation in asphalt concrete.", Geotechnical Special Publication, n 130-142, *Geo-Frontiers 200*5, p 189-198

Sousa, J., Weissman, S. L., Sackman, J. L., and Monismith, C. L. (1999), "Nonlinear elastic viscous with damage model to predict permanent deformation of asphalt concrete mixes**",** *Transportation Research Record*, Issue 1384.

Souza, F.V., Soares, J.B., Allen, D.H., and Evangelista, F. (2004), "Model for Predicting Damage Evolution in Heterogeneous Viscoelastic Asphaltic Mixture", *Transportation research Record*, No 1891, pp 131-139.

Sprague, C.J., Allen, S., and Tribbett, W. (1998), "Tensile properties of asphalt overlay geosynthetic reinforcement," *Transportation Research Record*, No. 1611, pp 65-69.

Sprague, C.J., Lothspeich, S., Chuck, F., Goodrum, R. (2004), "Geogrid Reinforcement of Road Base Aggregate – Measuring the Confinement Benefit," proceedings, *Geeo-Trans 2004*, Conference, Los Angeles.

Tavarez, F. and Plesha, M. E. (2007), "Discrete element method for modeling solid and particulate materials", *Int. J. Numer. Meth. Engng*, 70: pp. 379-404

Thornton, C. (2000), "Numerical simulations of deviatoric shear deformation of granular media", *Geotechnique*, 50(1), pp.465-481.

Tutumluer, E., Huang, H., Hashash, Y.M.A., and Ghaboussi, J. (2009). "AREMA Gradations Affecting Ballast Performance Using Discrete Element Modeling (DEM) Approach," In Proceedings of the AREMA 2009 Annual Conference, Chicago, Illinois, September 20-23.

Tvergaard, V. (1990), "Effect of Fiber Debonding in a Whisker-Reinforced Metal", *Materials Science and Engineering*, Vol. 125, pp. 203-213.

Ullidtz, P. (2001), "Distinct Element Method for Study of Failure in Cohesive Particulate Media", *Transportation Research Record: Journal of the Transportation Research Board*, Vol. 1757.

Vallejo, L.E., Sebastian Lobo-Guerrero and Hammer, K. (2006). "Degradation of a Granular Base under a Flexible Pavement: DEM Simulation", *International Journal of Geomechanics*, Vol. 6, No. 6, pp. 435-439.

Villard, P., Chareyre, B. (2004), “Design methods for geosynthetic anchor trenches on the basis of true scale experiments and discrete element modeling”, *Canadian Geotechnical Journal* 41, 1193–1205.

Villard, P., and Giraud, H. (1998), “Three-Dimensional Modeling of the Behavior of Geotextile Sheets as Membranes”, *Textile Research Journal*, November, vol. 68 no. 11, pp. 797-806.

Voigt, W. (1889), “A Unified Micromechanical Approach”, *Mechanics of composite materials*, 12-21. Elsevier.

Waddoups, M. E., Eisenmann, J. R. and Kaminski, B. E. (1971), “Macroscopic Fracture Mechanics of Advanced Composite Materials”, *Journal of Composite Materials*, October, vol. 5 no. 4, pp 446-454

Wagoner, M.P., Buttlar, W.G., and Paulino, G.H. (2005a), “Development of a Single-Edge Notched Beam Test for the Study of Asphalt Concrete Fracture”, Geotechnical Special Publication, n 130-142, *Geo-Frontiers 2005*.

Wagoner, M.P., Buttlar, W. G., and Paulino, G. H. (2005b), “Disk-shaped Compact Tension Test for Asphalt Concrete Fracture”, *Experimental Mechanics*, Vol. 45, No. 3, pp. 270-277.

Walton, K. (1987), “The effective elastic moduli of a random packing of spheres”, *J. Mech. Phys.* Solids 35:213-26.

Wells, A. A. (1963), ‘‘Application of Fracture Mechanics at and Beyond General Yielding,’’ Br. Weld. J., **10**, pp. 563–570.

Whitney, J. M., and Nuismer, R. J. (1974), ‘‘Stress Fracture Criteria for Laminated Composites Containing Stress Concentration,’’ *J. Compos. Mater*., **8**, pp.253–264.

Xu, X. P. and Needleman, A. (1994), "Numerical Simulations of Fast Crack Growth in Brittle Solids", *Journal of the Mechanics and Physics of Solids*, Vol. 42, No. 9, pp. 1397-1434.

Yamaoka, I., H. Miyai, K. Yasuda, and T. Hara (1990), "Testing of Asphalt Concrete Pavement with Fabric Interlayer and Long-Term Observation. *In Fourth International Conference*, Volume 2, The Hague, May.

Yang, B Jiao, Y and Lei, S. (2006), "A Study on the effects of microparameters on macroproperties for specimens created by bonded particles", Engineering Computations: *International Journal for Computer-Aided Engineering and Software*, Vol.23 No.6, pp. 607-631.

Yang, S.H. and Al-Qadi, I.L. (2006), "Cost-effectiveness of using geotextiles in flexible pavements", *Geosynthetics International*, Vol. 14, issue 1, pp. 2-12.

You, Z. and Buttlar, W.G. (2005), "Discrete Element Modeling to Predict the Modulus of Asphalt Concrete Mixtures", *ASCE Journal of Materials in Civil Engineering*, Vol. 17, pp. 140-146.

Zhang, R. and Li, J. (2006), "Simulation on mechanical behavior of cohesive soil by Distinct Element Method", *Journal of Terramechanics* 43, pp. 303-316.

Zhao, Xueliang (2009), "A Numerical Investigation of the Effect of Varying Loading Condition on Soil Response", Ph.D Dissertation, North Carolina State University.